# OPTICAL TECHNIQUES APPLIED TO
# MEASUREMENTS IN ART

by

Paolo Zanetta

A Doctoral Thesis
submitted in partial fulfillment of
the requirements for the award of
Doctor of Philosophy
of
Loughborough University of Technology
U.K.

June 1994

# Abstract

Optical diagnostic techniques are particularly attractive for the non destructive detection of incipient damage and the evaluation of the state of surface decay. Non contact, high precision measurements of the shape and deformation of an artifact can be performed using laser methods based on holographic and speckle interferometry.

The analysis of thermal deformation has allowed the detection of detachments, microcracks, and material defects in wooden panels and frescoes. Contour maps of stone, metal, and wooden objects have been produced with full-field imaging techniques. Image processing algorithms have been developed and applied to the extraction of quantitative data from the resulting interferograms.

Research and experimental validation for in-situ inspection of artworks have been carried out through the application of Electronic Speckle Pattern Interferometry. Optical fibres were used to reduce the number of optical elements and to increase the flexibility and compactness of the measuring system. Portable instruments able to fit the requirements of out-of-laboratory measurements have been developed. Measurements performed on easel paintings and frescoes are presented and discussed.

A novel method based on local correlation of laser speckles is proposed for the study of salt efflorescence on stone surfaces. A measure of local correlation is derived from the digital subtraction of speckle patterns. Aspects regarding the rate at which efflorescence occurs and the influence of geometrical discontinuities and material defects are investigated.

A review of non destructive testing techniques applied to the study and conservation of works of art is included. The role of optical techniques in artwork diagnostics is discussed and future developments in the field are presented.

# Acknowledgements

# Table of Contents

# Introduction

In recent decades, the world-wide concern for the environment has led to a renewed interest in the preservation of the cultural heritage. Damage affecting statues and paintings and threatening the existence of architectural monuments and archaeological sites may come in different forms. The principal cause of decay is natural ageing, which is related to weathering, earthquakes, and micro-organisms. However, many other factors, e.g. pollution, lack of maintenance, and excessive tourism, accelerate the mechanisms of deterioration and make repair work more urgent.

Scientific methods are increasingly being applied to conservation in order to provide effective solutions to the variety of problems affecting monuments and artifacts. A scientific approach also helps to avoid incorrect repair which has been one of the main causes of damage in the past.

Microanalytical techniques are usually applied to study the microstructural properties and the material composition of artifacts. Scanning electron microscopy, X-ray diffraction, X-ray fluorescence, mass spectrometry, colorimetry, and chemical analysis are some examples. These techniques are based on the analysis of fragments sampled with particular care and in small quantities. On the other hand, Non-Destructive-Testing (NDT) techniques offer the advantage of direct inspection as sampling is not necessary. Among NDT techniques applied to artifacts the most common are X-ray radiography, photogrammetry, and photography in the visible, infrared, and ultraviolet regions of the electromagnetic spectrum. To perform any investigation on artworks, it is important to ensure that the methods proposed do not alter the artistic content of the object.

Laser techniques, based on holographic interferometry, are particularly attractive as diagnostic tools since non-intrusive and non-contact inspection is performed with unrivalled precision. In the investigation of art objects, defects, such as detachments between the priming layers of a painting, can be revealed at their incipient stage. The effectiveness of repair work can be evaluated by comparison of the results before and after restoration. Since areas of high mechanical stress can be detected by observing the surface microdeformation, the formation of flaws can be predicted. The effects of daily

(or seasonal) variations of temperature and humidity can also be monitored. In general, the intensity of the laser beams used for the interferometric measurements is low and there is no risk of damage to the objects.

Optical contouring methods can be used for measuring the surface geometry of artworks. A quantitative description of the surface is normally missing in museum archives, the only exception is made for 1:1 scale moulds, which are occasionally produced to cast copies. Erosion and corrosion processes acting on stone monuments can be monitored. The comparison of 3D maps of the surface profile gives a quantitative evaluation of the wear which has occurred in the time elapsed between two measurements.

The application of laser techniques to conservation problems was envisaged in the seventies by scientists demonstrating the potential of laser light for cleaning, display, and diagnostics of artworks. These initial results were encouraging but at that time laser technology was at an early stage and presented some disadvantages, e.g. high costs and low flexibility, which hindered the widespread use of these techniques among restorers.

Artworks present a large variety of surfaces, differing in material, colour, roughness, etc. Unlike many other cases (e.g. mechanical applications), no treatment can be made to render the surface scattering more uniform and intense. Thus some limitations on the size of the inspected area and the fringe contrast have to be taken into account. Furthermore, since transportation risks and costs are very high for art objects, measurements should be performed in-situ or inside the restoration laboratories. The equipment has therefore to be portable and insensitive to disturbances such as mechanical vibrations, daylight, and so on.

On the basis of recent developments in optical and imaging technologies, the research work presented in this thesis aims at demonstrating the practical use of full-field interferometric techniques for the routine inspection of artifacts and for the characterisation of deterioration mechanisms. The development of simple and effective instruments for in-situ measurements has been considered. Collaboration with conservation scientists and restorers played an important role in familiarisation with various problems of conservation.

A brief review of the NDT techniques applied to the study and conservation of artworks is presented in chapter 1. Chapter 2 contains the fundamental principles of holography and laser speckle. The techniques of double-exposure, real-time holographic interferometry, and Electronic Speckle Pattern Interferometry (ESPI) are presented. The use of optical fibres in holographic and speckle systems is discussed.

2

Chapter 3 deals with the application of digital processing techniques to interferograms. The enhancement of fringe contrast, the reduction of speckle noise, and the extraction of the interferometric phase are illustrated with some examples. The practical use of Fourier techniques for the quantitative analysis of holographic and ESPI interferograms is investigated in detail.

The experimental work based on microdeformation measurements is presented in chapter 4. Initially the holographic detection of defects is illustrated for specimens of composite materials employed in the aircraft industry. The experiments allowed a familiarisation with the diagnostic use of interferometric techniques. Since the specimens have a layered structure, the holographic measurements can also be considered as preliminary tests for the detection of flaws in the priming layers of paintings. ESPI has been applied to investigate the static behaviour of violins under the load of the strings. Finally, the development and testing of two portable instruments for out-of-laboratory measurements are presented together with the results obtained in-situ for frescoes and paintings.

Contour measurements based on holography and fringe projection are the subject of chapter 5. A brief description of the principles and features of these techniques is included. The development of contour systems is illustrated and the results for objects of different materials, e.g. metal, stone, and wood, are presented. The application of image processing techniques for the retrieval of digital contour maps is discussed.

Chapter 6 describes how local modifications of the surface microstructure can be adequately monitored by recording the digital difference between two speckle patterns. The technique, based on local correlation of speckles, is applied to characterise the surface alteration mechanism in stones caused by salt efflorescence. Ageing by salt crystallisation cycles is employed to accelerate the decay of stone specimens.

In the conclusions, the main results of the work carried out are summarised and the role of optical techniques in conservation problems is discussed. Future trends for the research work are highlighted.

# Chapter 1

# A review of non destructive testing techniques applied to the study and conservation of works of art

## 1.1. Introduction

The aim of this chapter is to present the state of the art of the principal applications of Non Destructive Testing (NDT) techniques to the study of artworks. In general, restorers also claim that micro analytical methods, based on chemical and physical analysis of small samples, can be considered as non destructive since no structural or artistic alteration is produced. In this brief review, however, the term *NDT techniques* has been used to indicate those techniques which can be applied to an artifact without fragment sampling.

The review mainly deals with imaging techniques including X-rays, photography, photogrammetry, and thermography. For each technique presented the attention is focused onto its fundamental principles and the applications to the study of artworks. Among non-imaging techniques ultrasonic testing has been presented.

## 1.2. Imaging techniques

### 1.2.1. X-rays

An X-ray radiograph consists of the transmission image produced by irradiating an object with a beam whose electromagnetic frequency is in the range from $10^{16}$ to $10^{19}$ Hz. In laboratory intruments X-rays are produced by collision of accelerated electrons with a metal target. The penetrating depth of the X-ray radiation is directly proportional to its energy (or frequency). For a given frequency, X-ray absorption depends on the density, thickness, and atomic components of the inspected object.

These differences in absorption give rise to pictures (radiographs), which can readily be recorded. The use of X-ray radiography is very common among restorers as it can successfully be applied to a large variety of art objects. One of its most important achievement is the possibility to reconstruct the history of paintings. Since some pigments have a characteristic absorption of X-rays, subsurface pictorial layers are readily detected. In particular, it should be noted that X-rays are absorbed by lead white, a pigment that has widely been used in the preparation of many colours. The presence of artist's *pentimenti*, earlier underlying paintings, and unknown repair work can thus be unveiled. In addition, the precise detection of fine details, e.g. the canvas

structure, the craquelure pattern, and especially the brush strokes, can give important hints on the artistic process and in some cases can lead to establish the exact origin of a painting (artist, place, etc.).

On wooden panels X-rays give information on the structural elements of the support. The shape of internal joints between adjacent planks as well as the presence of dowels or nails can readily be highlighted. The type of wood and its state of conservation (e.g. the presence of woodworm tunnels, stuccoed parts, etc.) are usually determined from radiographic inspections.

According to the radiation energy, different kinds of artworks can be investigated [1]. For 5 to 30 kV voltage of the X-ray tube, it is possible to record radiographs of paintings on canvas or linen, whilst voltages in the range of 30-80 kV are best suited for the examination of paintings on wooden panels. Higher energies (80-250 kV) are used to inspect light metal sculptures and heavy wooden pieces. Metal or marble sculptures can also be studied by increasing the voltage up to 1000 kV. All the measurements are performed in laboratories which are usually built inside restoration centres. To inspect large objects the laboratory has to be equipped with appropriate structures for holding and scanning the artifacts with the X-ray beam.

In order to produce high-contrast images X-ray radiographs are recorded onto a charged Selenium plate, from which they are transferred to paper and finally fixed by heating. This technique is named Xeroradiography and offers a high resolving power and a large dynamic range which allows the distinction between regions of the same object having very different densities. The major applications of xerography have been in the field of archaeology for the study of ceramic objects [2,3].

When an artifact is very thick and its transparency to X-rays is very low, γ-radiography is an alternative. γ-rays are very penetrating due to their very high frequency. The γ-rays used in art are generated by radio-isotopes such as Indium 192, Caesium 137, and Cobalt 60. In spite of their penetrating power, the intensity is usually low and long exposure times are necessary. Another disadvantage is the requirement of strict safety precautions during the measurements.

In some cases it might be useful to take a pair of radiographs by displacing the X-ray source between the exposures. If viewed simultaneously in a stereoscope, object details can be observed in their own location in space. In this way painted surfaces on distinct planes can be examined one at a time. This technique is known as Stereoradiography.

X-ray computer tomography has recently been proposed for the study of small artifacts [4]. The results of tomographic inspection are 3-D density maps relating to sections of the object. From tomographic images it is possible to detect the presence of voids, inclusions, or to study material discontinuities such as cracks. The material thickness distribution of hollow objects can successfully be measured.

Another recent technique is Digital Radiography [5], which has opened new and interesting perspectives for in-field inspection of art objects. The recording medium is a fluorescent plate made of $F_2Ba$ crystals doped with Europium. The radiographic image is obtained by digitising the visible radiation emitted when the phosphor plate, after being exposed to X-rays, is scanned with a laser beam. The spatial resolution of the resulting images is however lower than in traditional radiography.

Finally, it is worth citing the application of Electron Emission Radiography [6] and Neutron Activation Autoradiography [7] to some cases of study.

## 1.2.2. Ultra-violet (UV) radiation

The ultra-violet spectrum lies in the frequency range from $8 \times 10^{14}$ to $3.4 \times 10^{16}$ Hz. UV rays have mostly been applied to the study of paintings [8]. Two techniques are now available: *UV photography* and *UV fluorescence*. The latter is the most used in practice.

### 1.2.2.1. UV Photography

UV photography exploits only a fraction of the UV spectrum since glass optical elements become opaque at wavelengths shorter than 320 nm[1]. The object is illuminated with a UV source (Hg-vapour, Wood's lamp) and the resulting image is recorded on a high-contrast black and white film. Since the source and the light scattered by the object surface usually have strong components in the visible region of the spectrum, UV filters are placed after the lamp and at the camera aperture. In general, the scattered UV radiation is not very intense and thus exposure times of some minutes are typical. UV images of paintings have successfully been used to detect the presence of some pigments in the pictorial layers. Underlying paintings and *pentimenti* can sometimes be highlighted.

---

[1]By using quartz lenses, which are however very expensive, this lower limit becomes 250 nm.

## 1.2.2.2. UV Fluorescence

When illuminated with UV radiation, many substances emit visible light as a result of luminescence mechanisms occurring in the atoms and molecules [9]. When luminescence occurs very rapidly after atomic excitation the phenomenon is usually referred to as fluorescence. The images produced by UV fluorescence are recorded on colour films with a conventional photographic camera. However the intensity of the fluorescent emission is normally very weak, and thus, although a high sensitivity emulsion is used, the exposure can last some minutes.

In the case of paintings illuminated with UV radiation, the colours of luminescent light can be associated with single pigments. These measurements can however be made only if the fluorescent light receives negligible contributions from the painting varnish. For this reason fluorescence analysis can readily be performed during repair work after the removal of the varnish layers. The technique can also be applied to detect stuccoed areas and small retouchings.

UV fluorescence has the advantage over UV photography that the fluorescent radiation can be observed directly by the unaided eye. This greatly simplifies its practical use as a non-destructive testing tool.

## 1.2.3. Visible light

Visual examination of objects illuminated with visible light ($3.84 \times 10^{14}$-$7.69 \times 10^{14}$ Hz) is the simplest form of inspection. Preliminary information on the state of conservation can readily be deduced by viewing the artifacts from many angles and under different illuminating conditions. Eroded or corroded surfaces, missing parts, colour alterations can, for example, indicate the presence of on-going deterioration processes.

When the illumination angle is almost parallel to the surface inspected, it is possible to detect surface irregularities such as swelled regions of the varnish in easel paintings, or of the plaster in frescoes. This technique is known as *raking light illumination* and has widely been used among restorers [10]. Common light sources are spotlights, microscope or halogen lamps, whose emitted light is often collimated to increase the sensitivity of the technique. A recent study [11] has proposed the use of a laser source. Since laser light has a very low divergence, raking light illumination can successfully be applied to detect fine surface reliefs.

Restoration scientists have adapted medical and industrial endoscopes for the inspection of the internal parts of bronze statues [12]. This has greatly contributed to a deeper understanding of the ancient processes adopted to fuse the bronze. Endoscopic vision has also been used to facilitate the sampling and cleaning of hidden regions of artifacts.

All the important events (e.g. exhibitions, conservation treatments) in the life of an art piece are usually recorded on video tapes, transparencies, etc. Although colour photography is still the most common technique used for documentation, the recent developments of video electronic technologies have introduced new interesting methods for recording, storage, and distribution of artwork pictures.

Images in digital form can now be entered into data bases, transmitted through informatic networks, and made available to museums, libraries, educational and research bodies, etc. High resolution digital photography has recently been proposed for the assessment of transportation damage in paintings [13]. 2-D cross correlation algorithms were developed for the detection of scratches, modifications of the craquelure pattern, and other alterations occurred during transportation.

The application of *photogrammetric techniques* [14] allows the reconstruction of the 3-D shape of an object from at least two pictures taken at different angles. The spatial co-ordinates of a point are calculated by evaluating the position of its image in the recorded pictures. Photographic cameras with metric calibration are used in order to correctly apply the triangulation algorithms.

Traditional methods of restitution, however, can take many hours or days for extracting the spatial co-ordinates of the points and lines representing the object geometry. Since artworks, in general, are rich in detail, the time required for obtaining the desired precision can be very long. It is expected that in the near future this disadvantage will be removed by the application of *digital photogrammetry*. This new technique, which has recently been applied for aerial surveys, is based on automatic processing of photographs, which have been converted into digital form with a high resolution scanner.

Beyond the valid application for documentation of art objects and monuments, photogrammetric measurements can also be very useful during repair work, especially if the 3-D results are combined with Computer Aided Design (CAD) systems [15].

## 1.2.4. Infrared (IR) radiation

### 1.2.4.1. IR Photography

This technique is based on the observation of the near infrared (730-900 nm) radiation scattered by an object under normal illumination. Common light sources in fact have frequency components in the near infrared band, which can be selected and photographed with the use of optical filters. The images obtained can be very helpful for the detection of painting underdrawings, since some colour pigments (e.g. red. white, brown) are transparent to near IR radiation [16].

Until recently, IR photographs have been taken on colour and black and white films, whose emulsions had been specially treated for IR wavelengths. These films, however, have several limitations which affect the reliability of the measurements [17]. In particular, the emulsion sensitivity is strongly dependent on the storage temperature and the development process. For these reasons, IR photography is now performed with CCD (Charge Coupled Device) video cameras, which, being based on semiconductor technology, have a good sensitivity in the near infrared range (wavelengths less than $1 \mu m$).

### 1.2.4.2. IR Reflectography

IR reflectography has been applied for the first time to artworks examination by Van Asperen de Boer in 1970 [18]. The technique is based on the formation of images in the near infrared at wavelengths of approximately 2 $\mu m$. The images recorded at this wavelength are useful for the detection of underdrawings and *pentimenti*, as the 2 $\mu m$ radiation penetrates the pictorial film of a large variety of pigments. The sensitivity of the method depends on the thickness of the pictorial film and on the contrast of the underdrawings.

The basic equipment for IR reflectography consists of a common IR lamp, a vidicon camera for converting the IR image into a video signal, and a monitor for display. These systems, however, give low resolution images, which in most cases are affected by geometric distorsion and non-linear response of the vidicon. Now, CCD arrays (based on PtSi, or HgCdTe) produce non distorted images with higher resolution. Their use in IR reflectometry systems for the examination of paintings has recently been investigated [19].

## 1.2.4.3. Thermography

Thermography is a contactless and non-intrusive technique based on the detection of infrared radiation in the wavelength region from 3-4 $\mu$m to 15 $\mu$m. Since at normal temperatures (270-300 K) most objects radiate thermal energy in this spectral range, thermographic images are closely related to the thermal properties of an object. Temperature changes as small as 0.1 °C are commonly resolved, and heat conductance differences can be detected.

A thermographic camera is more complicated and expensive than video cameras for the visible or near infrared. The lens is commonly made of Germanium, as this material is more transparent than glass in the range of wavelengths considered. The image is scanned with mechano-optical elements (rotating prisms, tilting mirrors) and is converted to a standard video signal by one or more photodetectors. The infrared detectors used are photosensitive elements (e.g. InSb, HgTeCd) operating at very low temperatures (-200 K). The thermal map can be viewed on a B/W monitor as a grey-level image where the bright points correspond to areas of high thermal irradiance. The most recent generation of IR detectors, known as Focal Plane Arrays (FPAs), are now also available in the 2D version. In spite of many advantages in terms of spatial resolution and distortion, the high cost of these devices limits their use to military applications.

In the field of artworks, thermography has been proposed for the inspection of architectural elements [20], frescoes [21], bronze statues [22], and easel paintings [23]. Thermographic examination can be carried out by observing either the natural infrared emission or the thermal response to artificially induced heating. Structural discontinuities, voids, detachments, material inhomogeneities, are some examples of defects which modify the thermal behaviour of objects. Damaged areas can be located in correspondence to abrupt changes and anomalous brightness distributions of thermal images. The sensitivity of the technique to several factors (temperature, thermal emissivity, conductance, reflectivity) has given rise to some problems in the interpretation of the results on artworks. This is due to the complex structure, to the variety of materials employed and to the modifications caused by ageing and deterioration mechanisms [24].

## 1.3. Non-Imaging techniques

### 1.3.1. Ultrasonic testing

Ultrasonic testing is one of the most popular techniques for non-destructive evaluation of materials and structures. The measurements rely on the study of the transmission of mechanical waves in solids. The frequencies of the mechanical waves used lie in the interval from 20 kHz to 15 MHz, i.e. in the ultrasound region. An ultrasonic beam is generated with a piezoelectric transducer and coupled to the object surface with liquids such as water, oil, or grease. For absorption measurements the transmitted beam is sensed by another transducer at the other side of the object. Alternatively, the echo signal is analysed. In this case a single transducer is operated as a transmitter and as a receiver.

As the velocity and the absorption coefficient of ultrasonic waves are typical properties of the component material, deviations from normal values indicate the presence of damage. In particular, since ultrasonic waves are strongly attenuated at the boundaries between two materials with different densities, absorption measurements can be useful for the detection of delaminations, cracks, and voids. In some cases the internal position of these flaws can also be located by measuring the time for the ultrasonic echo to be detected. By measuring the propagation velocity it is possible to evaluate variations of the material mechanical properties such as density, Young's modulus, and Poisson's ratio.

A large variety of artworks, e.g. metallic and wooden statues, frescoes, paintings, and stone monuments have been investigated with ultrasonic testing. Metal castings, for example, have been studied in order to calculate thickness and estimate their state of conservation [25]. Ultrasonic waves have the advantage over X-rays of being able to detect delamination and detachments situated between the layers of a painting, i.e. parallel to its surface.

The effectiveness of repair work on masonry structures has been assessed by performing measurements of the velocity and the waveform of ultrasonic waves before and after penetration and diffusion of grout by injection [26]. Ultrasonic testing has also been proposed for the evaluation *in-situ* of monumental stone deterioration [27]. Other studies have dealt with the relation between the humidity content of porous stone and the velocity of the ultrasonic waves [28].

In some cases, ultrasonic inspection can give rise to unwanted alterations of art objects. The mechanical waves, propagating in the material, could damage, for example, the fine particles of particular pigments, or decorations. Furthermore, the use of coupling liquids can be a limitation to the ultrasonic investigation of paintings. In this case it is worth citing the recent results on the use of an air-coupled ultrasonic system for the examination of wooden panels [29].

## 1.4. References

[1] Gilardoni A., Ascani Orsini R., Taccani S., "X-rays in Art", Gilardoni S.p.A. Mandello Lario (CO) Italy 1977

[2] Heinemann S., "Xeroradiography: a new archeological tool", American Antiquity, (1976), 41 106-111

[3] Glazman W.D., Fleming S.J., "Xeroradiography: A key to the nature of technological change in ancient pottery production", Nuclear Instruments and Methods in Physics Research, (1986), A242 588-595

[4] Cheng Y.T., Mishara J., "A computerized axial tomographic study of museum objects", Mat. Res. Soc. Symp. Proc., (1989), 123 19-24

[5] Harrison R.M., "Digital radiography", Phys. Med. Biol. Bul., (1989), 33 751-784

[6] Bridgman C.F., Michaels P., Sherwood H.F., "Radiography of a painting on copper by electron emission", Studies in Conservation, (1965), 10 1-7

[7] Syre E.V., Lechtman H.N., "Neutron activation autoradiography of oil paintings", Studies in Conservation, (1968), 13 161-185

[8] Matteini M., Moles A., "Scienza e restauro", (1984), Nardini Editore 175-182

[9] Alonso M., Finn E.J., "Fundamental University Physics: III Quantum and Statistical Physics", (1968) Addison-Wesley 274-277

[10] Stout G.L., "The Care of Pictures", (1975), Dover New York

[11] Asmus J.F., Marshack A., "Grazing-incidence laser photography", *2nd International Conference on Non-Destructive Testing, Microanalytical Methods and Environment Evaluation for Study and Conservation of Works of Art*, Perugia (Italy) 17-20 April 1988, I 6/1-9

[12] Accardo G., Ciabattoni R., Micheli M., "Applicazione di nuove tecniche endoscopiche nell'esame di opere d'arte", *2nd International Conference on Non-Destructive Testing, Microanalytical Methods and Environment Evaluation for Study and Conservation of Works of Art*, Perugia (Italy) 17-20 April 1988, I 2/1-11

[13] Burmester A., Cupitt J., Derrien H., Dessipris N., Hamber A., Martinez K., Müller M., Saunder D., "The examination of paintings by digital image analysis", *3rd International Conference on Non-Destructive Testing, Microanalytical Methods and Environment Evaluation for Study and Conservation of Works of Art*, Viterbo (Italy) 4-8 October 1992, 201-214

[14] American Society of Photogrammetry, "Manual of Photogrammetry", (1980) 4th Edition

[15] Belli A., Belli G., Mecozzi G., Rezzi S., "La ricollocazione su superfici curve di dipinti murali strappati mediante rilievo fotogrammetrico ed ipotesi formulate al C:A.D.: Teatro di Fano", *3rd International Conference on Non-Destructive Testing, Microanalytical Methods and Environment Evaluation for Study and Conservation of Works of Art*, Viterbo (Italy) 4-8 October 1992, 147-154

[16] "Examination by Infrared Radiation" in Van Schoute R., Verougstraete-Marcq H. (Eds), "Scientific Examination of Easel Paintings", PACT Journal of the European Study Group on Physical, Chemical and Mathematical Techniques Applied to Archeology, (1986) 13 pp. 109-130

[17] Caneva C., Pampallona A., Tittoni E., "Possibilità e limiti delle indagini all'IR e all'UV per l'approfondita lettura dei dipinti: *La buona ventura* del Caravaggio", *2nd International Conference on Non-Destructive Testing, Microanalytical Methods and Environment Evaluation for Study and Conservation of Works of Art*, Perugia (Italy) 17-20 April 1988, I 17/1-13

[18] Van Asperen de Boer J.R.J., "Infrared reflectography. A contribution to the Examination of Earlier European Paintings", (1970) Thesis, University of Amsterdam

[19] Bertani D., Cetica M., Poggi P., Buzzegoli E., Kunzelman D., "A way to shoot reflectograms ready to be juxtaposed in a mosaic", *3rd International Conference on Non-Destructive Testing, Microanalytical Methods and Environment Evaluation for Study and Conservation of Works of Art*, Viterbo (Italy) 4-8 October 1992, 173-174

[20] Baratono P., Cardellini F., Diana M., Trombetta C., Venturini G., "Termografia e analisi di immagine, ultime applicazioni su strutture architettoniche", *2nd International Conference on Non-Destructive Testing, Microanalytical Methods and Environment Evaluation for Study and Conservation of Works of Art*, Perugia (Italy) 17-20 April 1988, I 9/1-16

[21] Caneva C., Pampallona A., Testa G., "Le indagini termografiche e termoigrometriche per il rilievo dell'umidità edegli affreschi. Caso della 'Risurrezione della carne' di Luca Signorelli", *2nd International Conference on Non-Destructive Testing, Microanalytical Methods and Environment Evaluation for Study and Conservation of Works of Art*, Perugia (Italy) 17-20 April 1988, I 16/1-11

[22] Cagnetti V., Diana M., Ferretti M., Moioli P., "La Chimera di Arezzo: Studio di alcuni aspetti metallurgico-strutturali mediante fluorescenza X e termografia ad alta risoluzione", *3rd International Conference on Non-Destructive Testing, Microanalytical Methods and Environment Evaluation for Study and Conservation of Works of Art*, Viterbo (Italy) 4-8 October 1992, 217-228

[23] Miller B.F., "The thermographic detection of voids in panel paintings", *IIC Oxford Congress. Conservation of Wood in Painting and the Decorative Arts*, (1978) 145-148

[24] Kulicki J., "Use of thermography as an investigatory method in conservation research - outline of problems", in Baer N.S., Sabbioni C., Sors A.I., (Eds.), European Symposium "Science, technology and European cultural heritage" (1989 Bologna Italy), Butterworth-Heinemann Ltd., (1991) 566-570

[25] Gilardoni S.p.A., Laboratori di Ricerca, "Applicazioni dell'informatica alle indagini su reperti artistici con ultrasuoni", *2nd International Conference on Non-Destructive Testing, Microanalytical Methods and Environment Evaluation for Study and Conservation of Works of Art*, Perugia (Italy) 17-20 April 1988, IV 10/1-8

[26] Berra M., Binda L., Baronio G., Fatticcioni A., "Ultrasonic pulse transmission: a proposal to evaluate the efficiency of masonry strengthening by grouting", *2nd International Conference on Non-Destructive Testing, Microanalytical Methods and Environment Evaluation for Study and Conservation of Works of Art*, Perugia (Italy) 17-20 April 1988, I 10/1-18

[27] Montoto M., Calleja L., Perez Garcia B., Suarez Del Rio L.M., Ruiz De Argandoña, Esbert R.M., Grossi C.M., "Non-destructive ultrasonic procedure to evaluate in situ the relative deterioration of monumental stones: preliminary results", in

Baer N.S., Sabbioni C., Sors A.I., (Eds.), European Symposium "Science, technology and European cultural heritage" (1989 Bologna Italy), Butterworth-Heinemann Ltd., · (1991) 545-548

[28] Esbert R.M., Valdeon L., Ordaz J., Alonso F.J., Grossi C.M., "Ultrasonic velocity and humidity in monumental stones, in Baer N.S., Sabbioni C., Sors A.I., (Eds.), European Symposium "Science, technology and European cultural heritage" (1989 Bologna Italy), Butterworth-Heinemann Ltd., (1991) 597-600

[29] Murray A., Boltz E., Fortunko C.M., Mecklenburg M.F., Green R.E. Jr., "Air-coupled ultrasonic system for non-destructive evaluation of wooden panel paintings", *3rd International Conference on Non-Destructive Testing, Microanalytical Methods and Environment Evaluation for Study and Conservation of Works of Art*, Viterbo (Italy) 4-8 October 1992, 441-450

# Chapter 2

# Holographic and speckle measurements: background concepts

## 2.1. Interference of light

Light is composed of electric and magnetic fields oscillating at frequencies of the order of $10^{15}$ Hz and propagating in space at a speed $c = \dfrac{c_0}{n}$, where $c_0 = 2.998\,10^8$ m/s is the speed of light in vacuum and $n$ ($n>1$) is the refractive index of the medium. For a monochromatic and linearly polarised plane wave the optical field is fully described by the amplitude and phase distributions. Therefore, for a generic point $P$, a complex expression $U(P)$ can be used to represent the electric or magnetic component of light:

$$U(P) = U(P)\exp(-j\phi(P)) \tag{2.1}$$

$U(P)$ and $\phi(P)$ are the amplitude and the phase of the light wave respectively. Since the optical field oscillates at an extremely high rate, light detectors can measure only the time-averaged value of the optical power, namely *irradiance* or *intensity*. If $\varepsilon$ is the permittivity of the medium, and indicating with the asterisk the complex conjugate, the intensity $I(P)$ is expressed by

$$I(P) = \varepsilon c U(P) U^*(P) \tag{2.2}$$

Interference occurs at a point $P$ where two monochromatic light waves of the same frequency and polarisation are superimposed. In this case, the resulting intensity produced by the sum of the two optical fields is not the sum of the intensities. If $U_1$ and $U_2$ are the fields at a point $P$, the total intensity $I$ is proportional to the squared sum of the complex amplitudes and it is given by:

$$I = \varepsilon c (U_1 + U_2)^2 = \varepsilon c (U_1 + U_2)(U_1 + U_2)^*$$

and finally

$$I = I_1 + I_2 + 2\sqrt{I_1 I_2}\cos(\phi_1 - \phi_2) \tag{2.3}$$

18

It is worth noting that the third term of the previous equation contains the difference of the optical phases. Thus the optical phase can be evaluated indirectly from the intensity profile obtained by interference. The interference phenomenon is very clear when the two optical waves have the same intensity. In this case, if the phase difference is an integer multiple of $2\pi$ there is a constructive interference and the total intensity is four times that of a single wave. On the other hand, destructive interference occurs when the phase difference is an integer multiple of $\pi$, and the intensity is zero.

### 2.1.1. Interference conditions

Optical interference can be observed only if certain conditions are satisfied. The strongest constraint is the *temporal coherence* of light [1]. Conventional light sources emit a sequence of photon wave trains whose electromagnetic fields oscillate with a continuous phase function only for a small time, corresponding to the duration of an atomic transition. Therefore the optical wave is interrupted so frequently that any interference pattern cannot effectively be detected. This effect is closely related to the degree of monochromaticity of a light wave. In fact, any phase jump causes a broadening of the temporal bandwidth and consequently the number of optical frequencies is increased. The time during which the wave has regular oscillations is defined as the *coherence time*. The coherence time $\tau$ is inversely proportional to the bandwidth $\Delta v$ of the light source.

If it were possible to freeze in space the wave profile, on verage the optical field would appear as a continuous sinusoidal function over an interval $l_c = c\tau$, which is defined as the *coherence length*. An effective way to produce interference at a point $P$ is to split the light from a source into two beams, whose paths to $P$ differ less than the coherence length. By doing so the waves superimposing at $P$ belong to the same wave train emitted by the source and a stable interference pattern results.

Another property of light that plays a fundamental role in the phenomenon of interference is *polarisation* [2]. If two light waves are linearly polarised in two different states the interference term of the intensity resulting from their superposition contains the cosine of the angle between the two polarisation planes. In fact when squaring the sum of two vectors a scalar product is obtained in correspondence to the interference term. Therefore the maximum interference occurs if two waves have the same polarisation whilst no interference occurs if the polarisation vectors are perpendicular.

19

## 2.1.2. Coherent light sources

The coherence length of most light sources is normally very short, making the observation of interference a hard exercise of matching the optical paths. This can be illustrated by the following values [3]: for filtered sunlight (visible spectrum) $l_c \approx 800$ nm, for Light Emitting Diodes (LEDs) $l_c \approx 20\,\mu$m, for low pressure sodium lamp $l_c \approx 600\,\mu$m. These values are very small in comparison with the coherence length of any laser source. In fact, the light generation principle in a laser, i.e. stimulated emission, intrinsically generates a wave train of well ordered photons. In general, for a laser source the coherence length depends on the number of oscillating longitudinal modes in the cavity and on the width of their spectral lines [4]. With the appropriate active material, these parameters can be adjusted to such an extent that a coherence length of several metres can be obtained.

## 2.2. Laser speckle

When an object is illuminated by a coherent light wave, the intensity of the scattered field has a characteristic granular appearance. The diffused light appears as if it were composed of randomly distributed bright grains, called "speckles". This effect can be observed only when the object surface is optically rough, i.e. the standard deviation $\sigma$ of the surface profile is of the same order or greater than the wavelength $\lambda$ of the illuminating light (for visible light $\lambda \cong 0.5\,\mu$m). This condition is encountered for the surfaces of most materials and consequently speckles can easily be observed whenever an object is illuminated by a laser beam. The random nature of a speckle pattern is related to the microscopic variations of the surface profile. All the points of the surface act as sources of secondary wavelets which follow different optical paths and mutually interfere. In a similar way, it is possible to explain the presence of speckles when coherent light is transmitted through a diffusing object.

The accepted theory of laser speckle refers to the solution of the well-known statistical problem of the "drunkard's walk". The final position of the random walk is the sum of many independent steps, each of them represented by a displacement vector. For the speckle phenomenon the optical field at a given point $P$ is made of the independent contributions from each point of the rough surface. Mathematically, the two cases are identical since the final optical field at $P$ is the vectorial sum of many independent amplitudes associated with the scattered wavelets. In the statistical model the light is assumed to be perfectly monochromatic and linearly polarised. The $i$-th component of the optical amplitude is:

$$\mathbf{U}_i(P) = U_i(P)\exp(-j\phi_i(P))$$

If the surface is optically rough, i.e. $\lambda \ll \sigma$, the light wavelets have mutual phase delays of several $2\pi$ before leaving the surface and the elementary phase $\phi_i$ can be considered uniformly distributed in the interval from $-\pi$ to $+\pi$. The optical amplitudes $U_i$ are considered statistically independent if the heights of surface points are not correlated. Since the field at $P$ is made of a large number of wavelets, the complex amplitude is a circular complex Gaussian random variable. From these hypotheses Goodman [5] evaluated the fundamental properties of laser speckle. Some of his results are reported in the following. From the first-order statistics the probability that the intensity of a speckle lies between $I$ and $I+\mathrm{d}I$ is expressed by:

$$p(I)\mathrm{d}I = \frac{1}{\langle I \rangle}\exp(-\frac{I}{\langle I \rangle})\mathrm{d}I \qquad (2.4)$$

where $\langle I \rangle$ is the average intensity over many speckles. For the phase $\phi$ a uniform distribution is obtained between $-\pi$ and $+\pi$. Experimentally, Eqt. (2.4) can be confirmed by comparison with a histogram of a speckle image. It should also be observed that the most probable value for the intensity is zero.

The speckle contrast is defined as the ratio between the standard deviation $\sigma_I$ of the intensity and $\langle I \rangle$. For the negative exponential distribution in Eqt. (2.4), it is well known that $\sigma_I = \langle I \rangle$. Therefore the speckle contrast always equals unity.

In all the techniques based on a quantitative measurement of the intensity of light scattered by a rough surface, speckle behaves as a noise source. However, its effects are severe, since the signal to noise ratio $\dfrac{S}{N} = \dfrac{\langle I \rangle}{\sigma_I}$ is one whatever the value of $\langle I \rangle$.

The study of the second-order statistical properties has led to the quantitative evaluation of the speckle size, which has been defined as the distance at which the autocorrelation function has its first minimum. For the geometry in Fig. 2.1., the resulting size $b$ is given by:

21

$$b = \pi \frac{\lambda z}{l} \qquad (2.5)$$

The speckle pattern is observed on a screen at a distance $z$ from the illuminated surface of width $l$. The speckle size has no relation with the value of the surface roughness, it depends only on geometric parameters and the wavelength of light.
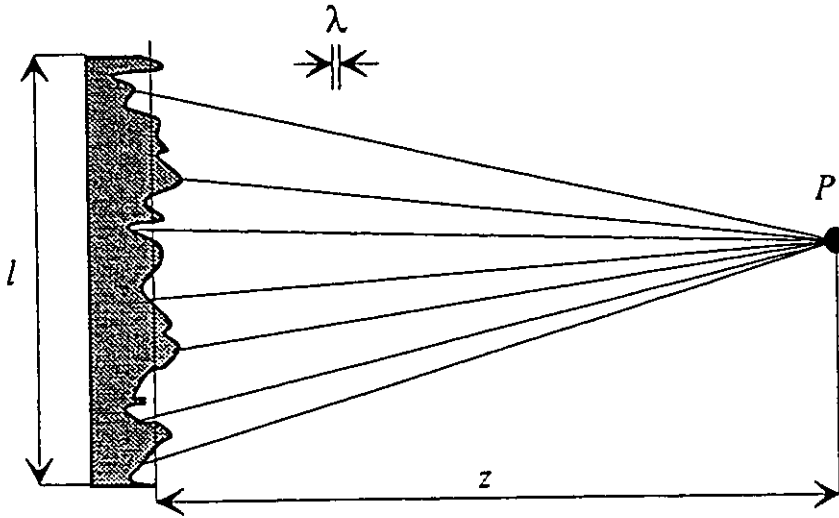


Figure 2.1. Speckle formation in a free-space geometry.
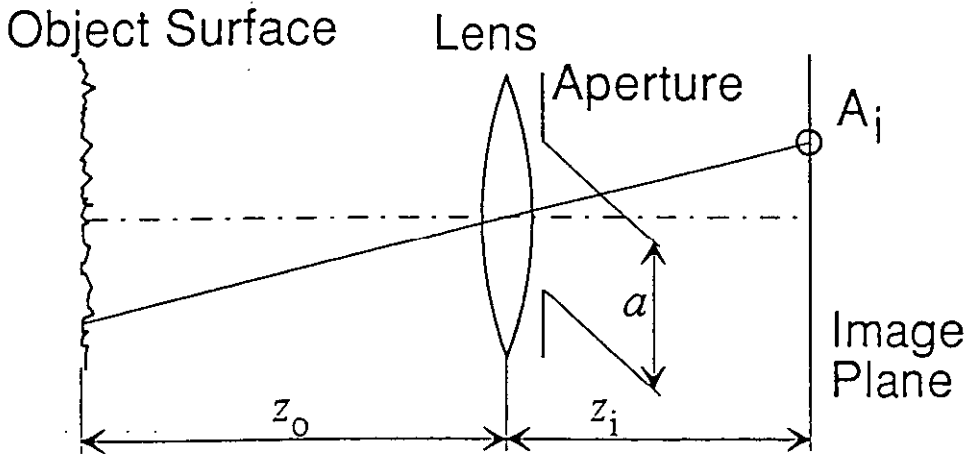


Figure 2.2. Speckle formation in a single-lens imaging system.

As long as free-space propagation of the scattered light is considered, interference concepts are sufficient to explain the formation of speckle patterns. When the object is viewed through an optical system, like the human eye or a camera, diffraction theory is also necessary to account for the appearance of the speckles in the image. This need is readily understood if an ideal (no diffraction) optical system is considered. In a single lens setup (see Fig. 2.2.) an object point is focused onto its conjugate in the image plane according to the laws of geometric optics. Each point is spatially separated from the others and no interference occurs. When diffraction effects are taken into account, the image of a single point is spread across an area $A_i$. Inversely, the intensity of an image point is made of contributions from an area $A_O$ in the object plane. Since the points in $A_O$ scatter spherical wavelets at different phases, speckles are generated by interference in the image plane. For a circular aperture the theory of diffraction [2] predicts that each point of the object produces a Fraunhofer diffraction pattern in the image plane. The resulting intensity spread function $I(r)$ for an image point is given by:

$$I(r) = I(0) \left[ \frac{2 J_1\left(\frac{\pi a r}{\lambda z_i}\right)}{\frac{\pi a r}{\lambda z_i}} \right]^2$$

where $r$ is the radial co-ordinate starting from the image point, $a$ is the aperture diameter, $z_i$ is the distance between the lens and the image plane, $\lambda$ is the light wavelength, and $J_1$ is the first order Bessel function of the first kind. The point spread function $I(r)$ has a central spot $A_i$, known in literature as the Airy disk, where most of the intensity is concentrated. The position of the first zero of the Bessel function $J_1$ defines the extension of the Airy disk and the speckle size[1]. It is thus readily found that the diameter of $A_i$ is

---

[1]This result is consistent with the aforementioned definition of the speckle size, since the autocorrelation function $R_I(r)$ of a speckle pattern in an imaging geometry [5] is given by

$R_I(r) = \langle I \rangle^2 \left[ 1 + \frac{I(r)}{I(0)} \right]$, whose first minimum corresponds to $r_i = 1.22 \frac{\lambda z_i}{a}$.

$$D_i = 2.4 \frac{\lambda z_i}{a} \qquad\qquad (2.6)$$

This equation can be generalised to describe speckle formation in any imaging system. Once the object is in focus, namely $z_i$ is fixed, the speckle size can be controlled by adjusting the aperture. The smaller the aperture the larger the speckles.

Reciprocally, it can be shown that the diameter $D_o$ of the area $A_O$ in the object plane is expressed by

$$D_o = 2.4 \frac{\lambda z_o}{a}. \qquad\qquad (2.7)$$

Finally it is noted that for an imaging geometry, speckle intensity and phase follow the same statistical distributions reported for the lensless situation. In the article by Goodman [5] the statistical properties of speckles for several cases with different assumptions about surface roughness and with speckle patterns resulting from the sum of two or more waves are presented.

## 2.3. Holographic interferometry

Holographic interferometry is based on holography's property of completely reconstructing the 3D-image of an object. The exact amplitude and phase information contained in a light wavefront can in fact be obtained by suitably illuminating a hologram with coherent light. The holographic image appears indistinguishable from that of the original object [6]. Interferometric fringes can be observed whenever two or more optical wavefronts, representing different states of an object, are reconstructed simultaneously. Since the pioneering work of Stetson [7], holographic interferometry has had an incredible number of applications in many fields and disciplines. As an experimental tool, it measures micro displacements and vibrations with a precision of the order of few tenths of a micron. However, the accuracy of the measurements results in a very high sensitivity of the experimental apparatus to the effects of external disturbances such as thermal gradients, air turbulence, mechanical movements or vibrations. It should also be noted that holographic interferometry provides a full field and contactless inspection of the surface of an object.

Holographic interferometry is often applied as a non-intrusive, non-contact, and full-field technique for non destructive testing. Its high sensitivity is exploited to detect the presence of invisible defects, (e.g. microcracks, detachments, delaminations). When the object being inspected is slightly stressed, defects reveal themselves in correspondence to irregularities of the deformation fringes. The choice of the stressing method is very important for the success of the tests. The stressing can be either thermal (heating or cooling), or mechanical (static loading, pressure variations, or vibrational excitation).

## 2.3.1. Principle of holography

The holographic technique is composed of two distinct steps: recording and reconstruction. During recording the wavefront scattered from the object is made to interfere with the light of a reference beam. The resulting distribution of intensity contains all the information about amplitude and phase of the two waves. The complex amplitudes of the object and the reference wavefronts at the recording plane $xy$ are respectively

$$\mathbf{O}(x,y) = O(x,y)\exp(-j\phi(x,y))$$
$$\mathbf{R}(x,y) = R(x,y)\exp(-j\psi(x,y))$$

Summing and squaring the two preceding expressions, the intensity of the interference pattern is obtained

$$I(x,y) = |\mathbf{O}(x,y)|^2 + |\mathbf{R}(x,y)|^2 + 2O(x,y)R(x,y)\cos(\phi(x,y) - \psi(x,y))$$

the first two terms depend on the amplitudes of the interfering waves, whilst the third contains the information relating to their phase difference.

Therefore it becomes clear that the interference between the light of the object with a reference beam is a way to preserve phase information using recording media which are only sensitive to light intensity. A holographic plate (or film) in an $xy$ plane, correctly

impressed and developed, is a hologram[2]. By illumination of the hologram with a reconstruction wave $R'(x,y)$, a wavefront $U(x,y)$ composed of four distinct terms is formed:

$$U(x,y) = \beta R'(RR^* + OO^* + R^*O + RO^*) \qquad (2.8)$$

where $\beta$ is a constant factor depending on the development process of the emulsion. In the second term of Eqt. (2.8) the two variables, $x,y$ have not been shown explicitly in order to simplify the expression. If $R' \equiv R$ the third term becomes $\beta |R|^2 O$. Normally the reference $R(x,y)$ is taken so that its intensity is constant, and $O(x,y)$ is reconstructed. An exact replica of the object optical field can thus be produced on the $xy$ plane with the equiphase surfaces of the original wavefront propagating from the hologram.

Up to now, several types of lasers have been used in holographic applications. Gas lasers are normally employed as continuous wave sources. In particular He-Ne lasers ($\lambda = 633$ nm), now available at reasonable prices, produce a beam of light with coherence lengths from 15 to 50 cm and with good polarisation characteristics. They provide typical output powers of few tens of milliwatts. He-Ne lasers can be easily operated and practically no maintenance is required. Better performances are offered by Ar$^+$ lasers ($\lambda = 488$ nm). When an etalon is inserted in the oscillator cavity, the coherence length can be several meters. In this configuration the output power is about a few Watts. However, a water circuit is often necessary for the cooling of the gas tube, and some precautions should be taken during operation. Ion sources have been successfully applied to record holograms of large objects. In those applications where pulsed operation is necessary, as in the case of moving objects or rapid phenomena, solid-state lasers are normally employed. Q-switched Ruby lasers (694 nm) can deliver high energy pulses (1 to 25 Joules) in very short times (10-30 nsec). The special design of ring laser cavities has led to almost perfect monochromatic radiation (single longitudinal mode $\Delta\lambda = 0.0004$ Å). Frequency-doubled Nd$^{3+}$ solid-state lasers have also been developed to serve as coherent sources providing a wide range of pulse repetition rates.

---

[2] A review of the principal types of holographic recording materials can be found in [8].

## 2.3.2. Double-exposure holographic interferometry

In double-exposure holographic interferometry, two holograms are superimposed on the same holographic plate with each one capturing the object in a different state separated by a fixed time interval. During the reconstruction stage of the hologram the three-dimensional virtual image of the object appears overlaid with a set of fringes. Since holography can be considered a linear process [9], two wavefronts, recorded sequentially, can both be simultaneously obtained without distortions. The holographic plate is exposed at time $t_1$ to the optical wave $O_1(x,y)$ together with a reference wave $R(x,y)$, and then at time $t_2$ to the wave $O_2(x,y)$ together with $R(x,y)$. When the hologram formed after developing the plate is illuminated by $R(x,y)$, the complex amplitude of the reconstructed wave will be proportional to $O_1(x,y)+O_2(x,y)$. In applications to solid mechanics, $O_1$ represents the light scattered to the hologram by some object, and $O_2$ represents the light from the same object after it has been slightly deformed or changed in some manner. Slight deformations or changes of the object (due to displacement, rotation, strain etc.) primarily affect the phase of the wave, so one can write:

$$O_1(x,y) = O(x,y)\exp(-j\phi(x,y))$$
$$O_2(x,y) = O(x,y)\exp(-j(\phi(x,y)+\Delta\phi(x,y)))$$

The intensity of the reconstructed wave will then be proportional to

$$I(x,y) = |O_1(x,y,)+O_2(x,y)|^2 = 2O^2(x,y)[1+\cos(\Delta\phi(x,y))] \quad (2.9)$$

This equation represents the intensity of the object, $O^2(x,y)$, modulated by the system of fringes, $2[1+\cos(\Delta\phi(x,y))]$. Dark fringes are contours of constant values of $\Delta\phi$, which are odd-integer multiples of $\pi$. Bright fringes are contours of constant values of $\Delta\phi$, which are even-integer multiples of $\pi$.

## 2.3.3. Real-time holographic interferometry

In real-time holographic interferometry a single hologram of the investigated object is recorded. The interference fringes are produced directly by superposition of the optical field emanating from the object to that reconstructed holographically. After

development the holographic plate must be replaced exactly at the same place where it was during recording in order to reproduce exactly the wavefront of the object. Hologram repositioning is extremely critical since a precision of the order of the light wavelength is required. Thus the use of holographic plates is very impractical, though in the past in-situ development was performed by means of special holders consisting of a small tank where the chemicals were poured in. This solution had the drawback that several minutes passed from recording to reconstruction. Nowadays, thermoplastic materials are an excellent solution to repositioning problems, even though a few seconds are necessary to complete the development process. It is hoped that photorefractive materials will further decrease the time gap between recording and reconstruction. In real-time holography, best results are obtained when the optical setup is protected against external factors like mechanical vibrations, unwanted temperature gradients, air turbulence, etc.

## 2.3.4. Sensitivity of the measurements

In this section the relation between the phase distribution $\Delta\phi(x, y)$ recorded in a double-exposure hologram and the displacement L of a generic point P of the object surface is presented. It is assumed that the object is illuminated with a point source O and viewed from the point Q (see Fig. 2.3.).
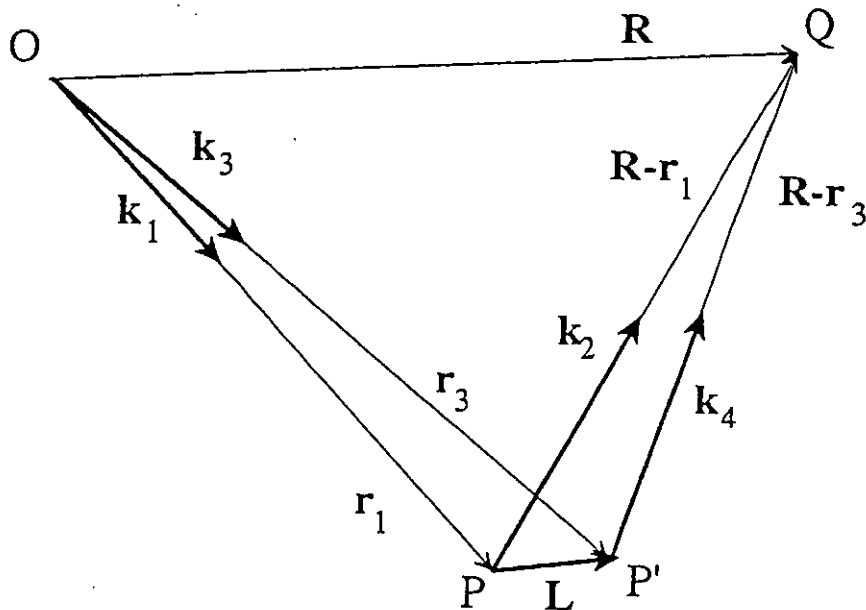


Figure 2.3. Geometry illustrating the relation between the interferometric phase and surface displacement.

By taking O as a reference point, three vectors $\mathbf{R}$, $\mathbf{r}_1$, and $\mathbf{r}_2$, are defined for the points Q, P, and P' respectively. In Fig. 2.3. the wave vectors $\mathbf{k}_1$ and $\mathbf{k}_2$ indicate the illumination and the viewing direction for the point P, whilst $\mathbf{k}_3$ and $\mathbf{k}_4$ refer to point P'. The optical phase in Q before and after deformation is therefore given by:

$$\phi_{before} = \mathbf{k}_1 \cdot \mathbf{r}_1 + \mathbf{k}_2 \cdot (\mathbf{R} - \mathbf{r}_1) + \phi_O$$
$$\phi_{after} = \mathbf{k}_3 \cdot \mathbf{r}_3 + \mathbf{k}_4 \cdot (\mathbf{R} - \mathbf{r}_3) + \phi_O \qquad (2.10)$$

where $\phi_O$ is the arbitrary phase value of the light in O. The phase difference $\Delta\phi(x,y)$ in Q can be calculated by evaluating the following expression

$$\Delta\phi = \phi_{after} - \phi_{before} = (\mathbf{k}_2 - \mathbf{k}_1)(\mathbf{r}_1 - \mathbf{r}_3) + (\mathbf{k}_3 - \mathbf{k}_1)\mathbf{r}_3 + (\mathbf{k}_4 - \mathbf{k}_2)(\mathbf{R} - \mathbf{r}_3)$$

Since in general $|\mathbf{r}_1|, |\mathbf{r}_3| \gg |\mathbf{L}| = |\mathbf{r}_3 - \mathbf{r}_1|$, it can be assumed that $(\mathbf{k}_3 - \mathbf{k}_1) \perp \mathbf{r}_3$ and $(\mathbf{k}_4 - \mathbf{k}_2) \perp (\mathbf{R} - \mathbf{r}_3)$ and thus a simplified form is obtained, i.e.

$$\Delta\phi = (\mathbf{k}_1 - \mathbf{k}_2) \cdot \mathbf{L} \qquad (2.11)$$

If the wave vectors $\mathbf{k}_1$ and $\mathbf{k}_2$ are expressed as functions of the illumination and observation vectors $\mathbf{u}_1$ and $\mathbf{u}_o$, Eqt. (2.11) becomes

$$\Delta\phi = \frac{2\pi}{\lambda}(\mathbf{u}_1 - \mathbf{u}_o) \cdot \mathbf{L} \qquad (2.12)$$

This means that the maximum sensitivity is obtained for displacements along the bisector of the angle formed by the illumination and observation vectors.

The sensitivity of the method depends on the angle between the illumination and viewing directions as well as on the direction of displacement.

## 2.4. Electronic speckle pattern interferometry

Electronic Speckle Pattern Interferometry (ESPI) is based on the idea of using a video camera as a recording medium in speckle interferometry [10]. ESPI was initially investigated by Butters and Leendertz [11] at Loughborough University and by Macowksy *et al* [12] in the early seventies. Since then ESPI has frequently been used as an alternative to holographic interferometry for vibration, deformation and contouring measurements [13].

### 2.4.1. Fundamental concepts

Consider the superposition of two speckle fields in the interferometer presented in Fig. 2.4. The optical field of the object is made to interfere with the field of a reference surface. The resulting speckle pattern is then recorded by a videocamera. If the optical field of each interfering beam is expressed in a complex form as in Eqt. (2.1), the intensity $I(x,y)$ for a generic point $x,y$ at the video camera plate will be given by (see also Eqt. (2.3))

$$I(x,y) = I_o(x,y) + I_r(x,y) + 2\sqrt{I_o(x,y)I_r(x,y)}\cos(\phi(x,y)) \qquad (2.13)$$

where $I_o(x,y)$ and $I_r(x,y)$ are the intensities of the object and reference beams, and $\phi(x,y)$ is the difference between their optical phases. The deformation of the object points will introduce an additional phase term $\Delta\phi(x,y)$, and a new intensity pattern $I'(x,y)$ results

$$I'(x,y) = I_o(x,y) + I_r(x,y) + 2\sqrt{I_o(x,y)I_r(x,y)}\cos(\phi(x,y) + \Delta\phi(x,y)) \qquad (2.14)$$

If the squared difference between the speckle patterns, recorded before and after deformation, is taken, the following is obtained

$$\Delta I(x,y) = 16 I_o(x,y) I_r(x,y) \sin^2\left[\phi(x,y) + \frac{\Delta\phi(x,y)}{2}\right] \sin^2\left[\frac{\Delta\phi(x,y)}{2}\right] \qquad (2.15)$$

Since $\phi(x,y)$ represents the speckle phase term, which is uniformly distributed in the range from 0 to $2\pi$, for a given phase variation $\Delta\phi(x,y)$

30

$$\left\langle \sin^2\left[\phi(x,y)+\frac{\Delta\phi(x,y)}{2}\right]\right\rangle = \frac{1}{2}$$

where the angular brackets denote the average operation over many speckles. After few steps using trigonometric relations Eqt. (2.15) becomes

$$\Delta I = 4I_o(x,y)I_r(x,y)\{1-\cos[\Delta\phi(x,y)]\} \qquad (2.16)$$

Apart from the sign of the cosine function, Eqt. (2.16) is equivalent to Eqt. (2.9), which has been obtained for holographic interferometry.

**Reference surface**

Object before and
after deformation

**Reference & Object beams**
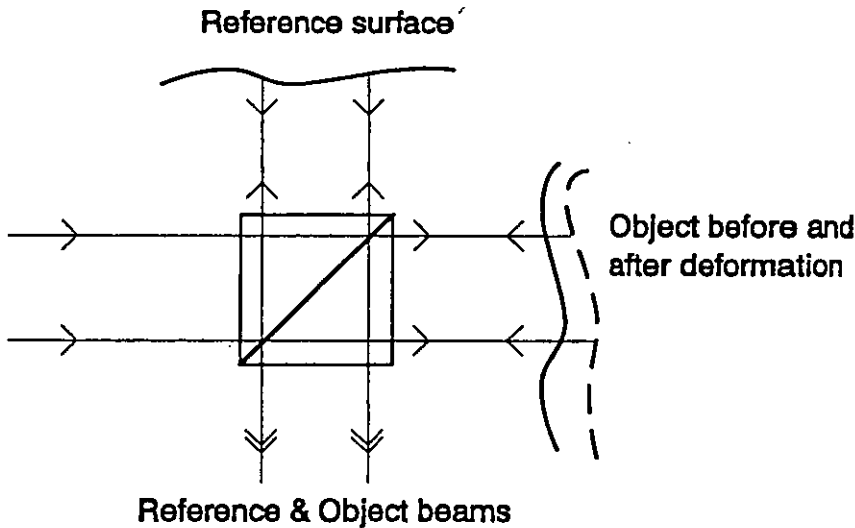
*Figure 2.4. Superposition of two speckle fields in a interferometer.*

In an ESPI system there is no need to use photographic plates and chemical processing, since the image of the object is formed on the sensor plate of a video camera and directly displayed on a video monitor. The power of the video system to resolve small details of an image is however limited. The spatial resolution and the dynamic range are considerably less than for the holographic emulsions.

Until recently, the ESPI fringes have been formed by electronic processing of the video signal, which was high-pass filtered and rectified before being displayed on a monitor (see [14]). For measurements of static deformation, the reference speckle image was stored in a video frame store and analogically subtracted from the speckle field from the video camera, yielding a real-time visualisation of the deformation fringes.

Nowadays, as digital frame stores are available at reasonable prices, ESPI fringes are obtained by digital subtraction[3]. In practice, the image of the object at rest is acquired and stored in the memory of a digital card hosted in a computer. From this image, the image of the deforming object is continuously subtracted and the resulting fringes can be viewed on a monitor at the video frame rate.

## 2.4.2. ESPI interferometers

ESPI interferometers can be made sensitive to either in-plane or out-of-plane displacement of the object surface [13]. By illuminating in a symmetric way the object with two beams at an angle $\vartheta$ to the surface normal, the interferometer is sensitive, for collimated illumination, only to in-plane displacement along the $x$ direction (see Fig. 2.5.). The in-plane displacement $d$ between two adjacent fringes is given by

$$d = \frac{\lambda}{2 \sin \vartheta}$$ (2.17)

where $\lambda$ is the laser wavelength. For complete in-plane measurements, it is necessary to rotate the illuminating beams 90° about the viewing axis to make the system sensitive to displacements along the $y$ direction.

In order to measure the out-of-plane displacement a smooth reference beam, which diverges from a point coinciding with the centre of the aperture of the camera lens is commonly used (see Fig. 2.6.). The out-of-plane displacement $d$ between two adjacent fringes is given by

$$d = \frac{\lambda}{1 + \cos \vartheta}$$ (2.18)

Other designs of ESPI systems are described in the book by Jones and Wykes [13].

---

[3] For this reason the acronym DSPI (Digital Speckle Pattern Interferometry) is often encountered instead of ESPI.

Video camera

Object surface
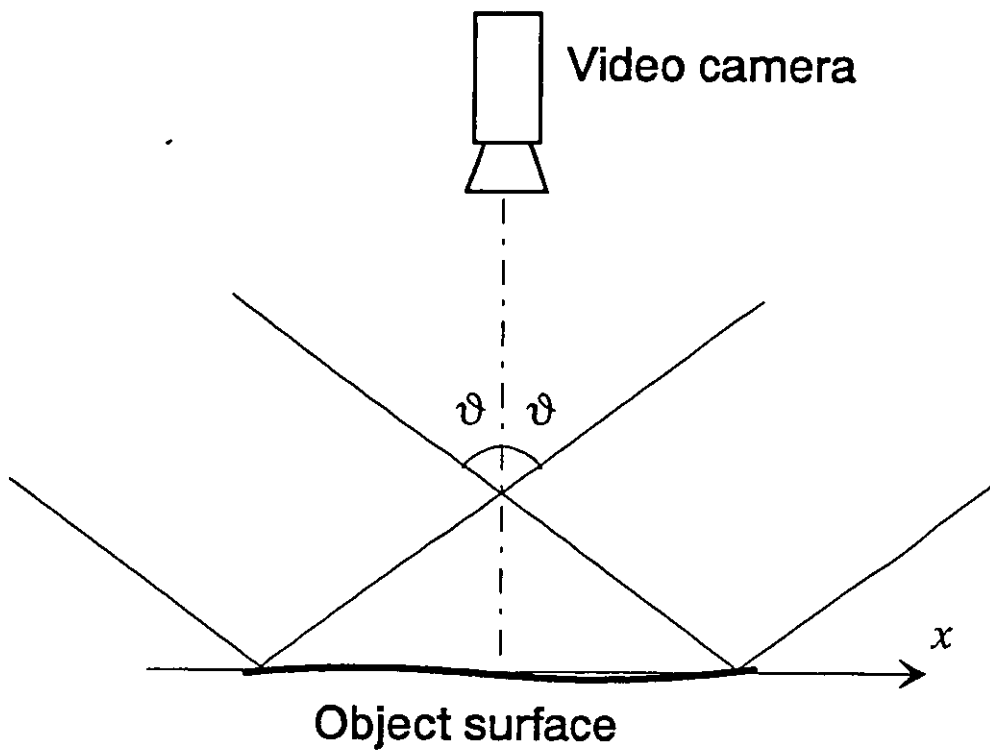
*Figure 2.5. Configuration sensitive to in-plane displacement.*



Reference beam

Lens    Camera plate

Object
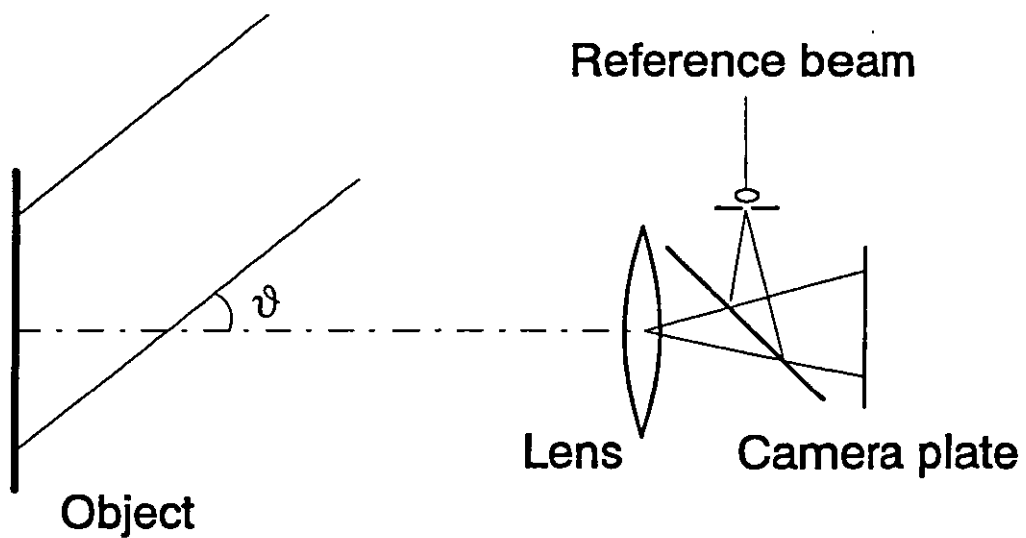
*Figure 2.6. Configuration sensitive to out-of-plane displacement*

## 2.4.3. Advantages and limitations of ESPI measurements

Electronic Speckle Pattern Interferometry presents some advantages over holographic interferometry, which make it suited to routine inspection and out-of-lab operation. First of all the use of a video camera and electronic (or digital) equipment allows a drastic reduction of the processing time and the chemical development of holographic plates is no longer necessary. As the images are acquired and stored at the video frame rate, the exposure time is very short (20 milliseconds). The effects caused by mechanical vibrations and other external disturbances are thus reduced.

When operating in subtraction mode, darkening is not necessary to record the interferograms. It is sufficient that the background light is low enough to detect the speckles scattered from the inspected surface. With the use of narrow band filters, centred at the laser wavelength, ESPI systems can also be operated in daylight conditions.

ESPI fringes however are affected by both optical and electronic noise, which degrades the quality of the interferograms. The optical noise is intrinsically caused by the presence of speckles. The electronic noise is related to the video camera output and to the digitisation process. Spatial resolution is limited by the speckle size and by the resolution of the video camera. Fringe contrast reduction is often caused by speckle decorrelation effects [15].

It is noted that with holography the interferometric fringes are superimposed onto the object, which is still visible during reconstruction. In Espi subtraction images the object is however no longer visible.

## 2.5. Optical fibres

Optical fibres are waveguides made of transparent material, typically glass, which have the function of conducting visible and infrared radiation for considerable distances with small losses. An optical fibre consists of an internal cylindrical part made of glass called the core, surrounded by an external part also cylindrical, called the cladding. The cladding has a refractive index $n_2$ which is slightly less than the refractive index of the core region $n_1$ and could be made of glass with a high silicon content, multicomponent glass or a plastic material.

34

## 2.5.1. Total reflection and mode propagation.

The important physical phenomenon of optical fibres is the total reflection of light which occurs at the interface between the core and the cladding with different optical densities (Fig. 2.7.). The maximum input angle $\alpha$ thus allowed for a ray to propagate inside a fibre is

$$\alpha = \arcsin \frac{NA}{n_0}$$

where $n_0$ is the refractive index of air and NA is the numerical aperture of the fibre which is defined by

$$NA = \sqrt{n_1^2 - n_2^2} \ .$$
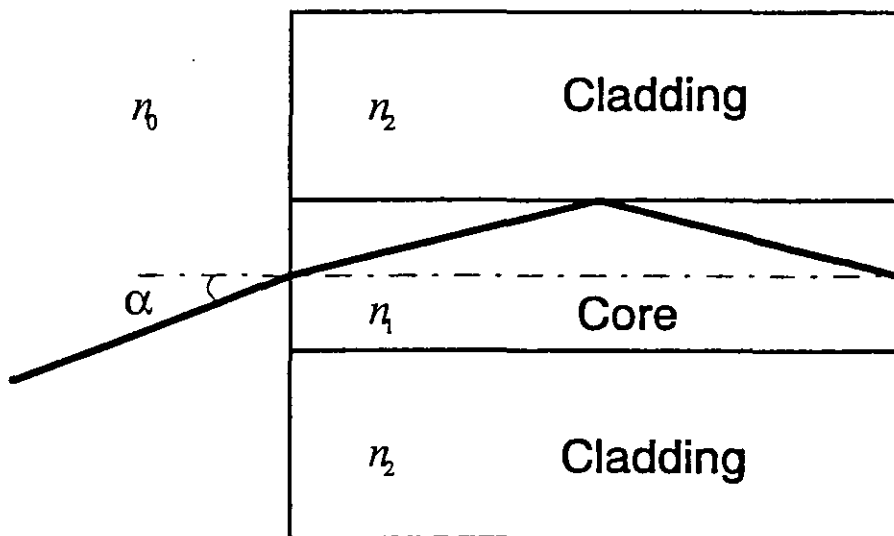


*Figure 2.7. Light coupling and transmission in an optical fibre.*

For a greater understanding of the behaviour of light inside an optical fibre, the Maxwell equations for electromagnetic radiation must be solved [16]. Confinement of the optical field inside the guide leads to a mode structure, typical of resonant cavities. A mode can be defined as a distribution of radiation in an $xy$ plane orthogonal to the direction of propagation which satisfies Maxwell's equations in the core and the

cladding and the boundary conditions at the interfaces. The total number of modes which propagate depends on the fibre characteristics and can be calculated by the parameter V

$$V = \frac{2\pi a}{\lambda} NA$$

Only one mode can propagate if V<2.405. For any value of V the number of modes $N$ is well approximated by the formula

$$N = \frac{4V^2}{\pi^2}.$$

## 2.5.2. Application of optical fibres to holography and ESPI

Optical fibres are used in holographic or ESPI systems to transmit reference and illumination beams in order to improve the flexibility of the recording setup [17]. The optical fibres can be classified in terms of the profile of the core refractive index or the number of modes which propagate in the guide (multimode or singlemode). If the core has a uniform refractive index $n_1$ the optical fibre is called step-index. If instead the core has a refractive index which decreases gradually from the centre toward the interface with the cladding, the fibre is called graded-index.

Singlemode fibres are commonly used in holographic and ESPI systems with continuous wave lasers. Because of the small dimensions of the core (few microns diameter), the output radiation is very close to an ideal spherical wave. This compares with the traditional beam expander (microscope lens and pin-hole), where the pin-hole aperture is much larger than the aperture of the fibre. This can be a disadvantage whenever large surfaces have to be illuminated.

The intensity pattern at the output of multimode fibre appears to be speckled, because of the mode structure inside the fibre. As coupling effects frequently occur between the different modes, the output pattern is not stable. Multimode fibres have found successful application in pulsed laser holography [18].

The insertion of the optical fibres in holographic or ESPI setups allows a considerable reduction of the number of optical elements. As a direct consequence the alignement

time is shortened. Because the fibres are easy to handle during the preparation of the experiments, the geometrical requirements on the paths of rays are no longer a constraint. The matching of the optical paths, caused by the limited coherence lenght of some lasers, can readily be satisfied by choosing a fibre section of suitable length.

The sensitivity of the fibres to external factors (mechanical vibrations, air turbulence,thermal drifts, etc.) can sometimes cause a contrast loss in the interferograms. These disturbances can be compensated with automatic control systems as proposed by Jones *et al* [19].

An interesting application is also the development of endoscopic probes for the holographic [20] or ESPI [21] inspection of narrow or inner parts of objects. Fiber-optic image guides are used to transport the object wavefront to the recording plate, where it is made to interfere with the reference beam.

## 2.6. References

[1] Marathay A.S., "Elements of Optical Coherence Theory", John Wiley & Sons, (1982)

[2] Hecht E., "Optics" 2nd Edition, Addison-Wesley Publishing Company (1987)

[3] Saleh B.E.A., Teich M.C., "Fundamentals of Photonics", John Wiley & Sons, (1991)

[4] Svelto O., "Principles of lasers" 3rd Edition, Plenum Press, (1989)

[5] Goodman J.W, "Statistical properties of laser speckle patterns", in "Laser Speckle and related Phenomena", J.C.Dainty, ed. (Springler-Verlag, Berlin, 1975), pp 9-75

[6] Vest C.M., "Holographic interferometry", John Wiley & Sons, (1979)

[7] Powell R.L., Stetson K.A.,"Interferometric vibration analysis by wavefront reconstruction", Journal of the Optical Society of America A (1965), 55 1593-1598

[8] Caulfield H.J., "Handbook of Optical Holography", Academic Press (1979)

[9] Goodman J.W, "Introduction to Fourier optics", McGraw-Hill (1968)

[10] Ennos A.E., "Speckle Interferometry", in "Laser Speckle and related Phenomena", J.C.Dainty, ed. (Springler-Verlag, Berlin, 1975), pp 203-253

[11] Butters J.N., Leendertz J.A., "Holographic and video techniques applied to engineering measurement", Transactions of the Institute of Measurement and Control, (1971) **4** 349-354

[12] Macowsky A., Ramsey S.D., Schaefer L.F.,"Time-lapse interferometry and contouring using television systems", Applied Optics, (1971) **10** 2722-2727

[13] Jones R., Wykes C., "Holographic and speckle interferometry", Cambridge University Press (1983)

[14] Løkberg O., "Electronic Speckle Pattern Interferometry", Physics in Technology (1980) **11** 16-22

[15] Owner-Petersen M., "Decorrelation and fringe visibility: on the limiting behavior of various electronic speckle-pattern correlation interferometers" Journal of the Optical Society of America A, (1991) **8** 1082 -1089

[16] Cherin A., "An introduction to optical fibres", Mc Graw Hill (1983)

[17] Bjelkhagen H., "Fiber optics in holography", (1986), Proceedings of the SPIE, **615** 13-18

[18] Albe F., Fagot H., Smigielski P., "Use of optical fibers in pulsed holography", Proceedings SPIE, (1984) **492** 324-329

[19] Jones J.D.C., Corke M., Kersey A.D., Jackson D.A., "Single-mode fibre-optic holography", Journal of Physics E: Scientific Instruments, (1984) **17** 271-273

[20] Von Bally G., "Holography and endoscopy", International Journal of Optoelectronics, (1991) **6** 491 -502

[21] Facchini M., Zanetta P., Paoletti D., Schirripa Spagnolo G., "An endoscopic system for DSPI", Optik, (1993) **95** 27-30

# Chapter 3

# Digital processing of interferometric and speckle images

.

.

## 3.1. Introduction

Holographic and speckle techniques produce results in the form of images (fringe patterns), which, if properly interpreted, offer a whole-field description of the physical properties being investigated. However, in the past, these optical techniques were widely used for qualitative studies in many disciplines, but, in general, were scarcely considered for quantitative analysis. The reason lies in the difficulty of dealing with two dimensional data with both sufficient speed and resolution. At present, progress in computer technology has achieved remarkable results, e.g., digitisation and processing of a video image at the standard frame rate, and high resolution digital scanning of colour images. Image processing techniques have also been considerably developed and have found a variety of applications in many fields; medicine (X-ray pictures), earth science (satellite images), pattern recognition, etc.

Fundamental digital operations [1] are often performed on interferometric images in order to facilitate the use of fringe analysis algorithms and to improve the display of final results. Image enhancement techniques, for example, can be very helpful to reduce unwanted fluctuations of brightness (image noise) and to increase the fringe contrast. In addition, the use of false colours can clarify details and highlight important features of the images.

The great interest in the quantitative evaluation of interferograms and the spread of image processing have given rise to a specific subject, referred to as "Fringe analysis" among the people working in interferometry. The birth of Fringe Analysis can be dated back to the formation of the Fringe Analysis Special Interest Group (FASIG) in 1985 in the UK. Today, conferences and seminars dedicated to this subject alone are held periodically in many parts of the world. A self-contained explanation of the principles of fringe analysis can be found in the book recently edited by Robinson and Reid [2].

In this chapter, the fundamental concepts of image processing are presented together with the description of a complete system which can be used for image acquisition and digitisation. Common operations such as histogram equalisation, pseudo-colour display, spatial and frequency filtering are briefly illustrated with some applications to real interferograms. Sec. 3.3. deals with phase extraction and phase unwrapping algorithms, which have been used in practice for the interpretation of the interferometric images. Particular emphasis has been given to the use of Fourier analysis for phase evaluation both in holographic and speckle interferometry, because this approach can, in some cases, give the phase map from a single fringe pattern. Thus all those errors which could be introduced by external disturbances during the acquisition of phase shifted images

40

will be avoided. Although phase extraction by Fourier techniques has intensely been studied in relation to holographic or interferometric images, their novel application to some practical cases and in particular to speckle interferograms has been investigated here. The source code (written in C language) developed in-house, and the main features of a commercial package named HOLOPHASE II employed in the experimental work, have been included in Appendix A at the end of the thesis.

## 3.2. Fundamentals of digital image processing

### 3.2.1. Image processing systems

A digital image can be considered as a numerical matrix, whose elements (pixels) are associated with the brightness and colour properties of the image points. Since interferograms and speckle patterns can be considered monochromatic, black and white (B/W) imaging and processing devices will be presented. Therefore, the pixel values are positive integer numbers (grey levels), representing the image brightness. The resolution of a digital image is directly proportional to the number of pixels per unit area and to the number of grey levels. However, the higher the precision, the larger the amount of data, and thus a trade-off is often made between image quality and computing power. Although several types of digitising devices are commercially available, interferograms are mostly digitised in a video system (see Fig. 3.1.). A B/W digital image is usually composed of 512 x 512 pixels with a resolution of 8-bits (1 byte) corresponding to 256 grey levels.

In recent years the development of solid state light sensors has led to the widespread use of Charge Coupled Devices (CCDs) in imaging systems. The technical performance of CCD sensors is superior to vidicon tubes in terms of linear response, durability, and sensitivity. Other important advantages are also their compactness, low cost, and low power consumption. The optical image is focused onto the camera plate, where a regular 2-D matrix of MOS (Metal Oxide Semiconductor) sensors (or more simply pixels) is located. The electric charge of each sensor, whose sensitive area can be of only few squared microns, is proportional to the intensity of the incident light. Although CCD plates of the last generation can have up to 5000 x 5000 elements, a number of approximately 512 x 512 pixels is typical for a general purpose B/W camera.

Image digitisation is made by sampling the output analogue signal (CCIR standard) from the video camera with a frame grabber hosted in a computer. A frame grabber is an electronic card whose principal task is to convert the analogue video signal into a

digital map representing the image. Images can be acquired and displayed on an auxiliary monitor at the video frame rate (1/25 of a second). The frame grabber card is equipped with some memory (frame buffers) where the digitised images can be temporarily stored. Dedicated hardware circuits such as Look Up Tables (LUTs) and Arithmetic Logic Unit (ALU) are sometimes available in order to control the display features and perform real-time operations between digital images. More advanced processing can be accelerated by using extra cards performing convolution and Fast Fourier Transform operations via hardware. Transputer cards can also be included for the implementation of parallel computing routines, which can simultaneously operate on many pixels with a great reduction of the processing time.
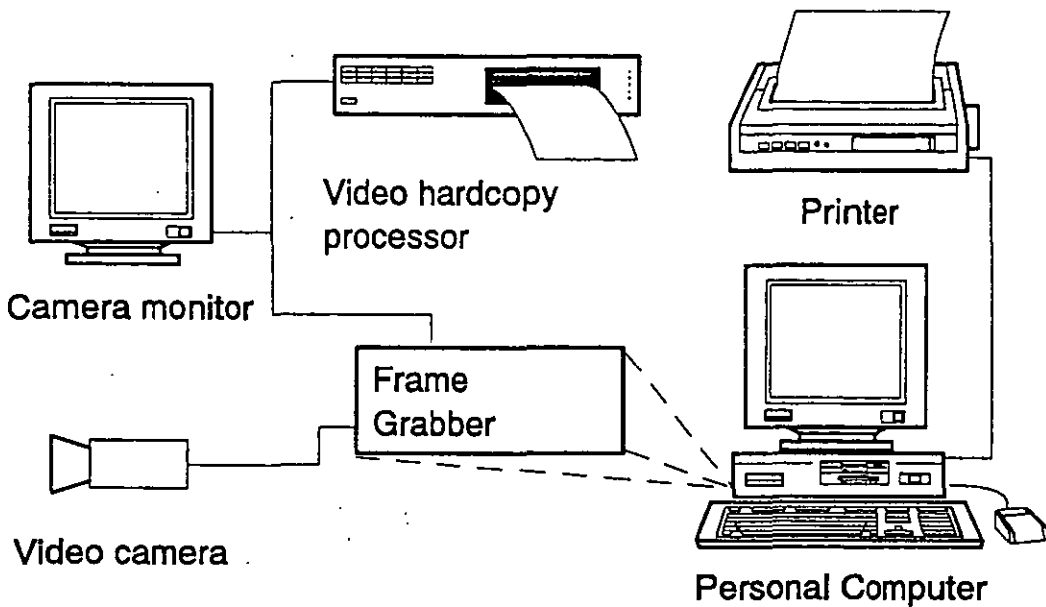


*Figure 3.1. An example of a PC-based video system for image digitisation and processing.*

Software libraries containing the functions performed by the frame grabber (or other cards) can be used to control acquisition and storage and to implement the desired image processing algorithms. These libraries are a collection of subroutines (written in programming languages such as FORTRAN, C, PASCAL) which can readily be linked to programs made by the user. User friendly software packages are also available for general purpose image processing. Although in some cases they cope very well with the most common frame grabbers, their use, however, is often limited to interferogram pre-processing. Finally it is noted that some software for fringe analysis is supplied with' many instruments for testing optical elements, or with holographic and ESPI systems (see for example Appendix 2.A.). In this case the processing facilities are very specific

and self-contained. However, the user cannot add or modify any function and, since the source code is generally not included, the software portability is very low.

## 3.2.2. Fundamental operations on interferograms

### 3.2.2.1. Filtering

The major source of noise afflicting real interferograms is the formation of laser speckles in imaging systems. It is noted that, in general, the average speckle size is much smaller than the fringe spacing, which is equivalent to saying that the spatial frequency components of speckle noise are much higher than those of the signal. For this reason low-pass filtering (or smoothing) is usually applied to reduce speckle noise effects.

It is well-known from the theory of signals [3] that filtering operations can be either performed in the spatial or in the frequency domain. Spatial filtering consists of the discrete convolution of the image pixel map with a small matrix (kernel), which performs a weighted average in the neighbourhood of image points. An example will illustrate how discrete convolution is practically implemented (see Fig. 3.2.). If a square kernel ($L \times L$) is centred at a generic pixel ($x,y$) of the image, an ($L \times L$) subimage is uniquely determined by the kernel position. Each element of the kernel is multiplied with the corresponding pixel in the subimage. The results obtained are summed to yield the new filtered value for pixel ($x,y$). This operation is repeated for each image pixel in order to obtain the filtered image. Mathematically, this discrete convolution is expressed as follows [4]

$$I_{FILT}(x,y) = \sum \sum I(m,n) K(m-x-C, n-y-C) \qquad (3.1)$$

where $m,n$ are integration variables; $K(x,y)$, $I(x,y)$, and $I_{FILT}(x,y)$ are the kernel, image, and filtered image pixel values, respectively; and $C$ is a constant related to the kernel size $L$ by $C = (L+1)/2$.

Several types of spatial filters can readily be obtained by designing different kernels. For example a $3 \times 3$ kernel with each matrix element equal to one corresponds to a simple low-pass filter. By increasing the kernel size, the filtering effects will be more pronounced. Squared kernels with an odd number of pixels are the most used as they can readily be applied to a large variety of images. In the case of images with particular

symmetries, it might be convenient to vary the kernel shape according to the type of symmetry encountered.
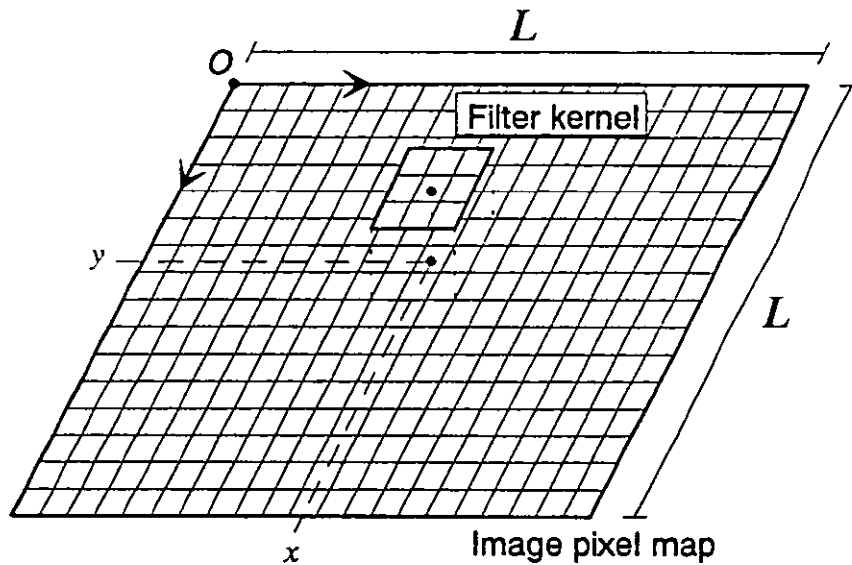


*Figure 3.2. Discrete convolution of an image with a 3 x 3 kernel.*

Frequency filtering is based on Fourier signal analysis, which allows a decomposition of the image into spatial sinusoidal components. This gives a more intuitive representation of filtering and as far as the noise characteristics are known, frequency filtering can be much more effective than spatial filtering. The method [1] consists of the multiplication of the Fourier spectrum of the image with a filter function which suppresses the frequency components of noise. The cleaned image is recovered by performing the inverse transform operation. It should be noted that all these operations are made on matrices of complex numbers and therefore a much larger computational effort is necessary than in the case of spatial filtering.

Finally, the effects of low-pass filtering on a real interferogram are presented in Fig. 3.3., where a noisy fringe pattern has been filtered both in the spatial and in the frequency domains. No contrast enhancement technique has been used in order to provide a significant comparison between the results.

44
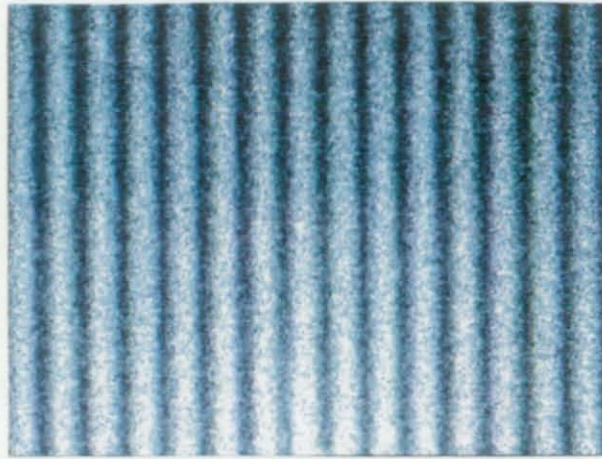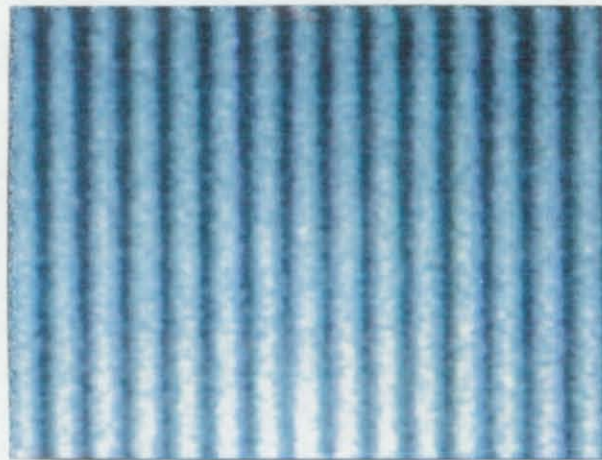
*Figure 3.3. Interferogram filtering. a) Original image. b) Spatially filtered image. c) Frequency filtered image.*

### 3.2.2.2. Contrast enhancement

Inaccurate adjustments of the polarisation or of the ratio between the intensities of the reference and object beams, speckle decorrelation, low dynamic range, non-uniform object reflectance, and optical misalignments are but some of the factors causing poorly contrasted fringe patterns. A reduction of fringe quality in fact may occur for many other reasons, which are often related to the experimental conditions (e.g. the presence of micro-vibrations, ambient light) or to the image processing operations (e.g. power signal loss due to filtering). Contrast enhancement techniques are therefore very useful and are commonly applied for preliminary processing of interferograms.

Contrast manipulation is based on the principle of image transformation or mapping. In this respect, a transformation is defined as an operation which performs a redistribution of the image grey levels. In practice, the grey level of a pixel will be changed into a new value according to a defined transformation function (see Fig. 3.4.). An ever increasing function will preserve a correct restitution of pixels from dark to bright values.
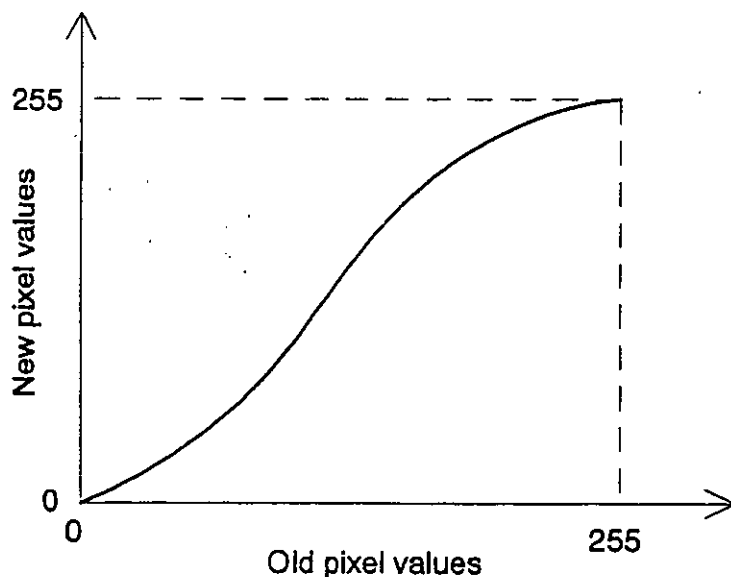


*Figure 3.4. A grey-level transformation function.*

From a statistical point of view an image can be characterised by its histogram which represents the number of pixels per grey level. It could be shown [1] that transformation concepts can be successfully applied to obtain an image with a desired histogram. A commonly used transformation is histogram equalisation which aims at producing a uniform distribution of grey levels. Another important operation is amplitude scaling

46

[4], which is very useful when the pixels values are grouped in a small interval of grey levels. The scaling transformation distributes the pixel values over all the range of levels available with positive effects on the image contrast.

In Fig. 3.5. the original ESPI fringes recorded during *in-situ* inspection on a fresco (see also Fig.4.49) and the result obtained after manipulation with contrast enhancement techniques are both presented.



a)                                    b)
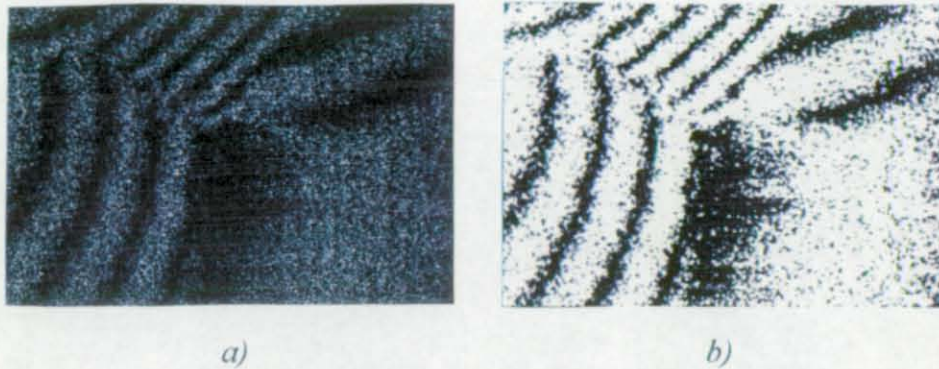
*Figure 3.5. Contrast enhancement of an ESPI interferogram. a) Original fringes. b) Final image.*

### 3.2.2.3. Pseudo-colour images

Pseudo-colour processing consists of assigning a correspondence between grey levels and colours. To do this three distinct transformation functions, one for each primary colour (Red, Green, and Blue), have to be specified. These functions will give the fractions of primaries which, when added together, will form the desired colour. An example presenting an application of pseudo-colours to an image whose brightness increases linearly from left to right is presented in Fig. 3.6. Colours can be very helpful in highlighting details which are scarcely visible in grey-scaled images. For this reason, in fringe analysis, pseudo-colour techniques are commonly used for the final display of deformation and contour maps.

In most frame grabbers colour mapping can be performed by programming the LUTs, which give the possibility of real-time pseudo-colour display. This feature has successfully been used during the thesis' work in order to avoid the acquisition of saturated images. In practice, all the pixels reaching a value of 255 were coloured with

bright red. Thus the detection of saturated areas, appearing as red spots, was straightforward.
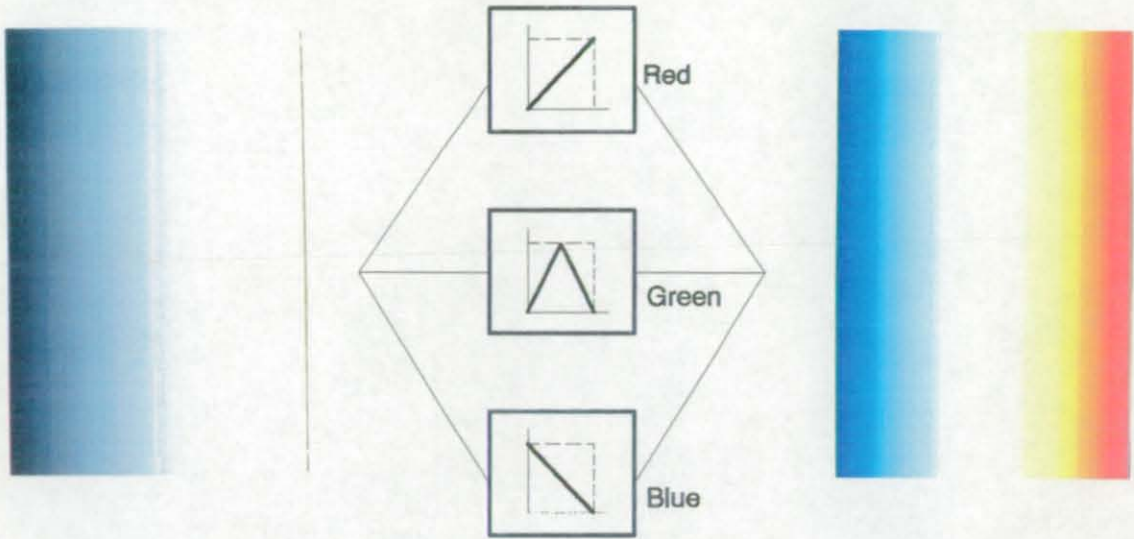


*Figure 3.6. Pseudo-colour transformation applied to a computer generated B/W image of 256 x 256 pixels with 8-bits resolution.*

## 3.3. Phase measurement techniques

In optical interferometry the relation between the intensity $I$ and the spatial co-ordinates $x,y$ of a generic interferogram can be written as [5]:

$$I(x,y) = a(x,y) + b(x,y)\cos[\phi(x,y)] \qquad (3.2)$$

where $\phi(x,y)$ is the interferometric phase, whilst $a(x,y)$ and $b(x,y)$ represent the background and the contrast modulation, respectively.

It can readily be demonstrated that Eqt. (3.2) is valid both for holographic and speckle fringes. In fact, in the case of double-exposure or real-time holography the fringe pattern expressed by Eqt.(2.9) can be rewritten in the above form by letting $a(x,y) = b(x,y) = 2O^2(x,y)$. Accordingly, for electronic speckle fringes if in Eqt.(2.16) it is assumed that $a(x,y) = -b(x,y) = 4I_o(x,y)I_r(x,y)$ an expression corresponding to Eqt. (3.2) is readily obtained. It is noted that because of the high speckle noise, the phase extraction problem is more critical for ESPI fringes.

### 3.3.1. Phase shifting techniques

Phase shifting techniques are widely used for the retrieval of the phase map of an interferogram. The main reasons for their success are the high precision of the measurements and the simple experimental arrangement. The phase of a point can be evaluated with a typical precision of $2\pi /100$ radians, which is equivalent to one hundredth of the fringe period [6]. The principle is based on the analysis of at least three fringe patterns differing by a known amount of phase introduced in one of the two arms of the interferometer. The resulting visual effect is a shift of the intensity peaks across the interference pattern. By the computational point of view, a variety of versions of the method exist, all of them sharing the ability to eliminate the background and contrast terms by simple arithmetic or trigonometric operations on the acquired images. Phase shifts can be produced in many ways, e.g. a micrometric movement of a piezoelectric driven mirror, a tilt of a glass plate, or a translation of a grating. A review of phase modulators is contained in Ref. [7].

Phase shifting techniques are also known as "quasi-heterodyne" techniques with reference to heterodyne techniques [8], which can produce phase data with an outstanding accuracy of 0.006 radians. However, in spite of this precision, heterodyne

techniques are less utilised than phase-shifting techniques, because, the introduction of controlled frequency shifts implies the use of more sophisticated electronic equipment.

### 3.3.1.1. The four images algorithm

Although a great variety of phase shifting techniques have been proposed [6], it seems more appropriate here to focus the attention onto the four-images or four-shifts algorithm which has extensively been used during the experimental work (see Appendix A.1.1.). The interferometric phase is mathematically derived by considering the intensities $I_k(x,y)$ ($k=1,2,3,4$) of each pixel when phase shifts of

$\varphi_1 = 0, \varphi_2 = \dfrac{\pi}{2}, \varphi_3 = \pi, \varphi_4 = \dfrac{3\pi}{2}$ respectively are added to the reference beam of the interferometer. With the use of simple trigonometric relations the following equations are readily obtained

$$I_1(x,y) = a(x,y) + b(x,y)\cos[\phi(x,y)]$$

$$I_2(x,y) = a(x,y) - b(x,y)\sin[\phi(x,y)]$$

$$I_3(x,y) = a(x,y) - b(x,y)\cos[\phi(x,y)]$$

$$I_4(x,y) = a(x,y) + b(x,y)\sin[\phi(x,y)]$$

(3.3)

By subtracting and dividing the above equations $a(x,y)$ and $b(x,y)$ can be eliminated, whilst the phase is expressed by

$$\phi(x,y) = \arctan\frac{I_4 - I_2}{I_1 - I_3}$$

(3.4)

However, since the arctan() function gives values between $-\pi/2$ and $+\pi/2$, the phase cannot be directly evaluated over a $2\pi$ interval. This inconsistency can be removed by taking into account the signs of $(I_4 - I_2)$ and $(I_1 - I_3)$ which correspond to $\sin[\phi(x,y)]$ and $\cos[\phi(x,y)]$, respectively. Thus the phase can be determined modulo $2\pi$ and the so-called wrapped phase diagram results.

In practice, a mirror, mounted on a piezoelectric crystal, has been used to introduce the desired phase shifts. Calibration was performed in most cases with a dedicated routine of the program HOLOPHASE II (see Appendix A.2). The output of a Digital-to-Analogue (DA) card in the PC host computer was fed to the high-voltage driver of the crystal. For a pixel the intensity modulation produced by a voltage ramp of the DA output was recorded and the resulting sinusoidal diagram was displayed on the monitor. By indicating the distance between two adjacent peaks or valleys in this diagram, the voltage V corresponding to a phase shift of $2\pi$ could be automatically identified. Then a second voltage ramp was started and four images, shifted by $\pi/2$ were acquired in separate memory buffers of the frame grabber when the output of the DA card reached a multiple integer of V/4.

A detailed analysis of the error sources affecting the measurement accuracy in a phase shifting system, is contained in the article by Creath [6]. It is noted that the 4-images algorithm is classified as particularly sensitive to erroneous calibration and non-linear response of the phase modulator, whilst the non-linearity of the detector response have negligible effects on the algorithm performance. In general, during acquisition of the shifted images, vibrations and air turbulence cause the major problems. For this reason it is recommended to place the system on a vibration-free table and to protect the shifting device from the external disturbances.

### 3.3.1.2. Application to holographic and speckle interferometry

In real-time holographic interferometry four interferograms, each shifted by $\pi/2$, can be acquired by varying the phase of the reference beam. The phase shifts, however, have to be introduced when the fringes are perfectly still. In this case the application of phase shifting techniques is limited only to static or quasi-static deformation measurements. This constraint is no longer present in the double-exposure version as the shifted interferograms can readily be acquired during reconstruction by using two distinct reference beams, one for each exposure (see for example Sec. 4.2.3.). It is also noted that switching from one beam to the other will require extra equipment when very rapid phenomena are to be studied with pulsed holography [9].

Phase shifting can be applied to ESPI fringes in a simple and effective manner. Four images of the interference pattern between the object and reference beams, conveniently shifted in phase, are acquired before deformation. The speckle image corresponding to deformation is then subtracted from each of the initial images. By doing so four interferograms, shifted in phase by $\pi/2$, can be obtained and used as inputs for the four-images algorithm.

In the case of speckle pattern interferometry, the measurement accuracy will be strongly affected by the high content of speckle noise. Jones and Wykes [10] reported that phase shifting techniques can reach a resolution of approximately $2\pi/5$ radians, which is twenty times less than the value obtained for holographic or interferometric images. Further studies [11] on the quality of ESPI fringes demonstrated that remarkable improvements can be achieved by filtering and enhancing the contrast of the speckle interferograms before applying any phase extraction algorithm. From a quantitative point of view [12], spatial pre-filtering of ESPI images can increase the precision up to the values which are typical in interferometry ($2\pi/100$).

## 3.3.2. Techniques based on Fourier analysis

Until recently numerical techniques based on Fourier signal analysis were mostly implemented on mainframes because of the large amount of data to be processed. Another solution consisted of the design of ad-hoc hardware processors installed in smaller machines. In spite of their high speed, these processors present two important disadvantages: high cost and low flexibility. The latest developments in information technology have led to a more favourable situation in which Fast Fourier Transform (FFT) algorithms, running on workstations or PCs, handle image matrixes of 512 x 512 pixels very quickly. These software solutions are intrinsically very flexible and cheap, encouraging the spread of Fourier techniques for image processing.

The application of Fourier techniques to fringe analysis has been the subject of many scientific investigations [13] in the field of interferometric measurements. The interest is justified since the interference phase can be retrieved from one or two interferograms. Moreover the experimental constraints typical of phase-shifting based systems are greatly reduced. In fact, phase-stepping devices can be eliminated in most cases or their calibration does not need to be highly accurate.

### 3.3.2.1. Background concepts

For the analysis with Fourier methods, Eqt. (3.2) is complex. If $j$ is the imaginary unit defined by $j = \sqrt{-1}$, then

$$I(x,y) = a(x,y) + \frac{1}{2}b(x,y)\exp\left[j\phi(x,y)\right] + \frac{1}{2}b(x,y)\exp\left[-j\phi(x,y)\right] \quad (3.5)$$

letting $c(x,y) = \frac{1}{2}b(x,y)\exp[j\phi(x,y)]$, and denoting with the asterisk the complex conjugate, a more elegant expression is obtained

$$I(x,y) = a(x,y) + c(x,y) + c^*(x,y) \qquad (3.6)$$

The two-dimensional Fourier transform of the previous equation can be written as

$$I(f_x,f_y) = \mathcal{A}(f_x,f_y) + C(f_x,f_y) + C^*(-f_x,-f_y) \qquad (3.7)$$

where $\mathcal{A}(f_x,f_y)$ and $C(f_x,f_y)$ denote the Fourier transforms of $a(x,y)$ and $c(x,y)$, respectively. In most cases $a(x,y)$ is a slowly varying function, whose frequency components are grouped around the zero frequency. The mutually point symmetric terms $C(f_x,f_y)$ and $C^*(-f_x,-f_y)$ contain higher frequency components that are related to the spatial variation of $\phi(x,y)$. Each of these terms can be isolated by using an asymmetric band pass filter, which also suppresses the background term $\mathcal{A}(f_x,f_y)$. Further application of the inverse Fourier transform gives one of the complex functions $c(x,y)$ or $c^*(x,y)$ with non-vanishing real and imaginary parts. The interference phase can be calculated for each image point according to one of this relations:

$$\phi(x,y) = \arctan\frac{Im[c(x,y)]}{\mathcal{Re}[c(x,y)]} \quad \text{or} \quad \phi(x,y) = -\arctan\frac{Im[c^*(x,y)]}{\mathcal{Re}[c^*(x,y)]} \qquad (3.8)$$

The arctan() function returns a value in the range 0-$\pi$, but when the signs of the real and imaginary parts are taken into account then the phase can be evaluated from 0 to $2\pi$.

Since it is not known whether the result of filtering is $c(x,y)$ or $c^*(x,y)$, the phase $\phi(x,y)$ suffers from a sign ambiguity as demonstrated by substituting $c(x,y)$ for $c^*(x,y)$ in Eqt. (3.8). In practice, the absolute sign of the phase normally has no particular relevance or it is sometimes known prior to the experiments. For this reason, attention is focused on another aspect that is more important for the application of the method. Filtering the signal in an asymmetric way, i.e. taking only one lateral lobe,

implies that the phase is a monotonic function. Assuming that $C(f_x, f_y)$ is in the positive part of the Fourier plane (respect to $f_x$), Eqt. (3.8) can be written as [14]

$$\phi(x,y) = \arctan \frac{\iint |C(f_x,f_y)| \sin\left[2\pi(f_x x + f_y y) + \arg C(f_x,f_y)\right] df_x df_y}{\iint |C(f_x,f_y)| \cos\left[2\pi(f_x x + f_y y) + \arg C(f_x,f_y)\right] df_x df_y}$$

where | | and arg() denote the modulus and the argument of $C(f_x, f_y)$, respectively. After few passages, a simple expression is obtained for the derivatives of $\phi(x, y)$ with respect to $x$ (or $y$)

$$\frac{\partial \phi(x,y)}{\partial x} = 2\pi f_x \quad \left( \text{or } \frac{\partial \phi(x,y)}{\partial y} = 2\pi f_y \right)$$

If the band pass filter selects the part of the spectrum where the $x$ frequencies are positive (or negative) then the phase will increase (or decrease) monotonically along the $x$ direction. The consequences of this are significant since the method presented can only be applied without modifications to those cases where it is known that the phase has a monotonic behaviour. For this reason the extension of the method to interferometric images resulting from non monotonic phase distributions is not trivial.

Some solutions to this problem have already been suggested in the literature. In his work concerning interferometric and holographic images, Kreis proposed two techniques that, in principle, could also be applied to ESPI fringes. The first technique [15] is based on the combination of two phase images obtained by filtering the interferogram twice. Once the first phase map has been built following the described algorithm, the second map is produced by rotating the band pass filter by ninety degrees about the origin of the Fourier plane. Further detection of the loci of points, where the phase value is the same, leads to the identification of image areas, where the first or the second image can be taken as the correct phase with an eventual change of sign. However, it is very difficult to perform the area partition automatically. This is particularly true for ESPI interferograms, where there is a great deal of speckle noise. Therefore, this technique seems impractical for routine analysis, although it could be used for very special interferograms where interactive analysis to delimit the areas of correct phase are justified.

The second solution proposed by Kreis [16] allows the evaluation of the correct phase slope by comparison of two images shifted in phase by less than $\pi$. One single interferogram does not contain any information concerning whether the phase is

increasing or decreasing along a chosen direction. Nevertheless, this can be resolved by recording another interferogram, slightly shifted in phase. If $\alpha$ ($0<\alpha<\pi$) is a constant phase shift introduced between two interferograms, the fringe patterns will be expressed by

$$I_0(x,y) = a(x,y) + b(x,y)\cos[\phi(x,y)] \tag{3.9.a}$$

$$I_\alpha(x,y) = a(x,y) + b(x,y)\cos[\phi(x,y) + \alpha] \tag{3.8.b}$$

It can be shown that the shift $\alpha$ can be related to the real and imaginary parts of $c_0(x,y)$ and $c_\alpha(x,y)$, defined as in Eqt. (3.6), according to the following

$$\alpha(x,y) = \arctan\frac{\mathcal{R}e[c_0(x,y)]\mathcal{I}m[c_\alpha(x,y)] - \mathcal{I}m[c_0(x,y)]\mathcal{R}e[c_\alpha(x,y)]}{\mathcal{R}e[c_0(x,y)]\mathcal{R}e[c_\alpha(x,y)] + \mathcal{I}m[c_0(x,y)]\mathcal{I}m[c_\alpha(x,y)]} \tag{3.10}$$

However, when evaluated with the previous expression $\alpha = \alpha(x,y)$ is no longer a constant. Unavoidable ripples and abrupt sign changes are detected. It can be demonstrated that if the phase $\phi(x,y)$ is a monotonic function then $\alpha(x,y)$ will have a constant sign. Otherwise the calculated $\alpha(x,y)$ will be positive in certain areas and negative in others. By multiplying the phase diagram by +1 or -1 according to the sign of $\alpha(x,y)$, the phase discontinuities can be removed and the phase distribution will be properly corrected.

Another technique, based on the introduction of a set of carrier fringes, was successfully proposed for interferometric and holographic images by Takeda et al [17]. In almost every interferometric setup, including speckle interferometry, a linear phase function, corresponding to sinusoidal equispaced fringes, can readily be introduced by tilting the beam illuminating the object after the first exposure. If it is assumed without any lack of generality that the carrier fringes are parallel to the $y$ axis, then the fringe pattern will be given by

$$I(x,y) = a(x,y) + b(x,y)\cos[\phi(x,y) + 2\pi f_c x] \tag{3.11}$$

55

where $f_c$ indicates the frequency of the carrier fringes. In this case the Fourier transform of the image becomes:

$$I(f_x, f_y) = \mathcal{A}(f_x, f_y) + C(f_x - f_c, f_y) + C^*(-f_x + f_c, -f_y) \qquad (3.12)$$

The separation introduced in the frequency domain implies, as an immediate consequence, that filtering can be performed more precisely. It should be noted that by adding a linear phase term, the global phase function has become monotonical. To do this, however, the carrier frequency has to be greater than the maximum phase gradient, i.e. $2\pi|f_c| > \max|\text{grad}\phi(x, y)|$. On the other hand, $f_c$ has an upper limit fixed by the sampling theorem, which states that the maximum resolvable frequency is twice that of the image digitiser. If the above conditions are satisfied, after filtering, the linear phase function can be eliminated by shifting the spectrum by $f_c$ toward the origin. Now $c(x,y)$ can be obtained by inverse transformation and the correct phase is evaluated according to Eqt. (3.8).

In principle, Fourier based techniques are expected to reach the same accuracy of phase shifting measurements. However the application of the Fourier transform algorithm to a finite set of data produces some effects [3] which have to be carefully taken into account in order to obtain correct results. Major errors occur at the edge of the image or where the phase presents some discontinuities. In these regions, the Fourier algorithms tend to smooth the phase by interpolating the data with the selected frequencies. A detailed discussion of boundary effects has been presented by Kujawinska and Wojciak in [18]. In general it can be observed that very accurate phase values can be obtained by neglecting a few pixels at the image edges, if the phase $\phi(x, y)$ is a continuous function of $x,y$.

### 3.3.2.2. Experimental results

All the reported examples and experiments refer to real interferograms; computer simulated fringe patterns have not been used. This approach has been chosen to demonstrate the possibilities and limitations of the numerical techniques applied to practical cases. The images have been processed using a Sun Sparc-10 (85 Mips & 10 Mflops; 1152 x 900 & 8 bits / 24 screen display). The software package Khoros 1.0 patch 5 with in house C-routines has been run under Unix O.S. 4.3.1.

Firstly, the case of deformation fringes produced by holographic interferometry was considered. In particular, the studied image (see Fig. 3.7.) was the result of an endoscopic investigation of the interior of a cylinder using fiber optic holography [19]. Since the recording geometry was that of an image plane hologram, the fringes were reconstructed by white light illumination, therefore the speckle noise was absent. However, the fringe pattern is superimposed with the honeycomb pattern of the image guide, which is composed of well ordered 17000 multimode optical fibres (12 $\mu$m diameter). It is shown that the regular pattern can be eliminated by filtering. From the experimental arrangement, the mechanical displacement of the cylinder caused by the external system of forces was a monotonic function along the vertical direction and the absolute sign was known. Therefore the optical phase could be retrieved without uncertainties with the first technique described in Sec. 3.3.2.1.

Subsequently the same technique has been applied to the analysis of ESPI fringes (Fig. 3.8.a). In the Fourier spectrum (see Fig. 3.8.b), the phase information is concentrated in the first peak along the horizontal axis. For simplicity, the applied filter is unity inside a rectangle and zero elsewhere. A frequency unit (f.u.) of 1/512 fringes/pixel, corresponding to one fringe per image, was defined. The filter was centred at the horizontal frequency of 22 f.u.; the horizontal width is 24 f.u. and the vertical height is 64 f.u. From the experimental setup it was known that the phase was increasing from left to right. Fig. 3.8.c. shows the wrapped phase map produced by the processing.
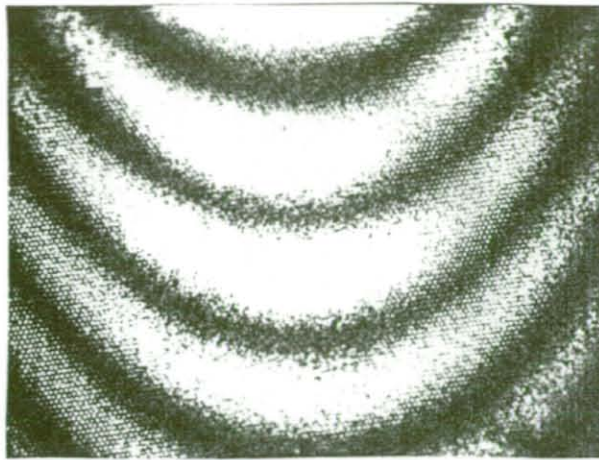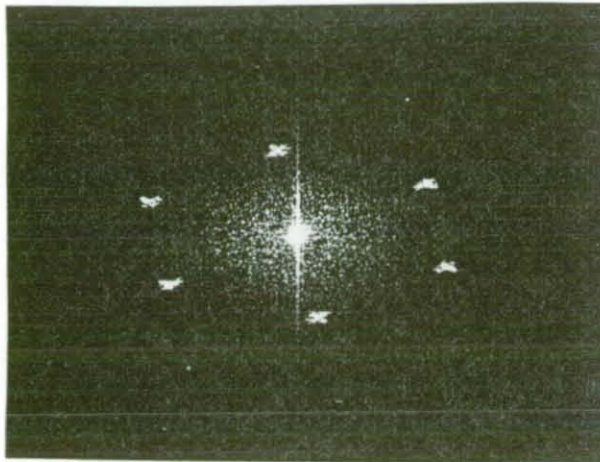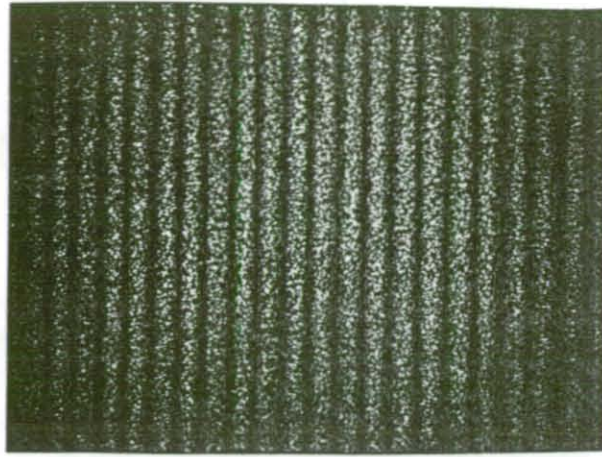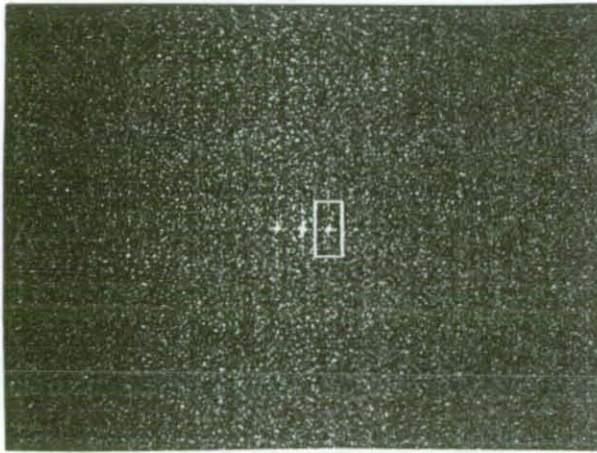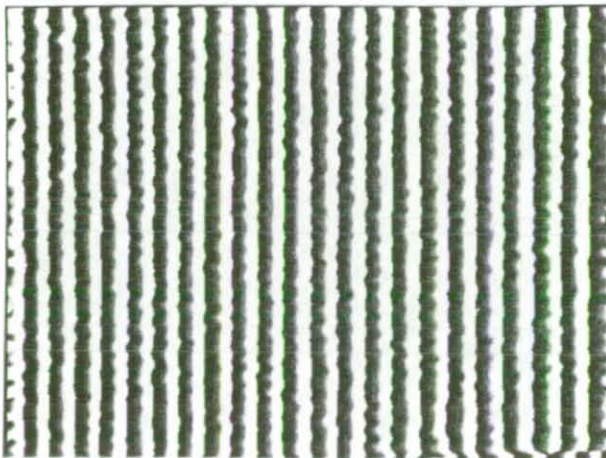
Figure 3.7. a) Endoscopic fringes obtained by holographic inspection with optical
fibres. White light reconstruction. b) Power spectrum. c) Phase diagram
modulo 2π.

*Figure 3.8. a) 2D-image of TV-holographic fringes. b) Power spectrum. The white rectangle delimits the borders of the filter. c) Phase diagram modulo $2\pi$.*

In the next example, to illustrate the problems arising when this technique is applied to a non monotonic phase distribution, ESPI circular fringes have been considered. The chosen filter was a rectangle centred at 8 f.u. in the horizontal direction and it was located symmetrically with respect to the horizontal axis. The horizontal width was 12 f.u. and the vertical height was 16 f.u. The filter location implied that the extracted phase was a monotonic function along the horizontal direction. In particular, the phase was decreasing from left to right with discontinuities along the central vertical line where it actually had its minima. The detection of these discontinuities could be automatically performed, but this would not be sufficient to solve the problem. In fact, the discontinuities cannot be located along every horizontal line, and thus alternative solutions should be found.
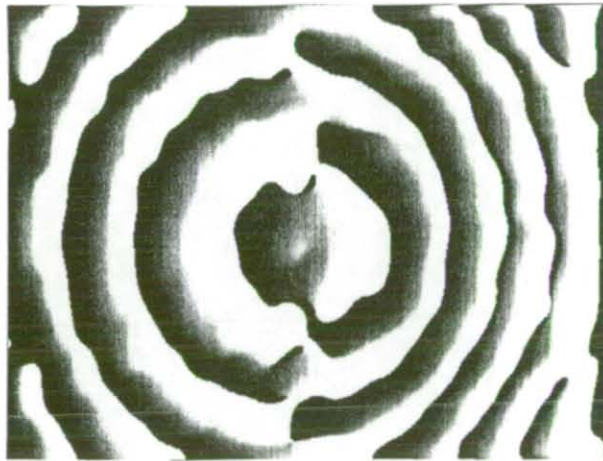


*Figure 3.9. Phase diagram obtained by filtering circular TV-holographic fringes with a band-pass filter in the $f_x$ positive half-plane.*

Some examples, using the technique with a single phase shift, are now presented. Fig. 3.10. depicts the circular fringes corresponding to a static deflection of an aluminium plate due to a central point load. A phase shift $\alpha \approx \pi/2$ was introduced by appropriate manipulation of a sandwich hologram [20]. The images were processed with a bandpass filter. The filter shape, depicted in Fig. 3.10.b, has been chosen to minimise the effect of noise on the results. The phase diagram (Fig. 3.10.c) reveals the presence of small imperfections along the central vertical line where for a similar pattern (Fig. 3.10.) several phase jumps have been detected. Border effects are also visible at the corners of the interferogram. These anomalies are caused by poor fringe contrast or by the absence of fringes. This technique has been also applied to ESPI fringes (see Fig. 3.11.). However, the large amount of speckle noise produced uncontrollable fluctuations on $\alpha(x,y)$, especially where the phase changed its slope. The phase diagram was altered as a consequence.
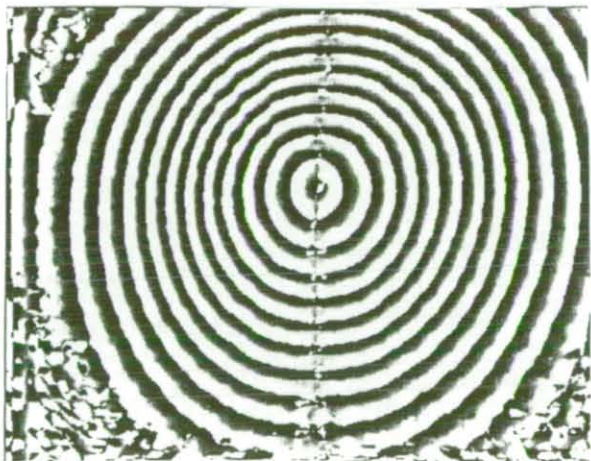
*Figure 3.10. a) Circular fringes of a sandwich hologram. b) Power spectrum. c) Phase diagram.*
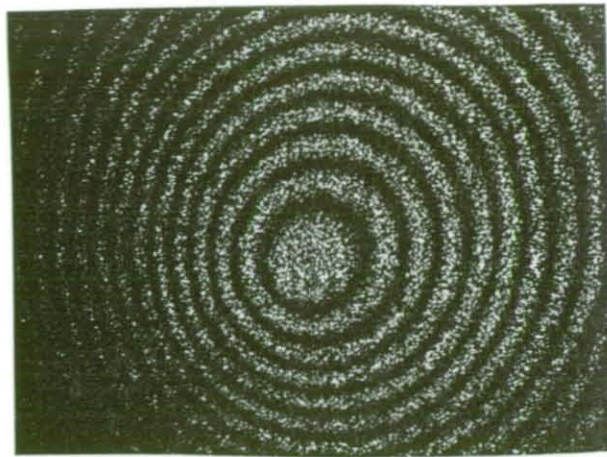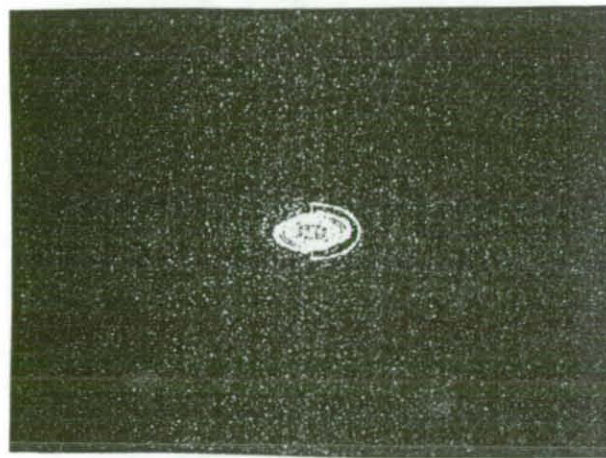
*Figure 3.11. a) Circular fringes of an ESPI interferogram. b) Power spectrum. c) Phase diagram.*
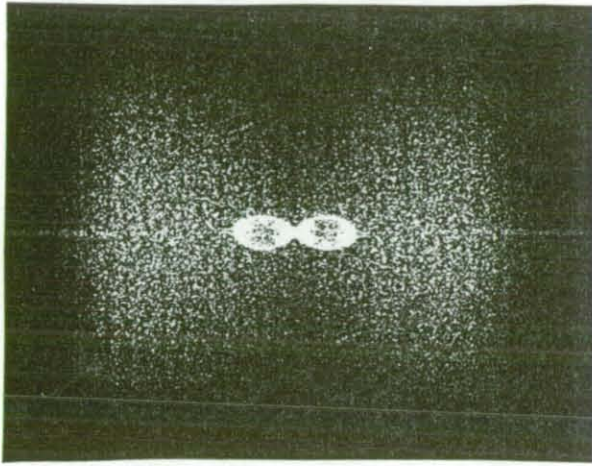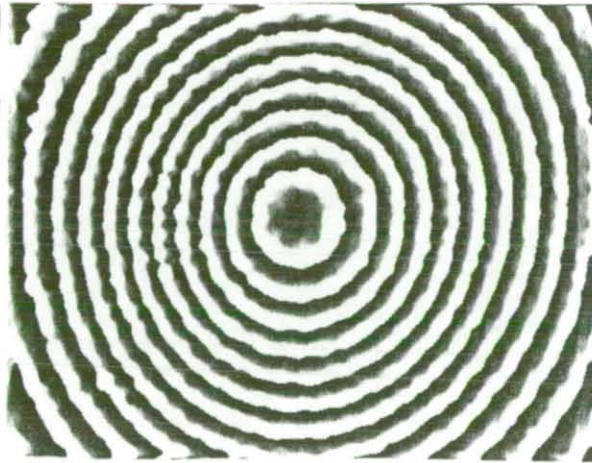
*Figure 3.12. a) Speckle interferogram with added carrier fringes in the horizontal direction. b) Power spectrum c) Final result.*

For ESPI fringes, better results have been obtained by introducing a set of carrier fringes along the $x$ axis to the interference pattern. A deformation of the same type as that producing the circular fringes has been evaluated. The resulting interferogram, its Fourier spectrum and the phase diagram are depicted in Fig. 3.12.

### 3.3.3. Phase unwrapping

Once the phase data have been extracted with phase-shifting or Fourier techniques, final processing is necessary to eliminate the discontinuities which are still present in the wrapped phase map. Phase unwrapping consists of preliminary detection of the fringe order, and further reconstruction of the absolute phase function. The wrapped map is scanned pixel by pixel to detect the positions of the phase jumps between two adjacent fringes. If the difference between two phases of two pixels $P_1$ and $P_2$ is greater (or smaller) than a defined threshold (normally taken as $\pi$) then it is assumed that the pixels lies in two distinct fringes. The absolute phase value is obtained by adding (or subtracting) $2\pi$ to the phase of $P_2$.

Up to now many studies [2] have dealt with the design of phase unwrapping algorithms, and the research on this topic is still very intense. In real fringe patterns, many difficulties arise from the presence of abrupt phase changes, image noise and signal under-sampling [21]. Very often solutions are suggested on the basis of *a priori* knowledge of the physical phenomena involved. However, a trade off has to be made between precision, processing time, and intelligence of the algorithm. Very fast routines give results that depend on the path followed during the scanning. A typical example is the line by line algorithm (see Appendix A.1.2.), which, depending on the input image, will correctly unwrap the phase only if the right selection between the horizontal and vertical directions is made. Path independent algorithms have a higher noise rejection but can be extremely time consuming as, for example, in some iterative algorithms [22], where the use of parallel processing is recommended. Latest research in this field deals with the application of neural network concepts [23] to provide a more intelligent algorithm being able to deal with many different types of interferograms.

In practice, most of the unwrapping used for the final processing of the interferograms presented in the next chapters has been performed with HOLOPHASE II (see Appendix A.2.). It is worth noting that the possibility of selecting an image polygon with the PC mouse was particularly helpful to mask out the areas where the algorithm failed or where fringes were not present.

## 3.4. Conclusions

The fundamental principles of digital image processing have been presented. Attention has been focused on the application of digital techniques to the study of fringe patterns. It has been shown that a reduction of speckle noise can be obtained by applying filtering techniques. Spatial filters have the advantage of being simple to implement as they operate locally on a limited number of pixels. On the other hand, filters in the frequency domain are more selective but require a much larger computational effort.

Contrast enhancement techniques are very useful for display and pre-processing operations, especially when the interferograms are recorded in the presence of vibrations, or other noise sources. However, the parameters of the transformation function used to improve the contrast have to be readjusted from one interferogram to another and a general approach to this problem has not yet been found.

The problem of phase extraction has been considered. The principle of phase shifting techniques and some aspects of their practical use in both holographic and speckle interferometry have been briefly described. Moreover the application of 2D Fourier transform methods has been investigated in more detail. Some algorithms, normally used with holographic and interferometric fringes, have been tested on ESPI subtraction images.

With interferograms having a monotonic phase, very good results have been obtained with an algorithm operating on a single image. Initially the image was filtered asymmetrically in the Fourier domain. This operation created a complex image, from which the phase was readily evaluated for each pixel. A fully automatic system would be very difficult to implement, because the filtering operation is an interactive procedure. However, when the phase was not monotonic, this algorithm could not be applied in its simple version. With some modifications holographic images could successfully be processed, but this was not the case for ESPI images because of the high content of speckle noise. The results have demonstrated that the best solution for speckle interferograms was obtained by the superposition of carrier fringes.

The extraction of phase information from a single ESPI image makes Fourier techniques a very promising alternative to phase-shifting techniques in real-time applications and *in situ* experiments where external disturbances (vibrations, thermal drifts, etc.) can introduce errors in the phase steps.

## 3.5. References

[1] Gonzales R.C., Wintz P., "Digital Image Processing", 2nd Edition, Addison Wesley (1987)

[2] Robinson D.W., Reid G.T., "Interferogram Analysis: Digital Fringe Pattern Measurement Techniques", Iop Publishing Ltd, (1993)

[3] Oppenheim A.V., Schafer R.W., "Digital signal processing", Prentice Hall (1975)

[4] Pratt W.K., "Digital Image Processing", 2nd Edition, John Wiley (1991)

[5] Klein M.V., Furtak T.E., "Optics", John Wiley & Sons, New York (1986)

[6] Creath K., "Phase-measurement interferometry techniques" in E.Wolf, Progress in Optics XXVI, (1988), 25 349-393

[7] Schwider J., "Advanced evaluation techniques in interferometry" in E.Wolf, Progress in Optics XXVIII, (1990) 271-359

[8] Dandliker R., "Heterodyne holographic interferometry", in E.Wolf, Progress in Optics XVII, (1980), 17 1-84

[9] Lai G., Yatagai T., "Dual-reference holographic interferometry with a double pulsed laser", Applied Optics, (1988) 27 3855-3858

[10] Jones R., Wykes C., "Holographic and speckle interferometry", Cambridge U.P. London, (1983)

[11] Kerr D., Mendoza Santoyo F., Tyrer J.R., "Manipulation of the Fourier components of speckle fringe patterns as part of an interferometric analysis process", Journal of Modern Optics, (1989) 36 195-203

[12] Vikhagen E., "TV holography: spatial resolution in deformation analysis", Applied Optics, (1991) 30 420-425

[13] Kujawinska M., "Spatial phase measurement methods", in "Interferogram Analysis: Digital Fringe Pattern Measurement Techniques", Robinson D.W., Reid G.T. eds. (Iop Publishing Ltd, 1993)

[14] Bracewell R.N., "The Fourier transform and its applications", McGraw-Hill Singapore (1986)

[15] Kreis T., "Digital Holographic Interference-Phase Measurement using the Fourier-Transform Method", Journal of the Optical Society of America A, (1986) **3** 847-855

[16] Kreis T., Jüptner W.P.J., "Fourier-Transform evaluation of interference patterns: demodulation and sign ambiguity", Proceedings SPIE **1553** (1991) 263-273

[17] Takeda M., Ina H., Kobayashi S., "Fourier-Transform method of fringe-pattern analysis for computer-based topography and interferometry", Journal of the Optical Society of America A, (1982) **72** 156-160

[18] Kujawinska M., Wojciak J., "High accuracy Fourier transform fringe pattern analysis", Optics and Lasers in Engineering, (1991) **14** 325-339

[19] Lucia A.C., Lacchin P., Zanetta P., "Endoscopia a Fibre Ottiche per Interferometria Olografica nella Diagnostica Strutturale", Proceedings of ELETTROOTTICA '90 Milan (Italy), 16-18 October 1990

[20] Paoletti D., Schirripa Spagnolo G., D'Altorio A., "Sandwich hologram for displacement derivative", Optics Communications, (1986) **56** 325-329

[21] Itoh K., "Analysis of the phase unwrapping algorithm", Applied Optics, (1982) **21** 2470

[22] Ghiglia D.C., Mastin G.A., Romero L.A., "Cellular automata method for phase unwrapping", Journal of the Optical Society of America A, (1987) **4** 267-280

[23] Takeda M., Nagatome K., Watanabe Y., "Phase unwrapping by neural network", in FRINGE'93 Proceedings of the 2nd International Workshop on Automatic Processing of Fringe Patterns, Bremen (Germany) 19-21 October 1993, (ed. Jüptner W., Osten W.), Akademie Verlag (1993) 136-141

# Chapter 4

# Surface micro deformation analysis

## 4.1. Holographic detection of defects in composites

### 4.1.1. Introduction

Fibre-reinforced composite laminates have been proposed as a very interesting alternative to metals whenever high strength and stiffness per unit density are demanded. Composite components, for example, have been successfully employed as structural elements in the aerospace and aircraft industries. Other relevant users of composites have been the automotive and sport industries. The advanced mechanical properties together with the low fabrication and material costs are the major reasons of the successful growth of composite applications in recent years [1].

A composite layer or ply consists of unidirectional fibres embedded in a resin or a polymer matrix. A set of plies, oriented along different directions, are stacked to form a multidirectional laminate. Variations in the relative orientation of the plies and different combinations of the constituent materials give rise to a large number of composite laminates. However, since these materials are anisotropic and heterogeneous, the characterisation of their mechanical behaviour is much more complicated than it is for metals, which are completely defined by two scalars; the Young's modulus and the Poisson's ratio. In fact, tensor theory is generally used to describe the properties of composite materials.

Apart from the presence of cracks, dislocations and vacancies in the matrix, which are also typical for metals, composite structures might be seriously damaged by microscopic debonds of the fibre-matrix interface, fibre breakage, and delaminations. All these defects are usually caused by unavoidable errors during fabrication or by in-service factors such as impacts with dropped tools, stones, or hail grains. Therefore, non destructive techniques have been greatly considered for diagnostics before and during the regular service of a component. The aircraft industry, in particular, is greatly concerned with detection and assessment of delamination caused by impact damage, which is the most frequent failure mechanism in composite structural elements.

A variety of non destructive evaluation (NDE) techniques are used for assessing the integrity of these materials [2] and each of them is best suited for detecting some particular type of defect. They fall broadly into the general classes of radiographic, optical, thermographic, acoustic, embedded-sensor, ultrasonic and electromagnetic techniques. Among them, the optical method of laser holographic interferometry proved to be very efficient, especially in producing qualitative results [5]. Other advantages are that it is non-contact and non-intrusive, it is applied remotely and it yields full-field

measurements. Citing some of its disadvantages, its over-sensitivity to environmental disturbances (when a continuous wave laser is used), and the need of cumbersome image processing to obtain quantitative results.

The experimental work reported here dealt with the application of real-time holographic interferometry to monitor the thermal deformation of multidirectional composite laminates. In particular, the method was employed for the detection and visualisation of impact induced damage and built-in defects in specimens of carbon fibres with an epoxy resin matrix. A comparison with the results obtained by ultrasound examination has also been included to validate the experimental results. Double-reference holographic interferometry was finally used to provide a numerical description of the interferograms. All the specimens were kindly supplied by Agusta Helicopters S.p.a. (Italy).

## 4.1.2. Composite specimens

For the impact tests the specimens were 16-ply graphite-epoxy coupons with glass-epoxy end tabs and with dimensions as shown in Fig. 4.1. Their stacking sequence was the symmetric $[(45/-45/0/90)_2]_s$ thus producing a quasi isotropic material. The density of the material was known to be 1470 kg/m$^3$ with a fibre-volume ratio of $42\pm2\%$. No information was available on the thermal properties. Holographic investigation was performed on eleven specimens. Two were in their virgin state whereas the remaining nine were damaged by impact using the standard drop weight test. The technique was to lay a specimen onto a plate with a central hole of radius 40 mm. The impacter head was spherical of 0.5" diameter and was dropped directly over the centre of the hole, hidden by the specimen. The level of damage, the term referring to the impacted energy over the thickness of the specimen, was graded as follows: 0.5 J/mm, 1.0 J/mm and 1.5 J/mm. It is worth noting that the impacted surface showed no visible signs of damage. The only visible damage was on the underside of the specimens, in the form of localised delamination. For the holographic tests, the impacted specimens were grouped in four series V, A, B, C, and labelled as shown in Table 4.1.

The built-in defects considered are also known as marcels among people working in the aeronautic industry. One specimen of orthogonal parallelepiped form, Fig. 4.2.a, has been cut out of a thick composite component. These defects are frequently encountered in thick components and are generated during the polymerisation process. Marcels do not manifest themselves on the surface of the component and are undetected using ultrasound examination. From the lateral section in Fig. 4.2.b it is evident that the investigated specimen is made of many unidirectional laminae, stacked with different

orientations. Marcels are only visible at a section through the thickness (i.e., destructively), where the layers appear to be wavy instead of plane.

| Specimens | | | Impact energy [Joules/mm] |
|---|---|---|---|
| V1 | V2 | | none |
| A05 | B05 | C05 | 0.5 |
| A10 | B10 | C10 | 1.0 |
| A15 | B15 | C15 | 1.5 |

*Table 4.1. Impact energies for carbon/epoxy specimens under investigation.*
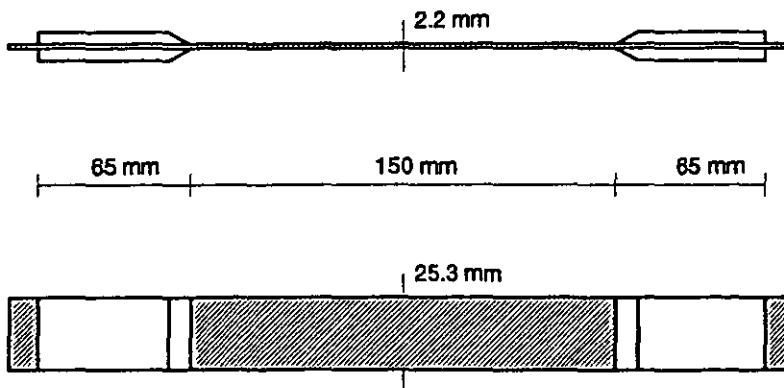


*Figure 4.1. Geometry and dimensions of impacted specimens.*

Being naturally black coloured all the specimens were painted white before examination. This was necessary to increase the reflectivity of the specimens and to reduce the exposure time during the holographic recording. The thin layer of paint had no influence on the shape of the holographic fringes that were only produced by the surface deformation of the specimen.

72
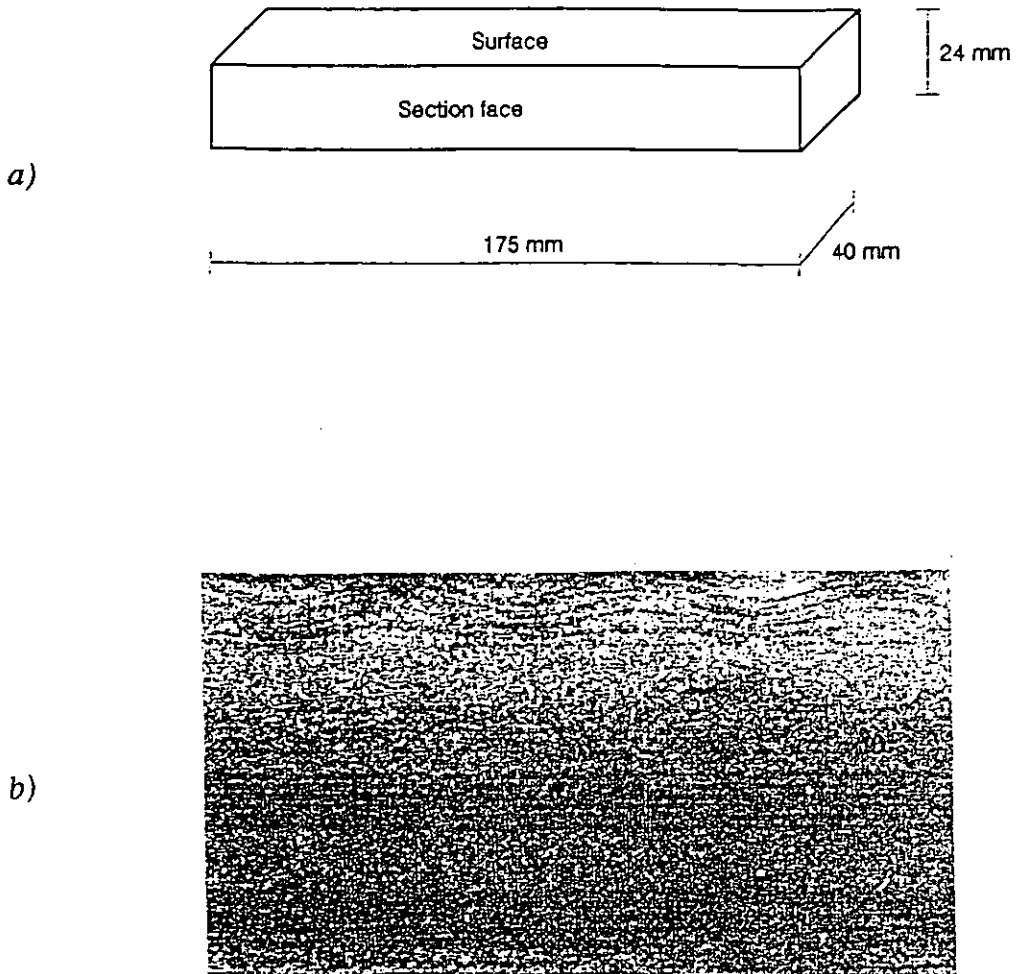
*Figure 4.2. a) Geometry and dimensions of the marcels-containing specimen. b) Photograph of the section face.*

## 4.1.3. Optical setup

The optical setup included primarily a holocamera (Rottenkolber HSB-85) with thermoplastic film, which was found particularly convenient for real time tests as the hologram development took place on the holocamera, within approximately 30 seconds, and thus plate repositioning problems were avoided. It should be noted that the film cost is drastically less than that of the holographic plate. The lower resolution (maximum 850 lines/mm) of the thermoplastic film and the lower quality hologram with respect to a holographic plate were of secondary importance in this application. Further, the deterioration of the hologram with time was of no real concern, as the fringe formation was monitored on a TV screen through a video camera and permanently recorded on tape or disk thereafter.

The coherent light source was a Spectra Physics mod. 127 He-Ne continuous wave laser (output power $P = 35\,mW$; wavelength $\lambda = 633\,nm$). The laser beam was split into the reference and illumination beams by a variable beam splitter (see Fig. 4.3.). The splitting ratio was chosen to let the intensities of the reference and of the object waves be equal at the recording plane. An exposure time of 2 seconds was set. In order to illuminate the object uniformly the laser beam was expanded by a 40 x microscope lens, and the resulting spherical wavefront was filtered by means of a pin-hole of $10\,\mu m$ diameter. A 10 x lens was sufficient to expand the reference beam. The optical table was a hydraulically isolated bench (Newport M-MST-48-8 size 1.2 x 1.8 m) which eliminated any mechanical vibration that could have affected hologram recording or real-time observation. The local heating system was turned off to reduce air turbulence in the laboratory. Real-time sequences of holographic images were recorded on a video recorder, wherefrom they could readily be replayed later.
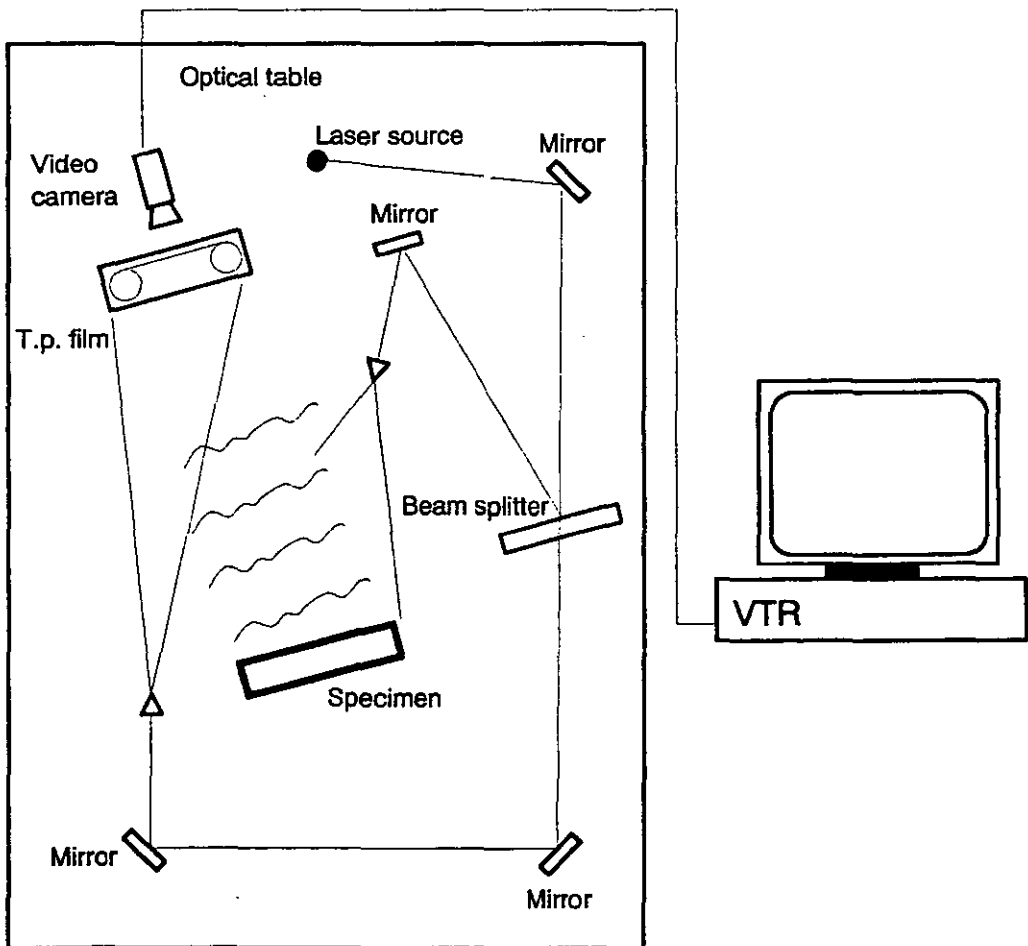


*Figure 4.3. Sketch of the experimental setup for real time holographic interferometry.*

74

For a quantitative description of the results, double-reference holographic interferometry was used in the experiments. The principles are exactly the same as in double-exposure holographic interferometry except that two different reference waves are necessary. The holographic film is exposed at time $t_1$ to the optical wave $O_1$ together with a reference wave $R_2$, and then at time $t_2$ to the wave $O_2$ together with another reference $R_2$. During reconstruction, the hologram is illuminated by both reference beams $R_1$ and $R_2$ and yields a multiplicity (four virtual ones) of images, which can be properly manipulated to produce the desired interference patterns and optimised fringe contrast [3,4]. This technique is particularly suited for high resolution deformation measurements because it permits interpolation of the interference fringes. Otherwise, quantitative information on the interference phase $\Delta\phi$ can only be obtained reliably from the points of maximum and minimum intensity in the interferogram, which correspond to multiples of $\pi$. According to the "quasi-heterodyne" or "phase-step" technique applied here (see Sec.3.3.1.), the relative phase of the two reconstructed waves is changed stepwise, using at least three different values. Experimentally this was effectively accomplished by a mirror mounted on a piezoelectric element, which allowed the high precision variation of the path length of one reference beam, say $R_2$, and consequently the control of the relative phase of the two wave fields during reconstruction.

Slight modifications of the optical setup were introduced to perform measurements with double-reference holographic interferometry (see Fig. 4.4.). In particular, the two reference beams $R_1$ and $R_2$ were provided by a Michelson interferometer. The reference $R_1$ was employed for the first exposure ($R_2$ being blocked), and $R_2$ was employed for the second one ($R_1$ being blocked). The angle between the two reference waves at the output of the interferometer was approximately 3°. One of the two mirrors of the Michelson interferometer was mounted on a piezoelectric crystal. Varying its voltage it was possible to translate this mirror with high precision forward or backward, changing the optical path of $R_2$ and thus introducing the desired phase-shifts during reconstruction. The calibration of the piezo-voltage was computer controlled as explained in Sec.3.3.1.

Four images, shifted in phase by 90 degrees, were taken for each experiment. The interferometric images derived by the subsequent reconstructions were digitised and stored in a graphic board (IT/FG100 4 memory pages of 512 x 512 pixels at 8 bit resolution) installed in a Compaq 386/20e PC. Final digital processing led to the quantitative map of surface deformation.
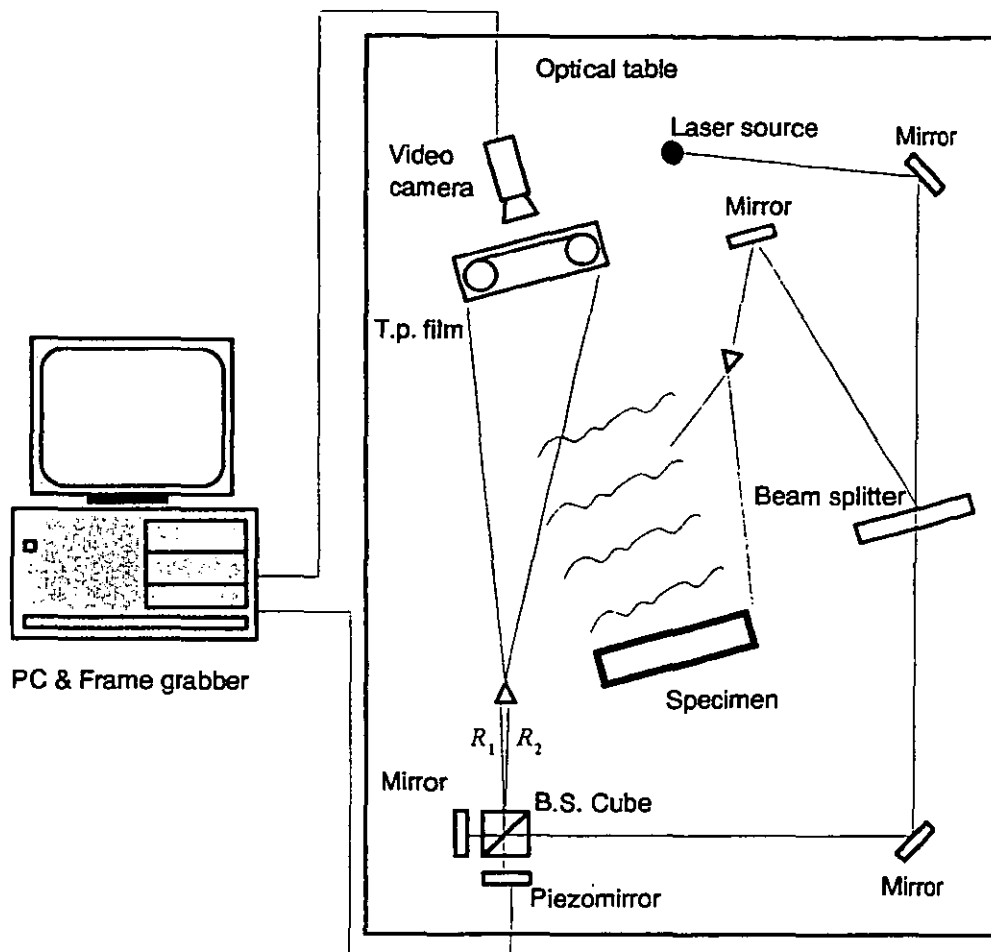
*Figure 4.4. Setup used for double-reference holographic interferometry measurements.*

## 4.1.4. Deformation arrangement

Part of the work was devoted to setting up the experimental arrangement for stressing and holding the specimens during the holographic tests. The shape of the interferometric fringes depends on the nature of the deformation mechanism as well as on the geometric constraints of the object. In his book Vest [5] reported that delamination in composites has been effectively detected by observing the micro deformation caused by mechanical loading, thermal stressing and pressure variations. The experimental work was mainly concentrated on thermal induced deformation, though final tests employing mechanical loading were also performed. The use of a pressurised system to exert a uniformly distributed load on the surface was excluded here because of the small area of the specimens.

76

Heating could be produced by a hot air gun or by direct exposure to an infrared lamp. In the present case, to provide uniform and controlled temperature variations of the object surface, a slightly more complicated arrangement was chosen (see Fig. 4.5.). The calibration procedure is reported in detail for the impact damaged specimens. The specimen containing the marcels was basically held and stressed in the same manner as the impacted specimens. The heating source was a halogen lamp with the filament parallel to the specimen. A dark metallic plate was placed between the lamp and the specimen in order to render the heating more uniform and to act as a screen to avoid the undesirable effects of the lamp light during hologram recording and reconstruction. The relative distances between the lamp, the plate and the specimen could be adjusted to control the heating. The lamp was turned on for 100 seconds and the temperature variations were measured for the plate and the specimen by placing a thermocouple at their central point on the opposite side from the heating source. For the metallic plate linear plots were obtained (see Fig. 4.6.), indicating that the cooling was slightly slower than the heating process. The composite specimen, on the other hand, did not show a linear response (see Fig. 4.7). On the whole, the maximum temperature change for the composite specimen was less than 3°C.
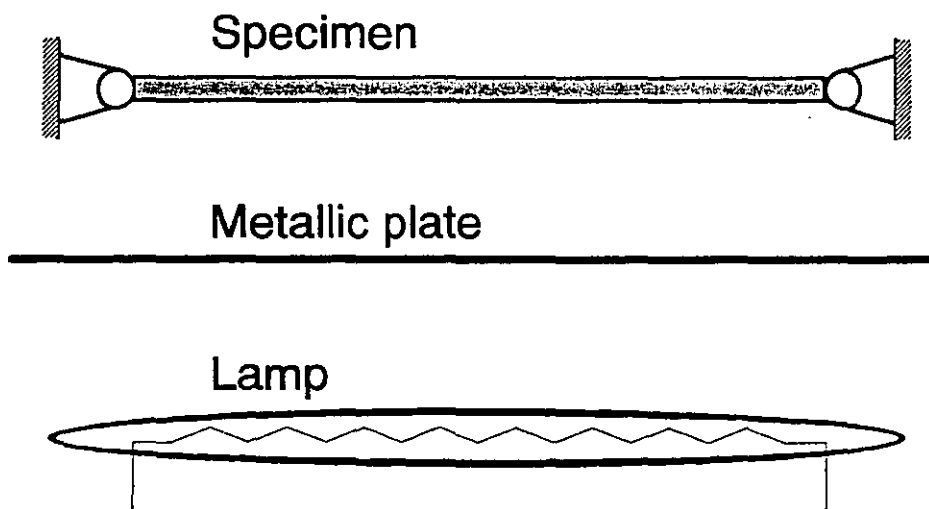


*Figure 4.5. Experimental arrangement used for uniformly heating of the composite specimens.*
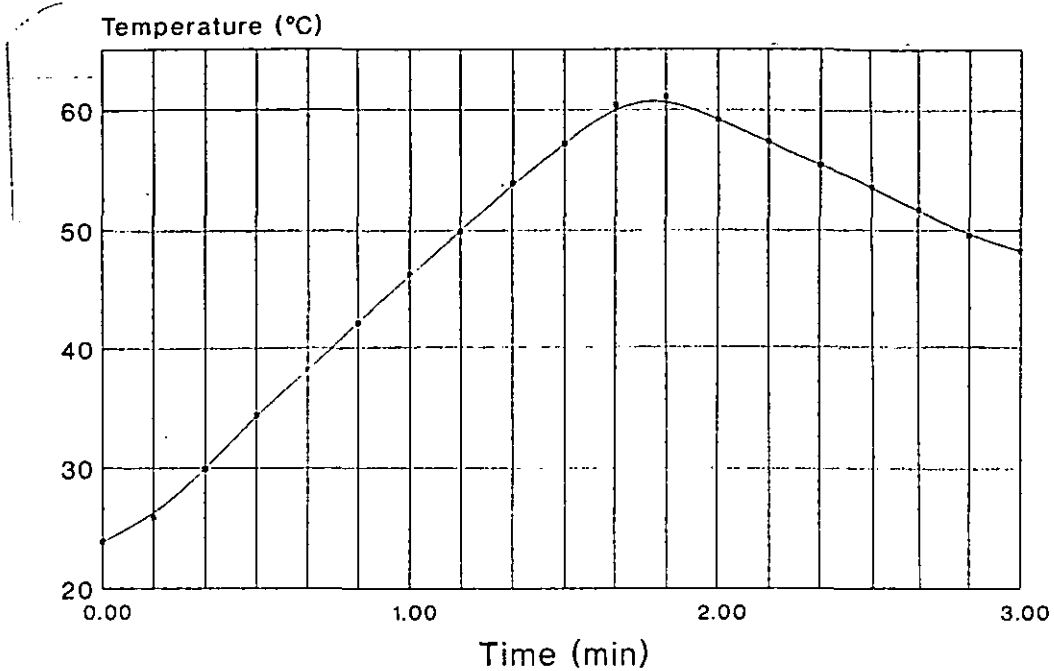
*Figure 4.6. Temperature versus time for the central point of the metallic plate (heating time was 100 seconds).*
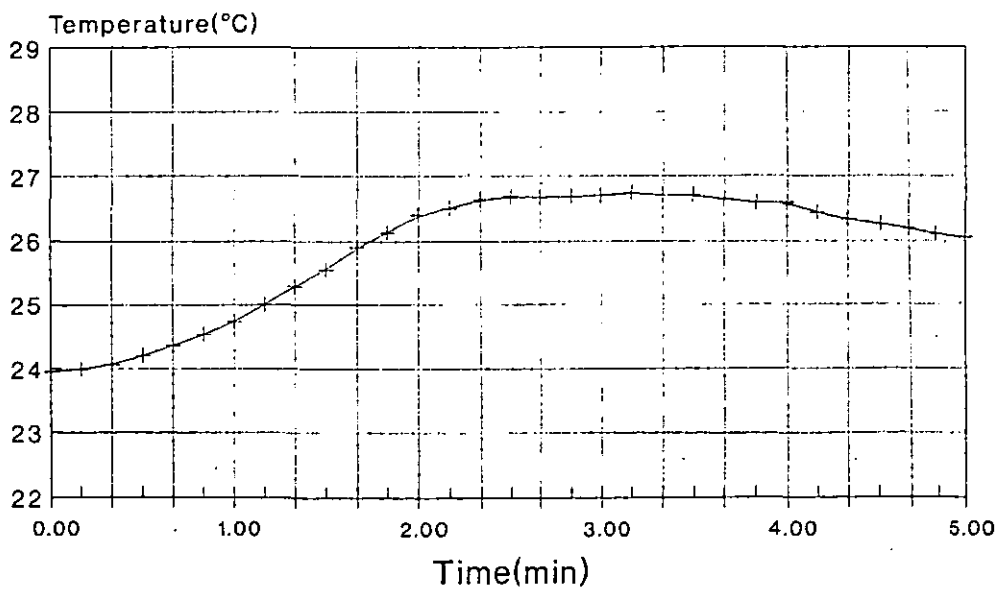


*Figure 4.7. Temperature versus time for the central point of the composite specimen (heating time was 100 seconds).*

The method of holding the specimens was also very important to determine surface deformation. Taking into account the elongated shape of the composite specimen, it seemed appropriate to hold it by its ends. Two immovable blocks having vertical V-shaped grooves were used as holders. The extremes of the specimen were free to rotate in these grooves about the vertical axis (hinge-type constraint). Thus, under heating, the deformation consisted of global compression and buckling. A small pre-loading was necessary to keep the specimen in place during holographic recording. Hinged-type supports were preferred to clamped constraints since a larger out-of-plane deformation was produced and the specimens were more readily replaced. Finally it is noted that unconstrained (free-free) conditions were of no concern here since negligible out-of-plane components would have resulted and the specimen would have lost the mechanical stability required for the holographic inspection.

### 4.1.5. Experimental results

#### 4.1.5.1. Impact damaged specimens

Real-time tests were performed on each specimen. A reference hologram was recorded and developed. The fringe pattern evolution was followed on the TV monitor for 3 minutes and recorded onto a video tape. The lamp had been heating the metallic plate for the initial 100 seconds. Fig. 4.8. shows a fairly well developed fringe pattern of the two virgin specimens. In both cases, the fringes are made up of parallel lines and correspond to some flexural mode of specimen deformation. This is exactly as expected; during heating the specimen expanded, but, being constrained at its extremes by the hinge supports, it was compressed and buckled. The deformation probably occurred in the direction of the metallic plate, because the first heated layers of the specimen were forced to buckle outwards by the inner colder layers. The few hyperbolic shaped fringes indicate the presence of a small anticlastic bending in the middle of the specimen, which was probably due to some temperature gradient. As demonstrated in Fig. 4.9., temperature differences of few tenths of a degree were typically measured between the centre point and the top and bottom edges.

For the impacted specimens it was observed that as the temperature increased discontinuities started to appear (see Fig. 4.10.). They were localised at the zone of the specimen where the impact took place. Normally this zone acted as a source and a sink of closed fringes for increasing temperature and for the cooling down phase, respectively.

*Figure 4.8. Fringe pattern of virgin specimens V1 and V2.*
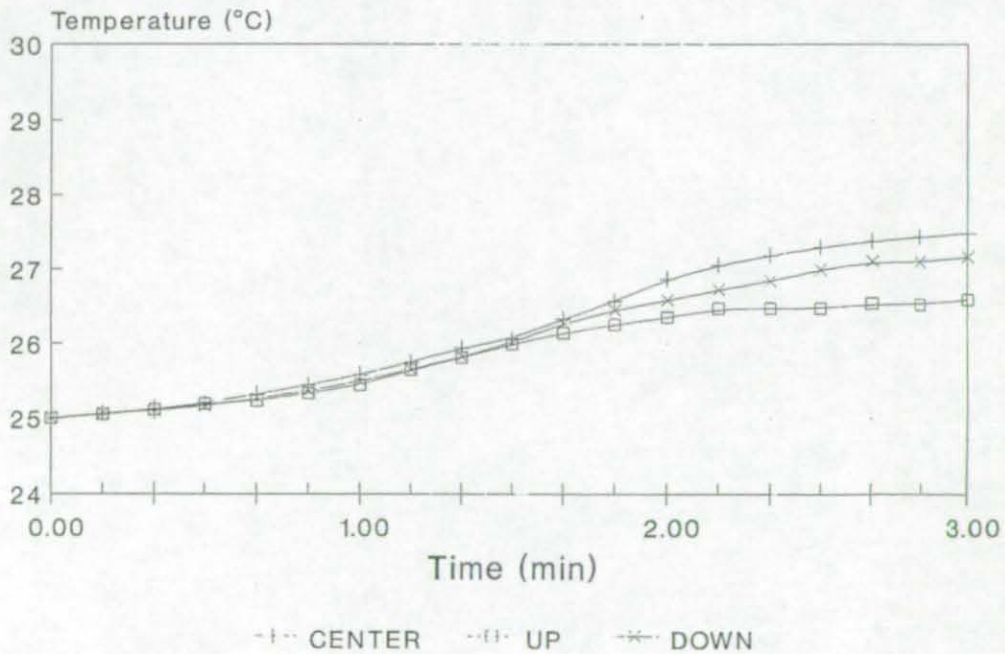


*Figure 4.9. Temperature diagrams for three surface points A, B, and C, lying along a central vertical line of the specimen.*

time:   0:39:4

time:   0:50:2

time:   1:13:0
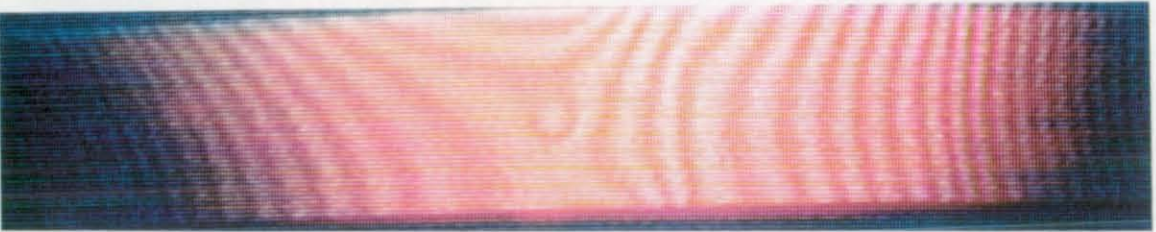
time:   1:28:3

time:   1:53:2

*Figure 4.10. Evolution of fringe pattern with temperature (specimen B10).*

81

Referring to Fig. 4.11., it was seen, for a given time, that the intensity and the extent of the pattern anomaly were proportional to the impacted energy and, consequently, to the incurred damage (mainly delamination). The imposed compression caused extensive local buckling at the impacted areas (in or out), which was superimposed to the global buckling of the specimens. This effect is known in composite science as delamination buckling under compression [6,7].

The interferograms of the non-impacted side of the specimens (see Fig. 4.12.) revealed a central zone with two small side lobes of fringe distortions. It is to be noted that they are aligned along a 45° angle, which coincides with the fiber direction in the surface ply. In this case, possible fibre breakages, added to delaminations, could have altered the buckling mechanism, considerably modifying the fringe pattern.

0.5 J/mm



1.0 J/mm



1.5 J/mm



*Figure 4.11. Fringe pattern of specimens with different levels of impact energy (A series).*

0.5 J/mm



1.0 J/mm



1.5 J/mm



*Figure 4.12. Fringe pattern of non-impacted side of specimens with different levels of impact energy (A series).*

Quantitative analysis of the interferometric results by means of double-reference double-exposure holographic interferometry supported some of the previous considerations about the deformation mechanisms. In the new setup (see Fig. 4.4.), the specimens were subjected to the same thermal stressing conditions reported for the real-time tests. On the basis of the first experiments it was decided that the measurements ought to refer to the relative deformation occurred between $t = 0$ (first exposure; specimen at rest), and $t = 140$ seconds (second exposure; during the cooling down phase). The angle of illumination and observation of the specimen were equal. Therefore, according to the theory on fringe formation presented in Chapter 2, the 3-D map of phase was proportional to the out-of-plane displacement.

The occurrence of delamination buckling is highlighted in Fig. 4.13. for the impacted side of specimen B10. The deformation profile of the central longitudinal section is also shown. The data regarding specimen A10 are shown in Fig. 4.14. Unlike the B10, delamination buckling took place in the same direction as the global deformation.



*a)*

## Deformation profile

### [Micrometric units]



*b)*
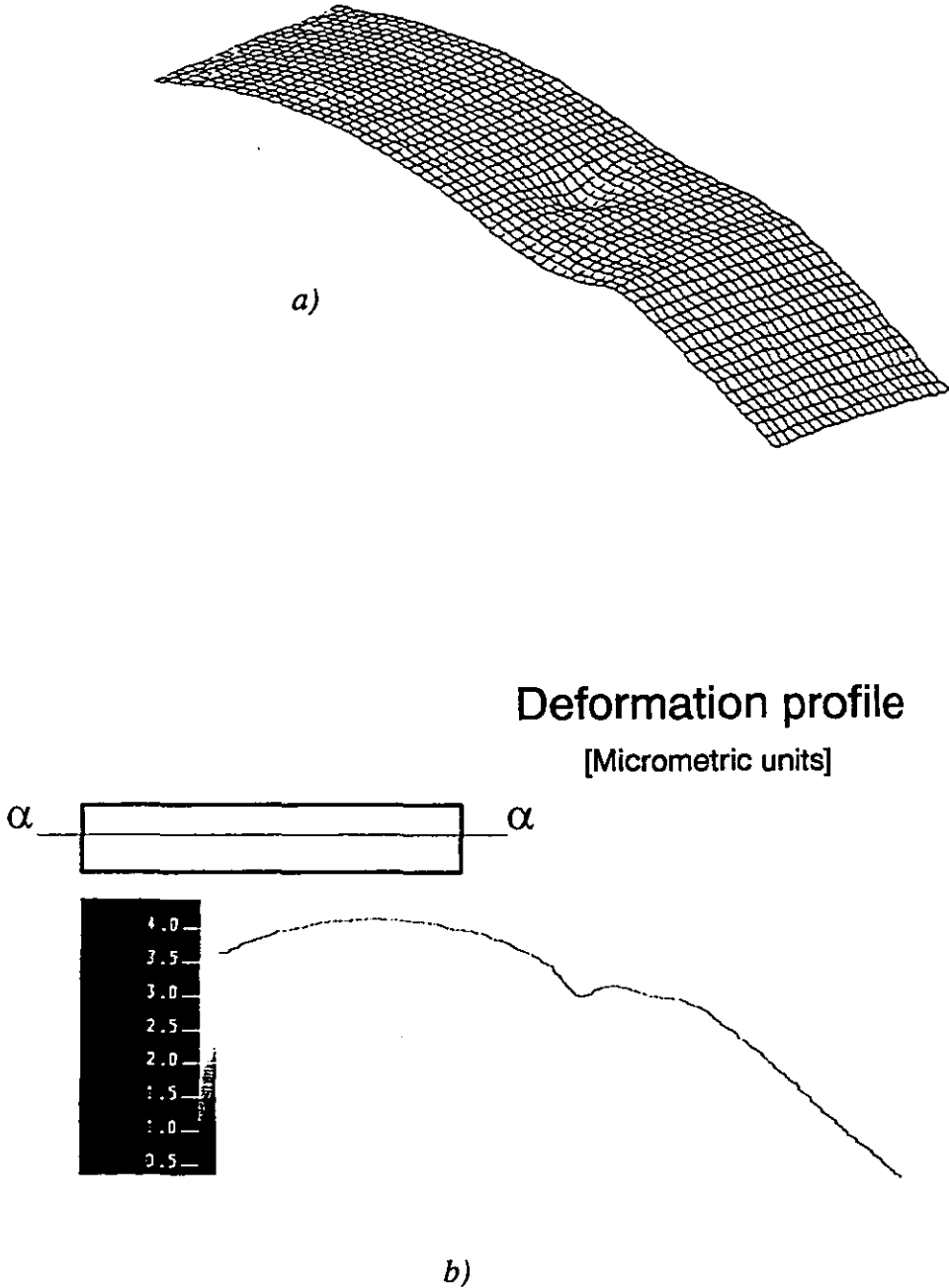
*Figure 4.13. a) 3-D image of out-of-plane deformation in specimen B10; b) Values of deflections along the line* $\alpha - \alpha$.

a)



## Deformation profile

[Micrometric units]

b)
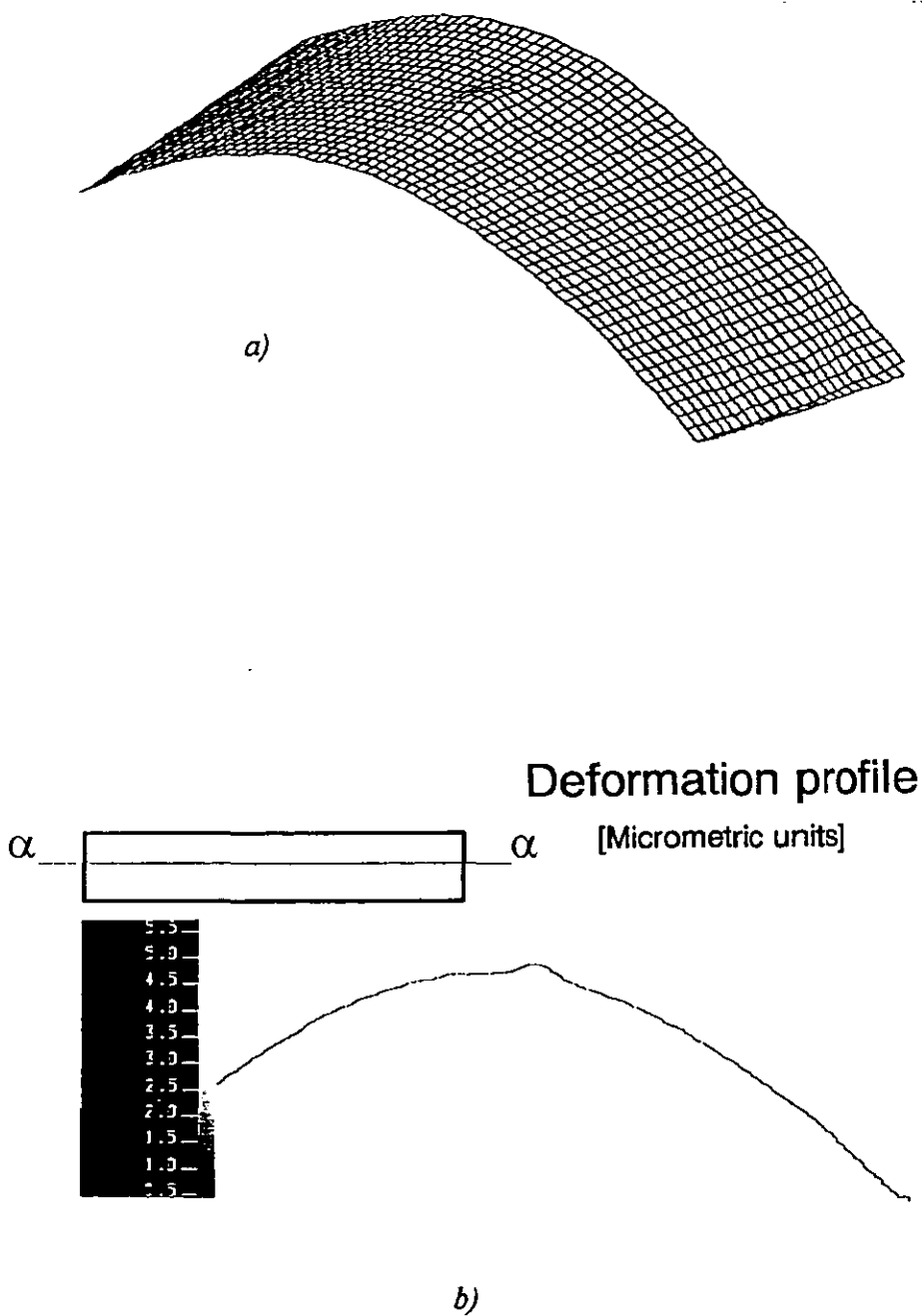
*Figure 4.14. a) 3-D image of out-of-plane deformation in specimen A10; b) Values of deflections along the line* $\alpha - \alpha$.

By neglecting the part of the data due to the effects of the defect, the deformation profile could be ideally reconstructed by tracing a curved line connecting the smooth lateral slopes (see previous figures). Local buckling could be quantified by the

maximum deviation δ of the real profile from the reconstructed one. Therefore δ could be related to the level of damage occurred by impact in the composite. A plot of δ versus impact energy is presented in Fig. 4.15. for the A specimens. However, the comparison of damage in terms of δ can only be performed when the global buckling profile is not too distorted and can be correctly reconstructed.
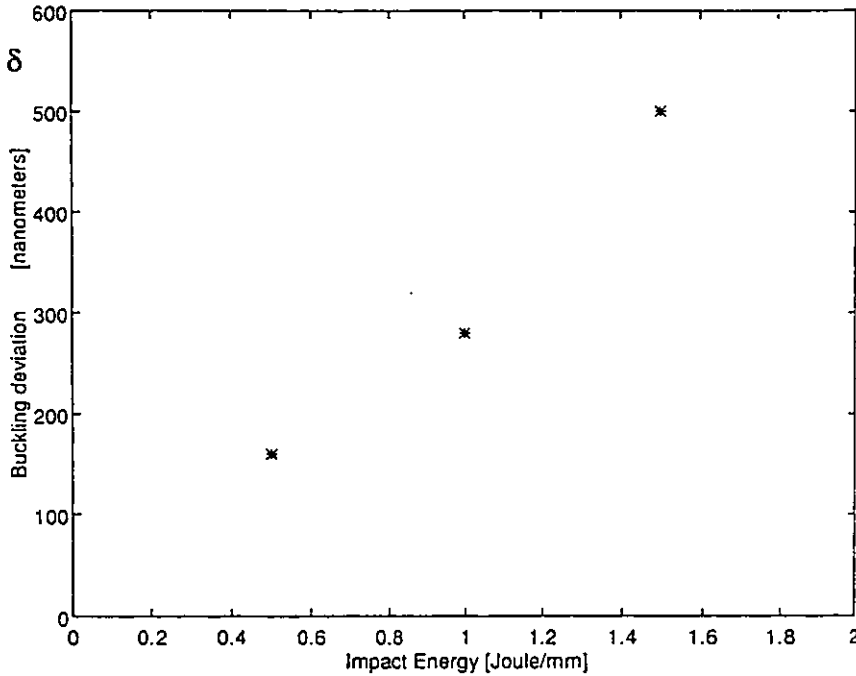


*Figure 4.15. Local buckling deviation δ for the A specimens.*

Fig. 4.16. shows very characteristically the deformation pattern of the non-impacted side of the specimen B10. It is seen that the two side lobes correspond to peaks while the middle anomaly corresponds to a depression of the surface.

The ultrasound examination of the delaminated specimens has confirmed the experimental results obtained by the holographic inspection. An ultrasonic C-scan was made on each of the specimens using a 0.5" diameter probe at 2.25 MHz, in a double-through transmission technique. The scan was performed by Agusta Helicopters. The results are shown, for the three specimens of the A series, in Fig. 4.17. The C-scans indicate the position and the extent of delamination (the central white area) according to the interferometric images in Fig. 4.11. The comparison is also satisfactory for the other specimens (see Fig. 4.18. and Fig. 4.19.). It is worth noting that in both series for the specimens impacted with 0.5 J/mm no noticeable damage was detected neither by ultrasound inspection or by holographic interferometry.
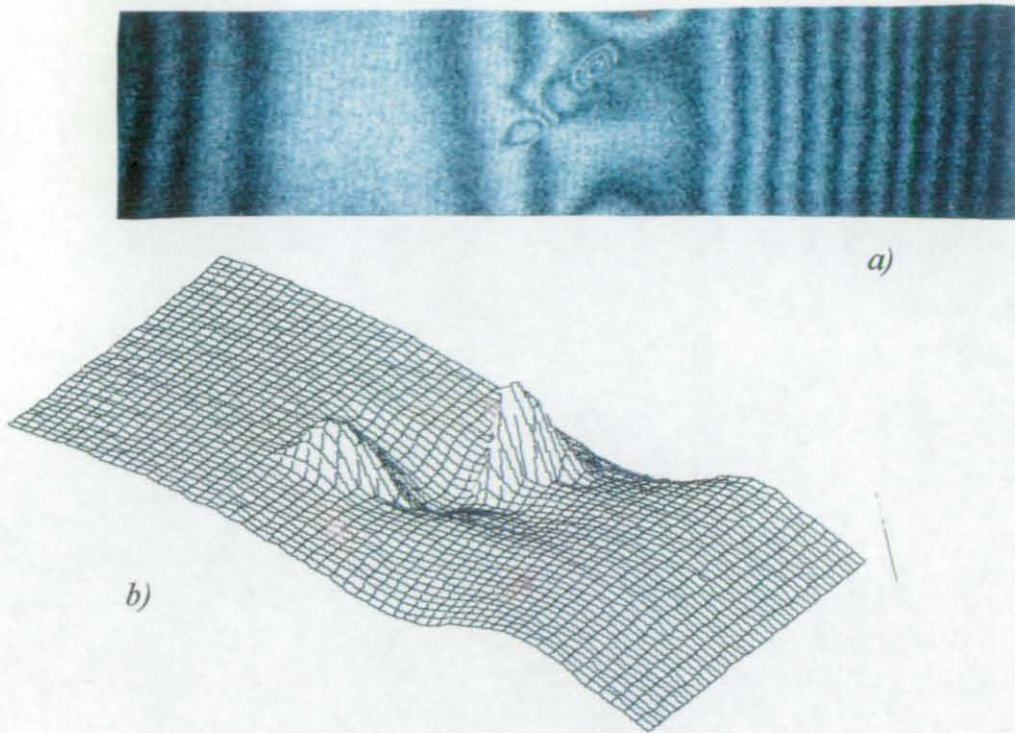
*Figure 4.16. a) Double-exposure interferogram of specimen B10 (non-impacted side); b) 3-D plot of the evaluated deformation.*
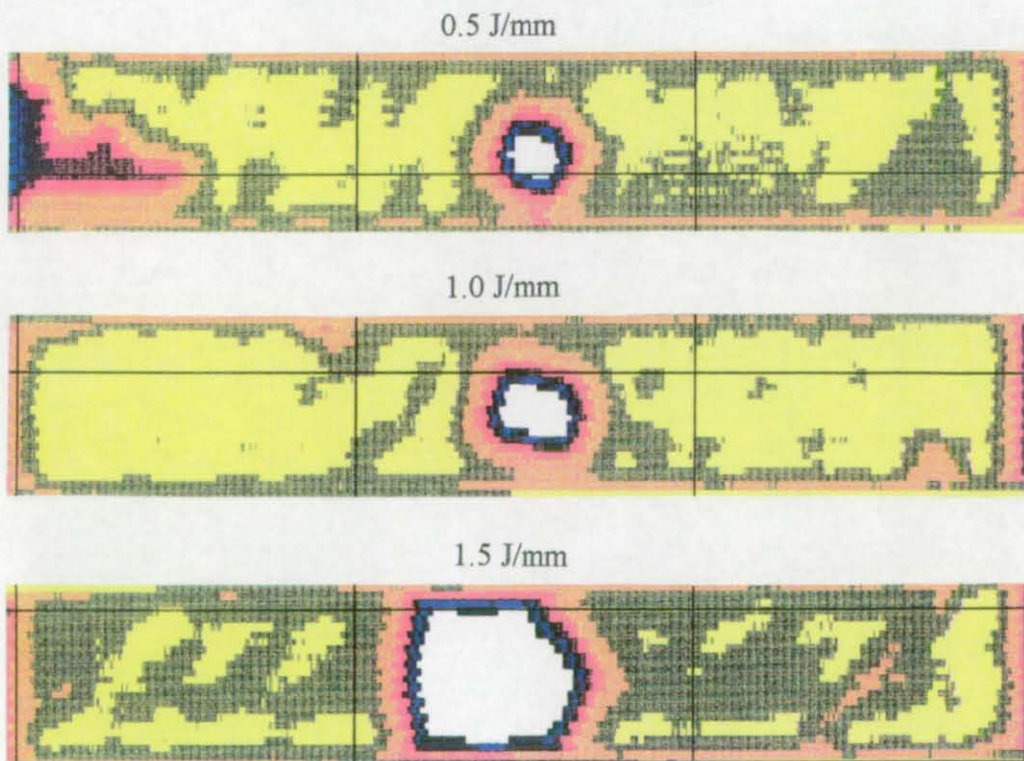
0.5 J/mm

1.0 J/mm

1.5 J/mm

*Figure 4.17. Ultrasonic examination of specimens with different levels of impact energy (A series).*

Series B 0.5 J/mm

1.0 J/mm

1.5 J/mm
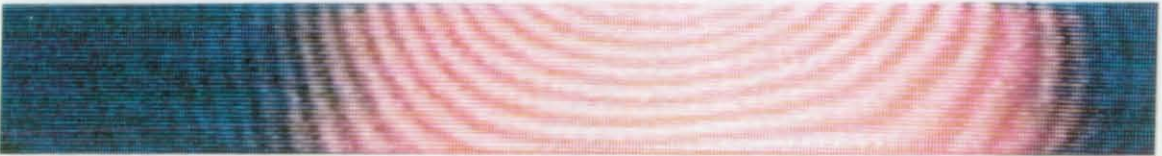
Series C 0.5 J/mm

1.0 J/mm

1.5 J/mm

*Figure 4.18. Fringe pattern of specimens with different levels of impact energy (B and C series).*

Series B                          0.5 J/mm
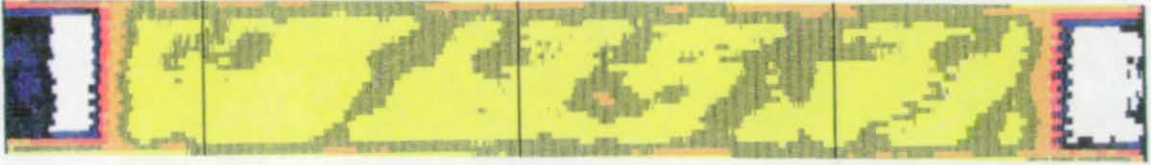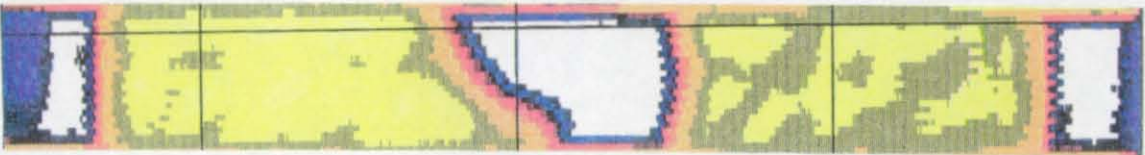
1.0 J/mm

1.5 J/mm

Series C                          0.5 J/mm
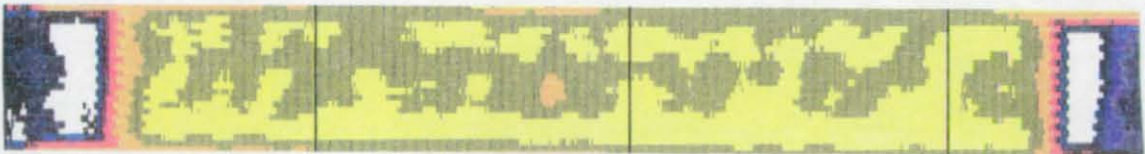
1.0 J/mm

1.5 J/mm

*Figure 4.19. Ultrasonic examination of specimens with different levels of impact energy (B and C series).*

Finally it should be noted that mechanical loading (bending and compression) has also been investigated, but with no positive results. Only the most damaged specimens showed slight anomalies in the resulting fringe patterns.

## 4.1.5.2. Built-in marcels

Real-time and double-reference holographic interferometry were applied to the marcels containing specimen under the same conditions (heating duration, holding arrangement, specimen orientation) as the experiments described in Sec. 4.1.5.1. Since the current specimen was noticeably thicker than the impact-damaged laminates the global buckling deformation was less pronounced. The presence of damage became evident by the inspection of the surface close to the flawed zone. In fact, the thermal response of the undulated layers immediately beneath the surface altered the out-of-plane displacement, displaying unambiguously the existence of the marcels. The resulting fringes (see Fig. 4.20.) showed a very characteristic wavy shape. This meant that the global out-of-plane displacement had been spatially modulated. The period of the fringe undulations in the interferograms corresponded to the period of the marcels, visible through the lateral section of the specimen. A simple explanation can be given by assuming that the composite layers predominantly expanded along the direction of the carbon fibres. Thus, when heated, the major contribution to the out-of-plane displacement of a sinusoidal shaped layer will be due by the points at maximum slope whereas the points close to the peaks and the valleys will only cause in-plane deformation (see also Fig. 4.21.). By neglecting the in-plane components that cannot be measured with this setup, the final result is that the relative displacements of the peaks and the valleys will introduce opposite phase changes at the same period of the layer undulations (marcels).
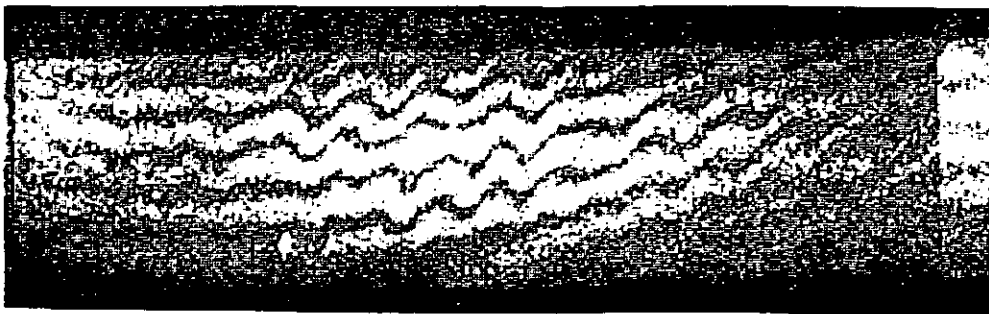


*Figure 4.20. Fringes of the marcels containing specimen.*
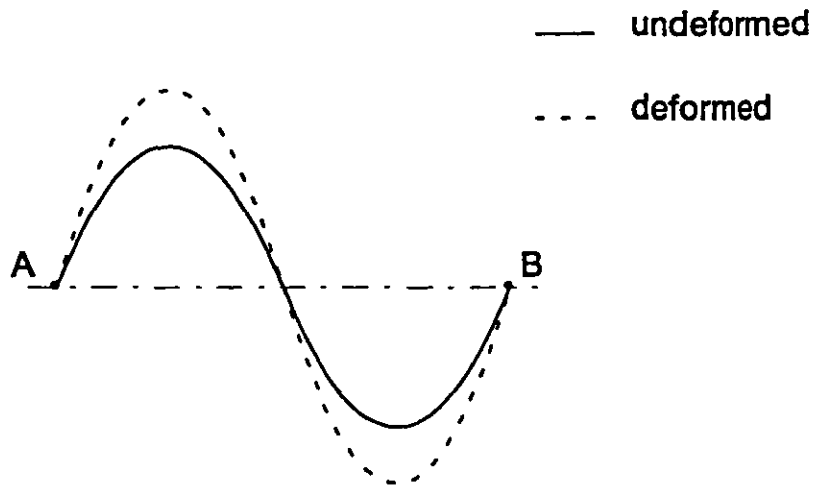
*Figure 4.21. Thermal deformation of a sinusoidal fibre whose ends are fixed. The out-of-plane deformation is along the vertical direction.*
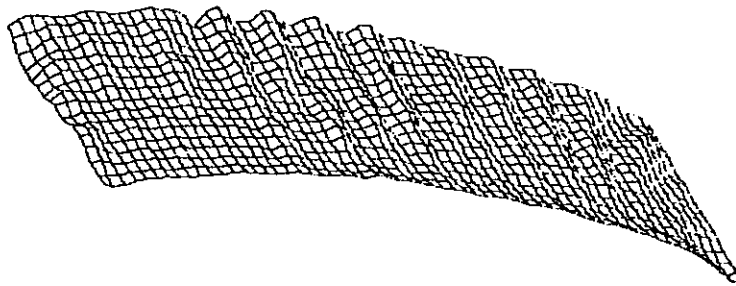


*Figure 4.22. Pseudo 3D image of surface deformation of the marcels containing specimen.*

Finally, it should be noted that the presence of marcels could not be detected by normal ultrasound inspection. The main problem is that the ultrasonic wave is not reflected by the defect since the marcels are not real material discontinuities as delaminations are. In the present case, another drawback is that to investigate thick specimens high energy ultrasonic pulses were necessary.

## 4.1.6. Concluding remarks

Laser holographic interferometry has been employed in an efficient manner for detecting impact induced delamination and marcels in graphite-epoxy composite specimens. The interferometric images, interpreted in a qualitative manner, portray the state of integrity of the material. The principle underlying the method is that for a stressed zone of a body without geometrical discontinuities, distortions of fringe patterns indicate abnormal surface deformation and, consequently, the presence of some type of material defect. In particular, the presence of delamination in the impacted specimens gave rise to local buckling, whereas the marcels produced micro undulations of the surface.

It has been shown that the delaminated areas were detected and evaluated in full agreement with the results of the ultrasound examination. The neatness of the full-field measurements yielded by the holographic method constitutes a remarkable advantage with respect to the point by point scanning and specimen water immersion required by the ultrasonics. The results obtained for the marcels, which were invisible to the C-scan, were also confirmed by visual inspection of the lateral section of the specimen.

The method described is well suited to the study of small parts which can be readily examined in the optical laboratory. For in-field operation the optical setup would require substantial modification. The use of a pulsed laser source is strongly recommended to avoid the negative effects of any external disturbance (mechanical vibrations, air turbulence, etc.). In an industrial environment, real-time holography can be at most an interesting but expensive preliminary test to be performed at night after having turned off all the main machines in the range of several hundreds metres.

It should be emphasised that a key element to the success of this holographic application is the manner the inspected objects are positioned and stressed. The necessary arrangement should be carefully considered for each object to be tested.

The technique of real-time holography was able to detect surface changes induced by temperature variations of only 2 °C. The potential of this approach as a NDT technique is clear as such a temperature rise can be easily effected (with a hot air gun, or with an IR lamp). Thermal stressing, if compared to mechanical loading, has the advantage of being contactless and easy to perform.

For the quantitative results of surface deformation sought in this study, double-reference double-exposure holographic interferometry was applied. The

numerical analysis has been possible by the introduction of digital image processing. The displacements of the deformed surfaces were measured with a precision of the order of ten nanometers. Three-dimensional images were produced allowing in many cases a unique visualisation of the deformation mode.

## 4.2. Deformation studies on violins by electronic speckle interferometry

### 4.2.1. Introduction

Since the nineteenth century violins have been the subject of many scientific investigations aiming at discovering the laws and secrets which give some instruments unrivalled sounds. It is worth citing the pioneering work of eminent scientists such as Savart, or Helmoltz, who performed the earliest studies on the vibration and acoustic properties of violins. However, at that time the existing technology was at a too basic level for such a complex task. In fact, violins are very complicated mechanical systems where the fundamental components (wood, paint) are skilfully worked and assembled by the violin maker following his or her own experience and genius.

In recent years the growth of technology and interdisciplinary connections have opened up new perspectives in violin research as the following examples clearly demonstrate. The acoustic waves, recorded through very precise microphones, can now be digitally stored and interpreted by computers. Paint composition can be readily identified by means of chromatography, mass spectroscopy and atomic fluorescence. Photogrammetry and structured light projection have been successfully used to measure the geometric dimensions of an instrument. Holographic [8] and speckle [9] interferometry applications have greatly enhanced the knowledge of the vibration properties of the violin. Nodal lines and vibration amplitude can be precisely determined by time-average techniques.

The violin has a lightweight structure ($\approx$380 g). The top plate is made of spruce and it is 2-3.5 mm thick; its weight is approximately 80 g. The bottom plate, made of maple, is stiffer than the top. The bottom thickness varies from point to point in the range between 2 and 5 mm, and the plate weight is approximately 120 g. A set of forces due to the violin strings heavily loads the structure. The tension of the strings is $\approx$200 N and the resulting force, normal to the top plate is $\approx$90 N. Thus, the arching of the two plates should be modelled to reduce the eventual stress in the material. However structural safety is not the primary scope of the violin plates. The violin maker works on the thickness distribution and arching in order to produce the desired acoustical properties, which depend on the dynamic behaviour of the plates. Having a strong structure is often in contrast with playing a good sound. The instrument might be very resistant but with a low performance or it might be seriously deformed in a short time in spite of its pleasant sound. Anyway, it is up to the violin maker to find the best compromise. Excellent instruments by A.Stradivari (1644-1737), for example, have not shown any visible

deformation for more than 300 years. Many other authors, e.g. Testore from Milan (1660-before 1710), modelled the violin structure to obtain a delightful performance, but his instruments underwent irreparable deformation with consequent loss of the acoustic quality. Nowadays violin makers seem to be very interested in this problem. Therefore it would be extremely important, for a given instrument, to know the exact distribution of deformation. With this information the most stressed zones can be precisely identified and reinforced, whereas the other parts could be freely modelled to optimise the acoustical performance.

At the present state of research, Finite Elements Methods (FEM) [10] have been applied to study the dynamic behaviour of the violin sounding box. However a major drawback of these numerical methods is the need for material characterisation. Normally, the available algorithms, used for industrial applications, dealing with isotropic materials and even those accepting an average elasticity tensor as input, cannot take into account the unavoidable discontinuities of the wooden structure. In reality, the spruce is made of narrow and tough autumn fibres combined with wider and softer spring fibres. Wood defects and medullary rays, perpendicular to the fibres, locally alter the material characteristics. A similar situation exists for the maple, though the difference between the autumn and spring fibres is less evident.

Another approach involves direct measurement of the effects of the string tension onto the 3D shape of the violin plates, which can be obtained by means of interferometric methods. A study, based on the accurate measurement of the micro deformation caused by the action of the strings, is proposed herein. For a new instrument it is assumed that the small surface displacement, produced by small changes of the string tension, will turn into visible alteration of the surface and possibly produce structural damage after some years. Besides, a full-field examination of the object will provide the map of the weak zones prone to failure. On the basis of micro deformation results, classification of the instruments might be eventually made in terms of their structural reliability.

In the experimental work electronic speckle pattern interferometry and speckle shear interferometry have been used to measure surface micro displacement and its derivatives. The top and bottom plates of two violins with different structural characteristics have been considered. The measuring system, operating in real-time mode, performed a continuous subtraction between two speckle images of the violin; the first image acquired before and the second after the tension of one string was varied by a fixed amount. The resulting interferograms, in spite of their higher noise content than in traditional holographic experiments, were successfully interpreted by appropriate image processing algorithms.

In the following sections a short description of the violin structure is included. The holder and the loading mechanism are also presented. The optical setups used for both speckle pattern interferometry and shear interferometry are reported. The last part deals with the presentation and discussions of the experimental results.

## 4.2.2. The violin structure

The main parts of a violin are the sounding box, the neck with the music board and the strings. The sounding box consists of the top and bottom plates, which generate the acoustic waves, and of two lateral ribs. There are four strings that are fixed to the tailpiece at their lower end, and wound around the tuning keys (or pegs) at the other. The strings transmit the vibrations to the top plate through the bridge. The back plate also vibrates because it is connected to the top plate through a small piece of wood known as sound post, which is placed inside the sounding box. Three reinforcements are present; the bass bar, glued to the top plate, two wooden blocks, one close to the neck and the other where the tailpiece is fixed to the violin body.
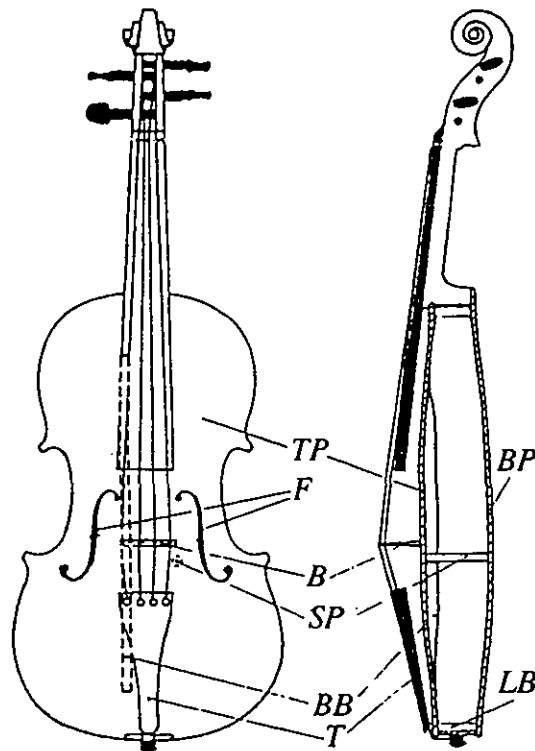


*Figure 4.23. The violin structure: a) front view, b) lateral section. Letters indicate the sound post (SP), the lower block (LB), the top plate (TP), the back plate (BP), the f-holes (F), the bridge (B), the tailpiece (T) and the bass bar (BB).*

### 4.2.3. Deformation arrangement

For the interferometric inspection the holding system was first considered. The violin should be kept firmly in place during the tests, and the influence of the holding system on the set of forces acting on the instrument should be as small as possible. A very stiff frame, blocking any rigid body movement of the object would have probably satisfied the first condition but surely not the second. Therefore it was decided to place the violin on four rubber bearings and to fix it using two elastic wires. The contact points were in vicinity of the reinforced parts at the lower and at the upper ends of the sounding box. The proposed solution is depicted in Fig. 4.24. The holder was built by the International Violin Making School in Cremona (Italy). Rubber bearings were used to let the violin return to its rest position after having adjusted the string tension. The mechanical hysteresis of the bearings was tested by speckle interferometry observing the residual fringe pattern on the surface after tilting and releasing the violin. In most cases there were no fringes left, indicating that the object returned with great precision to its initial position.

An efficient way to change the tension of a string by a small amount was to act on the corresponding fine tuner, placed at the point where the string is fixed to the tailpiece. A tiny metal stick was soldered onto the fine tuner to indicate the rotation of the tuning screw. Tests were also made acting on a peg, but it was found that the deformation was not easy to control and to reproduce.

A schematic description of the static load, which the sounding box is subjected to in the present configuration, is now given (see also Fig. 4.25.). The tension of the strings is transmitted to the violin at three points; the bridge, the lower block, and the upper part of the neck. The force ($F_3$) acting on the bridge depends on the relative angles between the strings and the bridge itself and has an intensity of approximately 90 N. The other effects of the strings can be represented by a force $F_1$ parallel to the plates at the lower block, and by the two forces $F_2$ and $F_4$ at the upper block, where a moment is transmitted through the neck. The resistant load caused by each bearing of the holder is schematically represented by a force normal to the back plate ($R_1$ and $R_2$). The weight of the violin and any friction force parallel to the plate can be eventually included in $F_1$ and $F_2$. However, the sizes of the forces applied to the sounding box cannot be easily determined and the consequent deformation is still more complicated to evaluate. This means that an experimental method such as holographic interferometry or ESPI is very appropriate for the characterisation of static deformation in violins.
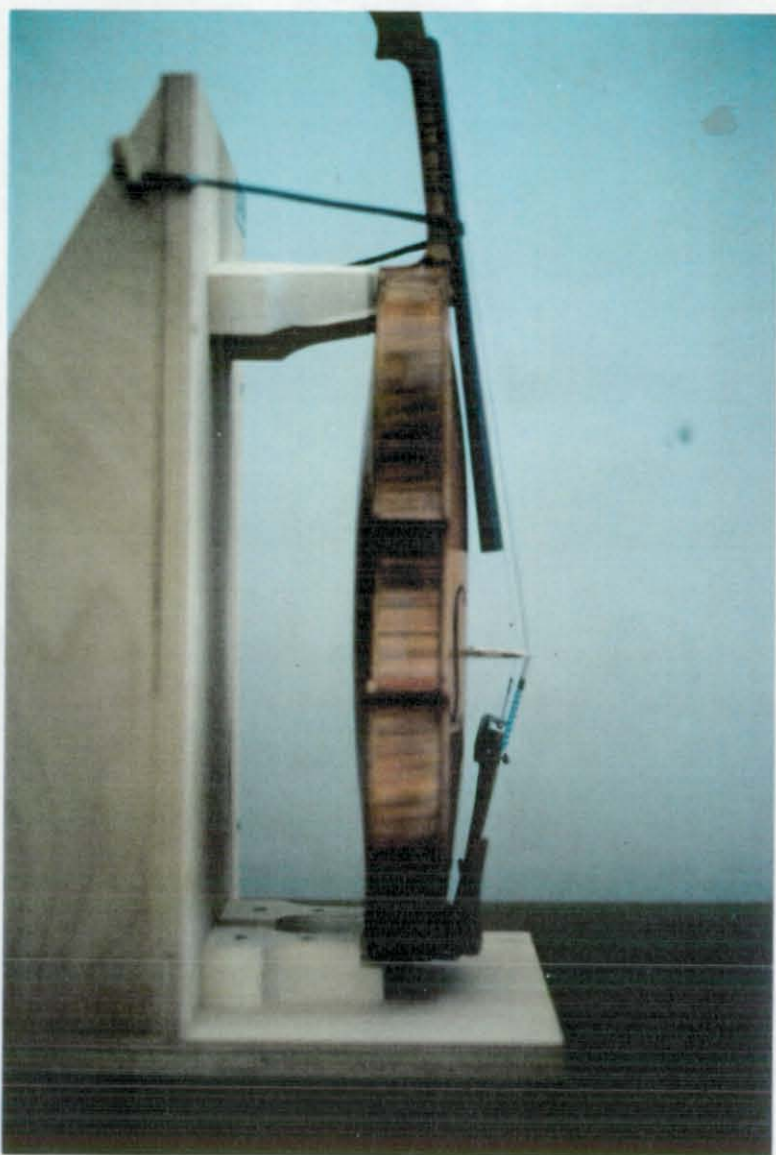
Figure 4.24. Lateral view of the violin holding system.
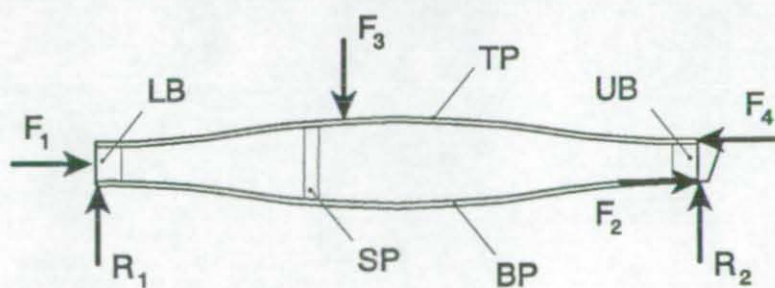


Figure 4.25. Sketch of a possible set of forces acting on the sounding box for a violin
in the holding system. Lateral section depicted showing the sound post
(SP), the lower block (LB), the upper block (UP), the top plate (TP), and
the back plate (BP).

## 4.2.4. Optical setup

The interferometric measurements were performed in the optical laboratory, where the experimental setup was mounted on a vibration free table by Newport (mod. M-MST-48-8 size 1.2 x 1.8 m). Special attention was devoted to eliminate any disturbance from air turbulence or temperature gradients that could eventually introduce spurious fringes in the results. Once the violin was tuned and placed in its holder it was necessary to wait for a settling time of several minutes (from 5 to 30 min) before starting the inspection. A Spectra Physics mod. 127 He-Ne continuous wave laser (output power $P = 35\,mW$; wavelength $\lambda = 633\,nm$) was used.

The surface micro deformation was measured with the setup depicted in Fig. 4.26. The laser beam was split into the reference and illumination rays by a variable beam splitter. The splitting ratio between the transmitted and reflected rays was 90:10. The object illumination beam was expanded by a 60 x microscope objective and filtered with a $10\,\mu m$ pin-hole. A coherent image of the object was formed on the CCD sensor of a B/W video camera Sony (mod. XC77CE 768 x 512 pixels), which was rotated by 90 degrees to include the whole image of the sounding box of the violin. A polarising beam splitter cube was positioned between the objective lens (focal length $f = 24$ mm) and the CCD sensor in order to superimpose the light of the reference beam on the object image. The ratio between the intensities of the reference and object beams at the CCD sensor plane was approximately 3:1.

Because of the limited coherence length of the laser light, the optical paths of the interferometer were matched by adjusting the reference path length. In practice, the two mirrors in the upper part of the setup were used to increase the reference path length by a relatively large extent. Final adjustments were readily performed by modifying the distance between the piezomirror and the glass cube. Before entering the polarising cube in the imaging system, the reference beam was expanded with a biconvex lens ($f = 20$ mm). This was necessary to fulfil the conjugation condition for the formation of ESPI fringes [11]. The mirror, mounted on a piezoelectric crystal was used to introduce the required phase changes for the final evaluation of the interferograms. The best working condition of the piezomirror is obtained when the laser beam direction is normal to the mirror surface. For this reason a glass beam-splitter cube was placed in front of the piezomirror. The PC and the frame grabber were those used for the investigation on composites (for their description see Sec. 4.1.3.)
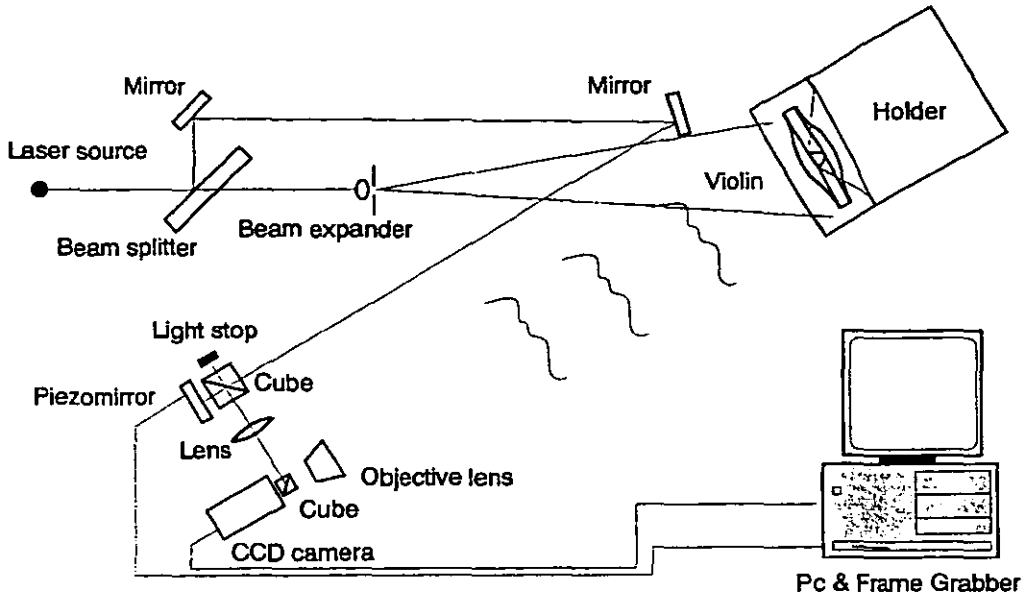
*Figure 4.26. Setup for deformation analysis based on Electronic Speckle Pattern Interferometry (ESPI).*

The setup used for tests with speckle shear interferometry is sketched in Fig. 4.27. It was substantially simpler than the previous one. The interferometer was built-up by simply using the two mirrors and the beam-splitter cube positioned in front of the video camera lens. With this arrangement two speckle images were superimposed at the CCD plane. The images could be shifted by turning the tilting screws on the mirrors. Let $\delta x$ be the lateral shift between the two images. During deformation, superimposed points, shifted by $\delta x$, will produce a relative phase difference $\Delta\phi$ given by [11]

$$\Delta\phi = \frac{4\pi}{\lambda} \frac{\partial d}{\partial x} \delta x$$

Where $\dfrac{\partial d}{\partial x}$ indicate the derivative of the out-of-plane displacement $d$ with respect to the direction of the image shear, and the observation and illumination directions have been assumed to be identical. According to theory, if $n$ is an integer number, bright fringes appear when

$$\frac{\partial d}{\partial x} = \frac{n\lambda}{2\delta x}$$

From this expression it is clear that the sensitivity of the method is proportional to the shift introduced between the images.

100
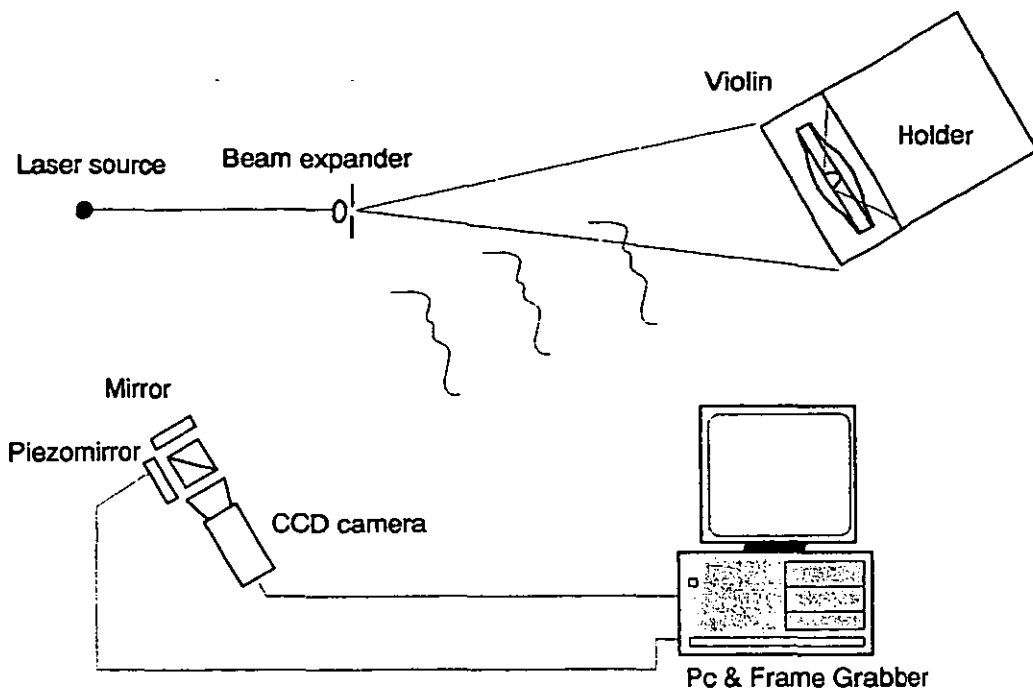
*Figure 4.27. Setup for strain analysis based on speckle shearing interferometry.*

## 4.2.5. Experimental results

The experiments were performed on two violins belonging to the Cremona Violin Making School. They were a Louis Fernandez [master V.Bissolotti] in white (violin A) and the matricule 1102 of the order number 98 (violin B). These two instruments, although very similar to the inexperienced, were very different. From a structural point of view it is noted that violin A was built with a much fuller arching in the flanks than violin B. As a common reference state for the tests both instruments were tuned at 440 Hz.

### 4.2.5.1. ESPI measurements

Deformation fringes could be produced by subtraction of two speckle images recorded one before and one after a change of the tension of a string. In practice, four speckle images of the object at rest were taken, each of them obtained by increasing the optical phase by ninety degrees. This phase change was produced by shifting the piezomirror at

101

steps of λ/8. Then the formation of fringes was monitored by continuous subtraction of the real-time speckle image with one of the four images previously recorded. The operator could be immediately aware of any fringe alteration caused by unwanted disturbances. After having pulled a string, continuous subtraction was stopped and the final speckle pattern was stored. The final step consisted of the subtraction of the speckle image, corresponding to the deformed object, with each of the four speckle patterns shifted in phase, corresponding to the object at rest. Therefore four speckle interferograms were obtained for each experiment. These interferograms were used for the quantitative evaluation of the deformation map by means of the four images phase shifting algorithm (see Sec.3.3.1.).

The mechanical load exerted through the bridge on the violin body by the strings can be represented by a force perpendicular to the top plate surface which is applied in a point very close to the second string. According to this it was decided to act on the second string to produce the deformation of the plates. Three interferograms of violin A were recorded by turning the fine tuner of the second string clockwise by 120°, 270°, and 540° respectively. Whilst considering the top plate (see Fig. 4.28.) it was clear that the peripheral zones deformed very little and approximately of the same amount in all the tests. On the other hand for the central zone between the two $f$-holes the number of fringes seemed to be proportional to the string tension. The presence of the bridge and some reflections from the strings reduced the contrast of the fringe pattern. The back plate of the violin was investigated next. In the results (see Fig. 4.29.) the concentric fringes clearly indicate a point load effect due to the sound post which pushed the plate outwards. As for the top plate, the outer zones showed no appreciable difference in the three interferograms.

The deformation caused by a tension variation of the first string was also considered (see Fig. 4.30.). In this experiment the top plate deformation was asymmetrical. As expected the half plate on the same side of the first string was covered with more fringes than the other half. On the back plate the concentric fringes were more numerous than those produced by pulling the second string of the same quantity. This fact can be explained by observing that the sound post is closer to the point where the load was applied than for the previous experiment. In fact, the sound post is positioned midway between the bridge and the $f$-hole at ≈1 cm from the first string[1].

---

[1] The distance between two consecutive strings is also ≈1 cm.
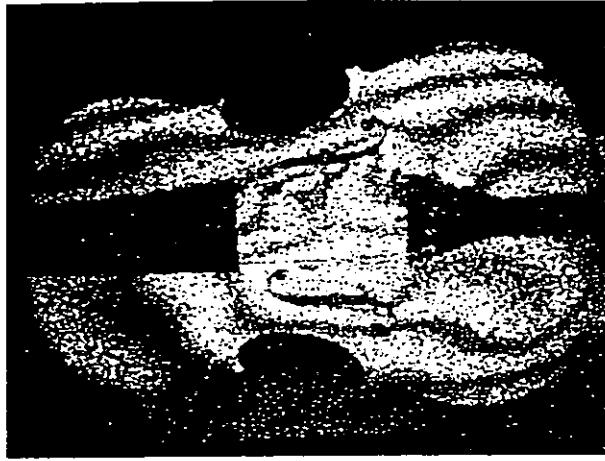
*Figure 4.28. Interferograms of the top plate of violin A. The tension of the second string has been increased with respect to its normal value by turning the fine tuner of a) 120°, b) 270°, c) 540°.*

a)



b)



c)

*Figure 4.29. Interferograms of the back plate of violin A. The tension of the second string has been increased with respect to its normal value by turning clockwise the fine tuner of a) 120°, b) 270°, c) 540°.*

<p align="center">a)            b)</p>
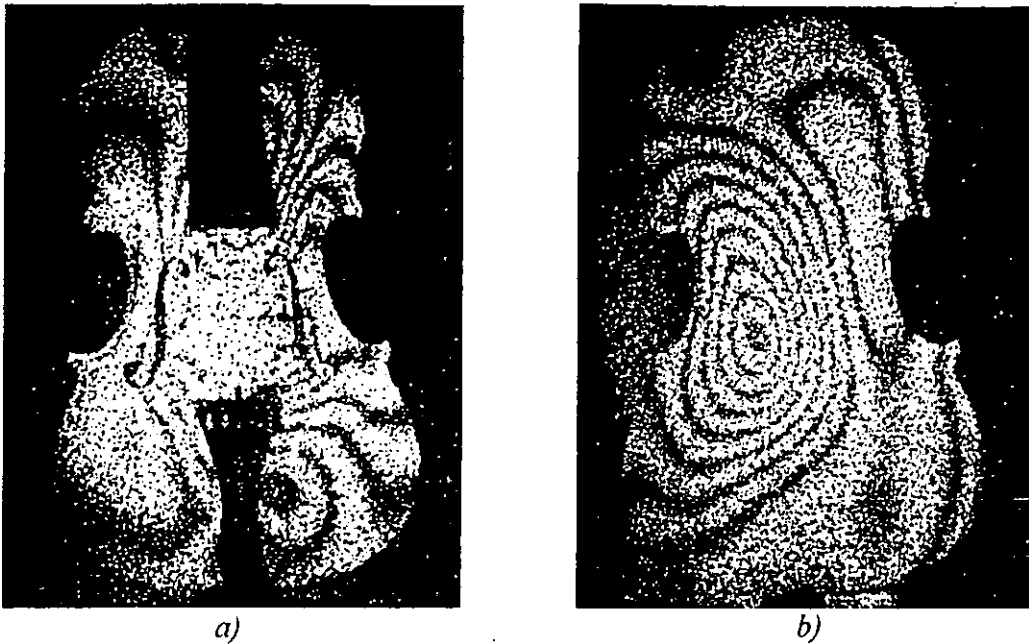
*Figure 4.30. Interferograms of the top a) and back b) plates of violin A for a change in the tension of the first string corresponding to a 270° clockwise turn of the fine tuner.*

Violin B was examined next. As in the case of violin A, three tests were performed at 120°, 270°, and 540° turns of the fine tuner. However in the third case the fringe density was too high to be resolved by the ESPI system. This means that for a given load the static deformation of violin B was relatively larger than that of violin A. For the top plate (see Fig. 4.31.) it is worth noting that the fringes about the tailpiece and the music board were round shaped. Moreover, unlike the case of violin A, their number was seen to be proportional to the applied stress. For the back plate (see Fig. 4.32.) the major out-of-plane displacement was in correspondence to the point where the sound post pushed the plate. The interferograms in Fig. 4.33. depict the deformation of the violin plates when the tension of the first string was modified. The asymmetrical deformation of the plates can be described in a similar manner as the results obtained for violin A (Fig. 4.30.).

The phase maps, derived by application of the phase stepping and unwrapping algorithms to four interferograms, contain information about the amount and sign of displacement and give a simple and intuitive representation of the surface micro deformation. Fig. 4.34. shows the final results for the interferograms of Fig. 4.31.a and Fig. 4.32.a. The phase maps corresponding to Fig. 4.28.b and Fig. 4.29.b are also reported (Fig. 4.35). The pixel colour is proportional to the surface displacement. In particular, red areas deformed outwards, and blue ones deformed inwards. Intermediate displacement was represented by green coloured pixels.

<p align="center">105</p>

$a)$            $b)$

*Figure 4.31. Interferograms of the top plate of violin B. The tension of the second string has been increased with respect to its normal value by turning the fine tuner of a) 120°, b) 270°.*
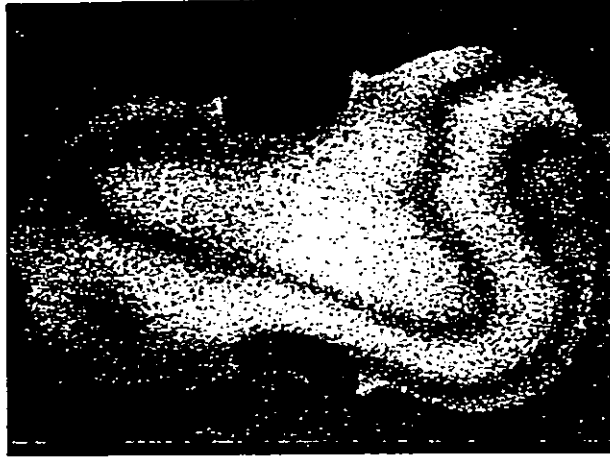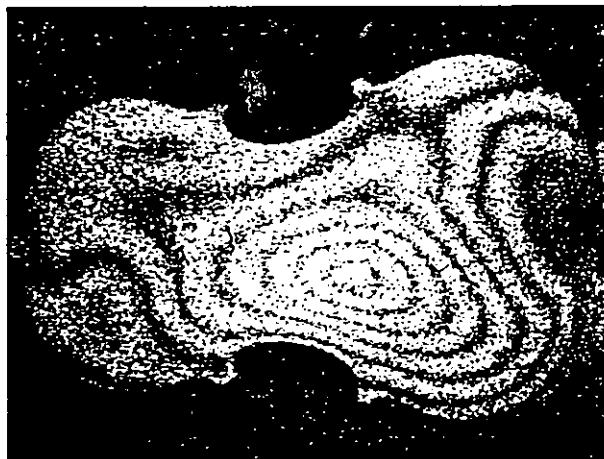


$a)$            $b)$

*Figure 4.32. Interferograms of the back plate of violin B. The tension of the second string has been increased with respect to its normal value by turning the fine tuner of a) 120°, b) 270°.*

106

<p style="text-align:center;">a)                                                     b)</p>
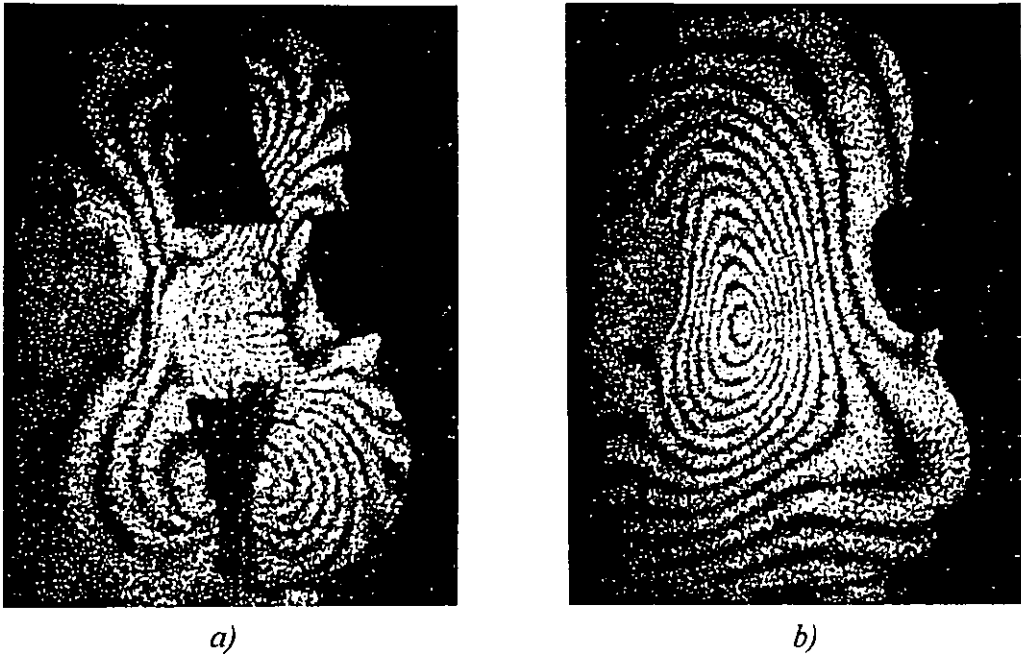
*Figure 4.33. Interferograms of the top a) and back b) plates of violin B for a change in the tension of the first string.*

The colour map in Fig. 4.34. indicates that the top plate of violin B deformed inwards in correspondence to the point where the pulled string meets the bridge. Outward displacement is revealed for the zones of the plate about the music board and the tailpiece. Presumably the lateral forces $F_1$ and $F_4$ in the qualitative model of Fig. 4.25. effectively compressed the top plate, which was forced to buckle outwards by the direction of its arching. On the other hand the central zone underwent a pronounced inward displacement caused by the point load $F_3$. For the back plate the major deformation occurred at the sound post as expected. The inward deformation of the upper right and lower zones of the plate should also be noted.

The out-of-plane displacement maps, obtained for violin A show that the plates had a more rigid behaviour than those of violin B. The results in Fig. 4.35. were obtained for a 270° turn of the fine tuner. Although the second string was stretched more than twice of the value for the maps in Fig. 4.34., the plates' deformation was substanstially low and uniform. The bridge load was distributed over the area between the *f*-holes. It is worth noting that the top plate produced a slight outward deformation of its lateral borders. The major contribution to the back plate deformation was given by the sound post pushing force.

<p style="text-align:center;">107</p>
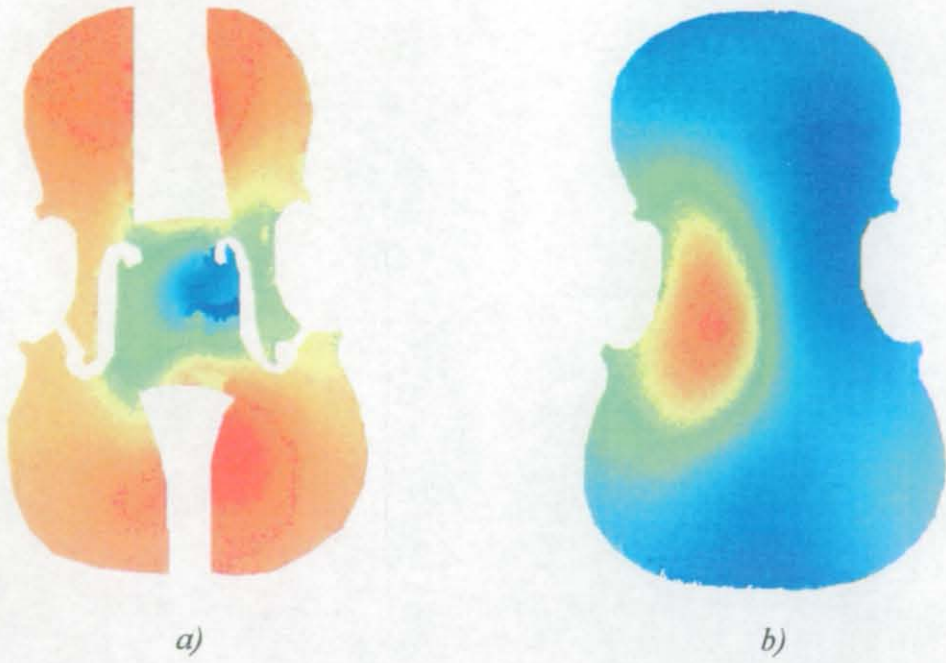
*Figure 4.34. Digital deformation maps corresponding to a fine tuning of the second string of violin B by 120°. a) Top plate. b) Back plate.*
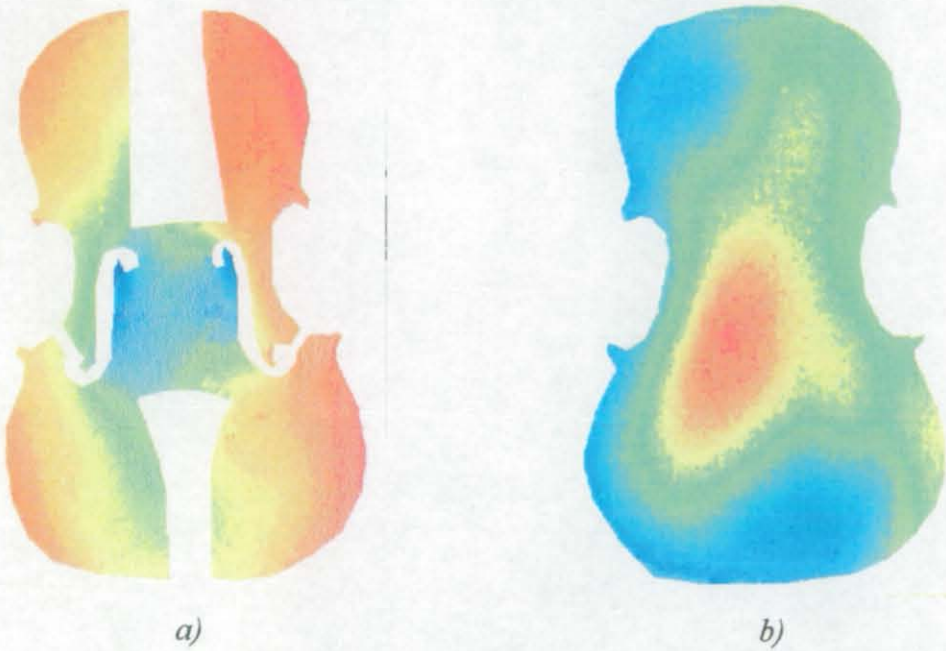


*Figure 4.35. Digital deformation maps corresponding to a fine tuning of the second string of violin A by 270°. a) Top plate. b) Back plate.*

## 4.2.5.2. Shearing interferometry tests

The lower sensitivity of this technique relative to ESPI was exploited to observe the effects of a larger variation of the string tension on the violin body deformation. In particular, the fringe patterns corresponding to four turns of the fine tuner were recorded. It should be remembered that the interferograms are proportional to the derivatives of surface displacement. Thus, for each plate, it was decided to consider the phase distributions along the horizontal and vertical directions. The two speckle patterns were first shifted by approximately ten pixels along the desired direction. Then the image obtained was phase shifted by means of the piezomirror and four images were recorded, as in the previous experiments. During real time subtraction, the violin was deformed by the desired amount and eventually the speckle interferogram was recorded. The shear value of ten pixels was the result of a trade-off between sensitivity and fringe contrast. It was clear from the experiments that the larger the image shift, the more noisy the interferograms. The reason for this is the occurrence of speckle decorrelation because of local object tilt [12] as in ESPI measurements.

The interferograms and the relative digital maps for the back plate of violin A are presented in Fig. 4.36. and Fig. 4.37. These results confirm the predominant role played by the sound post load on the back plate deformation. The effect of speckle noise on the digital maps is also clear in both figures. Results from the top plate and from violin B are in agreement with those already presented and have therefore been omitted.
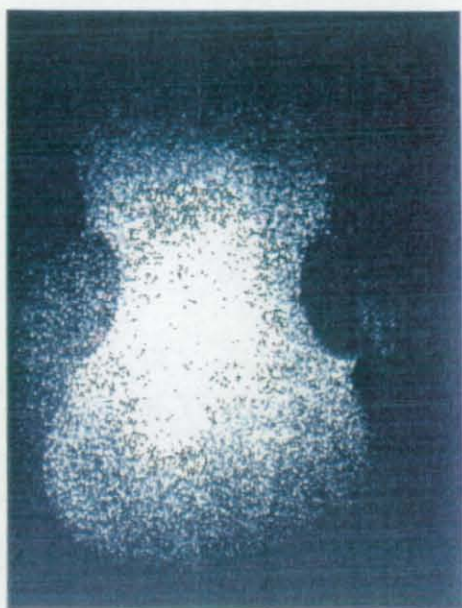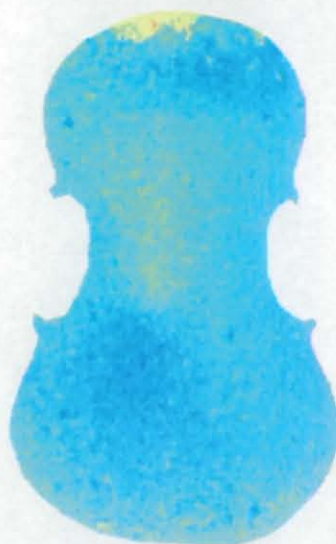
a)                              b)

*Figure 4.36. Vertical shear strain for four turns of the fine tuner at the second string of violin A. a) Interferogram; b) Digital map.*
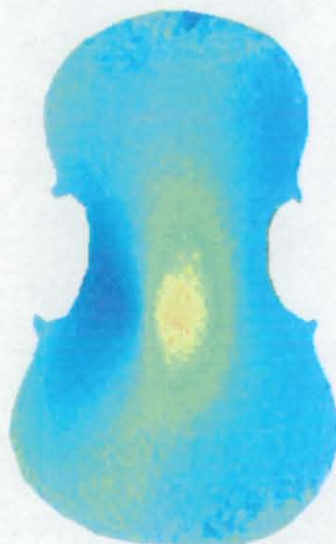


a)                              b)

*Figure 4.37. Horizontal shear strain for four turns of the fine tuner at the second string of violin A. a) Interferogram; b) Digital map.*

## 4.2.6. Concluding remarks

The static response of a violin body to a variation of the string tension has been successfully investigated by electronic speckle pattern interferometry. The CCD plate was used as a recording medium at the exposure time of 20 ms, corresponding to the video frame rate. Unlike real-time holography, no development was necessary, and the interferometric fringes could be observed with no delay between recording and fringe appearance. This was useful in detecting the presence of any spurious fringe due to external effects. The measurements were performed in an optical laboratory where suitable protection against thermal and mechanical disturbances were available. The image processing algorithms, developed for holographic images, could be readily applied to ESPI interferograms, but the presence of speckle noise sometimes affected the quality of the results. Shearing interferometry was finally applied to measure the gradient of larger deformations. In most cases speckle decorrelation effects greatly reduced fringe visibility. The derivatives of displacement were evaluated and although only a qualitative comparison with the micro deformation results was possible, on the whole shear results showed good agreement with micro displacement data.

Two violins, built with different arching and structure, were studied. The results showed that the instruments produced very different deformation shapes. The knowledge of the static micro deformation of the top and bottom plates of a violin can be useful at least for two main reasons. The former is that violin makers can receive fundamental information to prevent any eventual macro deformation or structural failure of their instruments. The latter is that since the arching of the instruments inevitably change because of ageing, the restorer, who knows the expected static behaviour, could infer the original arching.

In the future the application of the method to ancient instruments could be very helpful to evaluate the structural modifications introduced by any restoration work. New experiments could also be arranged where the loading of the strings could be replaced by three forces applied at the bridge, the tailpiece and the neck upper-end respectively. The measurement of the displacement separately caused by each of them, could eventually account for some unexplained aspects of deformation and at the same time suggest design improvements to the violin maker.

111

## 4.3. Development and testing of fibre optic ESPI systems for in-field measurements on artworks

### 4.3.1. Introduction

The application of holographic techniques to artwork diagnostics has been the subject of several scientific publications for many years. It has been widely demonstrated [13-16] that the interaction of an artifact with its surroundings can be successfully studied and that the location and size of defects, areas of excessive stress, or material discontinuities can be precisely determined. A knowledge of incipient and invisible flaws can be very important for conservation work. The effectiveness of the repair work can be also evaluated *a posteriori* by comparison of the interferometric fringes obtained before and after restoration [17].

Artwork restorers, in spite of these obvious advantages, have been reluctant to use holographic interferometry as a tool for non destructive testing. This can be attributed to a variety of factors, from the sceptical attitude on the use of new technologies to economical aspects. A major problem was however caused by the need for transportation of the objects to optical laboratories. In fact, the practical application of holographic interferometry has some disadvantages, which have, in general, hindered its widespread use *in situ* as a non-destructive testing tool. The optical alignment, the development and reconstruction of holograms, are time consuming processes, requiring skilled operators. Furthermore, the mechanical stability necessary for holographic measurements is not readily compatible with in-field conditions unless pulsed lasers are used [18]. However these lasers are not very flexible since an external water cooling circuit should be provided, and most systems have large size and weight. High energy radiation pulses and high voltages need special safety precautions. On the whole holographic measurements on artworks have seldom been applied for routine inspections since they have usually been confined to research laboratories.

A measuring instrument, which might become popular among conservators, should visualise deformation in the range of $0.1-10\,\mu\text{m}$, provide real-time analysis of micro displacement, and perform in-field measurements with a minimum of adjustments. These requirements can be fulfilled with systems based on electronic speckle pattern interferometry, as Gülker *et al* [19] recently demonstrated by using ESPI to monitor deformation and deterioration processes in historical buildings and monuments.

The aim of the present work has been to develop and test new ESPI systems meeting the requirements for out of laboratory operation on artworks. Optical fibres have been introduced in the setup and the use of laser diodes has been investigated in order to increase flexibility and compactness. As testing objects, wooden panels and frescoes have been primarily considered. For these artifacts, microdeformation analysis is particularly suited to study the damage produced by mechanical stress concentration. A painting on wood or on a wall can be regarded as a layered structure with a support. The wooden or mural support is coated with some priming layers or plaster, which serve as a base for the painting. These layers, normally made of mixtures of gesso and glue, are less thick and more fragile than the support. Expansion and contraction of the support due to daily fluctuations of ambient parameters can produce large strains and eventually cracks in the priming layers, as they become less flexible with age.

Furthermore, abrupt changes of humidity and temperature, traffic induced vibrations and heat exposure may also cause unpredictable stress distributions in the heterogeneous materials of the support, with consequent damage for the painting. All these mechanisms may lead to the formation of detachments and cracks which are very common in mural and wooden paintings. For conservation purposes it is very important to know the deformation of the artifact caused by ambient drifts and how the presence of support cracks or discontinuities alter the movements of the painted surface. Since the sensitivity to surface displacements is equal to that of holographic interferometry, ESPI has been used to design instruments capable of detecting all the above defects and studying several deterioration mechanisms.

In this section, the design and applications of two novel ESPI systems will be described. The first system is based on a fibre coupler device, which splits the visible light of a He-Ne laser into two fibres, used to illuminate the object and to provide the reference beam respectively. In the latter, the long coherence length of the infrared radiation from a temperature controlled semiconductor laser has been used to enhance the compactness of the measuring system. Preliminary tests on panels and frescoes have been performed in the optical laboratory. Finally the main results of in-field measurements in the Church *S.Maria di Collemaggio* (L'AQUILA-Italy), at the restoration laboratories of the *Opificio delle Pietre Dure* (FLORENCE-Italy), and in the Portinari Chapel (MILAN-Italy) have been presented and discussed.

## 4.3.2. Portable System 1

### 4.3.2.1. Optical setup

Optical fibres were introduced into an ESPI layout to make the measuring system very flexible and suited for *in-situ* operation. The polarised light of a He-Ne laser (Melles Griot mod. 05-LHP-991, $P = 10\,\text{mW}$; $\lambda = 633\,\text{nm}$) was launched into a single mode fibre, using a 20 x microscope objective mounted on a Newport optical fibre positioner (model F-915). A coupling efficiency of 50% was readily obtained when the fibre end was correctly cut and cleaned. The fibre, approximately one meter long, was the input fibre of a bi-directional coupler (Newport model F-506-A), which split the light with a 50% ± 5% ratio between two output single mode fibres. Small variations of temperature and polarisation had negligible effects on the splitting ratio of the coupler. However the coupler introduced an additional power reduction of 9%, specified by the manufacturer as intrinsic power loss.

Since the glass core of a monomode fibre at $\lambda = 633\,\text{nm}$ has a diameter of $4\,\mu\text{m}$, the output wavefronts can be considered as spherical and presented a smooth wavefront. For this reason spatial filtering was no longer necessary. Besides, the use of optical fibres offers the possibility to measure either in-plane or out-of-plane displacements by simple readjustments of the setup. The object was symmetrically illuminated, as depicted in Fig. 4.38.a), to obtain the maximum sensitivity to horizontal in-plane displacements. A complete study of the in-plane deformation can be performed if the illuminating fibres are rotated by ninety degrees about the viewing axis to make the system sensitive to vertical in-plane displacements. The sensitivity of the measurements depends on the angle $\vartheta$ (see Eqt.(2.17)) and in principle it can be varied between half the wavelength to infinity. However, in practice, small values of $\vartheta$ were used to give more compactness to the system and to avoid contrast losses due to speckle decorrelation effects. A typical value of $15°$ was chosen during the measurements. In this case the relative in-plane displacement between two adjacent fringes was $1.2\,\mu\text{m}$. A CCD video camera (VIDEOSYS CCD 500 614 x 806 pixels), with a zoom lens (MITAKON wide MC 1:2.8 f=28 mm) captured the speckle images, which were then digitised, stored and subtracted in an image frame grabber (CORECO OCULUS-200). The digitisation was done at 512 x 512 pixels with a grey scale range at 128 levels.

To measure out-of-plane displacements, it was decided to use a smooth in-line reference beam configuration. In this case a spherical reference beam, conjugated with the centre of the camera lens aperture, was required. In practice, the end of a single

114
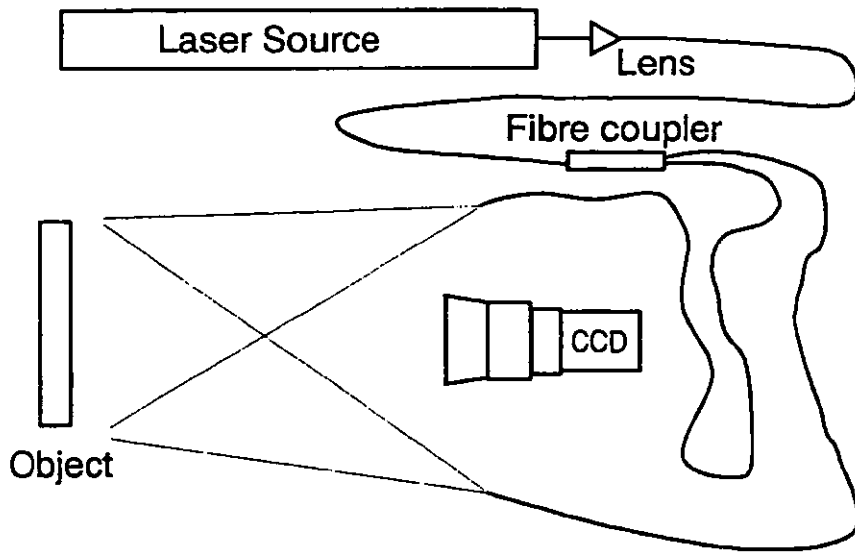
*a)*
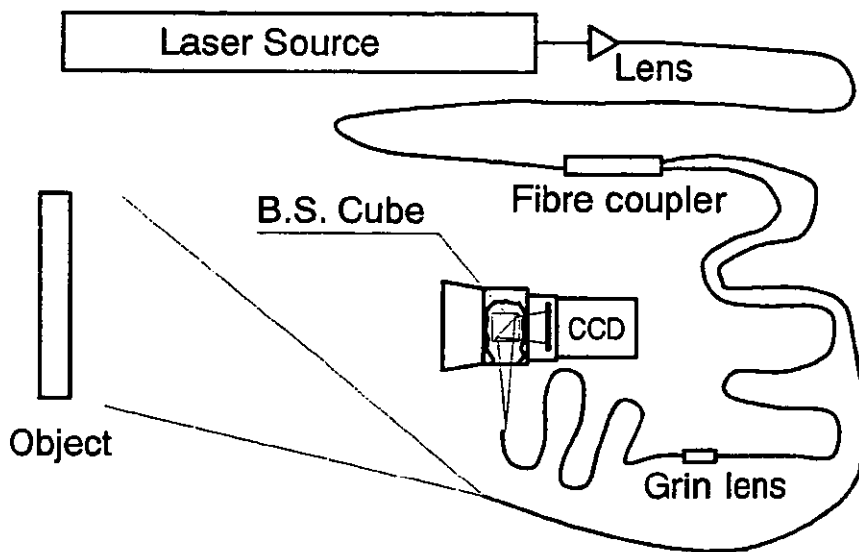


*b)*

*Figure 4.38. Experimental setup. Configurations sensitive to in-plane a) and out-of-plane b) displacements.*

mode fibre was used as a point source reference wave (see Fig. 4.38.b)). The fibre end was positioned at ninety degrees from the optical axis of the viewing lens. A beam splitter cube was finally used to align the reference and object beams. Unlike in the previous setup for in-plane displacements, the optical paths needed be matched. The optical path difference between reference and object beams was effectively reduced by increasing the reference path with the addition of a single mode fibre, coupled to the reference fibre using gradient-index (GRIN) lenses [20]. Power losses were intentionally introduced by misalignment of two GRIN lenses (SLW 1.8-0.25p-0.63, Nippon Glass Sheet) in order to control the intensity value of the reference beam at the CCD plane. The ratio between the reference and object beam intensities was set at a typical value of 3:1 for each measurement. The object was illuminated with the other output fibre from the coupler. Taking into account the losses along the optical path, the power of the light incident onto the object surface was 2.3 mW. At a working distance of 40 cm from the camera lens, an object area of approximately 10 x 10 cm was inspected.

## 4.3.2.2. Preliminary tests

The measuring system was initially tested on wooden samples, coated with some priming layers but no painting. The samples, prepared by the Istituto Centrale del Restauro (Rome-Italy), were made of poplar wood, which was the most common type of wood used by ancient Italian painters. Thin plastic sheets had been intentionally inserted among the layers to simulate the presence of detachments. These defects could be precisely detected by observing the thermal deformation of the surface. When the surface was slightly heated whether artificially or by ambient drifts, the heat diffusion toward the wood support occurred at a very slow rate in correspondence of the detached regions. Therefore the surface layers of these regions heated up rapidly and their thermal deformation was much larger than that of the non detached parts. This gave rise to a different fringe density between the damaged and flawless regions of the surface. From the fringe distribution it was possible to evaluate the location and extension of the detachments.

The speckle interferogram depicted in Fig. 4.39. shows the out-of-plane deformation of an area containing a round shaped defect. Before acquiring the first speckle image, the specimen had been heated by a moderately flow of warm air for 30 seconds. The second image was taken 10 seconds later. The displacement of the surface points corresponding to the simulated detachment gave rise to the concentric fringes, which are between two parallel fringes produced by the global deformation of the wooden panel.
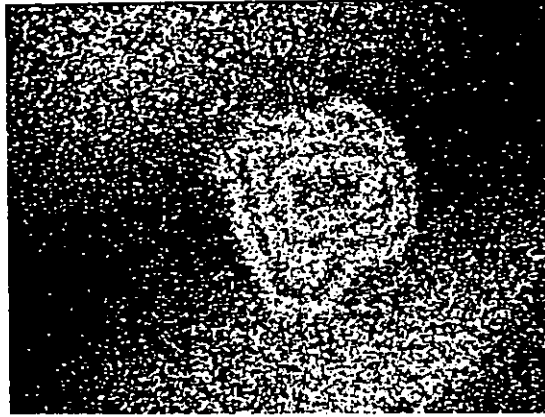
*Figure 4.39. Deformation fringes for a primed wooden sample containing a round shaped defect.*
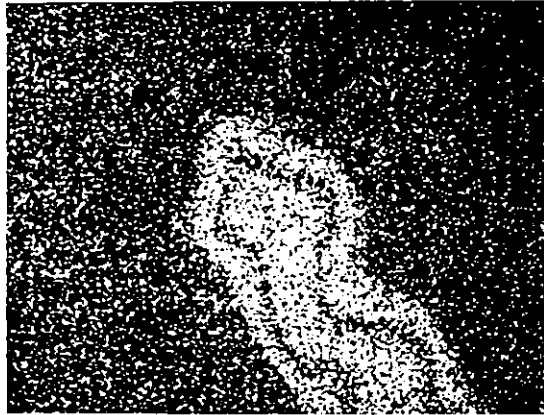


*Figure 4.40. Deformation fringes for a primed wooden sample. The shape of the fringes indicates the damaged area.*
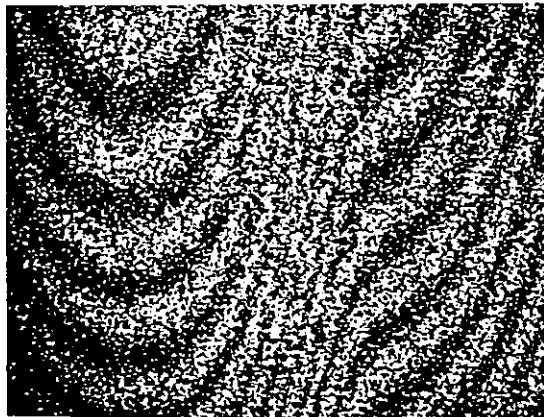


*Figure 4.41. In-plane deformation fringes revealing an invisible crack in a wooden panel.*

Detachments could also be revealed by slight heating of the object surface. As an example, the fringe pattern in Fig. 4.40. was obtained by holding a hand close to the surface for few seconds. In this case thermal deformation mainly occurred about the defect, as no fringes were detected outside the damaged area. The elongated shape of the defect was successfully detected.

Some tests, using the setup for in-plane deformation analysis, allowed the detection of cracks only visible by observing the lateral section of the wooden panel. Although the priming layers showed no visible sign of damage, the deformation gave rise to an anomalous fringe pattern (see Fig. 4.41.). The crack was found in correspondence to the central area of the image, where the fringes underwent an abrupt change of slope. Presumably the crack extension under the primed surface corresponds to the area of higher fringe density.

A sandstone sample simulating a typical inhomogeneous support of a fresco, with a visible surface crack was heated with an infrared lamp. During the cooling process the out-of-plane displacement was measured. The speckle fringes were interrupted along the crack as shown in Fig. 4.42.
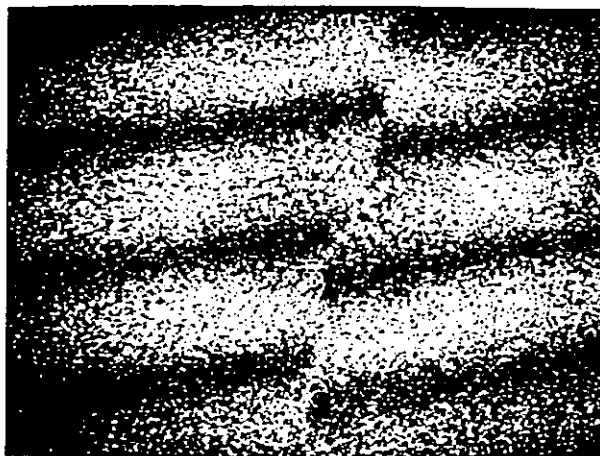


*Figure 4.42. Out-of-plane fringes in presence of a surface crack in a sandstone sample.*

A final example dealt with the application of the method to a real fresco (see Fig. 4.43.), kindly provided by the Museo Nazionale d'Abruzzo L'Aquila (Italy). For restoration purposes, the plaster was separated from the support wall. In the optical lab, a thermal stress of the painted surface was produced by a hot air flow. In Fig. 4.44. the ESPI fringes depict the out-of-plane deformation about a subsurface anomaly of the

fresco. The interrupted fringes suggest the presence of an incipient crack from the lower middle-left part to the upper right corner of the inspected area. In addition it should also be noted that on the left hand side of the crack, there is a very particular narrow white fringe between two wider bright lobes. In this case, the classification of the defect is not straightforward and would require an eventual more detailed analysis or comparison with the results obtained with other techniques.



*Figure 4.43. Photograph of the Santo Vescovo (Holy Bishop), a 15th century mural fresco.*



*Figure 4.44. Fringe pattern showing an incipient defect in a mural fresco.*

## 4.3.2.3. Experimental arrangement for in-field operation

Any relative motion of the order of the laser wavelength between the optical system and the object under investigation introduces unwanted fringes which inevitably alter the results. In particular, during in-field operation, the presence of mechanical vibrations is the major source of uncontrollable micro movements, which might have destructive effects on the measurements. When vibrations influence the interferometric system, the deformation fringes become barely visible as they are no longer stable. Consequently, any attempt to record the fringe pattern leads to very poor results. In the optical laboratories, these problems have been solved by the use of massive optical tables, whose design is based on the drastic reduction of the structure resonance peaks. It is evident that heavy and bulky tables do not comply with the portability of the optical system and its in-field operation. A simple and effective solution could consist of a rigid mechanical coupling between the optical system and the inspected object. However, to do this, a contact must be set between the measuring head and the object and the mechanical interactions transmitted through the contact points will influence the results. Moreover the mechanical coupling is likely to change from one object to another, according to its shape and location, causing a reduction of flexibility.

An alternative solution was chosen for the tests *in situ*. It was decided to assemble the video camera and the fibre ends in an optical head, mounted on a tripod. This arrangement seemed to provide the best flexibility. The tripod system, on the other hand, had to be as insensitive as possible to external vibrations. In a church, a museum or a conservation laboratory, floor resonance (5 to 50 Hz) and street traffic (5 to 100 Hz) are the main sources of micro vibrations. In general, in non-industrial environments, the common sources of mechanical instability have frequencies below 150 Hz [21]. Therefore if the measuring system has a resonance frequency greater than this value, vibration effects will be greatly reduced.

As a first approximation the mechanical system (tripod and optical head) was considered to be equivalent to a ground clamped beam with a mass mounted on its top (see Fig. 4.45.). From vibration theory [22] the resonance frequency $\omega_0$ is given by

$$\omega_0 = \sqrt{\frac{k}{m}} \tag{4.1}$$

where $k$ and $m$ are the beam stiffness and the mass, respectively. In practice, to have a sufficiently high resonant frequency, the mass of the optical head was kept as low as possible by fixing the CCD camera and the fibre ends on an aluminium plate, and a high stiffness tripod was used.
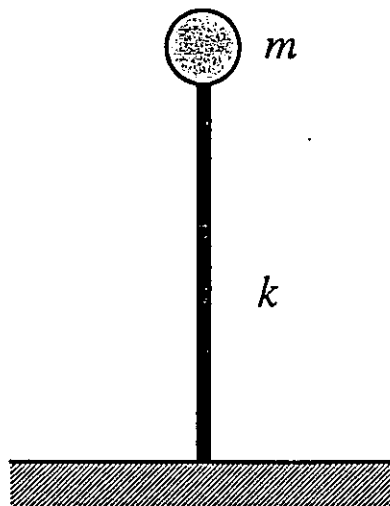


*Figure 4.45. A simple mechanical system made of a mass on top of a clamped ground beam.*

A lightweight wooden lid covered the optical head to eliminate excessive ambient light on the video camera sensor, and to allow daylight operation. The laser source and the beam-to-fibre coupling device were contained in a closed portable box, wherefrom the light was guided through the fibres to the optical head (see also Fig. 4.46.). The fibres were inserted into rubber pipes for their protection. Incidentally, mechanical disturbances or air turbulence led to local variations of the optical path in the fibres, and consequently the fringes were uniformly shifted in phase. These events had little or no effects on the fringe recording as they occurred at very low frequencies.

121
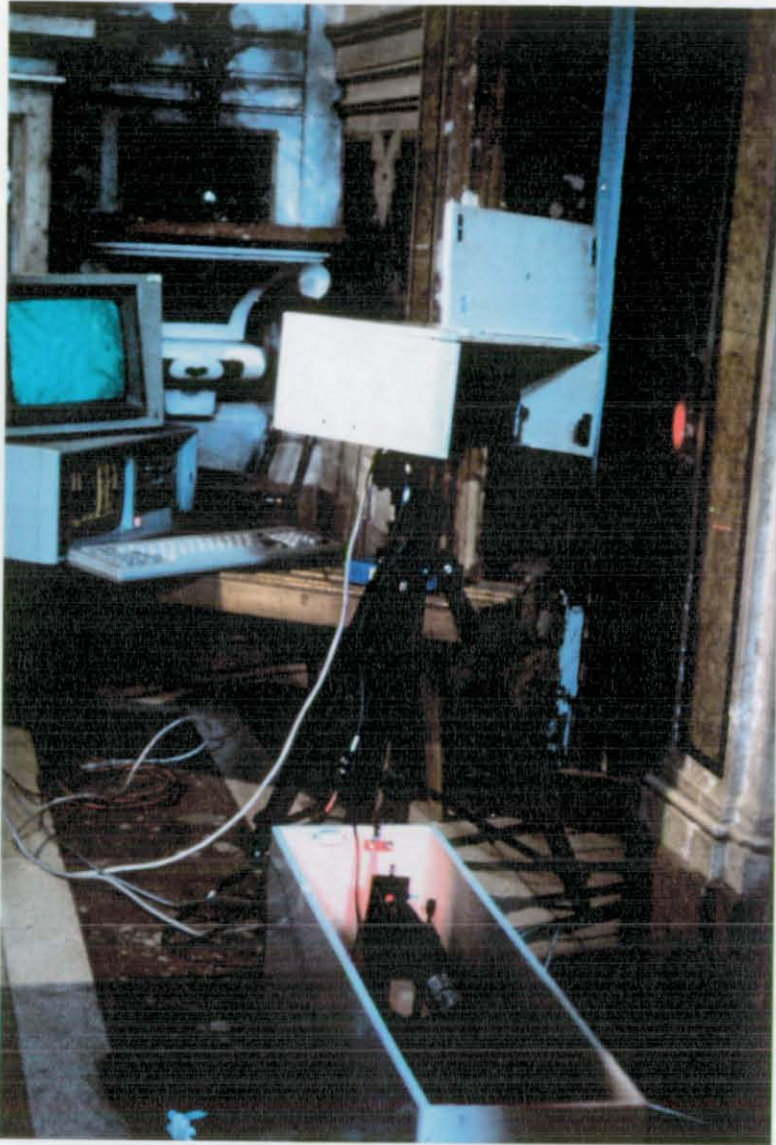
*Figure 4.46. Experimental equipment used for in situ measurements. The principal elements are the laser box (central down), the optical head on the tripod, and the PC unit with an external monitor.*

## 4.3.2.4. In-field measurements in the Church S.Maria di Collemaggio

The developed ESPI system was tested on a mural fresco; *Incoronazione dell'Assunta* (15th century), located inside the church *S. Maria di Collemaggio* (13th century) at L'Aquila, Italy (see Fig. 4.47.).

ESPI fringes were produced by thermal deformation of the plaster. A flow of moderately hot air was used to vary the temperature of the surface of few degrees (typically $\Delta T = 4° C$). Microcracks were the most common defects observed during ESPI measurements on the fresco surface. As demonstrated by the preliminary tests (Sec. 4.3.2.2.), cracks caused abrupt interruptions of the interferometric fringes obtained with the configuration sensitive to out-of-plane displacement. Fig. 4.49. portrays the ESPI fringes for a cracked region. In the image the profile of the cracks can readily be deduced by the location of fringe discontinuities.

The interferograms also revealed the presence of invisible micro defects. In particular Fig. 4.50.a. refers to a region containing a subsurface detachment of the plaster and possible local material discontinuities especially in correspondence to the bright area inside the defect fringes. Another interesting fringe pattern (see Fig. 4.50.b.) was obtained for a region with some visible cracks. Fringe discontinuities were detected in areas apparently faultless, indicating that the damage occurred at a larger extent than that indicated by visual inspection.

Figure 4.47. Church of "S. Maria di Collemaggio"-L'Aquila, Italy.



Figure 4.48. Experimental arrangement during the inspection of the fresco "Incoronazione dell'Assunta".

*Figure 4.49. Speckle interferogram of a region with crossed microcracks.*
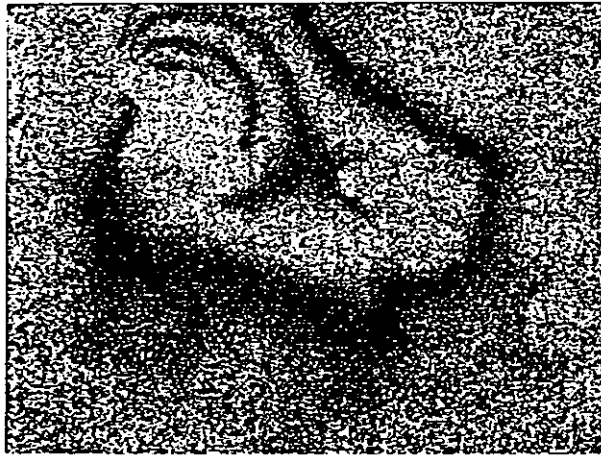


*a)*



*b)*

*Figure 4.50. Speckle interferograms of regions denoting characteristic damage. a) Material discontinuities inside a detachment. b) Multiple cracks: some of which escaped visual detection.*

### 4.3.3. Portable System 2

#### 4.3.3.1. Optical setup

The intrinsic small size of semiconductor lasers[2] makes their use as light sources very attractive in the design of portable systems. The development of these lasers has been boosted by the industry for data storage and fibre optic communications towards better performance in terms of delivered power and available wavelengths. As a result, diode laser systems have recently been applied to interferometry [23], holographic interferometry [24] and ESPI [25,26]. In particular, singlemode lasers are best suited for interferometric applications, since a high level of temporal coherence can be obtained by controlling the temperature of the diode junction. In today's market, for a given output power, near infrared lasers have better specifications with respect to beam quality (astigmatism, polarisation) than diodes emitting in the visible region. If operated with care, in order to prevent electrostatic damage, and if stabilised current drivers are used, laser diodes have lifetime better than $10^5$ hours.

In the present work, a system (mod PM-550I-780-HL7851G by Seastar Optics Inc.) composed of an optically isolated pigtailed laser diode with polarisation maintaining fibre and thermoelectric cooler was used (see Fig. 4.51.). The laser source (HITACHI HL7851G emitting an optical power of P=50 mW at the typical wavelength $\lambda$=785 nm), was coupled to a polarisation maintaining single mode fibre (YORK HB750). To avoid amplitude instabilities or frequency drifts of the optical radiation caused by reflections, the coupling arrangement included an optical isolator (35 dB) based on a Faraday crystal. The output light from the optical fibre had a spherical wavefront (no astigmatism), an excellent polarisation figure (640:1), and a power of $P$=6 mW at an operating diode current $I_{op}$= 129 mA. The laser diode junction was temperature stabilised by a thermoelectric controller (mod. TC5100) using a Peltier device driven by a feedback control circuit. The temperature could be controlled over the range 0-50 °C with a stability of $\pm$ 0.01 °C, and an absolute accuracy of $\pm$0.2 °C. With this control a coherence length longer than 4 meters was effectively measured in the laboratory using a Michelson interferometer. The laser system included a low noise current driver (mod.Ld-2310) in the range 0-200 mA. An external modulation signal could also be applied to modulate the diode current up to 1 MHz.

---

[2] Typical cavity dimensions of a laser diode are 1 x 5 x 300 $\mu$m.
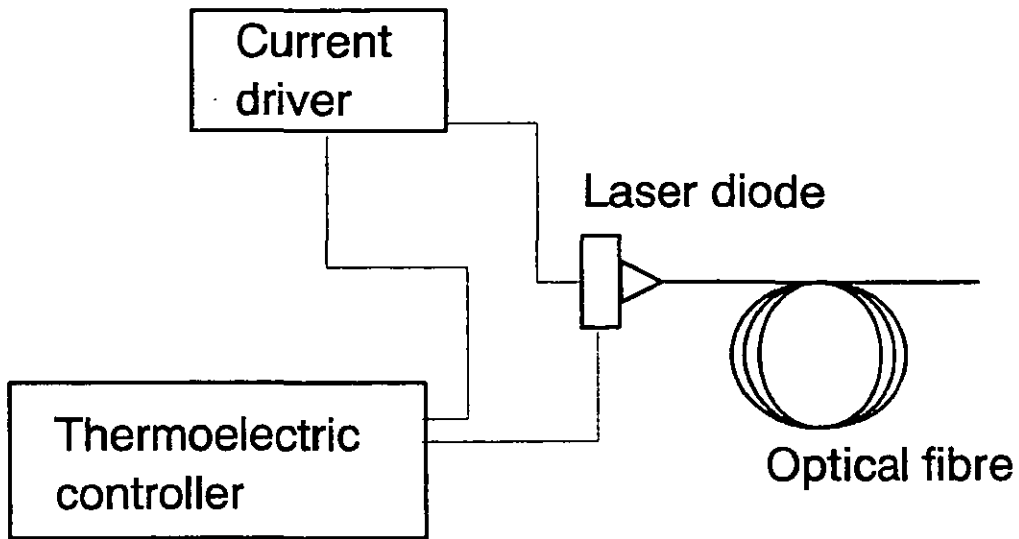
*Figure 4.51. Configuration of the laser diode system.*

It should be noted that, as demonstrated by the measurements presented in Sec. 4.3.2., most types of defects can be detected by direct observation of the out-of-plane deformation of the object surface. In order to minimise the number of adjustments and alignment procedures, a system was developed that was only sensitive to out-of-plane displacements. In this way the potential of the method has not been restricted, whereas its practical use has been greatly simplified. The laser light emitted by the output end of the optical fibre directly illuminated the surface under investigation. A small part of the spherical wavefront was caught by a polarising beam-splitter cube (BSC1, 0.5" side), and served as reference beam (see Fig. 4.52.). Another beam-splitter cube (BSC2, 0.5" side) reflected the reference light onto the CCD sensor, where the object image was focused by the objective lens L2. A 3:1 ratio between the object and reference beams could be obtained by changing the aperture of the viewing lens according to the object reflectivity. The light polarisation was adjusted by rotating the fibre output end until the reference beam intensity was minimised, i.e. the electric field was aligned along the transmission axis of the polarising cubes.

The setup was mounted on an aluminium plate (210 x 150 x 10 mm), which could readily be accomodated on a tripod for in-field operation (see also Sec. 4.3.2.4.). The camera sensor was protected from ambient light by a lightweight aluminium lid fixed to the aluminium plate.
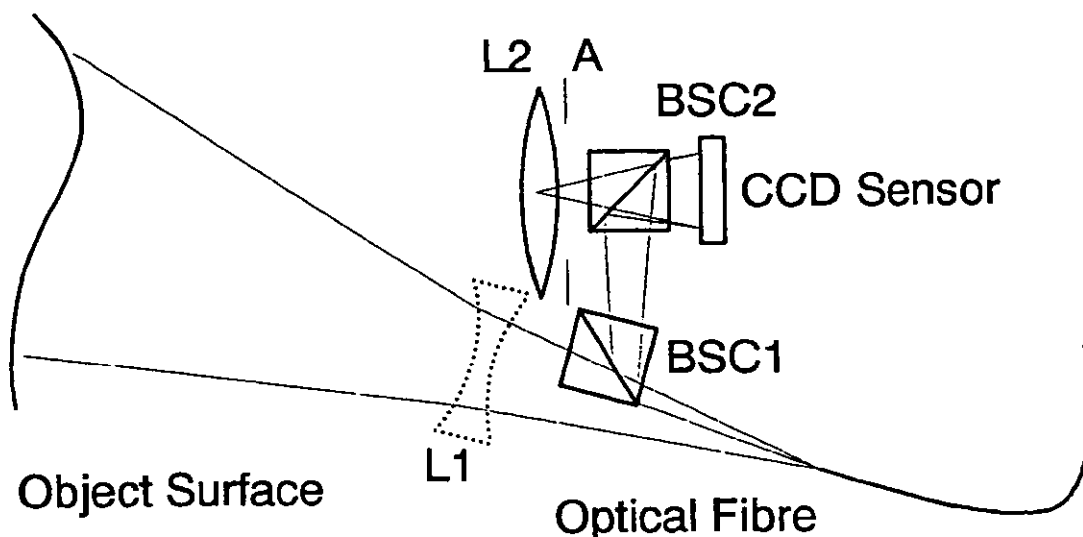
*Figure 4.52. Optical layout for in-field ESPI measurement; expanding lens (L1), viewing lens (L2), iris aperture (A), beam splitting cubes (BSC1 and BSC2).*

A TELI B/W CCD camera model CS3330L was used for image acquisition. The camera head was very compact and lightweight, since most of the electronic circuitry was contained in an external control unit. The sensor matrix had 756 x 581 pixels, each of which had a unit cell 11 x 11 μm resulting in a detection area of 8.8 x 6.6 mm. The signal to noise ratio, specified in the data sheets, was 50 dB. A DATA TRANSLATION DT-2862 frame grabber was used to digitise and process the speckle images. This graphic board had a memory of 1 Mbyte divided into four pages of 512 x 512 pixels, with 8 bit resolution each. A portable TOSHIBA T3200SXC (5 Mbyte RAM, 100 Mbyte hard disk) served as host computer for the frame grabber.

### 4.3.3.2. Preliminary tests

Initial experiments were devoted to establishing the optimal dimensions of the inspected area in order to minimise the number of adjustments necessary during in-field operation. In the setup the size of the inspected area depended on four factors; the angular aperture of the illumination beam, the viewing system, the power of the laser beam, and the object reflectivity. Since the fibre had a numerical aperture of N.A.= 0.1, an area of 100 x 100 mm of the object could be illuminated from a distance of 500 mm from the output of the optical fibre. This area could be imaged by using a CCD lens with a focal length $f$=25 mm at a working distance of $z$= 420 mm between the object and the optical head. The possibility to add a biconcave lens along the illumination beam allowed the inspection of a larger area, whose maximum size was limited by the power of the laser source. For the developed setup, experiments showed that a surface of a white-painted

plate up to an area of 300 x 300 mm could be successfully investigated. This result was obtained with the optical head placed at 660 mm from the object, a 12.5 mm CCD lens, and the diode operating at a current of 130 mA.

If the surface scattering is not uniform and the incident light is partially absorbed, e.g. surfaces of paintings or frescoes, the extent of the examinable area might be drastically reduced. The amount of the reduction is strongly dependent on the object characteristics. It was therefore decided to set the parameters of the optical systems in such a way that two alternatives could readily be available during inspection. The solution consisted of the use of two interchangeable CCD lenses with different focal lengths. An area of approximately 200 x 200 mm was inspected with a 12.5 mm lens at a working distance of 500 mm, whilst, for a low reflecting object, a lens with focal length $f$=25 mm was used to image a 100 x 100 mm surface. In the latter case no divergent lens was necessary to expand the illumination beam and thus power losses due to unavoidable reflections at the lens surface were eliminated.

Thermal fringes obtained by heating a colour image, printed on paper glued onto a wood support, with a hot air flow are presented in Fig. 4.53. This example demonstrated the practical application of the instrument to measure microdeformation of an object with a complex pattern, whose reflectivity was not uniform. It should, however be noted that the fringe visibility is reduced in correspondence to the object regions with low reflectivity.



a)

b)
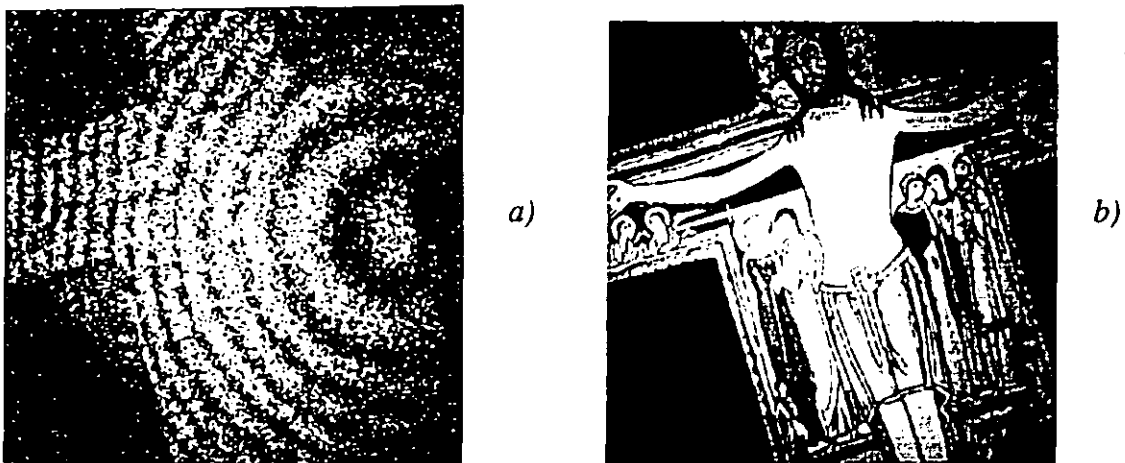
*Figure 4.53. Interference fringes (a) obtained by heating a paper icon (b) glued onto the wooden support.*

## 4.3.3.3. In-field measurements at the Opificio delle Pietre Dure e Laboratori di Restauro

The portable ESPI instrumentation has been used to examine ancient paintings on wood at the restoration laboratories of the *Opificio delle Pietre Dure e Laboratori di Restauro* (FLORENCE-Italy). The *Opificio* is part of the Italian ministry for cultural heritage (it. Ministero per i Beni Culturali e Ambientali). The interferometric measurements were performed during working hours in a building having an extensive floor and large windows. A partial reduction of the ambient light was necessary to eliminate the occurrence of parasitic reflections onto the videocamera plate.

A preliminary test of the ESPI system on a wall revealed the presence of micro vibrations, which were clearly visible by operating in real-time subtraction mode. These disturbances were probably induced by the road traffic, which was very heavy in the area, and by the vicinity of the main railway station. Furthermore it was not possible to turn off the central heating system which caused unwanted air turbulence. In spite of these sources of noise, well contrasted interferograms could be recorded. Unless otherwise specified, each interferogram presented in this section refers to a 100 x 100 mm area, whose surface has been heated with an infrared lamp for some seconds before or between the two exposures.

Firstly, the wooden panel (190 x 97 cm) "Madonna in trono con bambino" by Giotto (1266-1337) was inspected. In particular the surface behaviour in correspondence to joints and nails in the wooden support was considered. The panel was leaned against the wall and rested on two wooden blocks at the ground (see Fig. 4.54.).

Fig. 4.55. presents an interferogram relative to an area in the middle of the panel where a nail was driven in from the back and bent down to the front surface. This nail originally served to fix two crossed planks (now absent) to the panel in order to increase the rigidity of the support. The anomalous density and shape of the fringes at the centre of the image clearly indicate the extension of the detachment and the occurrence of a crack along the horizontal direction.

130
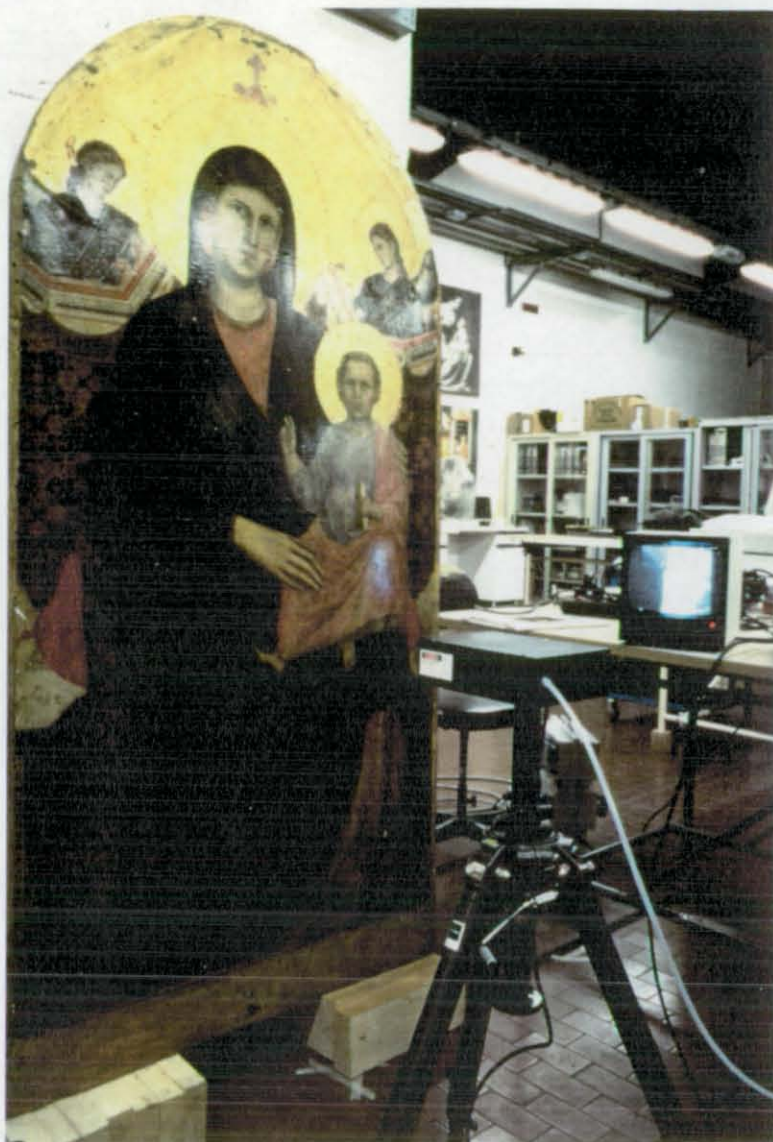
*Figure 4.54. Experimental arrangement for the inspection of the panel.*

The panel was composed of two parts held together by wooden joints. Although the vertical separation between the two parts was very small (2-4 mm), the corresponding void under the priming layers could lead to the formation of detachments. One of these detachments has been successfully detected and the resulting interferogram is presented in Fig. 4.56. The defect was revealed by the elliptical black fringe labelled A. It was also found by comparison with the radiographic inspection performed at the *Opificio* that the small fringe anomalies (B) observed in the central region of the interferogram are related to the local characteristics of the priming layers. In fact, the fine meshed canvases, which were usually inserted between the primings, did not cover the whole surface leaving horizontal stripes (1-2 cm wide) with no canvas reinforcement. This

type of discontinuity caused small detachments, which resulted in the irregularities observed in the interferograms.
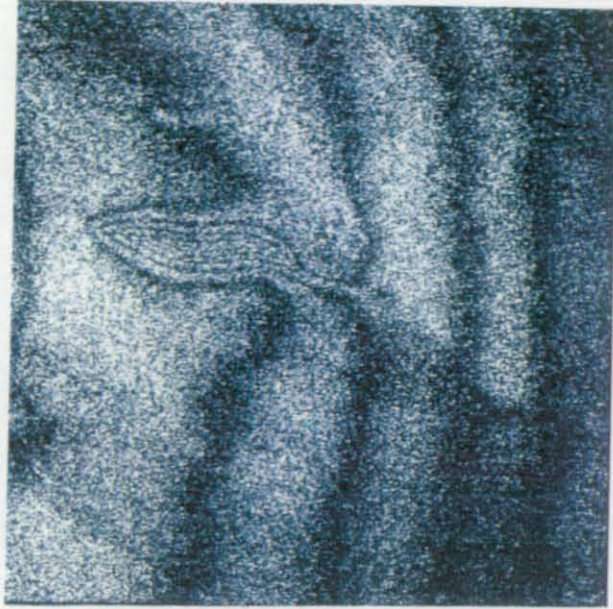


*Figure 4.55. Interferogram of a detachment with a horizontal crack.*
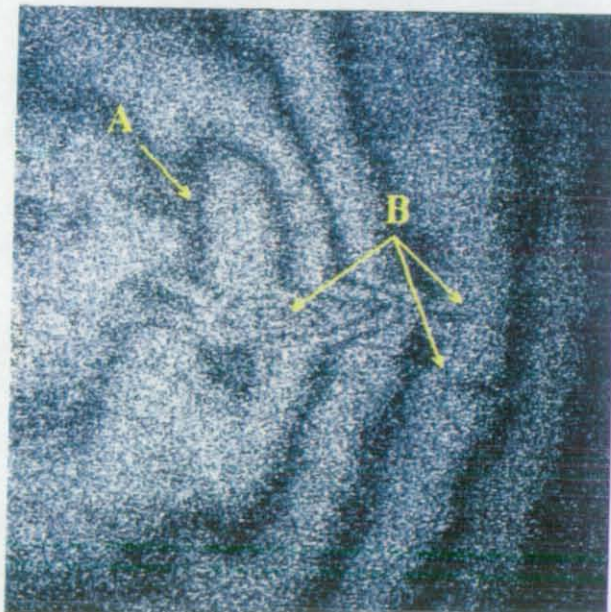


*Figure 4.56. A vertical detachment is revealed along the separation between the two parts of the panel (A). Small fringe irregularities along the horizontal direction are also visible (B).*

The interferogram in Fig. 4.57. refers to a region where a nail was driven in from the painted surface of the panel. From the fringe pattern the presence of the nail seems to have no effects on the thermal deformation of the surface. Final attention was drawn to the deformation of the painted surface in correspondence to the curved metals fixed in the wood to hang the panel to the wall. On the left hand side there was a very clear crack on the surface (Fig. 4.58.a.) which gave rise by heating to the fringe pattern in Fig. 4.58.b. On the right-hand side of the panel the interferometric inspection highlighted the presence of a double detachment (see Fig. 4.59.).



a)                                    b)
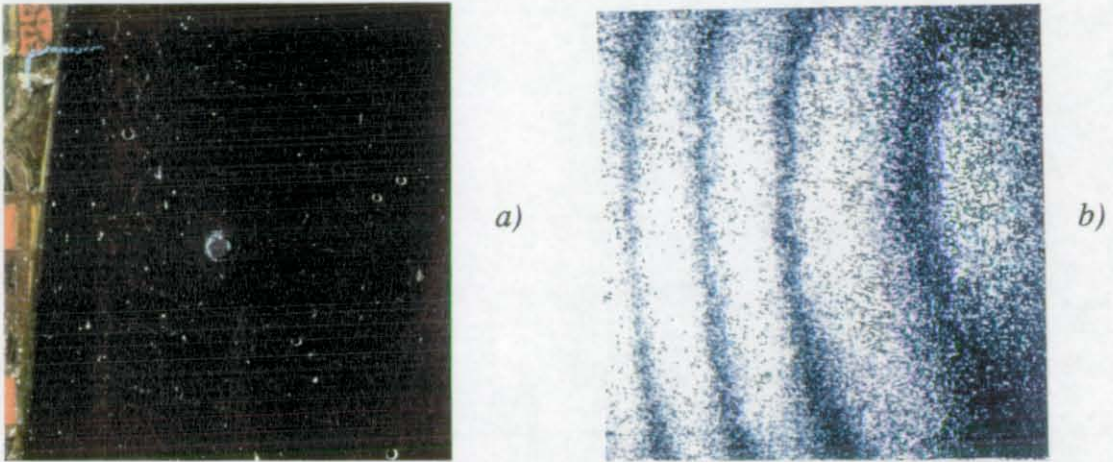
Figure 4.57. Inspection of an area with an iron nail. a) View of the area. b) Interferogram.



a)                                    b)

Figure 4.58. a) Detail of the painting (angel on the top left) showing a crack produced by the curved metals used to hang the painting on the wall. b) Interferogram.
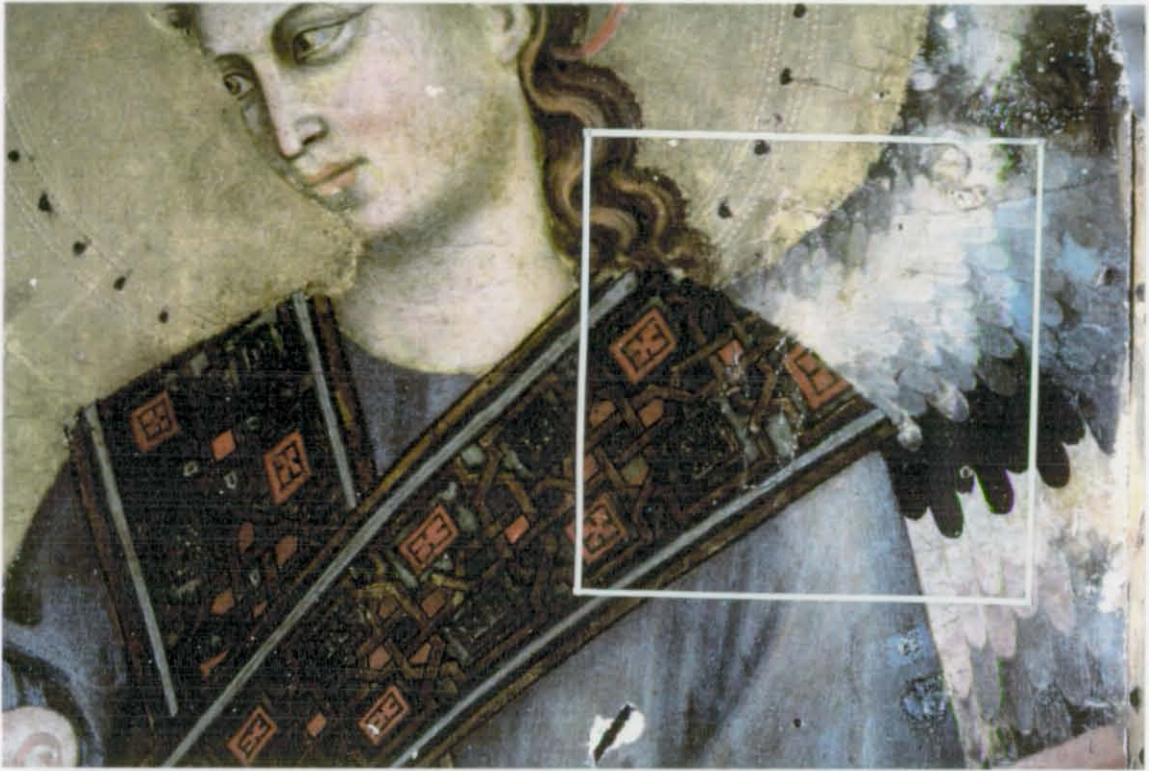
a)
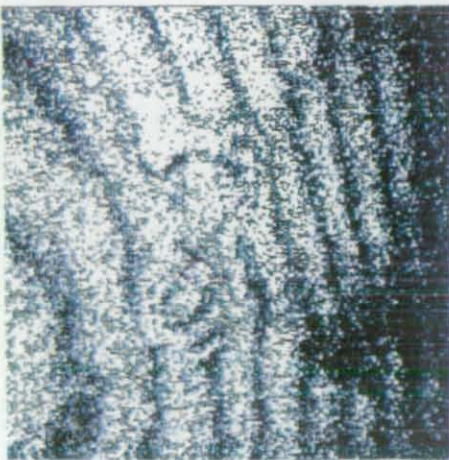


*Figure 4.59. a) Detail of the painting (angel on the top right) with the swelling produced by the curved b) metals used to hang the painting on the wall. b) Interferogram.*

A second set of measurements has been performed on the "Incoronazione della Vergine" (1414) by Lorenzo Monaco. This composition, which comes from the Galleria degli Uffizi (FIRENZE), consists of a panel (450 x 350 cm), a *predella* and three

*cuspidi*. By inspection of an extended detachment in one of the *cuspidi* the effects of the craquelure on the interferometric pattern were observed. It is clear from Fig. 4.60.a, that the fringes follow the micro crack pattern of the surface and assume a circular shape. A similar behaviour was observed in correspondence to undamaged areas by prolonging the surface heating. The region around a crack tip was also examined (see Fig. 4.60.b). In this example, although the craquelure effect is still present, the crack can readily be detected (A).

The simplest way to examine the *predella* was to lay it down on the floor and observe the painted surfaces from above (see Fig. 4.61.). To do this the optical head was mounted on a horizontal arm fixed to the tripod. The results obtained for two cracked regions are presented in Fig. 4.62. In both cases the extension of the fringe pattern in the vicinity of the cracks indicate that the painting was also detached.



a)                                    b)
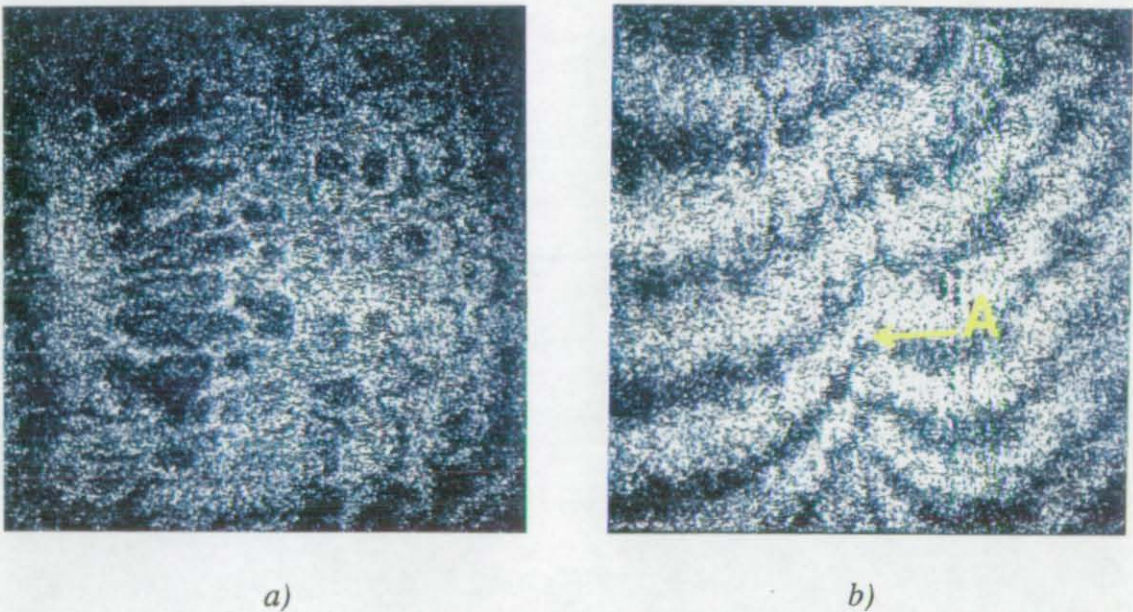
*Figure 4.60. a) ESPI fringes produced by the craquelure of the painting. b) Interferogram of a region of the painting at the crack tip (A).*

*Figure 4.61. Experimental arrangement for the inspection of the predella.*

Finally, the wooden panel (42 x 125 cm) "Trionfo di David" by Imitatore del Pesellino (15th century), from the Museo Horne (FIRENZE) was investigated. The measurements were performed before and after repair work on areas of the painting containing detachments. The panel was placed on a wooden support clamped to the wall. The first example relates to a region with two detachments (see Fig. 4.63.). Both defects were clearly revealed by heating the surface for two seconds with the infrared lamp. The same test was performed after one day from the consolidation of the damaged area. The closed-fringe, typical of detachments, was absent. However, minor anomalies were still observed when the heating time was increased to approximately 20 seconds (see Fig. 4.63.c).

*a)*
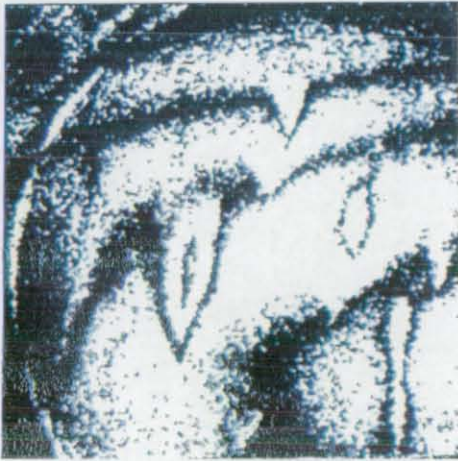


*b)*
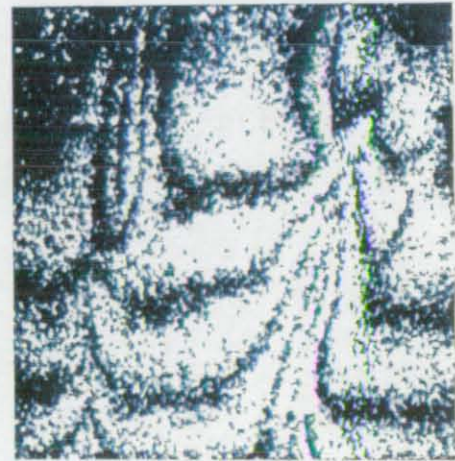


*c)*

*Figure 4.62. a) Painting on the predella. b) and c) Interferograms relative to cracked regions of the painting.*

*a)*



*b)*
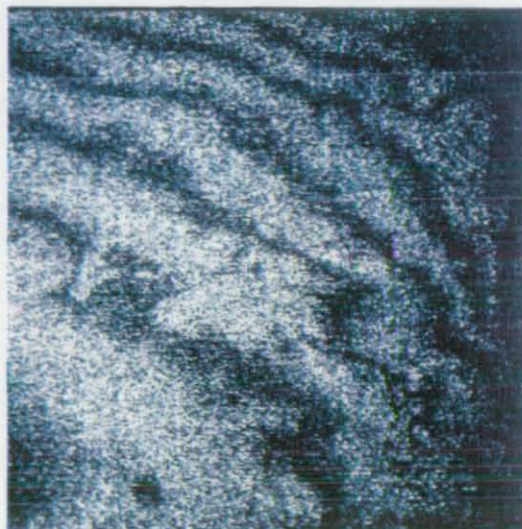


*c)*

*Figure 4.63. a) Inspected area. b) Interferogram before repair. c) Interferogram after repair.*
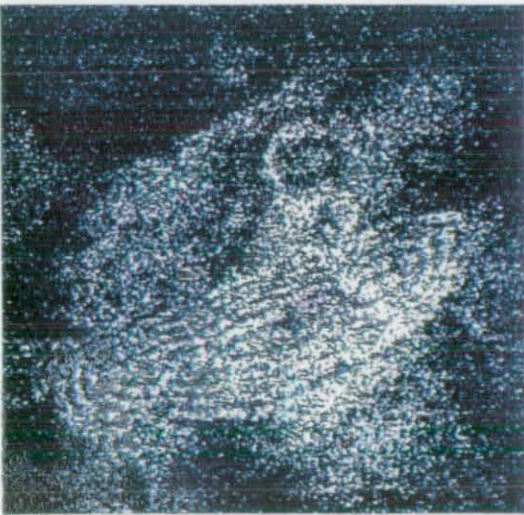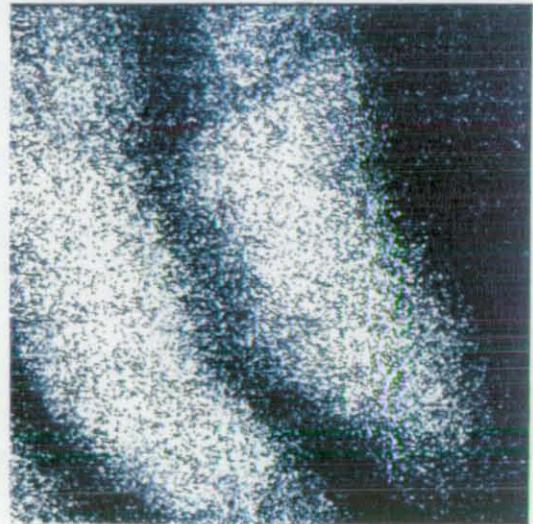
*Figure 4.64. a) Inspected area. b) Interferogram before repair. c) Interferogram after repair.*

In Fig. 4.64. the results for another region are presented. From the interferogram of Fig. 4.64.a, a large detachment was readily detected. Moreover, the small closed fringe above this defect indicated the presence of another detachment. In this case, once the defects had been repaired, the fringe pattern showed no anomalies.

Because of the subtraction nature of the ESPI measurements, the interferograms contain no visible details of the object. For the restorers it is however important to reconstruct the exact map of the defects. Digital techniques were used to resolve this problem. Fig. 4.65.a has been produced by digital addition of the two images in Fig. 4.63.b and c. A further example is presented in Fig. 4.65.b where a sketch[3] of the visible image has been superimposed on the interferogram.



a)                                          b)
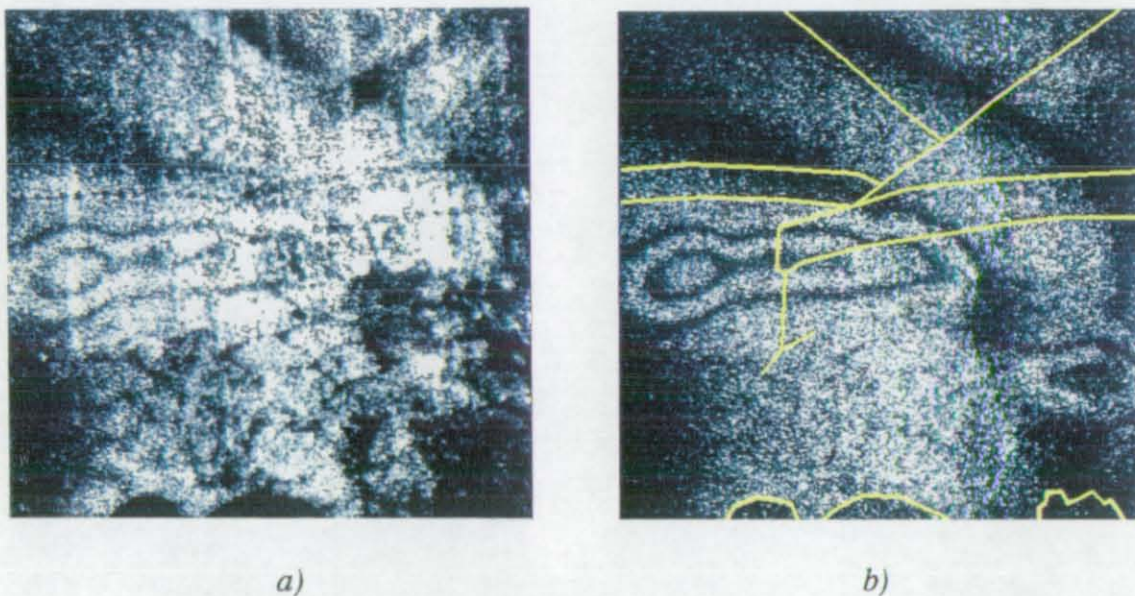
*Figure 4.65. Digital addition to an ESPI interferogram of the image a), and of a digital sketch b).*

---

[3]A very precise sketch can be obtained by performing an XOR (Exclusive Or) operation between the visible image of the surface and a copy where the main lines have been redrawn with an image editor program.

### 4.3.3.4. In-field measurements in the Cappella Portinari

The measurements reported here were performed on a terracotta angel located inside the Portinari Chapel (15th century) in the Church of S. Eustorgio (MILAN-Italy). The angel is part of the Tripudio Angelico, which occupies a vast area of the interior wall of the chapel at the height of approximately 13 meters from the ground.

The equipment was taken to the sixth floor of the scaffolding for the examination of the angel (see Fig. 4.66). One foot of the tripod was placed on the scaffolding, whilst the others rested on a small platform by the chapel wall. The personal computer and a monitor were positioned at the ground floor in order to control the acquisition of the interferograms from a point external to the scaffolding. A 22 metres cable was used to connect the optical head to the acquisition unit.



*Figure 4.66. Inspection of the angel of the Tripudio Angelico.*

A region containing a scaled area was chosen for inspection in order to test the feasibility of the measurements. The object surface had been heated with an infrared lamp for a few seconds between the exposures. The resulting interferogram is presented in Fig. 4.67. where the fringes clearly indicate the extension of the detached layers.
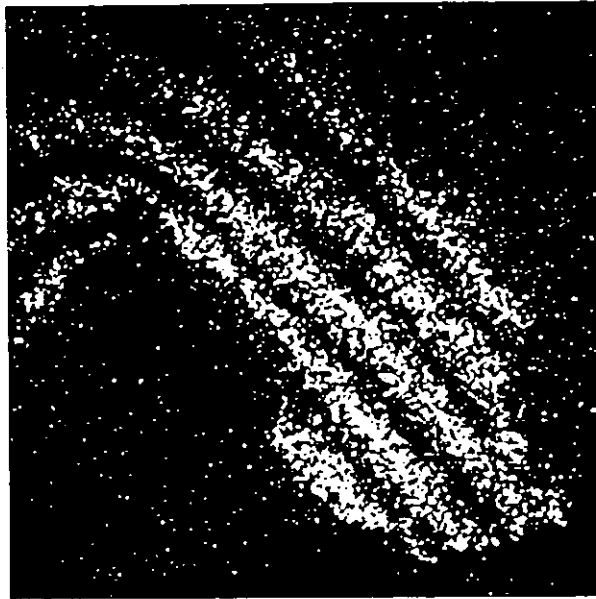
*Figure 4.67. Interferogram of a region containing a scaled area.*

## 4.3.4. Concluding remarks

Two ESPI interferometers have been proposed and tested for artwork diagnostics. Both systems shared the advantages of real-time fringe generation, daylight operation and portability. The use of optical fibres allowed a reduction of the optical elements and a simplification of the alignment procedure. The first interferometer was based on a single-mode fibre beam-splitter at an operating wavelength of 633 nm. The light source was a He-Ne laser coupled to the fibre optic device. In the second interferometer a pig-tailed infrared laser diode (785 nm) was used with the advantage that the manual coupling of light into the fibre was no longer necessary. Furthermore the intensity ratio between the illumination and reference beams could readily be adjusted by rotating the output end of the polarisation preserving fibre instead of acting on the GRIN-based connection used in the first interferometer.

Although it has been shown that a surface area of 30 x 30 cm could successfully be inspected on laboratory specimens, the experiments performed on real artworks have led to the conclusion that a 10 x 10 cm area must be considered as typical. This is a direct consequence of the variety of materials and scattering properties of artwork surfaces.

The results presented have demonstrated that ESPI deformation analysis is well suited to the investigation of initial damage on frescoes and paintings. Moreover a correspondence has been found between the anomalies of the fringe patterns and the most common types of defects (cracks, detachments). The discussions with the restorers highlighted the importance of ESPI measurements for assessing the quality of repair work. This has been confirmed experimentally by the results obtained for the wooden panel "Trionfo di David" (Museo Home - Florence, Italy).

When the measurements were performed out of the optical laboratory, external disturbances (e.g. traffic induced vibrations, air turbulence, excessive ambient light, people), and speckle decorrelation effects decreased the fringe contrast. It was therefore necessary to apply digital processing techniques to improve the quality of the interferograms. In all the in-field measurements described, the use of phase extraction techniques was hindered by the intensity of mechanical vibrations and the irregularity of the fringe patterns obtained for the damaged areas.

The feasibility of ESPI measurements on artworks situated at several metres from the ground level has been tested for the terracotta angel in the Portinari Chapel (Church of St. Eustorgio - Milan, Italy). The operative conditions of the ESPI system on scaffolding structures were extremely critical. The recent design of scaffoldings for monuments is aimed at minimising the number of contact points with the object to be restored. As a result the relative vibrations between an optical head on the scaffolding and the object will prevent any interferometric measurement.

Finally, it is worth noting that the colour pigments of paintings exhibit a characteristic behaviour according to the illumination wavelength. In particular, during the experiments some regions, which were dark in visible light, appeared bright when illuminated by the infrared radiation of the laser diode. Therefore the eventual use of two or more wavelengths should facilitate the ESPI inspection.

## 4.4. References

[1] Daniel, I.M., "Composite materials", in "Handbook on Experimental Mechanics" (ed. Kobayashi A.S.), Prentice Hall New Jersey, (1987) 8 14-890

[2] Adams A.D.,Cawley P., "A review of defect types and nondestructive testing techniques for composites and bonded joints", NDT International (1988) 21 208-222

[3] Tsuruta T., Shiotake N. and Yoshinobu I., "Hologram Interferometry Using Two Reference Beams", Japanese Journal of Applied Physics (1968) 7 1092-1100

[4] Dandliker R., Marom E. and Mottier F.M., "Two reference beam holographic interferometry," Journal of the Optical Society of America A (1976) 66 23-30

[5] Vest C.M., "Holographic interferometry", John Wiley & Sons, (1979)

[6] Chai H., Babcock C.D., Knauss W.G., "One dimensional modelling of failure in laminated plates by delamination buckling", Int. J. Solids Structures, (1981) 17 1069-1083

[7] Kardomates G.A., "Large deformation effects in the postbuckling behavior of composites with thin delamination", AIAA J., 27 (1989) 624-631

[8] Jansson E.V., Molin N.E., Sundin H., "Resonances of a violin body studied by hologram interferometry and acoustical methods", Optica Scripta, (1970) 2 243-256

[9] Ek L., Jansson E.V., "Vibravision and electroacoustical methods applied to determine vibration properties of wooden 'planks' for violin plates", Journal of the Catgut Acoustical Society, (1985) 44 16-22

[10] Knott G.A., "A dynamic analysis of the violin using finite elements", presented at JASA-Nashville USA (1985)

[11] Jones R., Wykes C., "Holographic and speckle interferometry", Cambridge U.P. London, (1983)

[12] Owner-Petersen M., "Digital speckle pattern shearing interferometry: limitations and prospects", Applied Optics, (1991) 30 2730-2738

[13] Amadesi S., Gori F, Grella R., Guattari G., "Holographic Methods for Painting Diagnostics", Applied Optics, (1974) 13 2009-2013

[14] Vlasov N.G., Ginzburg V.M., Novgodorov V.G., Protsenko V.N., Stepanov B.M., Ushkov F.V., "Application of holographic-interference methods to the determination of the optimal temperature-humidity conditions for preserving monumental paintings and works of art", Sov.Phys.Dokl. (1976) 20 859-861

[15] Amadesi S., Paoletti D., D'Altorio A., "Real-time holography for microcrack detection in ancient golden paintings", Optical Engineering, (1983) 22 660-662

[16] Paoletti D., D'Altorio A., Amadesi S., "Double Exposure Speckle Hologram for Strain Measurements in Frescoes Diagnostics", Optics Communications, (1984) 48 309-312

[17] Gori F., Urbani G., "L'olografia nel campo del restauro", Estratto da Le Scienze (1st ed., Italian, of Scientific American), no. 74, Oct. (1974).

[18] De Angelis A., Garosi F., "Indagini strutturali sul cavallo di bronzo dei Musei Capitolini di Roma mediante interferometria olografica a doppia esposizione con laser impulsato di alta potenza", Proceedings of the 2nd International Conference on Non-Destructive Testing, Microanalytical Methods and Environment Evaluation for Study and Conservation of Works of Art, Perugia (1988), Vol.1 20.1-20.12

[19] Gülker G., Hinsch K., Hölscher C., Kramer A., Neunaber H., "Espi System for in situ Deformation Monitoring on Buildings", Optical Engineering, (1990), 29 816-820

[20] Marchand E.W., "Gradient index optics", Academic Press, (1978)

[21] Newport Catalogue, (1992), N-15

[22] Thomson W.T., "Theory of Vibration with Applications", Prentice-Hall, (1972)

[23] Ishii Y., Chen J., Kazumi M., "Digital phase-measuring interferometry with a tunable laser diode", Optics Letters, (1987), 12 233-235

[24] Yonemura M., "Wavelength-change characteristics of semiconductor lasers and their application to holographic contouring", Optics Letters, (1985) 10 1-3

[25] Kato J., Yamaguchi I., Ping Q., "Automatic deformation analysis by a TV speckle interferometer using a laser diode", Applied Optics, (1993), 32 77-83

[26] Gülker G., Haack O., Hinsch K.D., Hölscher C., Kuls J., Platen W., "Two-wavelength electronic speckle-pattern interferometry for the analysis of discontinuous deformation fields", Applied Optics, (1992) 31 4519-4521

# Chapter 5

# Optical contouring measurements

## 5.1. Introduction

Contouring means examining the surface of an object in order to obtain a detailed description of its 3D profile. Common application areas are topography and mechanical profiling, but many other fields (e.g. medicine, dental research, machine vision, cloth design) benefit from the knowledge of the geometric shape of objects. Optical methods offer attractive alternatives to traditional techniques as the measurements are, in general, contactless, non-intrusive, and full-field.

Optical contouring techniques are based on a variety of principles including triangulation, moiré, photogrammetry, interferometry, holography, and speckle. Of these only photogrammetry has largely been accepted among restorers, but its use has often been hindered by the complexity of the measurements and the high costs. Nevertheless, on the whole, photogrammetry is unequalled for the study of large objects such as facades, monuments, and statues. ´

In the contouring of small artworks (e.g. archaeological relics, museum objects), for which a better resolution is desired, optical techniques have been at a research stage for many years. In a review paper [1] Owen and Sheets have demonstrated that line projection and moiré methods [2] comply with the needs of archaeology. Moreover, 3D laser scanners based on triangulation can successfully be applied to the 3D recording of museum objects for replication purposes [3].

Holographic contouring techniques have been proposed for studying the amount of wear and for the evaluation of position, depth, and volume of surface defects on stone samples, statues, etc. [4]. Similar measurements have recently been performed with a compact instrument based on Digital Speckle Pattern Interferometry (DSPI) [5].

At the present time, optical contouring systems, exploiting triangulation, moiré, or fringe projection techniques, are available in industry for full-field shape measurements. These systems consist of an optical unit for projection and image acquisition, a mechanical unit for scanning the object surface, and a computer unit for data processing. For a measuring volume of approximately 1 $dm^3$ a depth resolution of 0.1 mm is normally achieved. The contour data can readily be interfaced with standard software packages for analysis, representation, and modelling. However, because of their recent development and the high costs, these systems have scarcely been applied to the contouring of art objects. On the other hand, more specific studies [6] are necessary in order to deal with the pronounced shadowing problems and local scattering anomalies presented by artwork surfaces.

147

The experimental work presented in this chapter has been focused onto the contouring of small objects (some centimetres) by application and development of holographic and fringe projection methods. A brief description of the principles and of the main features of these methods have been included. The use of contour extraction algorithms based on phase-shifting and Fourier digital techniques has been discussed. Samples made of metal, wood, and stone have been considered for inspection.

## 5.2. Holographic generation of depth contour fringes

### 5.2.1. Background concepts

The fundamental property of holographic interferometry to record the optical phase of the light diffused from rough surfaces can be used for the generation of contour fringes. To do this the parameters of the optical system have to be modified in order to produce a path length difference which is proportional to the surface profile. An effective and simple method, proposed by Tsuruta and Shiotake [7] in early 1967, consists of replacing, between two holographic exposures, the medium surrounding the object. If the illumination and viewing directions, corresponding in Fig. 5.1. to the wave vectors $k_L$ and $k_O$ respectively, are parallel, then the optical phase $\phi_n(x,y,z)$ associated with a point $P(x,y,z)$ of the surface can be expressed by

$$\phi_n(x,y,z) = 2knz(x,y)$$

where $n$ is the refractive index of the medium in the cell containing the object, and $k$ is the wave number. After the first exposure, the refractive index is changed to $n'$, and the second exposure is taken. The interference phase of the resulting fringe pattern is therefore expressed by:

$$\varphi(x,y,z) = 2k(n-n')z(x,y) = 2k\Delta nz(x,y) \tag{5.1}$$

Since $\varphi(x,y,z)$ is directly proportional to the distance $z$ between surface points and the reference plane $xy$, the holographic fringes can be interpreted as depth contour lines on a topographic map. The distance $\Delta z$ between two adjacent contours is obtained by equating the phase difference to $2\pi$, which yields

$$\Delta z = \frac{\lambda}{2\Delta n} \qquad (5.2)$$

This equation demonstrates that by adjusting the difference of the refractive indexes the depth resolution can be readily controlled. This method applies well to optically rough surfaces, unlike high resolution interferometry which can only be applied to mirror-like surfaces.
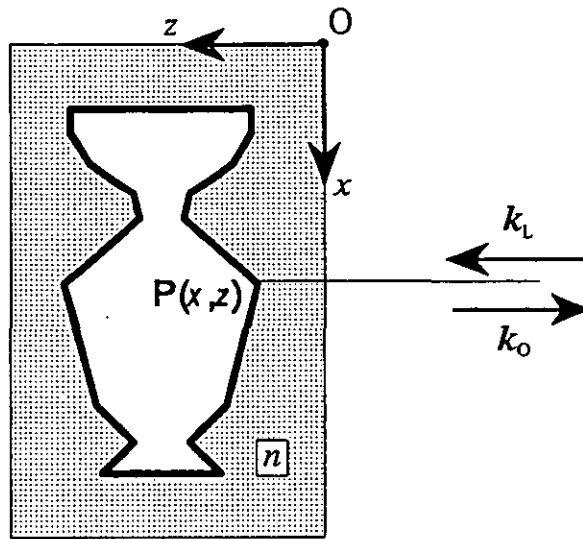


*Figure 5.1. Schematic diagram depicting the geometry used for measuring the object profile with the method of two index holography.*

Another well established method to produce depth contour fringes with holographic interferometry is based on the recording of a double exposure hologram of the object illuminated with laser light at a different frequency for each exposure [8]. During reconstruction, which is made with a single wavelength, it can be shown that contour fringes correspond to depth separations $\Delta z$ according to the following relation:

$$\Delta z = \frac{\lambda_1 \lambda_2}{2(\lambda_1 - \lambda_2)} \qquad (5.3)$$

where $\lambda_1$ and $\lambda_2$ are the laser wavelengths used for the first and second hologram respectively. When two wavelengths are used the contour interval depends on the spectral lines available in the laser source. As long as traditional holographic

lasers (Argon, He-Ne, Ruby) are used the possible values of $\Delta z$ belong to a very limited set. In literature the application of other multiple line lasers to holographic contouring has also been investigated [9,10]. However, in spite of the fact that extra contour intervals are available, some practical problems should be faced such as those related to the lack of coherence, beam quality, etc. In any case, it should be noted that since the first hologram is recorded at $\lambda_1$ and the second at $\lambda_2$, the two images are magnified with two different factors during simultaneous reconstruction. This can produce a contrast reduction of contour fringes especially when a small contour interval is desired.

In general, both Eqt. (5.2) and Eqt. (5.3), which correspond to the two-index and two-wavelength methods respectively, hold when the illumination and observation directions are parallel. When this condition is not fulfilled the expression for $\Delta z$ becomes more complicated and correction factors should be carefully evaluated and included in the formulas. If the object is not illuminated by a collimated beam or the viewing direction is not parallel to the $z$ axis, severe errors occur, especially when high resolution contour fringes are desired. Zelenka and Varner [11,12] suggested the use of a telescopic system to select only those rays which lie along the right direction. In this way, errors caused by the presence of multiple orientations of the vectors $k_O$ can be greatly reduced. Since the selectivity of the telescope is inversely proportional to the size of its pupil function, speckle noise will increase and ultimately limit the system resolution.

## 5.2.2. Optical setup

Depth contour fringes have been obtained with the optical layout depicted in Fig. 5.2. In order to view the object along the illumination direction a beam-splitter (50:50 splitting ratio) was positioned at 45° in front of the object. The light transmitted, which served as the reference beam, was attenuated by a neutral filter and reflected by a mirror toward the holographic plate. The attenuation of the filter should be adjusted according to the object reflectivity and the desired ratio between the intensities of the interfering beams.

The object was placed inside a cell (dimensions 170 x 100 x 30 mm) with a window through which it could be illuminated and viewed at the same time. Since the window surface can be considered as the reference plane $x,y$ defined in Sec. 5.2.1., the measurement reliability depends on the surface finishing. It is therefore clear that an optically flat glass was necessary. The cell was filled with an aqueous solution of sugar whose concentration was changed between the exposures. In practice, the liquid cell was connected to a simple system of pipes which allowed the replacement of the sugar solution. The object was firmly fixed to avoid any displacement due to filling or

emptying the cell with the solutions. A wait of several minutes was necessary before measurements to ensure that the liquid was free of turbulence which could introduce uncontrolled phase distorsions in the fringe pattern. The relationship between the refractive index and the concentration of the solution can be found in handbooks of chemistry and physics (see for example [13]). Some of these values have been reported in Table 5.1. together with $\Delta z$ which gives the corresponding depth distance between two adjacent fringe maxima. However, it should be noted that the values inferred from the handbook [13] must be considered as nominal since they hold for a wavelength $\lambda = 589.3$ nm and at a temperature of $20°$ C.
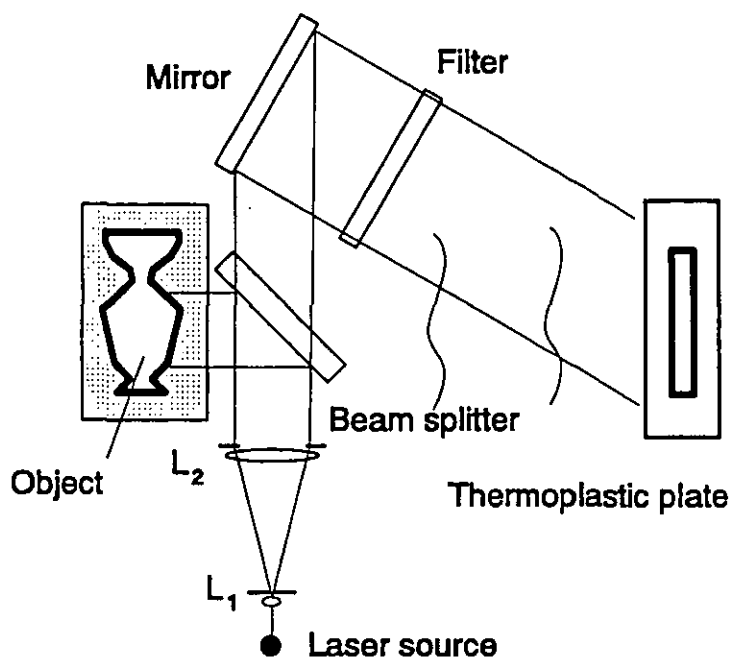


*Figure 5.2. Optical setup used for generating holographic depth contour fringes with the two-index method.*

| Concentration (%) | Refractive index | Contour interval $\Delta z$ ($\mu$m) |
|---|---|---|
| 1 | 1.3344 | 226.071 |
| 10 | 1.3479 | 21.241 |
| 20 | 1.3639 | 10.242 |
| 40 | 1.3997 | 4.745 |
| 80 | 1.4901 | 2.014 |

*Table 5.1. Refractive index values for some aqueous solutions of sugar. The values of $\Delta z$ are obtained by assuming that the object has been immersed in pure distilled water (n=1.3330) for the first exposure.*

The holograms were recorded with a thermoplastic camera (NEWPORT mod. HC-300) which offered the advantage of no chemical development. The setup was mounted on a vibration-free table and during the recording the laboratory was darkened until the development of the plate had taken place.

### 5.2.3. Experimental results

The two-index method was tested on a small sea shell. In particular, the external surface of one of its halves was considered for contouring. The shell was round shaped with a lateral diameter of approximately 4 cm. A small sized object was chosen because it had to fit into the narrow cell used in the setup (see Sec. 5.2.2.). The extent of the inspected area was limited by the aperture of the collimated beam illuminating the object, which in turn could not exceed the diameter of the beam-splitter. These parameters were adjusted in order to offer a whole-field view of the object. The internal side of the shell was glued to a metallic support, rigidly fixed to the walls of the liquid cell to avoid any displacement of the object. The shell was white and no painting was required to increase the amount of light reflected from its surface. The exposure time was four seconds for each hologram, and the ratio between the intensities of the reference and the object beams was set to 2 after a 100 times attenuation of the reference beam by using a neutral filter.
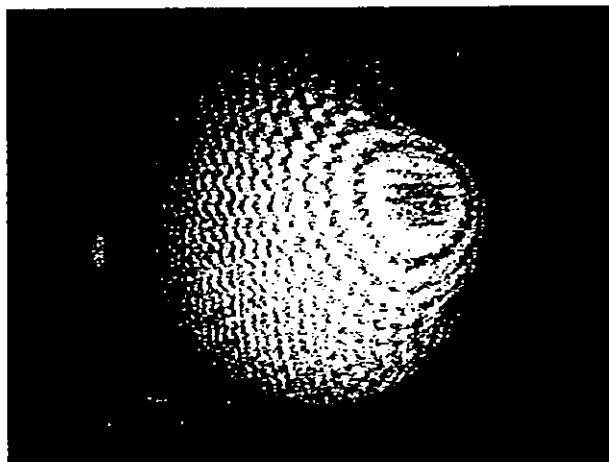


*Figure 5.3. Depth contour fringes on a sea shell. The contour interval (nominal) is 0.1 mm.*

Fig. 5.3. shows the holographic image of the shell with the superimposed contour fringes. The first hologram was taken with the object immersed in an aqueous solution with a percentage of sugar equal to 10% (10 grams of sugar in 0.1 litres of distilled

water) corresponding to a nominal refraction index $n = 1.3479$. The fringes were obtained by refilling the cell before taking the second hologram with a 12% solution ($n'=1.3510$). The corresponding nominal contour interval was $\Delta z = 0.1$ mm. The simplest way to determine the real contour intervals was to calibrate the contour system by considering an object whose shape and dimensions were well known. Moreover, from the tables about sugar solutions [13] it is also clear that the refractive index varies with temperature. For this reason a temperature stabilisation of the solution with an accuracy of $0.1°$ C is strongly recommended, but it was not implemented in these simple experiments.

Finally it was observed that the obtained fringes were slightly distorted if the observation point was moved. This effect, caused by the existence of a geometric relation between the pathlength difference and the viewing direction, is expected to be more pronounced when high resolution measurements are performed.

## 5.2.4. Concluding remarks

The use of holographic interferometry to produce whole-field maps of the surface geometry has been reviewed and investigated experimentally. The depth accuracy of the contour measurements lies in the range from few microns to several millimetres and is related either to the refractive index difference of the media surrounding the object or to the pair of laser wavelengths used for the holographic recordings. The major disadvantage of the two index approach, with respect to its application to artworks, is that the object has to be immersed. In the two wavelengths version, on the other hand, the measurements are contactless and non intrusive. In this case, however, the contour interval can be chosen amid a very limited set of wavelengths provided by the laser source.

In the above experiments, following the two-indexes approach, the illumination and the observation directions were made to be equal so that the holographic fringes represented real depth contours of the object surface. The quantitative evaluation of the contour interval could readily be provided if the refractive indexes of the sugar solutions were exactly known. The standard tables, however, contain values which are valid only under certain conditions of temperature and wavelength, therefore a calibration of the measuring system was necessary. The optical setup was very sensitive to external vibrations and to thermal gradients since the cell containing the object was emptied and refilled between the holographic exposures. The use of an isolated optical table was fundamental for producing acceptable results.

Although the main features of the holographic contouring method have been described and tested, it should be added that the evaluation of the phase distribution would be very helpful to distinguish peaks from valleys in the fringe patterns referring to surfaces of complex shape. Examples of the application of phase shifting techniques to retrieve phase maps either in the two-indexes and the two wavelengths methods are contained in ref. [14] and [15] respectively.

## 5.3. Fringe projection contouring using coherent light techniques

### 5.3.1. Background concepts

The principle of the method, illustrated for the first time by Rowe and Welford [16], consists of projecting a set of parallel fringes onto the surface of the object to be contoured. If the projected pattern is viewed at an angle $\vartheta$ from the illumination direction, the fringe profile is modulated by the object surface. Contour information can be represented by the distance between an object point P and its projection P' onto an arbitrarily chosen reference plane (see also Fig. 5.4.). This distance can be evaluated by considering the fringe pattern projected onto the object and the virtual fringe pattern which would have been formed on the reference plane. If it is assumed, without any lack of generality, that a fringe maximum is located at P, the distance PP' is given by

$$PP' = \frac{AP'}{\tan \vartheta} \qquad (5.4)$$

where A is the position of the fringe maximum on the reference plane.

It is clear from Fig. 5.4. that the phase of the fringe pattern at P and A is the same. Therefore, it can be demonstrated that the distance PP' is proportional to the difference $\Delta\phi$ between the phase of the interference pattern in P and the phase in P' on the reference plane. By letting $p$ be the distance between two adjacent fringe maxima along the reference plane, it follows that

$$AP' = p \frac{\Delta\phi}{2\pi}$$

and by using Eqt. (5.4), the final expression for PP' is

$$PP' = \frac{p}{\tan\vartheta}\frac{\Delta\phi}{2\pi}$$

(5.5)

Contour information is thus encoded in the phase modulation of the projected fringe pattern, whose expression in the recording plane $x,y$ of the viewing system can be written as

$$I(x,y) = a(x,y) + b(x,y)\cos\left(\frac{2\pi}{p}x + \Delta\phi(x,y)\right)$$

(5.6)

where $I(x,y)$ is the light intensity, $a(x,y)$ and $b(x,y)$ are the background and the intensity modulation terms, respectively. In Eqt. (5.6) it is implicitly assumed that the fringes are parallel to the y-axis in the reference plane.
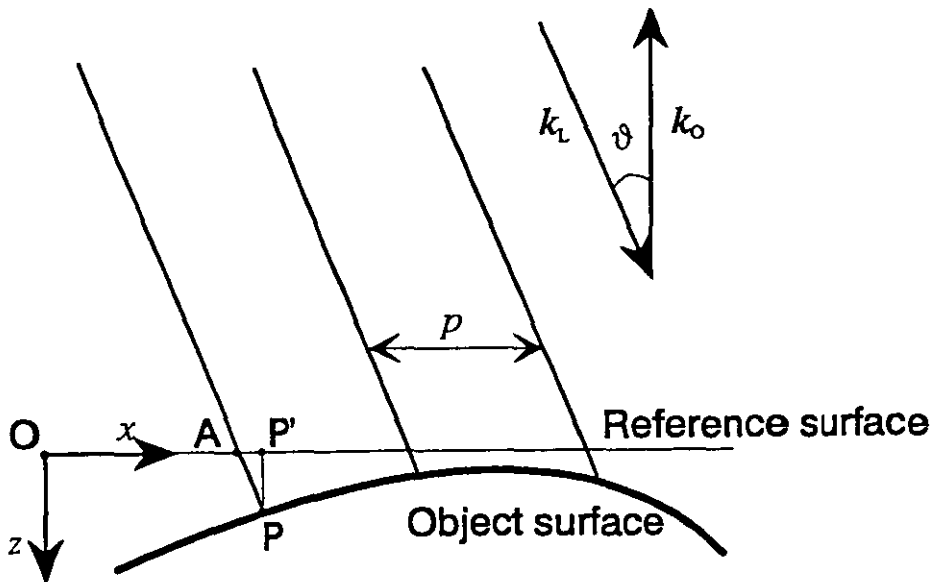


*Figure 5.4. Diagram depicting the projection of parallel fringes. The lines, parallel to the illumination vector $k_L$, represent the fringe maxima.*

Although the fringes are not depth contour lines, the shape values can be calculated for each object point from the phase map of the fringe pattern. The sensitivity of the method, which can be defined as the amount of phase change for a given depth, increases with $\vartheta$, and it is inversely proportional to the fringe spacing $p$. However, for large values of the illumination angle, some areas of the object might be shadowed and

cannot thus be contoured. The main advantage of the fringe projection method is to provide a whole-field measurement avoiding surface scanning as in the case of classical triangulation.

The depth resolution of a contouring system is indicated as the minimum interval $\Delta z_{min}$ that can be measured. In the present case, the ultimate limit for the accuracy is given by the diffraction effects of the optical system, which can be represented by the object, the imaging lens, the aperture, and the image plane. The centre-to-centre separation $b$ for two resolved points according to Rayleigh's criterion is given by $b = 1.22 \lambda f / D$, where $\lambda$ is the light wavelength, $f$ is the lens focal length, and $D$ is the aperture diameter. Therefore, by taking into account Eqt. (5.5), the depth resolution limit is

$$\Delta z_{min} = \frac{b}{m \tan \vartheta} \tag{5.7}$$

where $m$ is the demagnification factor. Another limitation to the system resolution can arise from a low density of light sensors in the image plane. When, for example, a digital video camera is used to record the fringe pattern, this fact can strongly affect the system resolution. If the distance $b'$ between the centres of two adjacent pixels in the camera plate is greater than the diffraction limit then, for a correct evaluation of $\Delta z_{min}$, $b'$ must replace $b$ in Eqt. (5.7). It should be finally noted that, for a fixed angle $\vartheta$, the depth resolution can be effectively increased by reducing the size of the inspected area, i.e. by increasing $m$.

Parallel sinusoidal fringes can be readily produced by the optical interference of two plane wavefronts. If their wave vectors form a small angle $\Delta\vartheta$, then the fringe spacing $d$ is given by the simple relation [17]

$$d = \frac{\lambda}{\Delta\vartheta} \tag{5.8}$$

where $\lambda$ is the laser wavelength. In this case the interference planes are parallel and directed along the bisector of the angle $\Delta\vartheta$.

## 5.3.2. Holographic fringe projection

It is well-known that holographic fringes result from the simultaneous reconstruction of two coherent wavefronts [17]. This property can be successfully applied to generate a set of parallel sinusoidal fringes suited for contouring measurements, as described by Hildebrand and Haines in [18]. It is sufficient to introduce a small tilt of the illumination beam between two holographic exposures. By doing so the reconstructed image portrays the object as if it were simultaneously illuminated by two tilted plane waves. It is therefore clear from Sec. 5.3.1. that the overlaid fringes can be considered as if they have been projected from the illumination direction.

For the measurements two holographic setups have been arranged and tested. The setup presented in Fig. 5.5. utilises a rotating mirror to tilt the illumination beam between the exposures. A circular mirror (3" diameter) was mounted on a rotating stage, whose position could be adjusted by a micrometric screw. The first tests revealed that a satisfactory control of the angle could not be obtained with ordinary micrometers. However, since micrometers with enhanced differential precision were not available in the laboratory, a simple optical measurement was alternatively performed. A narrow laser beam (1 mm diameter) was directed to the centre of the rotating mirror and the reflected ray was observed on a screen located at a distance of approximately two meters. By measuring the lateral shift of the laser spot it was possible to evaluate the angular deflection with an accuracy of approximately 2 mrad.

The extension of the illuminated area depends on the dimensions of the optical elements, used to produce the plane wavefront, and the light power available. In the setup described the light source was a 35 mW c.w. He-Ne laser (Spectra Physics mod.127) and its output beam was expanded by the combination of the microscope objective $L_1$ (40 x) and the lens $L_2$ (focal length $f = 300$ mm, diameter $d = 100$ mm). Collimated beams of large diameter (200-300 millimetres) would require bigger optical elements, like spherical mirrors, which are however very bulky and expensive. The use of holographic lenses could also be considered but for the low values of their diffraction efficiency, which would induce light power losses. In these cases, more powerful laser sources are recommended in order to avoid long exposure times.

157
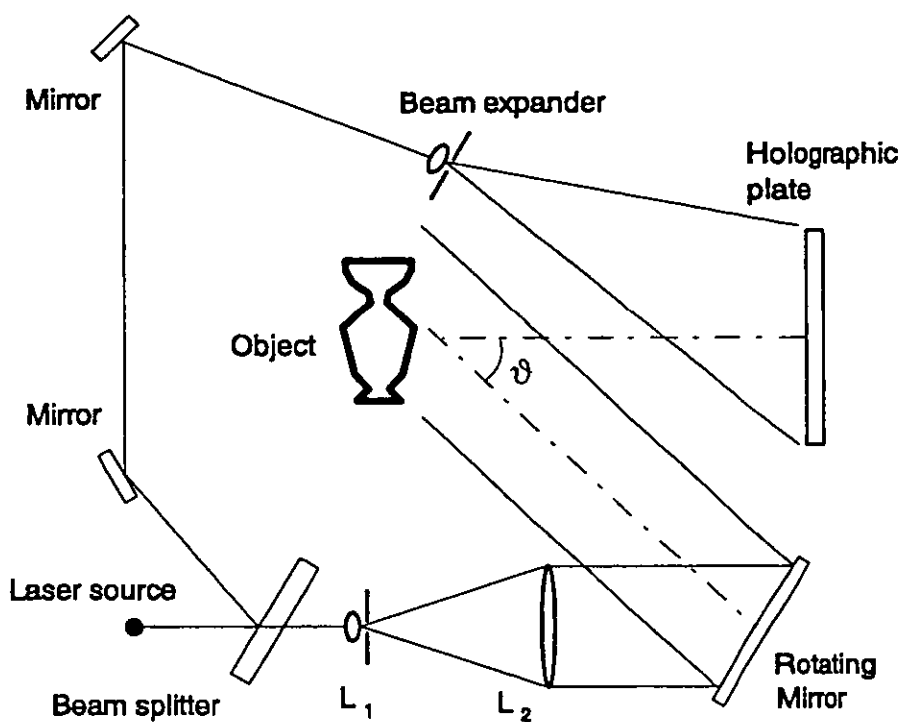
*Figure 5.5. Holographic setup using a rotating mirror for tilting the illumination beam.*
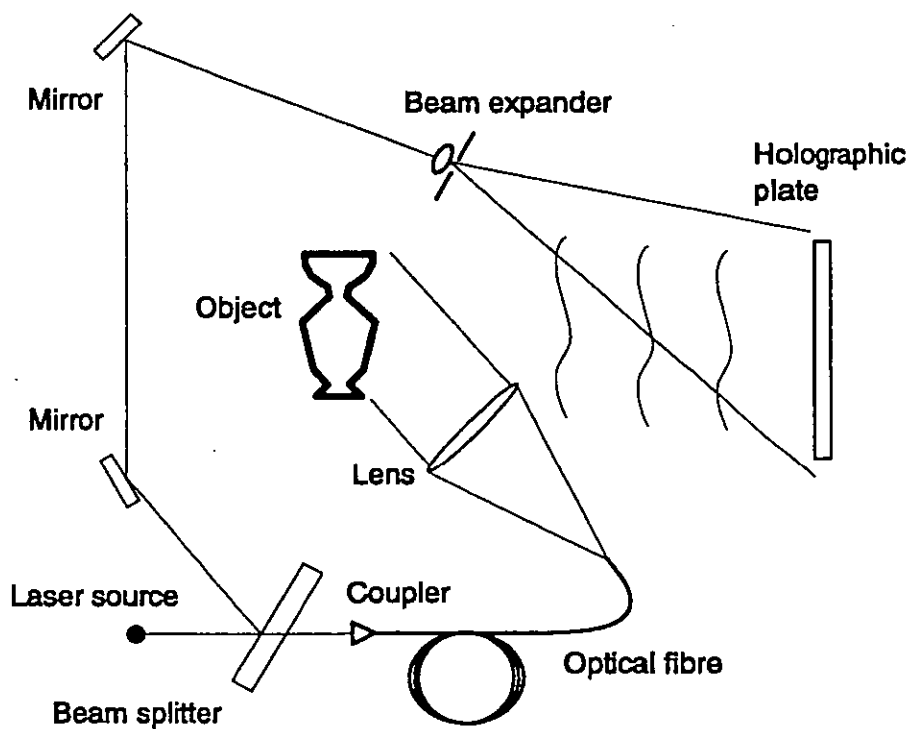


*Figure 5.6. Holographic setup using an optical fibre for tilting the illumination beam.*

In Fig. 5.6., the diagram of a setup is presented, where an optical fibre has been inserted along the object beam path. The fibre output end, which is considered as a point light source, was located at the back focal plane of a lens, so that the object was correctly illuminated by a a plane wavefront. A single mode fibre (mod. F-SV Newport) was used, and a collimating lens with a long focal length ($f$= 1000 mm) and a diameter of $D$=100 mm was necessary to compensate for the small numerical aperture (N.A.=0.1) of the fibre.

It should be noted that with an optical fibre the angle $\vartheta$ can be varied by several degrees with little or no modification of the object light path. Therefore, no further readjustments of the reference beam would be necessary to match the optical paths. Between the holographic exposures an angular shift $\Delta\vartheta$ was introduced by displacing the output fibre end in the lens focal plane by an amount $\Delta x = f\Delta\vartheta$. The manual adjustment of the fibre position was definitely less critical than in the case of the rotating mirror. In fact, an interval $\Delta\vartheta$=2 mrad corresponded to a displacement $\Delta x = 2$ mm. This means that for an error less than 1%, the fibre should be positioned with an accuracy of ±20 µm, which can be obtained with a standard micrometer.

Both experimental setups were mounted onto a vibration-free table in order to avoid mechanical disturbances during the hologram recording. However, for the second setup, temperature gradients and air turbulence along the fibre could introduce unwanted phase changes, which resulted in a drastic reduction of the hologram quality. These effects were effectively prevented by having short exposure times and by turning off the local heating system.

## 5.3.2.1. Experimental results

All the interferograms presented in this section have been obtained with an optical layout which included a single mode fibre (see Fig. 5.6.). The holograms were recorded onto AGFA 10E75 plates with the double-exposure technique. The ratio between the intensities of the reference and object beams was approximately 2:1 with typical exposure times of 2.5+2.5 seconds.

The surface (100 × 68 mm) of a wood specimen was examined. A sketch of the surface, where three different hollows were roughly carved, is depicted in Fig. 5.7. The specimen was painted white to obtain good quality holograms.
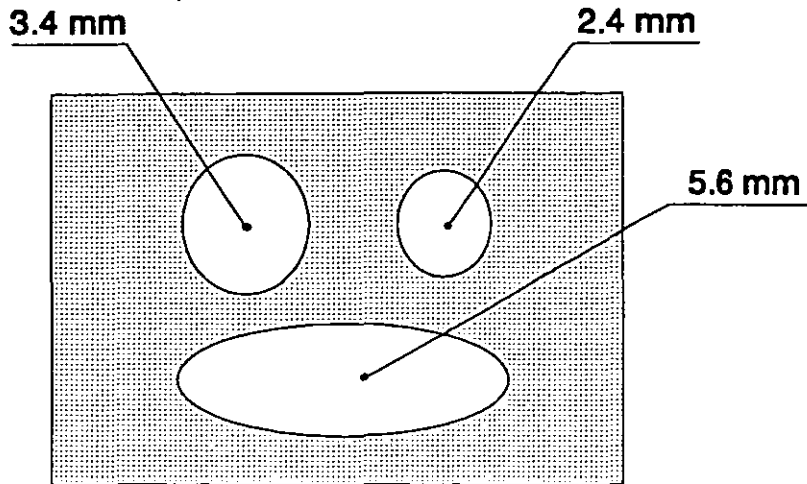
*Figure 5.7. Diagram of the surface of the wood specimen prepared for contouring. The measures in mm indicate the maximum depth of each hollow.*

The object was illuminated from the left at an angle of 45°. For this reason the interference fringes were shifted to the right in correspondence to the hollows, as shown in Fig. 5.8. As expected, the larger the deviation from the vertical profile, the deeper the hollow. It should be noted that the centre of the interferogram is brighter than the edges because the illumination beam had a gaussian intensity profile. The dark dots, horizontally aligned in the upper area of the object, were caused by a series of small cavities in the object.
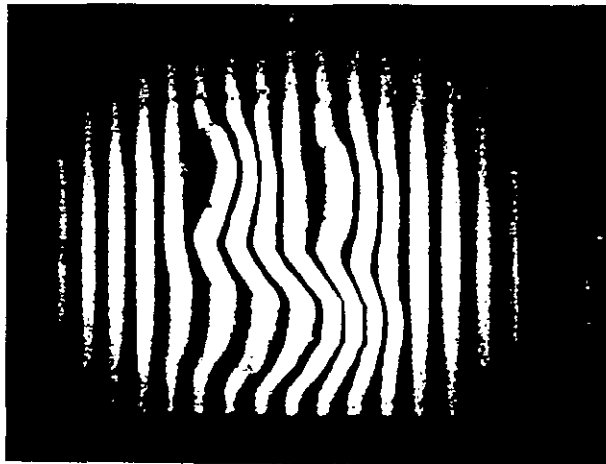


*Figure 5.8. Double-exposure hologram of the wood specimen illuminated at an angle* $\vartheta = 45°$ *with* $\Delta\vartheta = 4.7$ mrad.

The sensitivity of the measurements was increased by reducing the fringe spacing $d$. This was achieved, according to Eqt. (5.8), by increasing the tilt of the illumination beam from 4.7 mrads (Fig. 5.8.) to 15.6 mrads (Fig. 5.9.) and much more surface detail was revealed. First of all, the curved fringes between the cavities in the upper area, clearly indicated the presence of small channels, which could not be observed in the previous interferogram. It was also interesting to observe that in the magnified area represented in Fig. 5.9.b, the fringe interruptions inside the lower hollow, were produced by step-like discontinuities of the specimen surface along the horizontal direction.
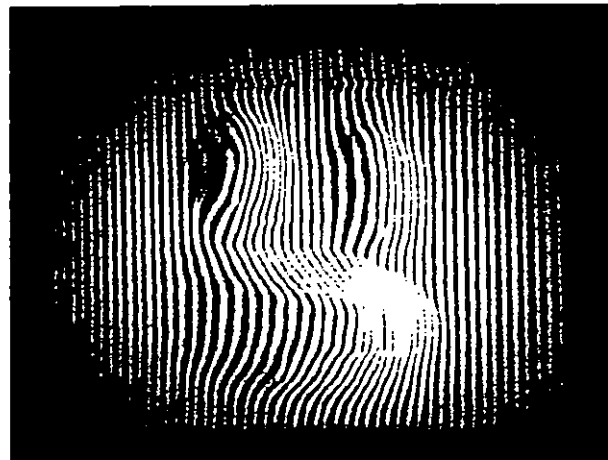


*a)*
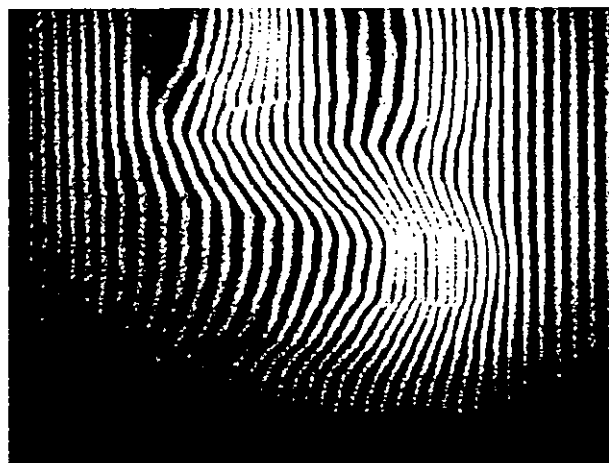
*b)*

*Figure 5.9. a) Double-exposure hologram of the wood specimen illuminated at an angle $\vartheta = 45°$ with $\Delta\vartheta = 15.6$ mrad. b) Detail about the lower hollow.*

The following examples illustrate the application of the contouring technique to stone surfaces. The specimens were kindly supplied by the quarries of the "Veneranda Fabbrica del Duomo di Milano" sited at Candoglia (NO)-Italy. The cathedral of Milan was built entirely of the marble form these quarries, which are today a source for the replacement of eroded elements. The finishing of the surfaces depends on their use; indoor decorative parts often have polished surfaces, whilst outdoor blocks or tiles usually bear no sign of treatment other than cutting. In Fig. 5.10. contouring fringes were formed on a piece of white marble, whose surface had been chiselled. This marble had recently been extracted and it was of the same type as those used to replace decayed parts. When the illumination angle was 45° (see Fig. 5.10.a), the fringes were almost rectilinear, showing no sign of surface preparation. The texture due to chiselling was readily detected by increasing the illumination angle to 70° (Fig. 5.10.b), as irregular undulations appeared in the fringe pattern. In both cases the inspected area was approximately 100 × 100 mm.
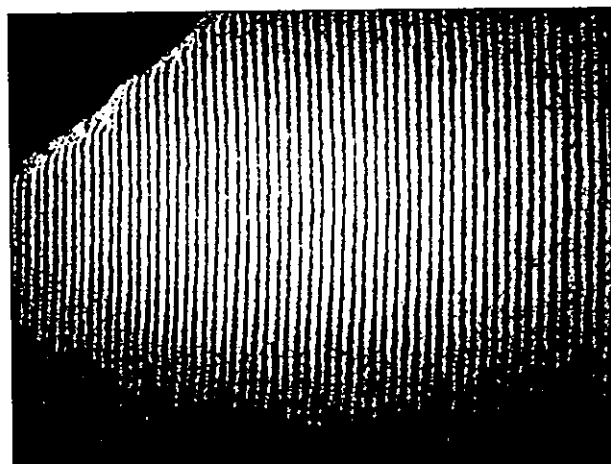


a)
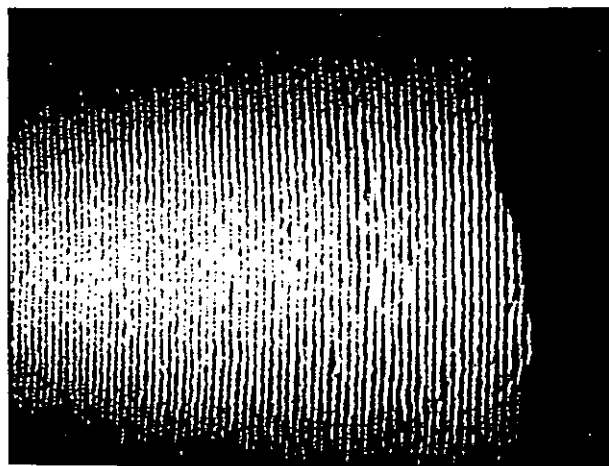
b)

*Figure 5.10. Marble surface illuminated at a) 45° or b) 70°.*

The interferogram, presented in Fig. 5.11., was obtained by illuminating at 45° the eroded surface of a piece of marble which had been exposed to weathering agents for approximately 200 years and was finally replaced. The holographic fringes were frequently interrupted because of step-like irregularities of the surface. Small black patches along the fringes were caused by shadows of isolated peaks (0.5 cm high), which were clearly visible on the surface.
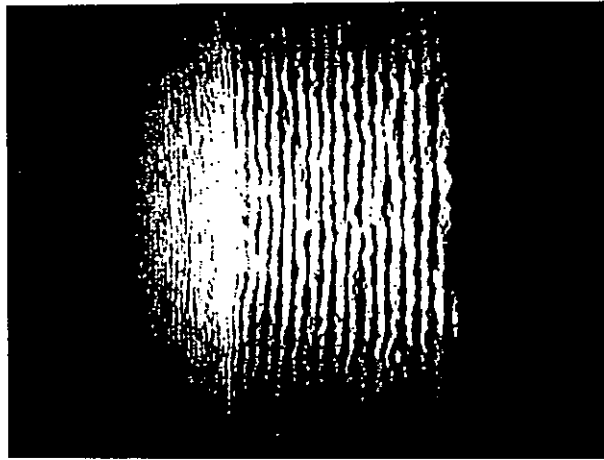


*Figure 5.11. Eroded marble surface illuminated at 45°.*

## 5.3.2.2. Concluding remarks

Double-exposure holographic interferometry has been successfully used for the production of projected-like fringes. The object was illuminated by a plane wavefront which was tilted by a small angle between the exposures. The main limitation for the size of the inspected surface were related to the dimensions of the optical elements. In the reported experiments, areas of 10 cm diameter were readily examined. The combination of an optical fibre and a collimating lens facilitated the control of the tilt of the illumination angle. The optical setup was adequately isolated from microvibrations, thermal gradients, and air turbulence, which could have spoiled the quality of the holograms.

The developed technique was applied to contour a wood specimen, whose surface presented three hollows with different shapes and depths, and the macro structure of marble surfaces, chiselled or weathered. The results experimentally illustrate the concepts presented in Sec. 5.3.1. regarding the dependence of the method sensitivity on the fringe spacing and the illumination angle.

## 5.3.3. Projection and processing of interference fringes

A set of equispaced sinusoidal fringes can be obtained, with few optical adjustments, from the output wavefronts of many types of interferometers. In this section a Michelson configuration, as depicted in Fig. 5.12, is considered. A 50:50 amplitude beam splitter divides the collimated wavefront at the input of the interferometer into two beams, which, after being reflected by the mirrors, recombine producing the desired fringe pattern. The angular separation of the two beams at the output of the interferometer is proportional to the tilt between the mirrors, which can be readily controlled with micrometer screws.
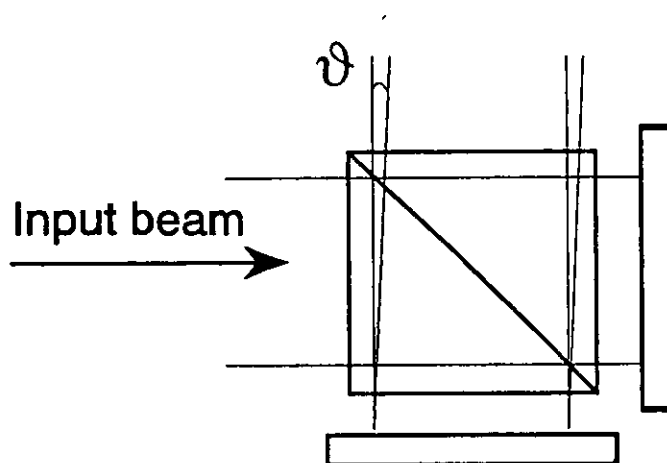


*Figure 5.12. Optical setup for the production of a set of equispaced sinusoidal fringes based on a Michelson interferometer.*

A projection unit has been designed and built in house [19]. The light source is a 5 mW c.w. He-Ne laser emitting at 633 nm with a coherence length of approximately 10 cm and an output beam 1 mm in diameter. Two lenses ($L_1$ and $L_2$ in Fig. 5.13.) expand the laser beam before the beam splitter cube (1" side). One of the interferometer mirrors is mounted on a piezoelectric crystal, which is used to introduce phase shifts in the fringes for the quantitative evaluation of the interferometric phase. The fringe pattern at the output of the interferometer is magnified by the lenses $L_3$ and $L_4$ resulting in an 8 cm diameter output beam. The characteristics of the lenses have been summarised in Table 5.2. The optical setup was mounted on a rectangular board 300 × 600 mm for portable operation.

164
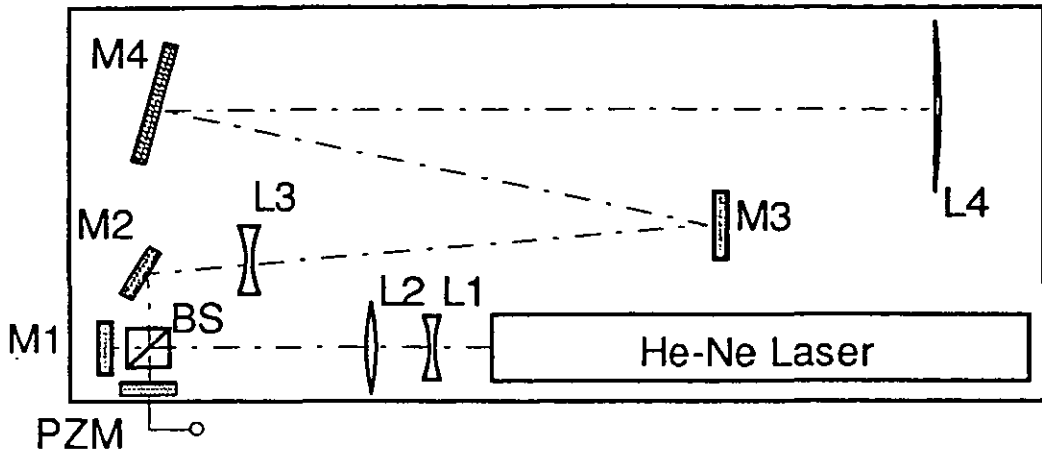
*Figure 5.13. Fringe projection system used for the experiments.*

| Lens | | Diameter (mm) | Focal Length (mm) |
|------|---|---------------|-------------------|
| L1 | (Biconcave) | 20 | 20 |
| L2 | (Biconvex) | 40 | 50 |
| L3 | (Biconcave) | 40 | 50 |
| L4 | (Planoconvex) | 80 | 1000 |

*Table 5.2. Specifications of the lenses utilised in the fringe projection unit.*

During measurements the reference plane is assumed to be perpendicular to the viewing direction. Whilst the distance of the projection unit from the object can be freely chosen, the illumination angle $\vartheta$ and the fringe spacing $p$ are fixed according to the desired contour sensitivity. It is finally recalled that the phase of the fringe pattern is directly proportional to the distance of a surface point from the reference plane (see Eqt. (5.5)). Therefore, the metric value corresponding to a digital grey level of the phase map can be found by calibrating the measuring system with an object whose shape is precisely known.

### 5.3.3.1. Preliminary experiments

Measurements were performed on the wood sample, which has already been described (see Fig. 5.7.). The image presented in Fig. 5.14., was obtained by projection of the fringe pattern onto the object at an angle of 45° from the right. A CCD videocamera Sony (B/W mod. XC77CE 768 x 512 pixels, pixel size 11 x 11 μm) was used for image acquisition. The PC based system presented in Sec. 4.2.3 was finally utilised to process

165

the interferograms. Two distinct algorithms have been separately tested to process the contour interferogram. They were based on phase-shifting and Fourier demodulation techniques respectively (for more details see Chap.3). The intermediate results of each algorithm have been reported here to illustrate the differences between the two approaches.
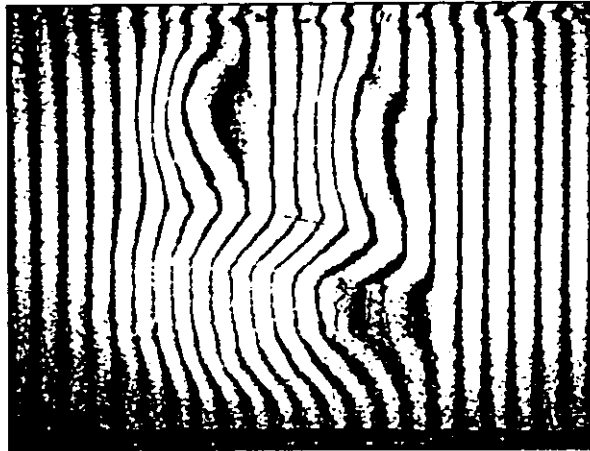


*Figure 5.14. Fringe pattern projected onto the test specimen.*

In order to apply the phase shifting algorithm, four interferograms, differing in phase by $\pi/2$, were acquired and stored in the memory of the frame grabber. The initial processing led to a wrapped phase image, which further unwrapping transformed into the absolute map of phase (see Fig. 5.15.a.b.). The last step consisted of the subtraction of a linear phase function from the unwrapped data to obtain the contour map of the object (Fig. 5.15.c.).

If care is taken to align the projected fringes along the vertical direction, the problem of phase demodulation can also be solved with the use of a monodimensional FFT algorithm applied line by line to the digital image. The resulting Fourier spectrum of the horizontal frequencies (see Fig. 5.16.a.) was filtered and translated by an amount corresponding to the frequency of the carrier fringes. The inverse Fourier transform allowed the evaluation of a phase diagram (Fig. 5.16.b.), which was directly proportional to the depth contours of the surface. Phase unwrapping was still necessary to reconstruct the contour data (Fig. 5.16.c.).
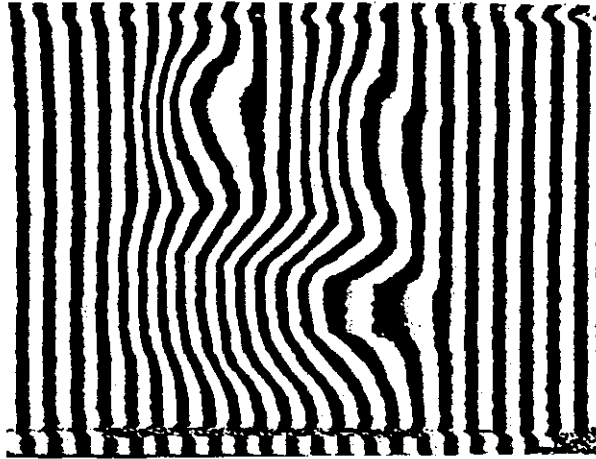
*a)*
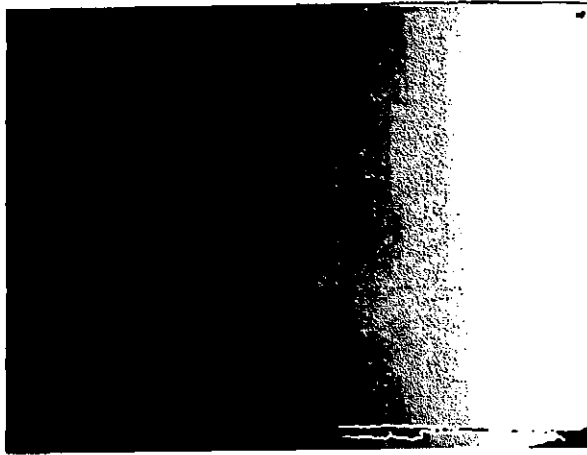
*b)*

*c)*

*Figure 5.15. a) Wrapped phase map. b) Unwrapped phase map. c) Contour image obtained from the unwrapped data by subtraction of a linear function corresponding to the phase behaviour on the reference plane.*
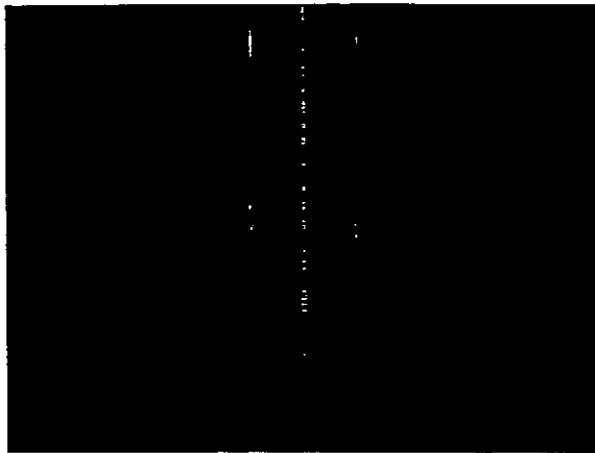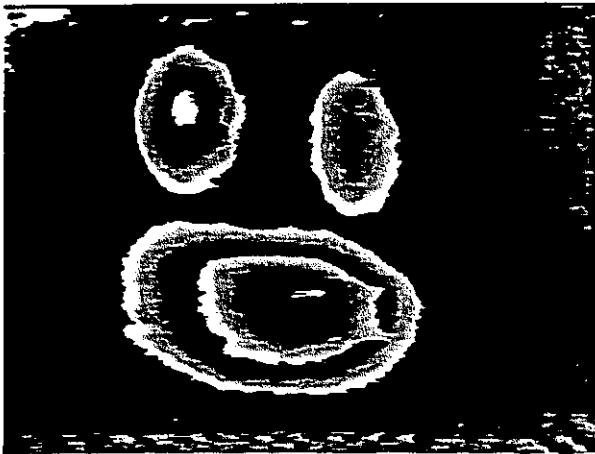
*Figure 5.16.* a) *Fourier spectrum of the projected fringe pattern, the central part corresponds to the background of the image (low frequencies) and contains no contour information. b) Wrapped phase diagram. c) Unwrapped phase image: contour information is proportional to the grey level values. The black spots are points where the unwrapping algorithm failed.*
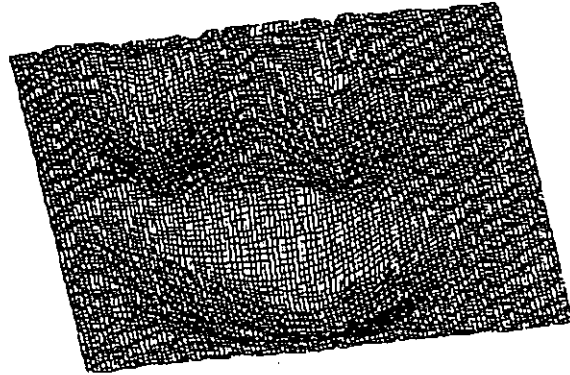
*Figure 5.17. 3D-mesh diagram of the wood specimen.*

The results obtained with the two algorithms converged to a unique profile of the specimen surface, whose 3D mesh diagram is depicted in Fig.4.12. The use of the Fourier approach seems appropriate for portable operation, because a single interferogram is required. However, when high resolution measurements are desired, the application of the Fourier algorithm might be hindered by high computing times if PCs or similar machines are employed. On the other hand, in spite of the higher speed of the phase-shifting algorithm, some extra equipment for the introduction and calibration of the phase steps has to be added.

## 5.3.3.2. Results

The experimental tests presented here aimed to demonstrate in practice the features of the method in terms of resolution and inspected area. The results have been produced with the phase-shifting algorithm and the measurements have been performed in the laboratory. At first, the fringe projection technique was successfully applied to record surface reliefs as small as $5-10\,\mu m$. To obtain such a resolution on an area of few squared centimetres, the illumination had to be almost parallel to the surface. In general, this gave rise to pronounced shadowing effects, unless very flat objects such as medals, coins, etc. were considered (see Fig. 5.18.).

The second application dealt with the measurement of the surface profile of a sandstone, which was heavily damaged during a compression test. The chipped area in the vicinity of the central hole of the stone specimen was illuminated at an angle $\vartheta = 45°$. A picture of the stone and the 3D mesh profile are presented in Fig. 5.19.
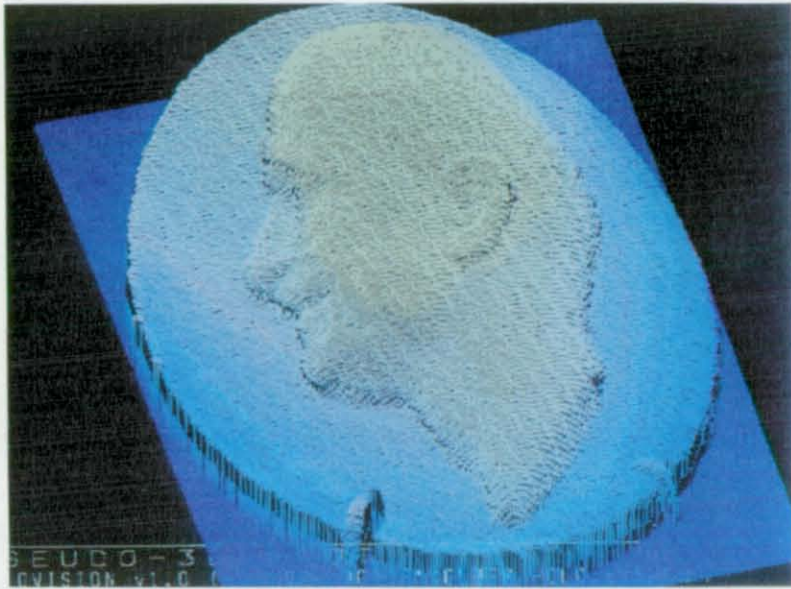
*a)*



*b)*

*Figure 5.18. Surface contour maps of: a) a medal b) an old British coin.*
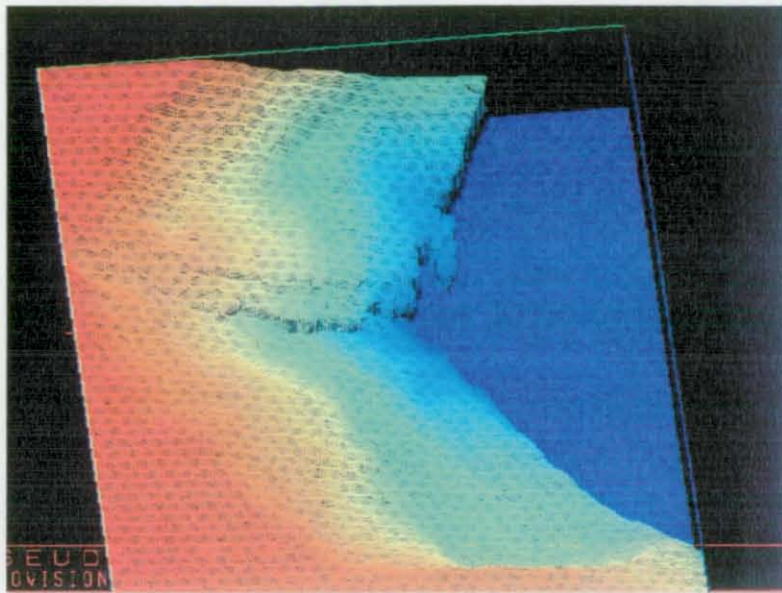
*a)*
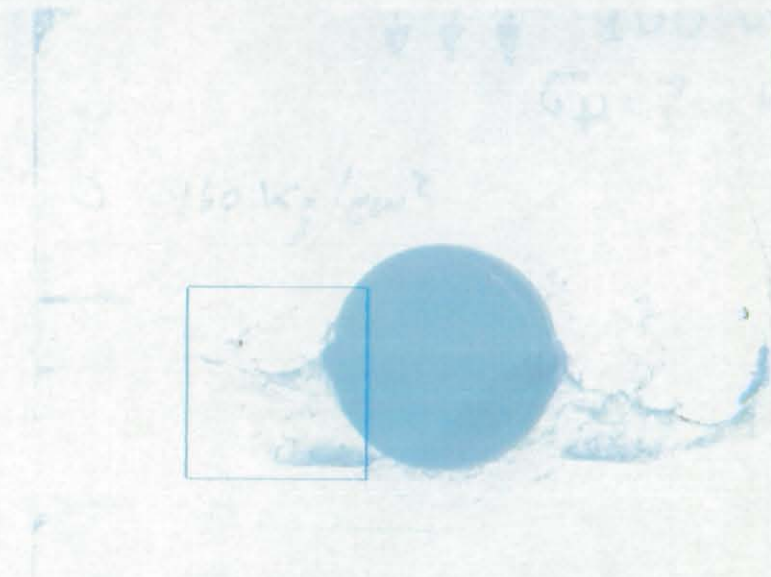
*b)*

*Figure 5.19. a) 3D map of a chipped sandstone surface. b) Photograph of the piece of stone (The blue rectangle indicates the contoured part).*

Finally the evaluation of the imprint left by a leaf in a fossil was performed. Once the contour values were obtained, the image was digitally inverted resulting in the reconstruction of the geometric profile of the leaf (see Fig. 5.20.).
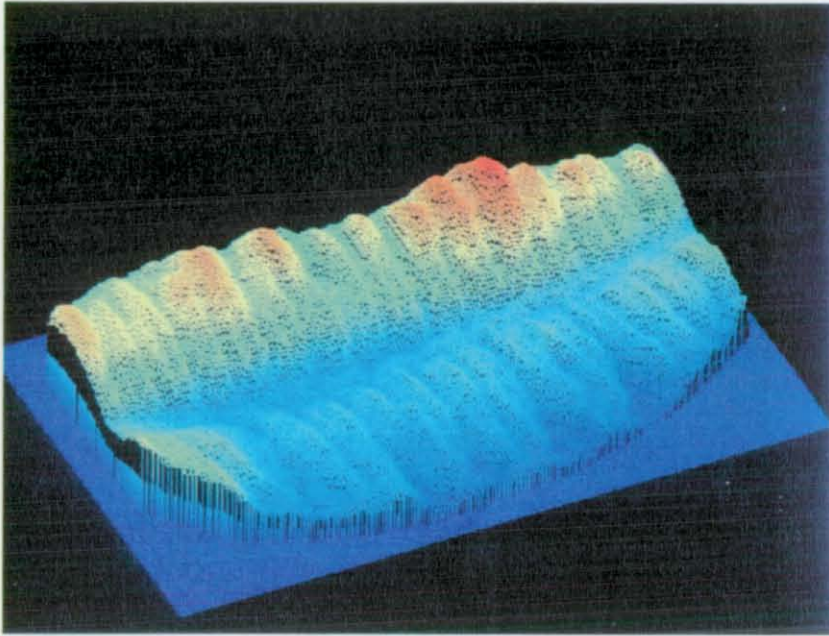


*Figure 5.20. The inverted image of a fossil with the imprint of a leaf.*

### 5.3.3.3. Concluding remarks

In this section, the design and the application of a fringe projection unit based on a Michelson interferometer has been presented. The dimensions of the inspected area were limited by the size of the collimating lens, which had a diameter of 8 cm. Since the arms of the interferometer were short, and the interferograms were recorded at a video frame time, external vibrations had negligible effects on the fringe quality. No room darkening was necessary, and the system calibration was not critical.

The principal steps of the interferogram processing, which led to the quantitative evaluation of the contour maps, have been described for the phase-shifting and the FFT-based demodulation algorithms. The contour data were expressed in terms of intensity values of the pixels in a 8-bit (256 grey levels) digital image. The application of the contour technique to different types of surfaces has been demonstrated for wooden, metallic, and stone objects.

## 5.3.4. Dual fibre fringe projection

The fringe projection system proposed here is based on an optical fibre version of the well-known Young's interferometer. Interference fringes are formed with the coherent light of two single-mode fibres, which replace the pair of pin-holes in the Young's configuration. In the classical version the power losses associated with the pin-holes are compensated by focusing the light onto their apertures. By doing so however Airy diffraction disks become visible and the regularity of the fringe pattern is altered as a consequence. These disadvantages are eliminated by the introduction of optical fibres, which allow Young's fringes to be projected with low power laser sources.

In the optical setup (see Fig. 5.21.), the light of a 35 mW He-Ne laser has been launched into the input fibre of a single mode coupler (Newport mod. F-506A) which equally divided the light between the two output fibres. After a careful alignment of polarisation, the output fibre ends have been positioned at a distance $a$ of approximately 1 mm. The fringe spacing $d$ on a screen normal to the propagation direction and at a distance $z$ from the fibre ends can be evaluated with Eqt. (5.8) where the angle $\Delta\vartheta$ is given by $a/z$. In order to have a set of parallel fringes, the fibre ends have been placed at the focal point of a collimating lens (focal length $f$=1000 mm, diameter $D$=800 mm). Therefore, the fringe spacing $d$ becomes independent on the distance from the point sources, and it is given by

$$d = \frac{\lambda f}{a} \qquad (5.9)$$

where $\lambda$ indicates the laser wavelength. In practice, the fringe spacing can readily be changed by adjusting the distance between the fibre ends. External disturbances such as temperature gradients cause local variations of the optical path inside the fibres. Consequently, the relative phase shifts between the two point sources affect the stability of the fringe pattern. If the contour information is extracted with algorithms operating on a single image and if the disturbances have low temporal frequency with respect to the image acquisition time, these phase shifts have negligible effects on the measurements.

During the experiments, the contour images have been acquired with a PC-based system, and then transferred to a SUN Sparc 10 workstation for processing with bidimensional Fourier Transform routines. In particular, the program carrier.c (see

Appendix A.1.4) has been applied to evaluate the phase distribution. Further scaling allowed a metric representation of the contour maps.
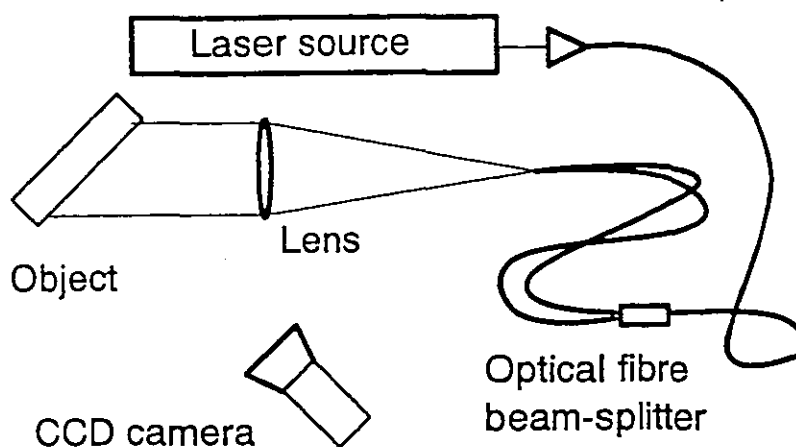


*Figure 5.21. Experimental setup used for dual fibre fringe projection.*

### 5.3.4.1. Results and discussion

Initially, the 3D-profile of a steel specimen with a step-like surface has been evaluated. An area containing a 300 μm step has been illuminated with a set of parallel fringes, projected from the right, and forming an angle $\vartheta = 45°$ with the normal to the object surface. In the resulting image (see Fig. 5.22.), the vertical fringes are interrupted in correspondence to the horizontal step. The result of processing is presented in Fig. 5.23.a in the form of a 3D-mesh plot. From the section profiles (Fig. 5.23.b) it can be inferred that a precision better than 50 μm can be guaranteed with the present configuration. However, the Fourier filtering performed during the processing of the fringe pattern has reduced the spatial bandwidth of the phase map and for this reason the sharp step profile could not be accurately reconstructed.

The case of non vertical fringes is now discussed. If $\psi$ is the angle between the projected fringes and the vertical direction, the Fourier terms containing the contour information will be rotated by the same angle $\psi$ from the horizontal frequency axis. A phase map can readily be calculated by translating one of these terms to the origin and applying the demodulation algorithm. Attention should be drawn to the sensitivity reduction which incurs with tilted fringes.
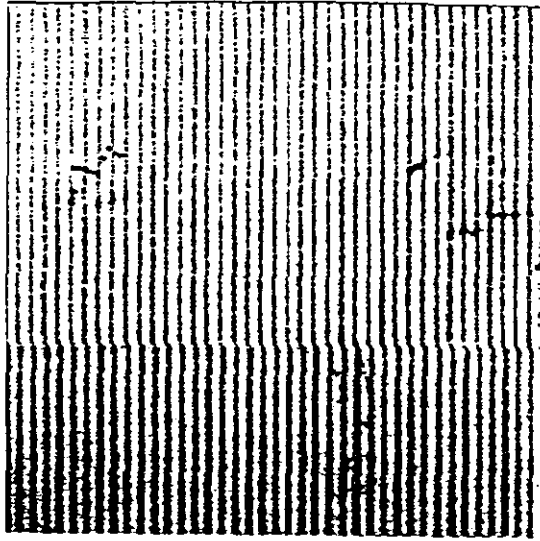
*Figure 5.22. Fringe pattern projected onto a test specimen with a horizontal step of 300 μm. The area depicted is 40 x 40 mm.*
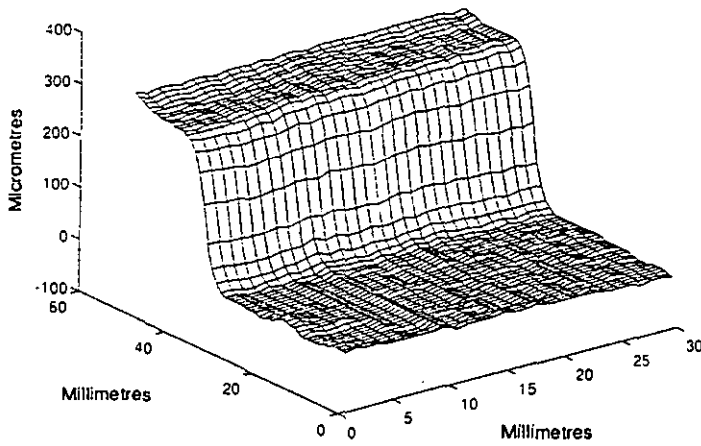


*a)*
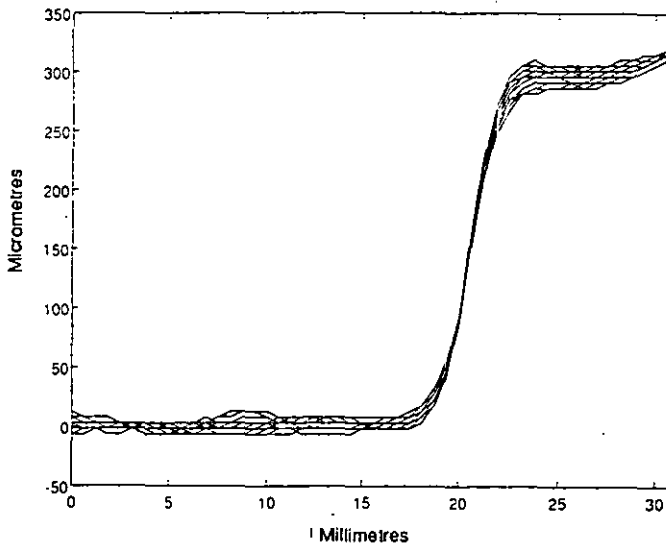


*b)*

*Figure 5.23. a) 3D-mesh plot of a 300 μm step. b) Profiles of the lateral section.*

Consider the position of two lines representing the fringe maxima on a step-like surface for vertical and tilted fringes, respectively. If the step is horizontal, the lines are split into two segments as depicted in Fig. 5.24. The distance between these segments is proportional to the measurement sensitivity according to the definition given in Sec. 5.3.1. Since the distance $AP'_{\psi}$ for the tilted fringes is given by $AP'_{\psi} = AP'\cos\psi$, the sensitivity is reduced by a factor $\cos\psi$. Therefore the sensitivity remains constant only for small tilt angles ($\cos\psi \approx 1$). These concepts have been applied to measure the profile of a wooden object containing a round hollow with a maximum depth of 1.5 mm.
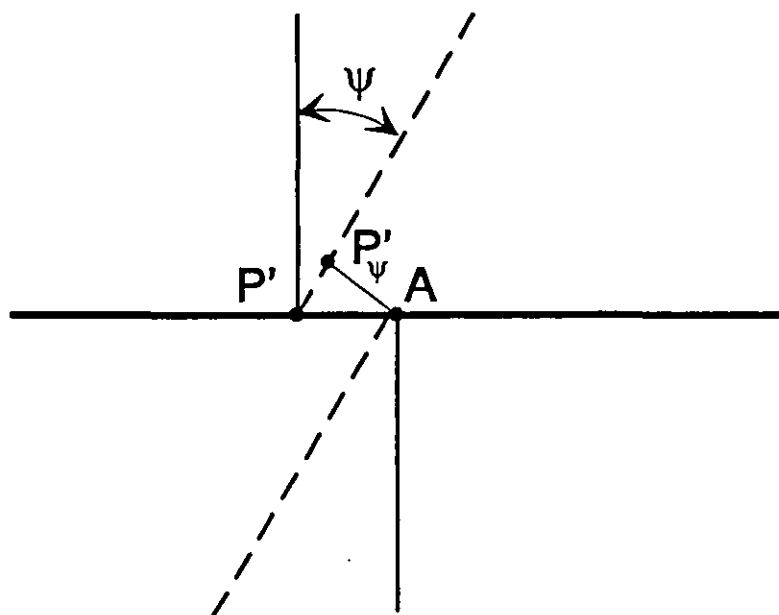
Figure 5.24. Position of equiphase fringe points on a surface with a horizontal step in case of no fringe tilt (solid line) and with a fringe tilt $\psi$ (dotted line).

The images of a 50 x 50 mm area, illuminated with vertical ($\psi = 0°$) and tilted fringes ($\psi = 45°$), are depicted in Fig. 5.25. By application of the Fourier-based algorithm, two phase maps have been obtained differing by a scale factor equal to $\cos\psi$, as expected. The diagrams corresponding to a section profile of the phase evaluated and a pseudo-colour contour map of the object surface are presented in Fig. 5.26.

176
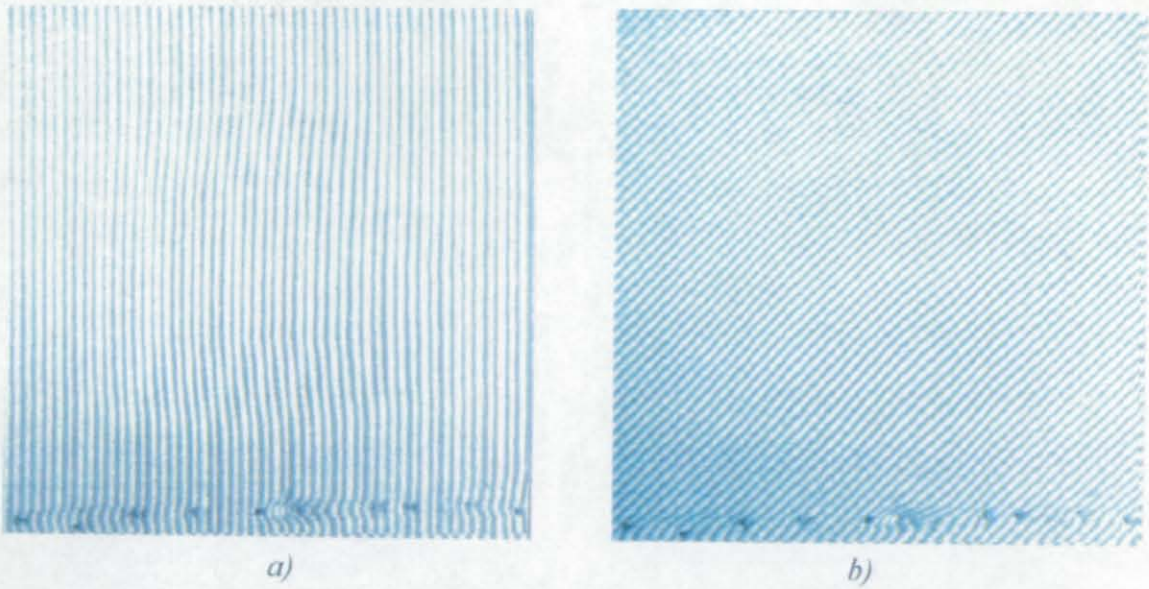
*Figure 5.25. Vertical a) and tilted b) fringes projected onto the object surface.*
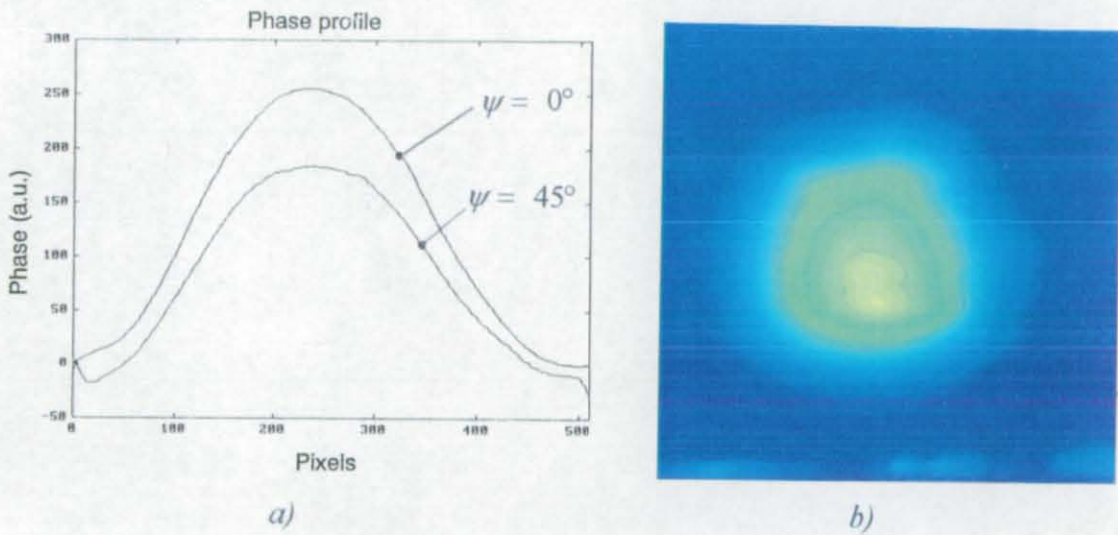


*Figure 5.26. a) Comparison of the profiles of the 250th horizontal line for $\psi = 0°$ and $\psi = 45°$. b) Pseudo-colour contour map of the surface.*

Finally measurements have been performed on marble samples in correspondence to surface regions altered by corrosion and erosion. The fringe pattern in Fig. 5.27. refers to a polished marble surface with a small hollow caused artificially by the action of a dilute solution of sulphuric acid. The material, being semitransparent to visible light, exhibited multiple-scattering phenomena which ultimately affected the fringe contrast. The contour map of the inspected area is presented as a 3D-mesh plot in Fig. 5.28.
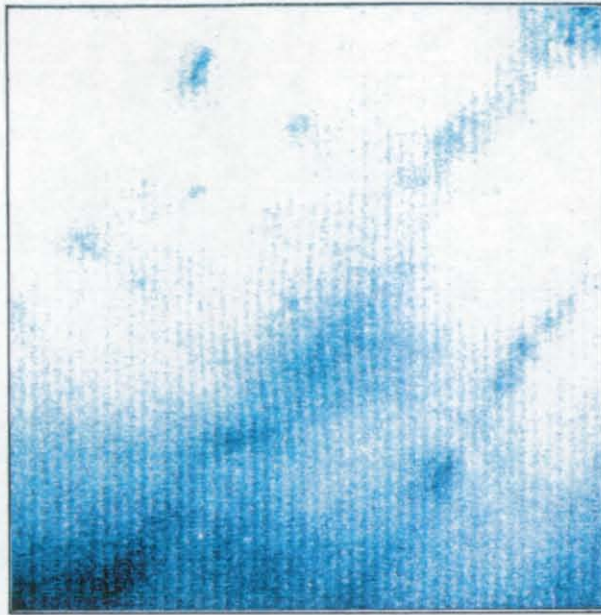
*Figure 5.27. Fringes projected onto a 50 × 50 mm area of a marble specimen corroded in the centre.*
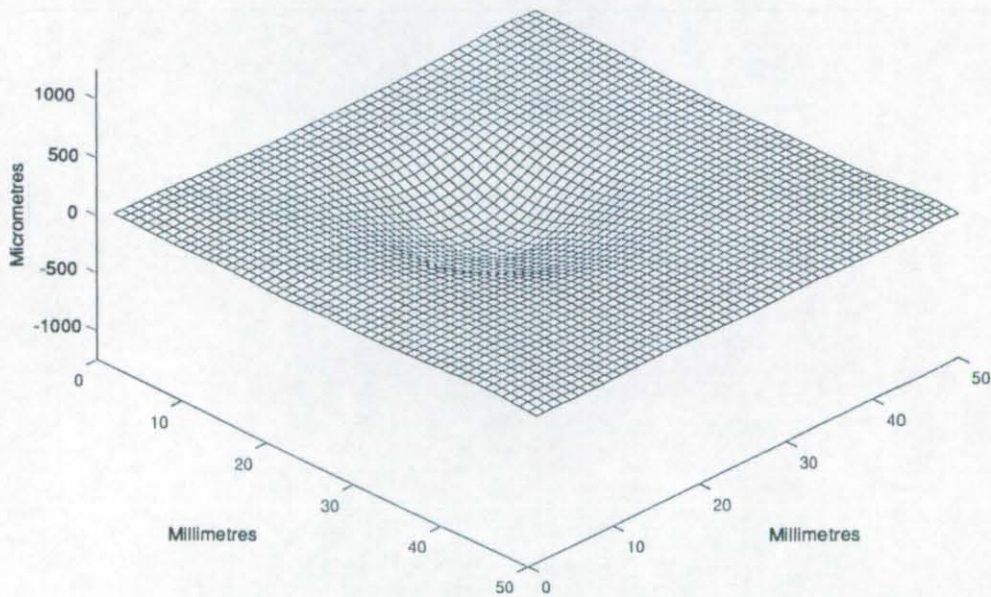


*Figure 5.28. Mesh plot of a defect caused by corrosion of a marble surface.*

The piece of naturally eroded marble, which has already been described in Sec. 5.3.2.1. (Fig. 5.11.), has been re-examined with the dual fibre contouring system. The contour fringes are depicted in Fig. 5.29. for a 40 x 40 mm area of the weathered surface. The smooth aspect of the contour image (Fig. 5.30.) is caused by frequency filtering.

178

*Figure 5.29. Contour fringes on a marble surface eroded by 200 years exposure to natural weathering on the Duomo of Milan.*
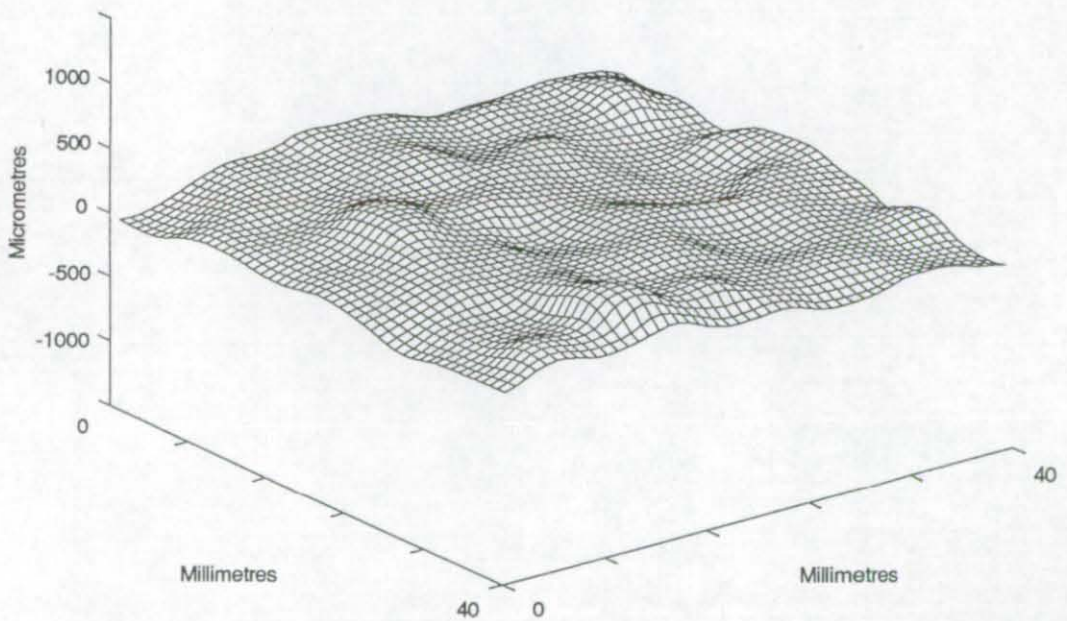


*Figure 5.30. Mesh plot of the eroded marble surface.*

## 5.3.4.2. Concluding remarks

A fringe projection system based on a dual fibre version of the Young's interferometer has been developed and tested. A small number of optical elements has been used in the optical setup which consisted of a laser source, a single mode fibre coupler, a collimating lens, and a videocamera. The effects of phase fluctuations due to external factors such as temperature gradients and mechanical vibrations have been minimised by extracting the phase information from a single interferogram. To this end the fringe processing has been performed with algorithms operating in the Fourier plane.

Despite the need of high performance computers, 2D-FFT routines offered a better data interpolation with respect to the monodimensional case considered in Sec. 5.3.3.1. Moreover, the constraint of accurate fringe orientation has been eliminated by 2D translation of the Fourier contour terms to the centre of in the frequency plane. The relation between the measurement sensitivity and the tilt angle of the projected fringes has also been derived and discussed.

The experimental results on marble samples have shown that the processing method is suited to deal with low-contrast fringes. However, sharp discontinuities of the surface profile (e.g. steps, cracked areas) cannot be reconstructed in detail since high spatial frequencies are cut off by Fourier low pass filtering. In the future this problem could be solved by extracting the interference phase with phase-shifting algorithms. To do this, the experimental setup has to be equipped with a phase control system which should be able both to control the fluctuations caused by external disturbances and the phase stepping.

## 5.4. Conclusions

The optical contouring methods investigated in detail in this chapter are non-intrusive, contactless, and measure the 3D profile of an object area without point-by-point scanning. In practice, contour data are retrieved by manipulation of an interferometric fringe pattern superimposed on the object image. This has been possible since fringe analysis methods allowed an accurate evaluation of the phase term in sinusoidal fringe patterns.

The holographic generation of depth contour fringes offers, in principle, the advantage of high resolution measurements and the possibility to choose the depth accuracy by adjusting some parameters of the optical setup. Alternatively, holography has also been used to contour objects by simulating the projection of parallel fringes. Despite the lower resolution of the second set of measurements, the optical layout has been simplified and is less critical to align than in the first case. However, the high sensitivity to external noise sources confines the holographic measurements to specialised laboratories where the experiments are performed on anti-vibration tables.

With the projection of interferometric fringes a depth resolution better than 50 μm has been obtained with contour systems developed in-house. The calibration of the measuring apparatus was rather simple since the projected fringes were parallel. In this case however the size of the inspected area is limited by the dimensions of the collimating element (lens or mirror). In other instruments, e.g. moiré projectors, where a spherical projection geometry is adopted in order to illuminate a larger area, the relative orientation of the elements in the measurement layout has to be precisely determined to compensate via software for the dependence of the fringe spacing on the distance from the light source [20].

Two projection systems have been proposed on the basis of the Michelson and Young interferometers, respectively. Of particular interest is the dual fibre projection system, where an enhanced flexibility and a significant reduction of the number of optical elements have been obtained by the use of optical fibres. Although fringe formation was based on optical interference, the effects of external disturbances on the results were negligible in comparison to those affecting holographic arrangements. The compactness of the optical setup makes them suited to out-of-lab operation, as the projection units can readily be mounted on a portable optical board with no need for special anti-vibration arrangements. Another advantage is that the measurements can be performed in ambient light, since no darkening is strictly necessary to record the fringe pattern.

181

Contour measurements have been performed on objects of different materials, e.g. metal, stone, wood. From the results the surface and volume of a defect can be eventually derived using simple integration algorithms [21]. Contour maps can be successfully employed during monitoring of decay processes acting on a variety of surfaces. Repeated measurements of the surface profile at different times can provide useful information about the speed of the deterioration mechanisms. When the object has a very complicated shape attention should be paid in order to avoid the presence of shadowing, which remains an intrinsic limit of the fringe projection technique.

Image processing played a fundamental role in the interpretation and description of the results. Many examples illustrate the algorithms and allow a comparison between the digital techniques used. FFT-based algorithms, which operate on a single interferogram, are more suited to out-of-lab operation than phase-shifting techniques. However, the smoothing of data implied by filtering operations causes a loss of details which can sometimes be significant for the contour measurement. Finally it is noted that the developed software is, in principle, applicable to the contouring methods based on white-light projection of gratings.

## 5.5. References

[1] Owen R.B., Sheets P.D., "The potential of holography and optical contouring for archaeometry", Archaeometry, (1989) 31 13 -25

[2] Kafri O., Glatt I., "The Physics of Moiré Metrology", John Wiley & Sons, Inc (1990)

[3] Taylor J.M., Wainwright I.N.M., Livingstone F.R., Rioux M., Boulanger P., "Applications of a laser scanner to the recording and replication of museum objects", in Scientific examination of works of art, ICOM Committee for Conservation (1987), 93-97

[4] Carelli P., Paoletti D., Schirripa Spagnolo G., "Multiple-source holography for artwork erosion measurements", Studies in Conservation, (1989) 35 64-68

[5] Paoletti D., Schirripa Spagnolo G., "Automated digital speckle pattern interferometry contouring in artwork surface inspection", Optical Engineering, (1993) 32 1348-1353

[6] Su X.Y., Von Bally G., "Optical profilometry for documentation in cultural heritage protection", in "Optics for Protection of Man and Environment against Natural and

Technological Disasters", Proceedings of the Second International Conference on Optics Within Life Science (OWLS II) Münster (Germany) 4-9 October 1992, (ed. Von Bally G., Bjelkhagen H.I.), (1993) Elsevier 159-163

[7] Tsuruta T., Shiotake N., "Holographic generation of contour map of diffusely reflecting surface by using immersion method", Japanese Journal of Applied Physics, (1967), **6** 661-662

[8] Haines K.A., Hildebrand B.P., "Contour generation by wavefront reconstruction", Physics Letters, (1965) **19** 10-11

[9] Friesem A.A., Levy U., Silberger Y., "Real-time holographic contour mapping with dye lasers", The Engineering Uses of Coherent Optics, (1976) 353-373

[10] Yonemura M., "Wavelength-change characteristics of semiconductor lasers and their application to holographic contouring", Optics Letters, (1985) **10** 1-3

[11] Zelenka J.S., Varner J.R., "A new method for generating depth contours holographically", Applied Optics, (1968) **7** 2107-2110

[12] Zelenka J.S., Varner J.R., "Multiple-index holographic contouring", Applied Optics, (1969) **8** 1431-1434

[13] Weast R.C., Astle M.J., Eds., "CRC Handbook of Chemistry and Physics", CRC Press, Boca Raton, 1982-1983, E386-387

[14] Hariharan P., Oreb B.F., "Two-index holographic contouring: Application of digital techniques", Optics Communications, (1984), **51** 142-144

[15] Cheng Y.Y., Wyant J.C., "Two-wavelength phase shifting interferometry", Applied Optics, (1984), **23** 4539-4543

[16] Rowe R.E., Welford W.T., "Surface topography of non-optical surfaces by projected interference fringes", Nature, (1967), **216** 786-787

[17] Vest C.M., "Holographic interferometry", John Wiley & Sons, (1979)

[18] Hildebrand B.P., Haines K.A., "Multiple-wavelegnth and multiple-source holography applied to contour generation", Journal of the Optical Society of America, (1967), **57** 155-162

[19] P.Zanetta, D.Albrecht, M.Facchini, C.Gianikas, "A Fringe Projection System for Contour Evaluation", Technical Note No.I.93.11 ISEI/IE/2400/93 Commission of the European Communities Joint Research Centre Ispra Site, February 1993

[20] Gåsvik K.J., Hovde T., Vadseth T., "Moirè technique in 3-D machine vision", Optics and Lasers in Engineering, (1989) 10 241

[21] Koukash M., Hobson C.A., Lalor M.J., Atkinson J.T., "Detection and measurement of surface defects by automatic fringe analysis", Optics and Lasers In Engineering, (1986/7) 7 125-135

# Chapter 6

# Local correlation of laser speckle

## 6.1. Introduction

Optical correlation measurements have normally been performed by holographic and speckle techniques. In diagnostic applications, holographic correlation has been used to evaluate fatigue damage [1], surface displacement [2], and to perform a quality control test [3]. Interesting results have been reported by Hinsch and co-workers [4], who successfully monitored the effects of humidity variations on stone surfaces. However, with holography the correlation signal refers to the whole illuminated surface, therefore it is not possible to distinguish the parts of a surface which contribute more than others to the measured change. Moreover the high mechanical stability required to perform the experiments is a heavy constraint.

In speckle correlation measurements the main results have been obtained in surface roughness studies [5], and particle sizing [6]. The fringe contrast produced by illumination of two superimposed speckle patterns has normally been used to estimate the existing amount of correlation. Only recently, digital methods for image processing have unfolded new perspectives in the analysis of correlation phenomena. In particular the work by Chu et al. [7] is an interesting example of local correlation between small areas of two speckle images in deformation analysis. Despite the fact that correlation measurements are well assessed for evaluating many physical properties, speckle correlation has been studied mostly for its negative effects on the interferometric quality of fringes in speckle photography and electronic speckle pattern interferometry (ESPI) [8]. The main problem is that a correlation loss between two recorded speckle images results in an appreciable reduction of the fringe contrast.

Speckles are generated by the optical interference of the wavelets scattered from the surface points regarded as spherical sources of coherent light. In an imaging system a close correspondence exists between the surface structure and the image speckles. Any local change of the surface profile induces a modification in the corresponding part of the speckle image. The principle of local correlation of laser speckle consists of the evaluation of a local parameter which estimates the correlation of the speckles after any modification of a surface element. This method can be used to characterise any physical or chemical mechanism which involves a surface alteration of the same order as the laser wavelength.

186

In the next section the basic concepts of local correlation are introduced together with a presentation of the principal sources of speckle decorrelation. A local correlation coefficient is defined and its relation with the subtraction of two speckle patterns is derived. The effects of speckle under sampling are also considered. The application of the method to the study of the deterioration mechanisms related to the formation of salt efflorescence on stone surfaces is described in Sec. 6.3. Aspects regarding the rate at which efflorescence occurs and the influence of geometrical discontinuities or structural defects are investigated. The measurements were performed in collaboration with the "Gino Bozza Centre" CNR (Consiglio Nazionale delle Ricerche), Milan (Italy). A collection of experimental results, from the detection of surface defects to vibration analysis, are presented and discussed in Sec. 6.4. in order to illustrate some of the potential applications of the local correlation method to other fields.

## 6.2. Theory

When the image of an object is focused onto the image plane of a coherent optical system, a local correspondence exists between the points of the illuminated surface and the speckles in the image plane. In particular, the intensity of a point in the speckle pattern is made of contributions from an area $A_0$ in the object plane (see Sec. 2.3). Consequentely, any surface alteration in $A_0$ accounts for a change of the speckle intensity. By using Eqt. (2.7) the dimensions of $A_0$ are readily evaluated. If, for example, the object is at a distance $z_0=50$ cm from the camera, the illuminating wavelength is $\lambda = 633$ nm, and the viewing aperture is a=1.5 cm, the diameter of the area $A_0$ is $D_0 \approx 50$ $\mu$m.

In an imaging system, speckle decorrelation can be attributed to a variety of factors which modify the light scattered by a surface element $A_0$. For perfectly conductive surfaces, previous studies (see for example [9]) have derived the relations existing between decorrelation and surface displacements. In particular, for an object, whose surface is perpendicular to the optical axis, it has been demonstrated that speckle decorrelation is much more sensitive to in-plane displacement and tilt, than to out-of-plane displacement.

As described by Ennos in [10], decorrelation can take place as a consequence of microscopic surface alterations caused by oxidation, corrosion, water condensation, etc. Moreover, if the object surface is not totally reflecting, (e.g. stone materials, paper), speckles are also produced by multiple scattering inside the volume. In this case the

analysis of decorrelation effects due to surface displacements becomes very complicated. Other sources of speckle decorrelation are laser wavelength shifts and polarisation changes of the illuminating light.

In the following paragraphs, the comparison of two speckle patterns is made on the basis of the correlation of their intensities, which can be regarded as two statistical variables. If $I_1$ and $I_2$ are the intensity values for a generic point at two different times $t_1$ and $t_2$, and $\langle I \rangle$ is the mean value of light intensity, then the correlation coefficient $\rho$ between $I_1$ and $I_2$ is expressed by:

$$\rho = \frac{\langle (I_1 - \langle I \rangle)(I_2 - \langle I \rangle) \rangle}{\sigma_I^2} \qquad (6.1)$$

where $\sigma_I$ is the intensity standard deviation, and the angular brackets denote an averaging operation. The average should be evaluated over many images for each point. Alternatively, if correlation is assumed constant for a small area of an image, the average can be spatially evaluated over a number of pixels in the close neighbourhood of a point. When the statistical distribution of the speckle intensity is a negative exponential, the standard deviation and the average value are equal, and thus Eqt. (6.1) becomes

$$\rho = \frac{\langle I_1 I_2 \rangle}{\langle I \rangle^2} - 1 \qquad (6.2)$$

If $I_1$ and $I_2$ are identical then total correlation exists between the variables. In this case $\langle I_1 I_2 \rangle = \langle I_1^2 \rangle$, and since the probability theory yields $\langle I_1^2 \rangle = \sigma_I^2 + \langle I \rangle^2 = 2\langle I \rangle^2$, the correlation coefficient is unity. On the other hand, when the two variables are independent, and consequently uncorrelated, $\langle I_1 I_2 \rangle = \langle I_1 \rangle \langle I_2 \rangle = \langle I \rangle^2$ and $\rho = 0$, as expected.

The relation between $\rho$ and $\langle (I_1 - I_2)^2 \rangle$ is now derived. Starting from

$$\left\langle \left( I_1 - I_2 \right)^2 \right\rangle = \left\langle I_1^2 + I_2^2 - 2 I_1 I_2 \right\rangle = 4 \langle I \rangle^2 - 2 \langle I_1 I_2 \rangle$$

it is readily seen that:

$$\langle I_1 I_2 \rangle = 2 \langle I \rangle^2 - \frac{1}{2} \left\langle \left( I_1 - I_2 \right)^2 \right\rangle$$

and finally, the correlation coefficient can be expressed as

$$\rho = 1 - \frac{\left\langle \left( I_1 - I_2 \right)^2 \right\rangle}{2 \langle I \rangle^2} \tag{6.3}$$

This demonstrates that the correlation coefficient can be effectively deduced by squaring and averaging the arithmetic difference between the speckle images $I_1$ and $I_2$.

The result of Eqt. (6.3) is valid under the assumption that the probability distribution of the speckle intensity is a negative exponential. However, in many practical cases, each pixel of the video camera integrates the light intensity of several speckles over its sensitive area. In order to estimate the correlation coefficient the results by Goodman [11] for the first order statistics of integrated speckle are considered. In this case the relation between the mean value and the standard deviation of the speckle intensity is $\langle I \rangle^2 = M \sigma_I^2$, where M represents the number of speckles per pixel[1]. Accordingly, an expression similar to Eqt. (6.2), has also been obtained, i.e.

$$\rho = 1 - M \frac{\left\langle \left( I_1 - I_2 \right) \right\rangle}{2 \langle I \rangle^2}. \tag{6.4}$$

---

[1] This interpretation of M is valid only for a high number of speckles per pixel.

## 6.3. Monitoring of salt efflorescence on stone surfaces

### 6.3.1. Introduction

The occurrence of salt efflorescence is a common degradation mechanism affecting stone materials employed in historical buildings, especially for those materials exhibiting high porosity (mortars, plasters, bricks and some stones) [12]. The moisture, which wets the surface and penetrates into the volume through the pores, contains the ions of several types of salts, e.g. nitrates, sulphates, chlorides. The concentration of the dissolved salts depends on the chemical composition of stone, cleaning products, natural aerosols, pollutants, and atmospheric agents [13]. When the moisture solution saturates because of water evaporation, salt ions crystallise. As a result efflorescence appears on the surface, whilst the salt grains formed inside the volume exert high pressures on the material structure and produce micro fractures. Since the rates of evaporation and condensation are related to the humidity fluctuations of the micro climate, the stone elements are very often subjected to periodic crystallisation, which gradually destroys the material. The damage associated with this mechanism can assume a variety of forms such as surface powdering, flaking, exfoliation, and scaling.

The localisation of salt efflorescence is usually based on the visual inspection of the surface. However, once a region is covered with salt it is impossible to identify the presence of preferential points where the phenomenon is still active. Since a close correspondence exists between the surface structure and its speckle pattern, the detection of any change in the speckle image means that the surface has been modified. The amount of surface change can be quantified when the correlation between two speckle patterns is known. Based on this principle, the surface changes caused by the formation of salt efflorescence can be analysed in detail.

When local speckle correlation is applied, the surface changes due to salt efflorescence can be monitored for the whole crystallisation period. The method offers an early detection of salt efflorescence together with a precise description of the spatial distribution of its intensity. New and interesting aspects of the efflorescence mechanism can thus be investigated and related to the results of characterisation tests using Scanning Electron Microscopy (SEM), X-ray diffraction, porosity, capillarity, etc.

Ageing tests have been carried out in the laboratory on samples of stones with different porosity. The formation of efflorescence on the samples has been artificially induced by capillary absorption and subsequent drying in room conditions. An automatic system for image acquisition and processing has been developed and employed to monitor the

evaporation stage of each ageing cycle. The influence of geometrical discontinuities and defects on the efflorescence mechanism has also been investigated.

## 6.3.2. Materials and specimens

Two kinds of stones were considered for the experiments: the *Biocalcarenite di Noto* (Sicily-Italy) and the *Pietra di Angera* (Lombardy-Italy). The biocalcarenite of Noto is a sedimentary carbonatic rock characterised by very high values of total porosity[2] ($P = 30 - 40\%$). This rock is characterised by the presence of cylindrical structures, called "tubuli", having an elliptical section with a diameter of $0.5 - 2$ cm. Micro analytical studies [14] have shown that the tubuli have the same composition and porosity of the bulk stone. It was also found that the faces of the tubuli consist of a compact layer (0.1-0.4 mm thick) of microfossil shells and calcite crystals. The typical decay of this rock is "alveolation", which manifests itself by formation of cavities of various shape and size (see Fig. 6.1.). The biocalcarenite of Noto has widely been used in buildings, where in some cases the deterioration effects caused by alveolation are particularly evident (see for example Fig. 6.2.).
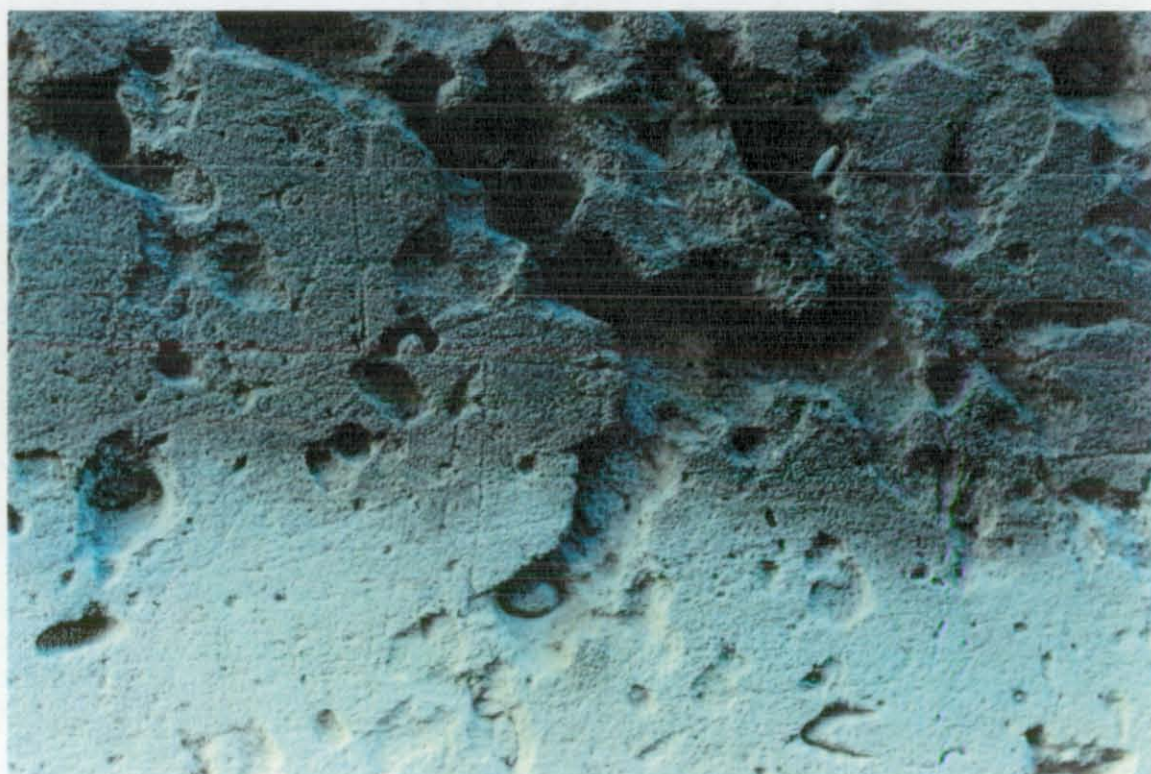


*Figure 6.1. Cavities caused by alveolation in the Noto stone.*

---

[2]Total porosity is defined as the percentage of pore volume relative to the total volume of rock.

*Figure 6.2. Effects caused by alveolation decay on a pillar.*

The Angera stone is a sedimentary dolomitic rock with three distinctive forms differing in colour: white, yellow, and pink corresponding to the presence of iron in different mineralogical phases [15]. The porosity values for this stone are in the range from 15-25 %. Monuments and churches in Lombardy have employed the Angera stone for building and decorative purposes. In Milan there are several examples such as the Churches of S.Fedele and S.Raffaele, the Cortile Richiniano of the Ca' Granda, and the Certosa.
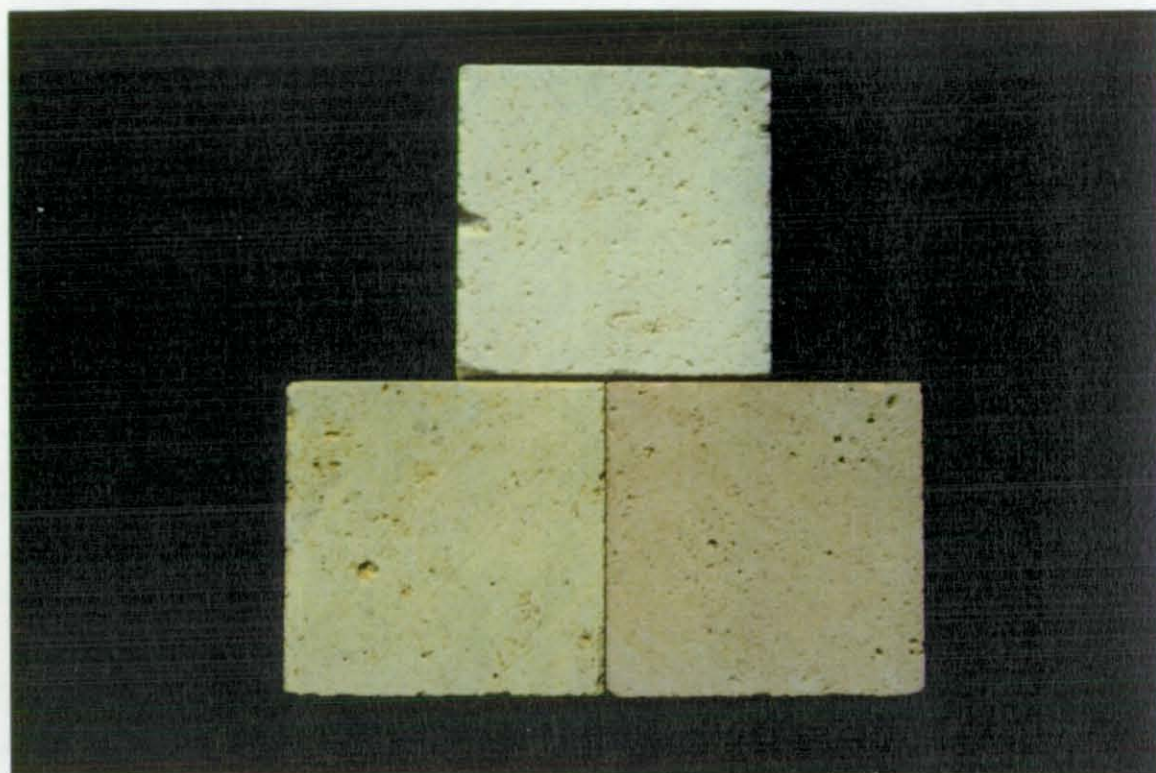
Figure 6.3. Specimens of the three forms (white, yellow, and pink) of the Angera stone.



Figure 6.4. Salt efflorescence on a building element made of Angera stone at the "Cortile Richiniano della Ca' Granda" in Milan.

193

The stone sample dimensions were 5 x 5 cm with thickness of 2 cm or 5 cm. The formation of salt efflorescence was artificially induced according to the following procedure.

1. Specimen washing with distilled water.

2. Drying at 60° C for 24 hours.

3. Capillary absorption on filter paper soaked with a 5% water solution of decahydrate sodium sulphate ($Na_2SO_4 \cdot 10H_2O$) for two hours or less depending on the thickness of the specimen.

4. Evaporation at room conditions.

Speckle correlation measurements were performed during the evaporation stage (4) of the ageing cycle.

### 6.3.3. Experimental setup

During evaporation, the specimen surface, which had been in contact with the wet filter paper, was illuminated by the expanded beam of a continuous wave laser. A He-Ne source of 10 mW minimum power at $\lambda = 633$ nm was used for the experiments. In order to have a uniform illumination of the stone surface, the laser beam, after being focused by a microscope objective, was filtered with a pin hole and in some cases was collimated by a lens (see Fig. 6.5.a). A CCD video camera (e.g. Sony B/N XC77CE 768 × 512 pixels) was used to acquire the speckle images of the surface.

Since, during the occurrence of salt efflorescence, speckle decorrelation was related to micro structural variations of the surface it was expected that the illumination angle had negligible effects on the correlation measurements. This fact was confirmed by the experimental tests. A slight difficulty was, however, caused by the appearance of shadowed areas in the speckle image. This was mainly the case when the specimen surface was not flat or when the laser beam formed a large angle with the normal direction to the surface. The introduction of a beam-splitter between the object and the video camera provided an excellent solution to this problem (see Fig. 6.5.b). In fact, the illumination could now be aligned with the viewing direction avoiding any shadow in the speckle image.
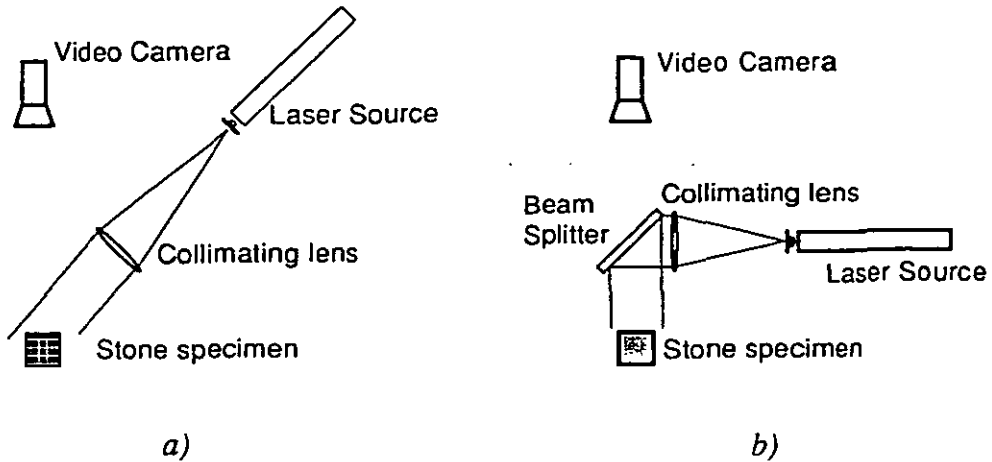
*Figure 6.5. Optical setups used for the acquisition of speckle images. a) simple version for flat stone surfaces. b) version using a beam-splitter to reduce shadowing effects.*

The signal from the video camera was digitised by a frame grabber card which was installed in a personal computer. Initial experiments were performed using the Image Technology FG 100 frame grabber, which is equipped with an arithmetic unit for real-time processing. The host computer was a Compaq Deskpro 386/20e. At first, an image of the speckle pattern was acquired and stored in the grabber memory. Subsequently, the speckle images from the video camera were subtracted from the reference pattern. The absolute value of the difference was displayed on a video monitor in real-time. According to Eqt. (6.3), where the structure of the surface had changed, bright areas became visible. It was also possible either to record the whole process with a video recorder or to stop the acquisition and store the difference image in digital form.

A second setup for the automatic monitoring of the efflorescence mechanism over many hours was arranged. The specimen was placed on an analytical balance (Sartorius Research R 200 D), so that the change in weight due to the loss of water could also be measured during the evaporation process. The balance operated with a precision of 0.1 mg and the weight data were sent to the serial port of a PC Olivetti M380 by means of an RS-232 interface. A correlation image was obtained by digital subtraction of two speckle patterns recorded at $t_0$ and $t_0+20$ seconds. In this case a frame grabber with no real-time arithmetic capabilities was sufficient to acquire the images and perform the necessary processing. As the Olivetti M380 was already equipped with a frame grabber (Image Technology Inc. Vision Plus AT 1024 x 512 pixels at 8 bits resolution) a C-program was developed to control the acquisition of both the weight data and the speckle images (see Appendix A.1.6.).

195

## 6.3.4. Results and discussion

Firstly, the correlation results obtained for a specimen (5 x 5 x 2 cm) of the Noto stone are presented and related to the alterations of the surface state during the evaporation stage of the ageing cycle (see Fig. 6.6.). Immediately following the absorption process, the specimen was still wet and the micro movements of the water film caused a rapid and intense decorrelation of the speckles. This became clear by watching the real-time subtraction images, which appeared like speckle patterns continuously modifying their shape (Fig. 6.6.a). The sporadic occurrence of sudden bursts of bright circular spots was also detected by real time observation. These spots, probably due to micro turbulence of the water film, originated from a single point and developed into circles (1-10 mm diameter) in less than a second.

After approximately two hours surface changes occurred which were attributed to salt formation. It is interesting to note that during this initial phase the maximum salt activity was located at the edge of the sample (Fig. 6.6.b), and the salt crystals were not yet visible on the surface. The salt formation proceeded towards the centre in a concentric way (Fig. 6.6.c). As the front of the salt development approached the centre, the process recommenced from the edge of the sample (Fig. 6.6.d). This observation highlights the importance of the local speckle correlation method, because after 13 hours the stone surface was completely covered with salt and it was impossible to detect the new crystallisation front by a visual inspection. The salt formation stopped after 24 hours.

For the Angera stone the phenomenon started from the edge as for the Noto stone, but it developed in a very different way. Subsequent areas of crystallisation were randomly distributed across the surface (Fig. 6.7.). This could be caused by the non homogeneous structure of the surface resulting in preferential areas for water evaporation.

Cubic stone specimens of 5 cm side were also examined. The major difference with the 5 x 5 x 2 cm specimens consisted of a prolonged duration of the efflorescence mechanism (typically 48 hours for the Noto stone). This can be explained by observing that for, relatively thin specimens, the amount of salt solution absorbed is proportional to the specimen volume.

196
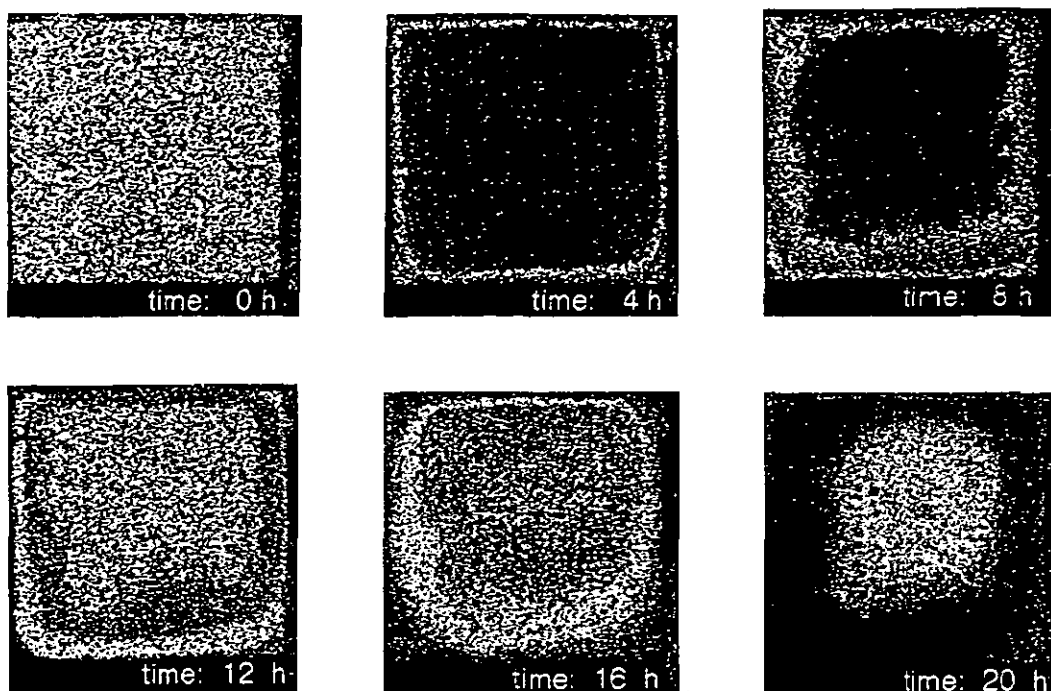
*Figure 6.6. Correlation images for the Noto stone during the evaporation stage of the ageing cycle. The time labels indicate the hours elapsed from the beginning of the evaporation stage.*
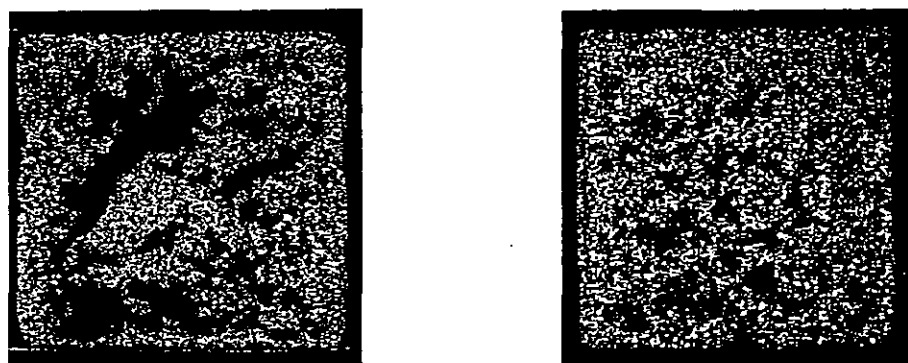


*Figure 6.7. Correlation images for specimens of the Angera stone.*

In order to concentrate the evaporation on the illuminated region, the lateral surface of the specimen was wrapped with a paraffin-based transparent laboratory film (PARAFILM "M"). The resulting effect was experimentally investigated by making a simple comparison between two 5 x 5 x 5 cm specimens, one of which was wrapped with the laboratory film. After 48 hours, as expected, the formation of salt efflorescence on the specimen with no film was almost terminated, whilst on the other specimen it was still very active. This is demonstrated in Fig. 6.8., where the correlation images

obtained for the two specimens are presented. It should be noted that the time intervals between the subtracted speckle patterns are 1 second and 60 seconds for the specimens with and without laboratory film, respectively.



a)          b)
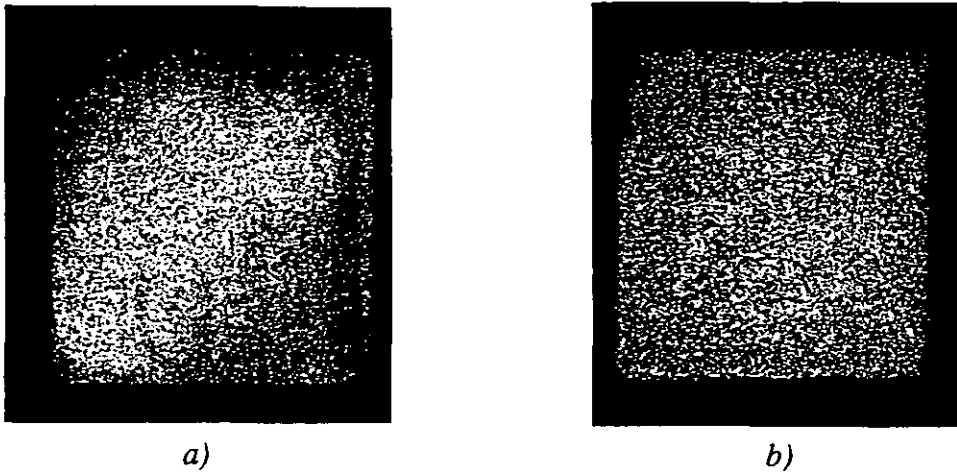
*Figure 6.8. Correlation images for a Noto specimen (5 × 5 × 5 cm) after 48 hours evaporation a) with (Δt = 1 second) and b) without laboratory film (Δt = 60 seconds).*

Although the evaporation on the lateral surface was partially blocked by the laboratory film, the efflorescence started, as before, at the edge of the specimen. Other experiments in which the lateral surface was sealed with silicone produced the same result. It was therefore clear that this *edge effect* had no relation with a possible movement of the moisture towards the regions having the largest evaporating surface area, as it was initially supposed. A more plausible hypothesis associates the *edge effect* with a greater recycle between humid and dry air in the proximity of the edge. The importance of air circulation was demonstrated by putting the specimen in a sealed glass case after absorption. Neither efflorescence or speckle decorrelation were observed on the stone surface for many days. When, however the glass case was removed, the crystallisation process started as usual.

For the biocalcarenite of Noto scientists found [14] that the alveolation process has its origin at the edge of the tubuli. The specimens after several ageing cycles showed a pronounced material loss around the tubuli, whose structure was not appreciably altered. Therefore a cubic sample (5 x 5 x 5 cm) with a tubular structure in its interior was considered. After absorption, the face including an elliptical section of the 'tubulo' was monitored with the local correlation method. During the first hours of observation, surface changes predominantly occurred along the external perimeter of the sample. Following 24 hours, the activity transferred to the central region, which contained the

'tubulo' (see Fig. 6.9.b). An elliptical line of maximum correlation was detected around it, indicating that at the edge of the 'tubulo' the response to salt absorption was anomalous. Twelve hours later, a line of minimum correlation was visible around the 'tubulo' suggesting that the local discontinuity in the material caused a delay in the efflorescence mechanism (see Fig. 6.9.c).



a)                    b)
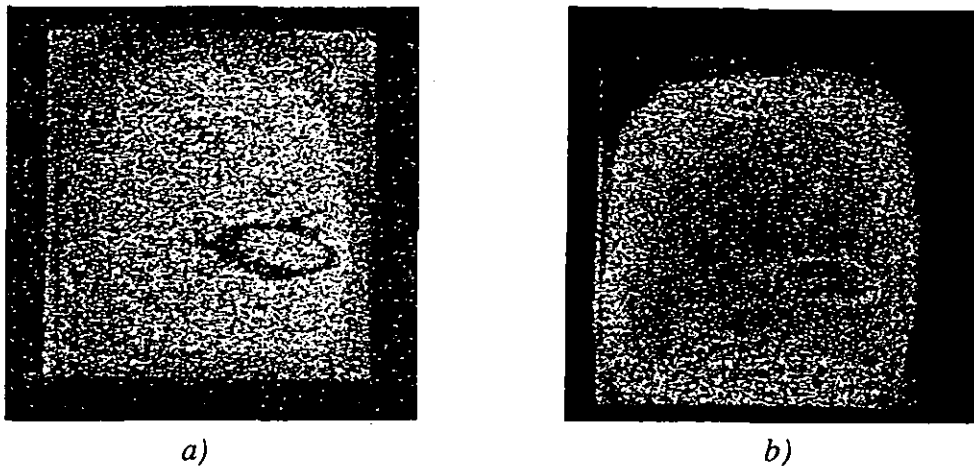
Figure 6.9. Effects of the presence of a tubulo on the efflorescence mechanism for a stone specimen of the Biocalcarenite di Noto. Correlation images after a) 24 hours (the efflorescence phenomenon was less active along the edge of the tubulo), and b) 36 hours (the situation was reversed).

Automatic monitoring of the efflorescence mechanism over many hours was performed by storing a subtraction image every 30 minutes. For each image the correlation parameter $\delta=(1-\rho)$ was evaluated by taking the average in Eqt. (6.3) over the entire surface. Fig. 6.10. shows the results obtained for a specimen (5 x 5 x 2 cm) of the biocalcarenite of Noto: the weight and the correlation parameter $\delta$ are plotted as functions of time. The coefficient $\delta$ is proportional to the surface changes and can be taken as an indicator of the efflorescence rate. In the first hour the high values of $\delta$ are caused by the evaporation of the relatively large amount of water present in the surface layers of the stone following absorption.

There was no direct correlation between the evaporation rate and the salt formation; a large amount of water was lost in the first hours of drying, but the salt formation seemed to have a delay. This was probably a consequence of the low concentration of the solution and of the formation of cryptoefflorescence inside the stone volume. The end of the salt formation corresponded to the end of the evaporation.
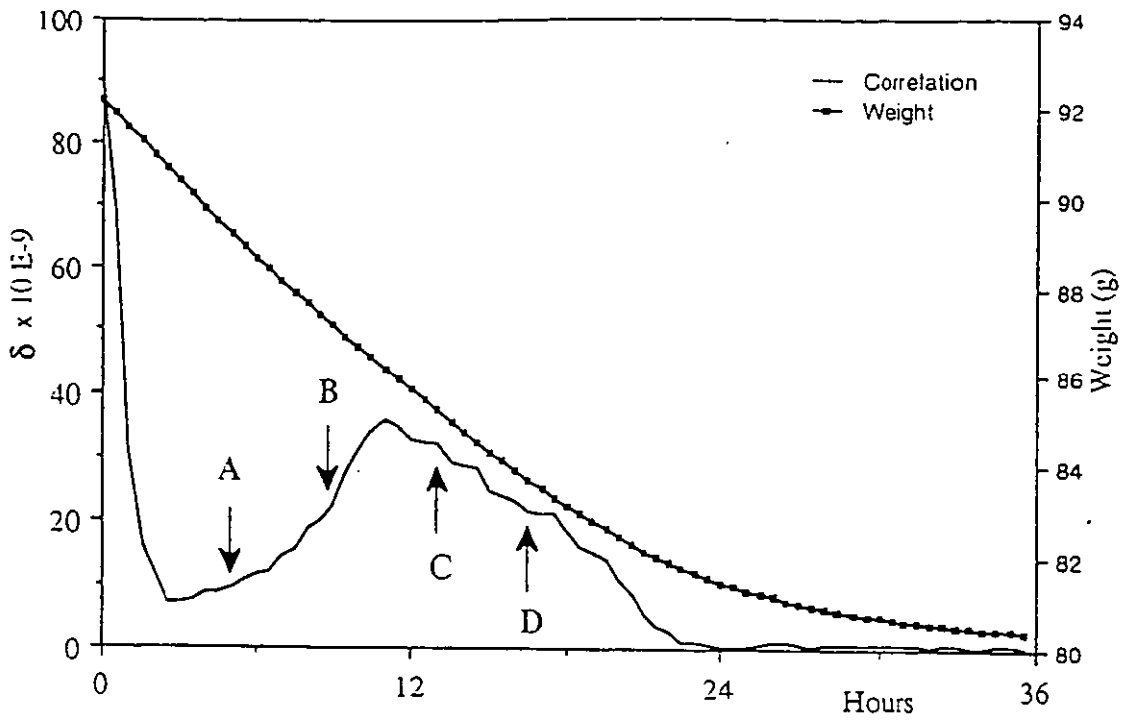
*Figure 6.10. Speckle correlation parameter* δ *and specimen weight as functions of the drying time for the Noto stone.*
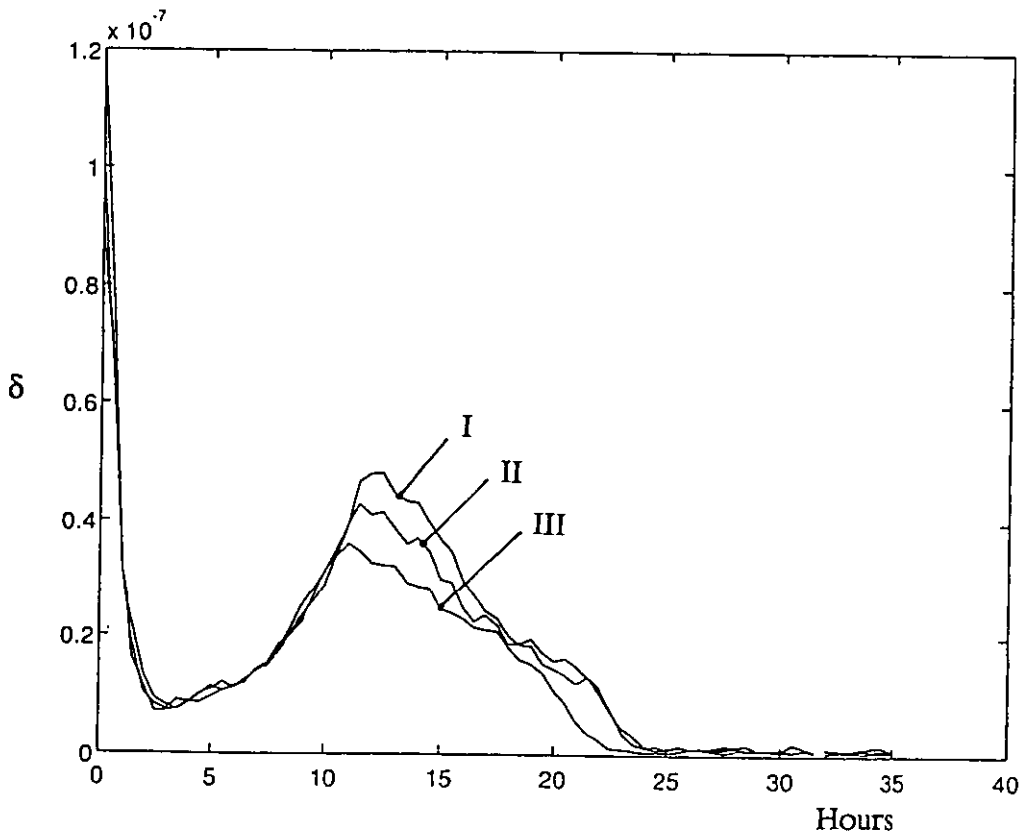


*Figure 6.11. Diagrams of* δ *for three successive cycles on a Noto specimen.*

Three diagrams of δ corresponding to ageing cycles performed in sequence on the same specimen are presented in Fig. 6.11. It is noted that the intensity of the efflorescence phenomenon gradually decreased from the first to the third cycle.

A local evaluation of the correlation parameters δ or ρ can be performed by segmenting the digital images into small subimages. The expression of Eqt. (6.3) is then calculated by arithmetic averaging or Fourier filtering [16] over the speckles contained in each subimage. Fig. 6.12. presents the result obtained by dividing the subtracion image of Fig. 6.9. in $8 \times 8$ cells and replacing all the pixels in the subimage with the corresponding value of δ. The mosaic effect in Fig. 6.12. is absent when spatial filtering is used. In this case, kernels should not exceed $9 \times 9$ pixels to prevent the occurrence of the Gibbs' phenomena [17].

Finally, in Fig. 6.13. the application of pseudo-colours to a correlation image is presented. The pink-white pixels indicate the regions where efflorescence occurred at the highest rate.
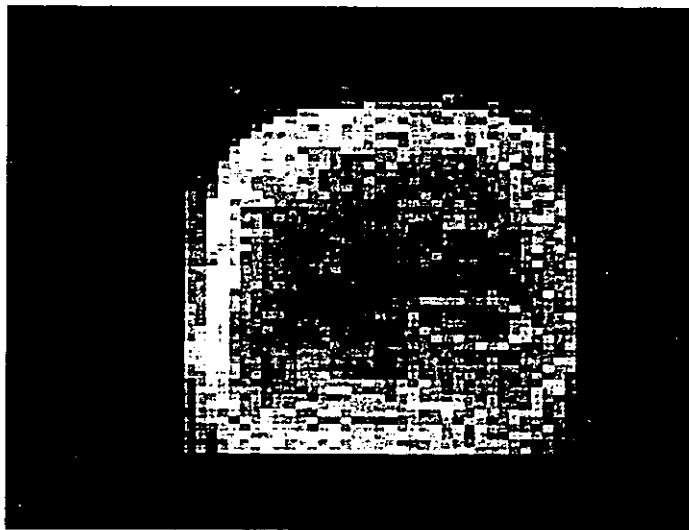


*Figure 6.12. Correlation image processed by segmentation into $8 \times 8$ cells, whose correlation parameter δ has been evaluated by local averaging.*
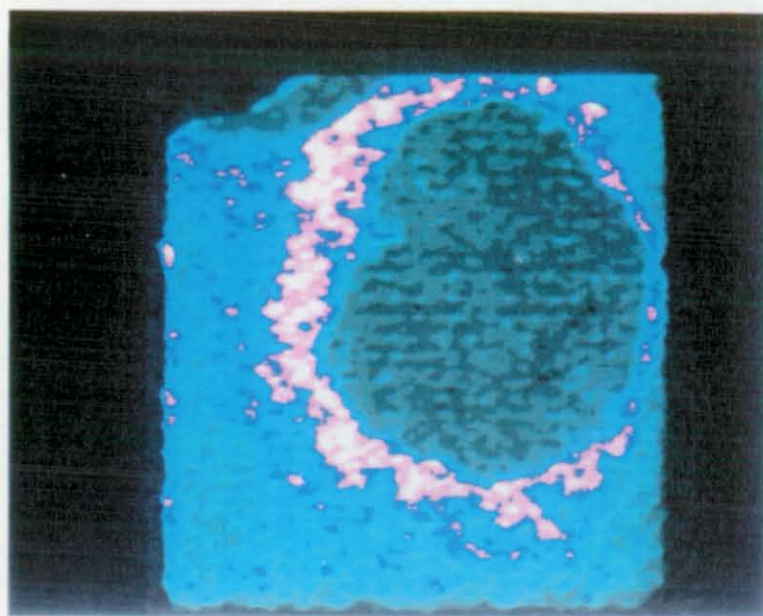
*Figure 6.13. Pseudo-colour representation of a correlation image during the formation of salt efflorescence.*

### 6.3.5. Concluding remarks

The large number of monuments and historical buildings exposed to salt weathering accounts for the great interest and the research efforts actually put into the study of the chemical and physical processes related to salt crystallisation mechanisms. In this respect, the local correlation of laser speckle is a novel method for monitoring the micro structural changes produced by the formation of salt efflorescence on the surface of stone materials.

Information can be obtained about the presence of micro fissures, defects, and other discontinuities which interfere with the water evaporation process. Thus, as well as allowing the study of the dynamics of the efflorescence phenomenon, this method provides useful information for restoration work. In the experiments local correlation has been applied to study the ageing of stone specimens by cyclic crystallisation. Surface monitoring has been performed during the evaporation stage of the cycle. The efflorescence behaviour depended on the kind of stone considered. The influence of material defects, such as the "tubuli" in the biocalcarenite of Noto, on the efflorescence formation has been successfully detected.

The interpretation of the speckle correlation results could greatly contribute to a better understanding of some decay mechanisms. However, the comparison of much more

data and the investigation of a large number of specimens is necessary. As the proposed method is much less sensitive to external vibrations or temperature gradients than other methods based on interferometry, it could be readily applied for *in-situ* measurements.

## 6.4. Other applications

### 6.4.1. Vibration studies

The method of local correlation of speckles has been applied to describe the stationary motion of a vibrating plate at its resonance frequencies. The dependence of speckle correlation on surface tilt and on in-plane translation has been studied for the static case by Owner-Petersen [8] relating to the problem of fringe visibility in ESPI interferometers. The correlation of the speckle intensity corresponding to a surface resolution element[3] $A_0$ has been evaluated theoretically by considering the superposition of the speckle patterns at the pupil of the viewing lens before and after deformation. In particular, the local correlation coefficient of the speckle intensities when the surface points are subjected to tilt is given by [8]

$$\rho = \frac{4}{\pi^2}\left\{\arccos\left(\frac{\gamma}{\Gamma}\right) - \frac{\gamma}{\Gamma}\sin\left[\arccos\left(\frac{\gamma}{\Gamma}\right)\right]\right\}^2 \qquad (6.5)$$

where $\gamma$ is the tilt angle of the resolution element $A_0$, and $\Gamma$ is the value of $\gamma$ for which the speckles are completely decorrelated. When $\gamma \geq \Gamma$ no superposition occurs at the lens aperture between the light scattered from $A_0$ before and after deformation (see Fig. 6.14.). Accordingly, if an object, placed at a distance $l$ from the aperture $D$ of the imaging lens, is viewed normally and it is illuminated at an angle $\vartheta$, then the tilt angle corresponding to the onset of complete decorrelation is

$$\Gamma = \frac{D}{l(1 + \cos\vartheta)} \qquad (6.6)$$

---

[3]For a definition of $A_0$ see Sec. 6.2.
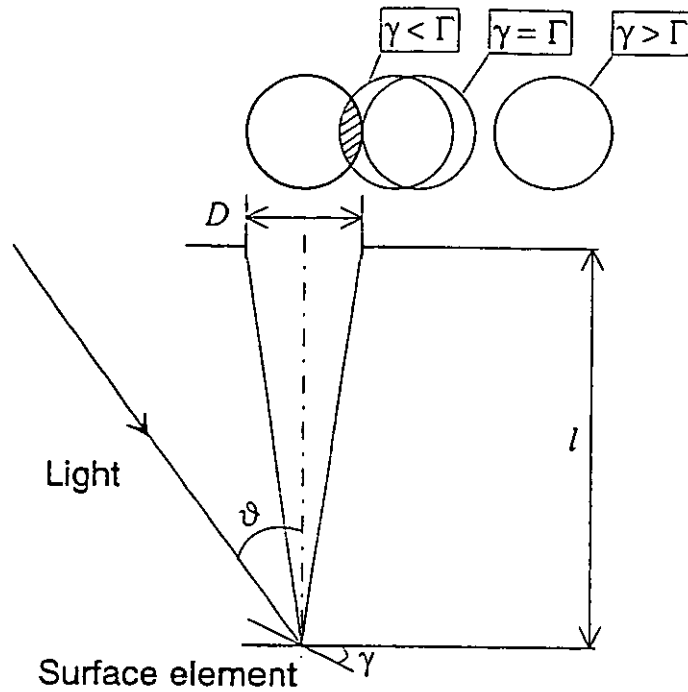
*Figure 6.14. Geometric parameters for the evaluation of the local correlation coefficient for the case of surface tilt.*

For a plate vibrating at one of its natural frequencies, it is well-known [18] that the transverse deflection function and its time-derivatives are sinusoidal functions of time. This means that, for small values of $\gamma$ ($\tan\gamma \approx \gamma$), the time dependence of the tilt angle can be expressed by $\gamma(t) = A\cos(\omega t)$, where $\omega/2\pi$ and $A$ indicate the vibration frequency and the maximum tilt angle of the vibrating element $A_o$, respectively. It can also be assumed that the motion of the surface points has no in-plane components and that the out-of-plane displacement gives negligible contributions to decorrelation.

For the study of stationary vibrations, it is convenient to consider the time-averaged correlation coefficient $\overline{\rho}$, which can be defined by

$$\overline{\rho} = \frac{1}{T}\int_0^T \rho(t)dt \tag{6.7}$$

where $T$ is the vibration period. This expression can be evaluated by taking into account the time dependence of $\gamma$ and replacing $\rho(t)$ with the expression in Eqt. (6.5). After few passages, where for simplicity $\phi = \omega t$ and $\eta = A/\Gamma$, $\overline{\rho}$ is given by

204

$$\bar{\rho} = \frac{8}{\pi^3} \int_0^{\frac{\pi}{2}} \left[ \arccos(\eta \cos\phi) - \eta \cos\phi \sin\left(\arccos(\eta \cos\phi)\right) \right]^2 d\phi \qquad (6.8)$$

As the vibrating element has a symmetric motion, the integral has been evaluated over one fourth of the oscillation period T. It is also noted that Eqt. (6.8) is valid only for $\eta < 1$, which means that the condition of total static decorrelation ($\gamma = \Gamma$) is never reached during the vibration period. In the case $\eta \geq 1$, it is important to note that $\rho(t)$ gives contributions to the integral of Eqt. (6.7) only when $\gamma < \Gamma$, i.e. $\eta \cos\phi < 1$. Thus for $\eta \geq 1$ the following expression must be considered

$$\bar{\rho} = \frac{8}{\pi^3} \int_{\arccos(1/\eta)}^{\frac{\pi}{2}} \left[ \arccos(\eta \cos\phi) - \eta \cos\phi \sin\left(\arccos(\eta \cos\phi)\right) \right]^2 d\phi \qquad (6.9)$$

The diagram of $\bar{\rho} = \bar{\rho}(\eta)$, presented in Fig. 6.15., has been obtained by combining the results of the numerical integration of Eqts. (6.8) and (6.9), performed on the PC with the program MATLAB® v.4.0. The diagram shows that the average correlation coefficient is a rapidly decreasing function of $\eta$. In particular it can be assumed that decorrelation occurs when $\bar{\rho} < 0.2$ (or equivalently $\eta > 1$), which corresponds to the condition of complete decorrelation for the static case.

Let $I(0)$ and $I(t)$ be the intensity values for a single point in the image plane of the viewing lens at times $t=0$ (object at rest) and at a generic instant $t$ (vibrating object). According to Eqt. (6.2), the correlation coefficient $\rho(t)$ can be written as

$$\rho(t) = \frac{\langle I(0)I(t) \rangle}{\langle I \rangle^2} - 1$$

The time average value of this expression is equivalent to

$$\bar{\rho} = \frac{\overline{\langle I(0)I(t)\rangle}}{\langle I\rangle^2} - 1. \tag{6.10}$$

For the surface points, which do not exhibit any tilt during vibration, $I(0) = I(t)$, and $\bar{\rho} = 1$, as expected. These points can readily be detected by digital subtraction of the speckle images corresponding to the object at rest ($I(0)$) and to the speckle averaged over many vibration periods ($\bar{I}(t)$).
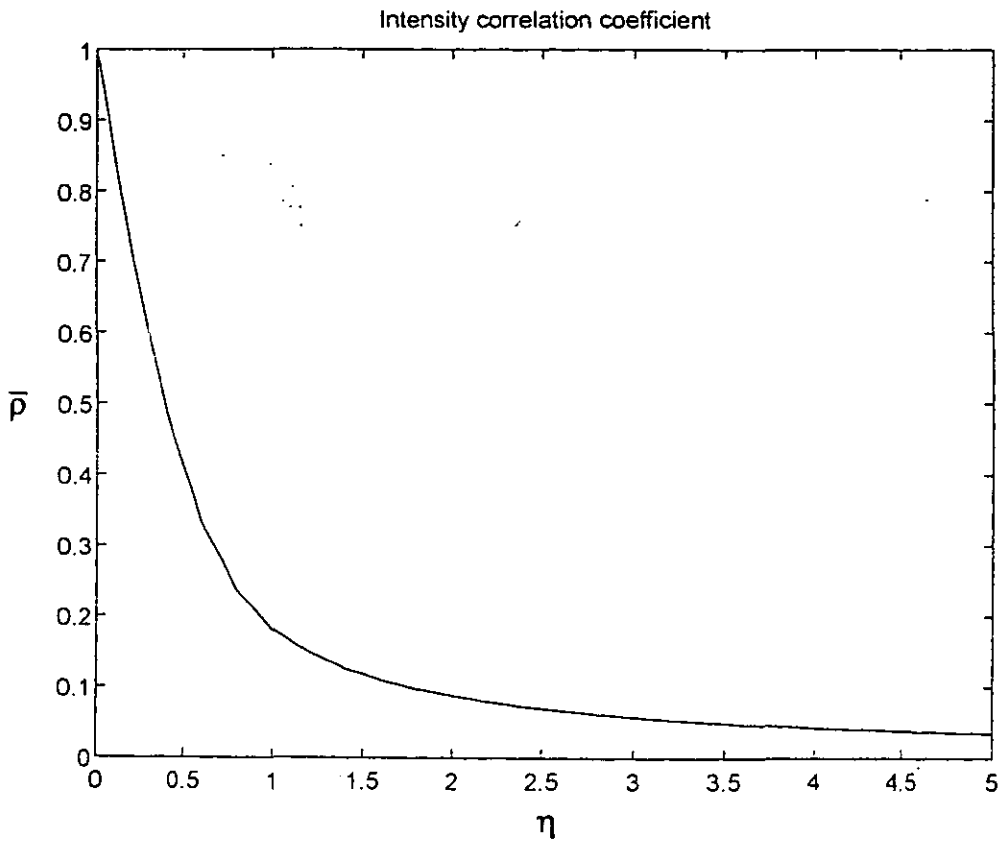


*Figure 6.15. Diagram of the time-averaged correlation coefficient as a function of the ratio* $\eta$ *=A/$\Gamma$.*

During the experiments the object was a square aluminium plate of thickness 1 mm, which was held between two heavy steel block frames having a circular opening of 30 cm. The plate was forced to vibrate by sound waves of sinusoidal form, emitted by a loudspeaker. The source of coherent light was a He-Ne continuous wave laser of 10 mW power, emitting at a wavelength $\lambda = 633$ nm. The expanded laser beam formed an angle of 5° with the viewing direction. A CCD videocamera with a 24 mm lens was placed at a distance of 1 m from the plate. The setup was arranged so as to include the opportunity to perform ESPI vibration measurements by superposing a reference beam

206

on the speckle image of the object (Fig. 6.16.). In this way a direct comparison between the correlation images and the interferograms was possible. The video signal was finally processed with a frame grabber which allowed arithmetic operations on images to be performed in real-time (Data Translation DT-2862, 4 page memory, 8-bit resolution).
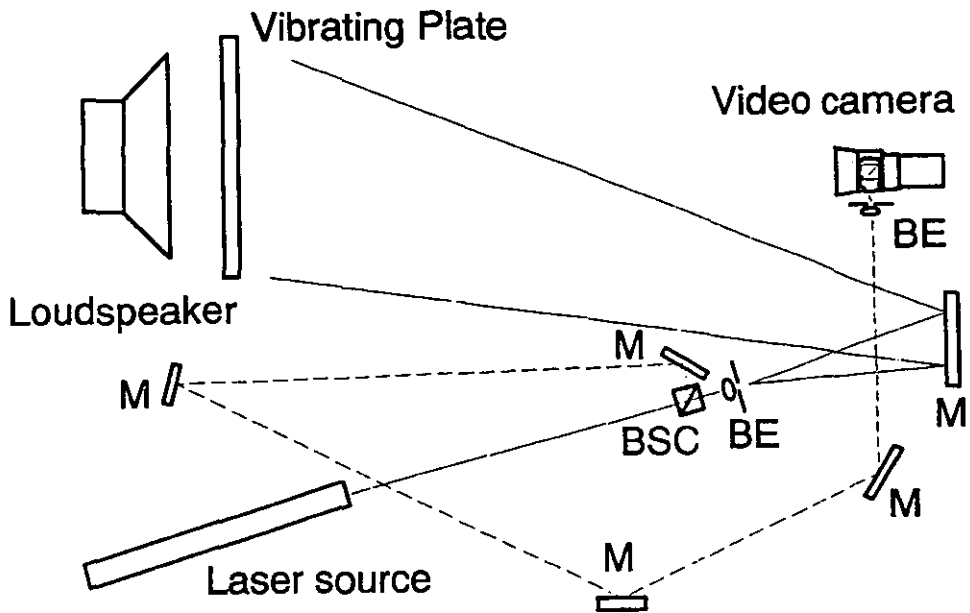


*Figure 6.16. Experimental setup for vibration analysis of a plate by local correlation of speckles or ESPI. The dotted line marks the path of the reference beam used only for the ESPI tests. Letters indicate the mirrors (M), the beam splitter cube (BSC), and the beam expanders (BE).*

Initially, a speckle image $I(0)$ of the plate at rest was acquired and stored in the memory of the frame grabber. The plate was then forced to vibration by sweeping through a range of frequencies. The digital subtraction between the speckle image $\bar{I}(t)$ of the vibrating object and $I(0)$ was performed and displayed on a B/W monitor in real-time. At the resonating frequencies of the plate, most pixels of the subtraction image became bright indicating the occurrence of speckle decorrelation. It was only in correspondence to antinodes and saddle points of the vibrating surface that the displacement had negligible tilt components and dark spots (or lines) were observed. This has been demonstrated in the following with a comparison between the subtraction images and the ESPI interferograms.

In Fig. 6.17.a, the results relating to a vibration mode with two nodal diameters are presented. As for time-average holography, the brightest fringes of the ESPI interferograms represent the nodal lines of the vibration modes. It is therefore clear that the central dark point in the subtraction image corresponds to a saddle point, whereas the other four indicate the positions of the antinodes. A mode with one nodal diameter has been considered in Fig. 6.17.b. Unlike the previous case, the central dark point of the subtraction image is an antinode, and the dark circle represent an antinode circular line. The correlation method has also been used for the detection of other vibration modes and their resonating frequencies, as illustrated in Fig. 6.18.
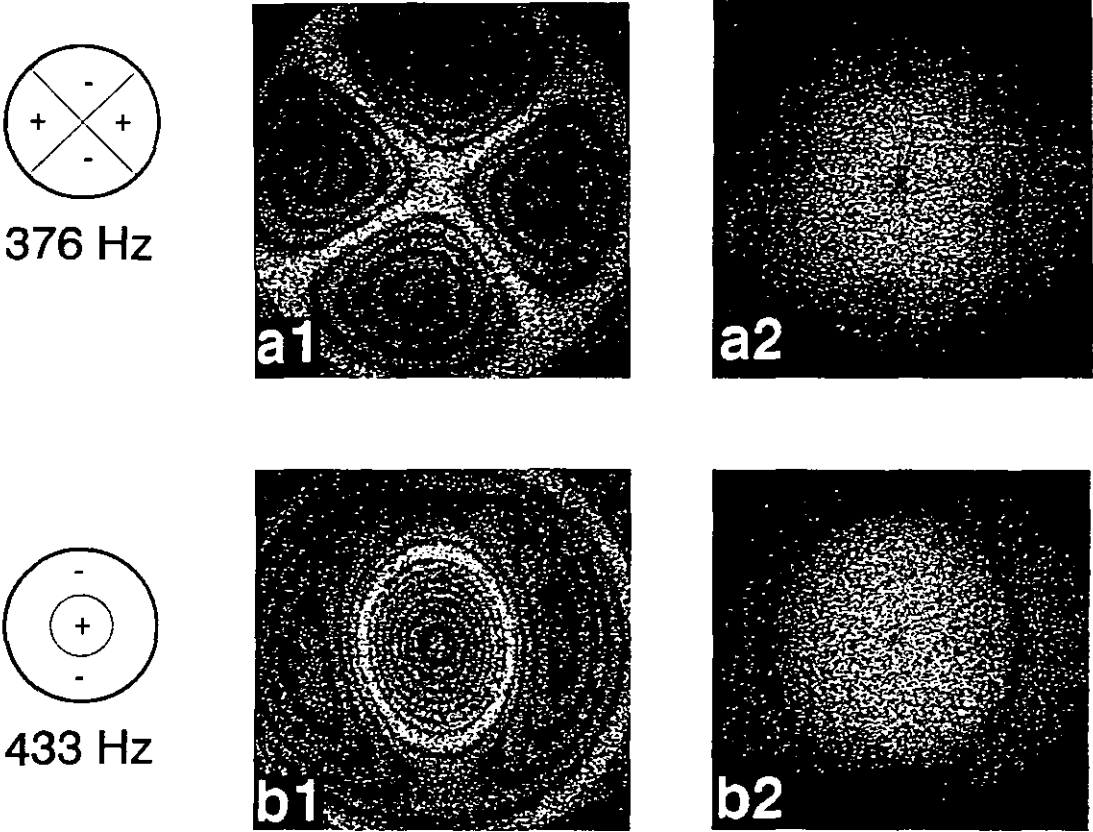


Figure 6.17. ESPI interferograms (a1 and b1) and correlation images (a2 and b2) for two vibration modes of a circular plate. A sketch of the theoretical nodal system has also been drawn.
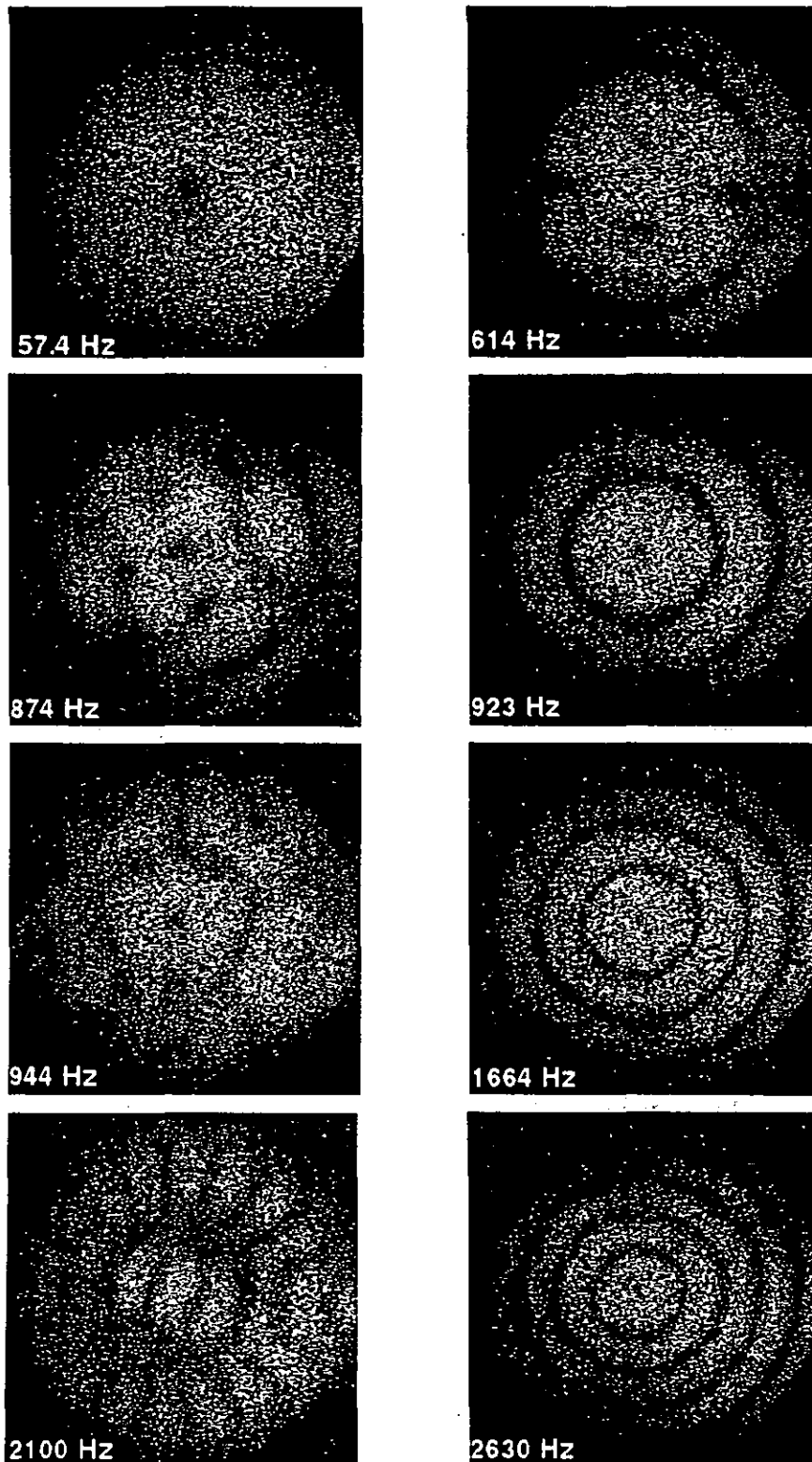
*Figure 6.18. Subtraction images of the aluminium plate vibrating at the indicated frequencies.*

These results clearly demonstrate the potentialities of the local correlation method for the detection and identification of resonance modes of a vibrating object. The proposed application can be considered to some extent a novel version of the speckle technique described by Ennos in [10] (p.248). Both techniques, in fact, rely on the detection of surface points not exhibiting tilt displacement. The experiments reported in [10] were performed by observing the spatial variations of speckle contrast in the image of the vibrating object.

With the correlation method, the antinode points (or lines) of the vibration profile are revealed as dark zones in the subtraction images. The presence of saddle points, which also appear dark, can, however, make the results difficult to interpret. In most cases possible ambiguities can readily be eliminated by taking into account the nodal system of the vibration mode being examined.

The sensitivity of the local correlation technique depends on the observation geometry. In fact, for a surface element speckle decorrelation occurs when $\eta = 1$, or in other words when its maximum tilt angle $A$ is equal to $\Gamma$, which is related to the geometric parameters of the optical layout through Eqt. (6.6). This means that the sensitivity can be increased by placing the object at a larger distance from the videocamera, by reducing the aperture diameter, and by increasing the illumination angle. It could be shown that the local correlation method is less sensitive than time-average holography or ESPI, which can measure vibration amplitudes in the submicrometric range.

## 6.4.2. Surface defect detection

It is well-known that when a non metallic object is illuminated, a fraction of the light impinging on the surface will be transmitted to the volume. According to the interactions between the optical radiation and the atoms of the material, the light transmitted will be absorbed, or scattered. Thus, in general, the speckle pattern obtained by illuminating a diffusing object with laser light can be considered as the result of both surface and volume scattering. To realise the importance of volume scattering in speckle formation it is sufficient to illuminate with a narrow laser beam a piece of finely-polished marble. Although the surface is smooth, well contrasted speckles can be observed on a screen.

Moreover it can be readily proved that volume scattering greatly contributes to speckle decorrelation phenomena. In fact, it is well known that when a metallic object is slightly tilted, the corresponding speckle pattern will be translated in the observation plane. If a piece of marble is tilted, the speckle pattern will modify its spatial distribution instead of

being translated. Multiple scattering effects inside the volume increase the decorrelation associated with surface displacements.

Apart from translucent materials for which volume scattering can be significant, there are many materials (paper, plastic, stone) which, albeit at a lower extent, exhibit amplified decorrelation effects when the object surface is deformed. Consequently, for objects made of these materials the local correlation method can be used to detect the presence of surface defects, which, as it has been demonstrated in Chapter 4, cause anomalous deformation.

Some experiments have been carried out on wooden samples, the surfaces of which were primed with layers of gesso and glue (see for more details Sec.4.4.2.2). Surface deformation was produced by heating the samples with an IR lamp. It was decided to use an ESPI setup (see Fig. 6.19.) where, by blocking the reference beam, local correlation tests were readily performed. This arrangement was chosen in order to allow a direct comparison between the two methods. For both techniques the resulting images were obtained by digital subtraction.
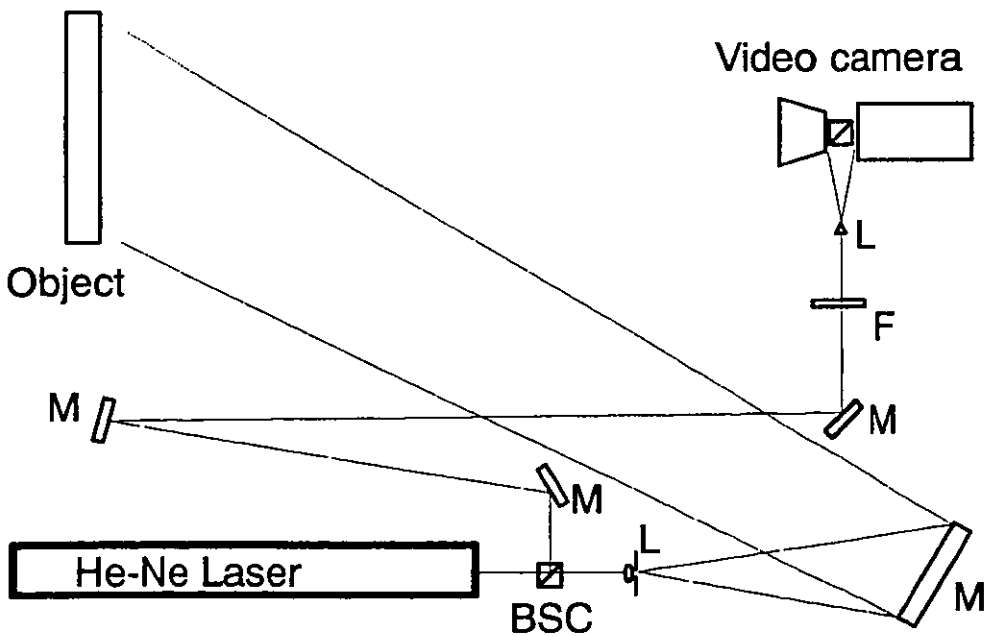


*Figure 6.19. Optical setup used for ESPI measurements sensitive to out-of-plane displacements and local correlation tests. M (mirror), L (lens), F (attenuation filter), BCS (beam splitter cube).*

211

In Fig. 6.20.a the ESPI interferogram of a squared panel containing several simulated detachments of priming layers is presented. The panel was heated for 30 seconds with a 100 W infrared lamp placed at 1 metre from the surface. The interferogram was recorded during the cooling phase. The time interval between the exposures was two seconds. The ring-shaped fringes indicate the presence of five detachments. The same defects were also detected with the local correlation method as depicted in Fig. 6.20.b. The cooling phase was still considered for image acquisition, but a longer interval ($\approx$ 20 seconds) between the exposures was necessary to observe the decorrelated areas.
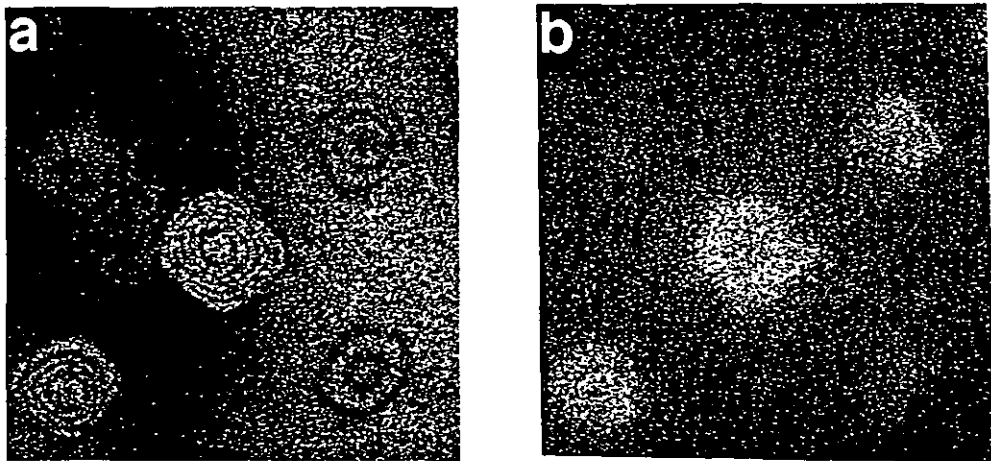


*Figure 6.20. Simulated detachments in a wooden panel: a) ESPI interferogram. b) Correlation image.*

The inspection of another wooden sample (see Fig. 6.21.) was made with the same experimental procedure. The illuminated area contained three detachments of different sizes. In the ESPI image of Fig. 6.21.a., two defects are clearly visible, whilst the third is almost completely hidden by the interferometric fringes. However, when local correlation is applied, the third defect is much more visible than the others and its shape can be precisely determined (see also Fig. 6.21.d.). Only by imaging the area around this small detachment, was it possible to obtain the relative deformation fringes (Fig. 6.21.c).
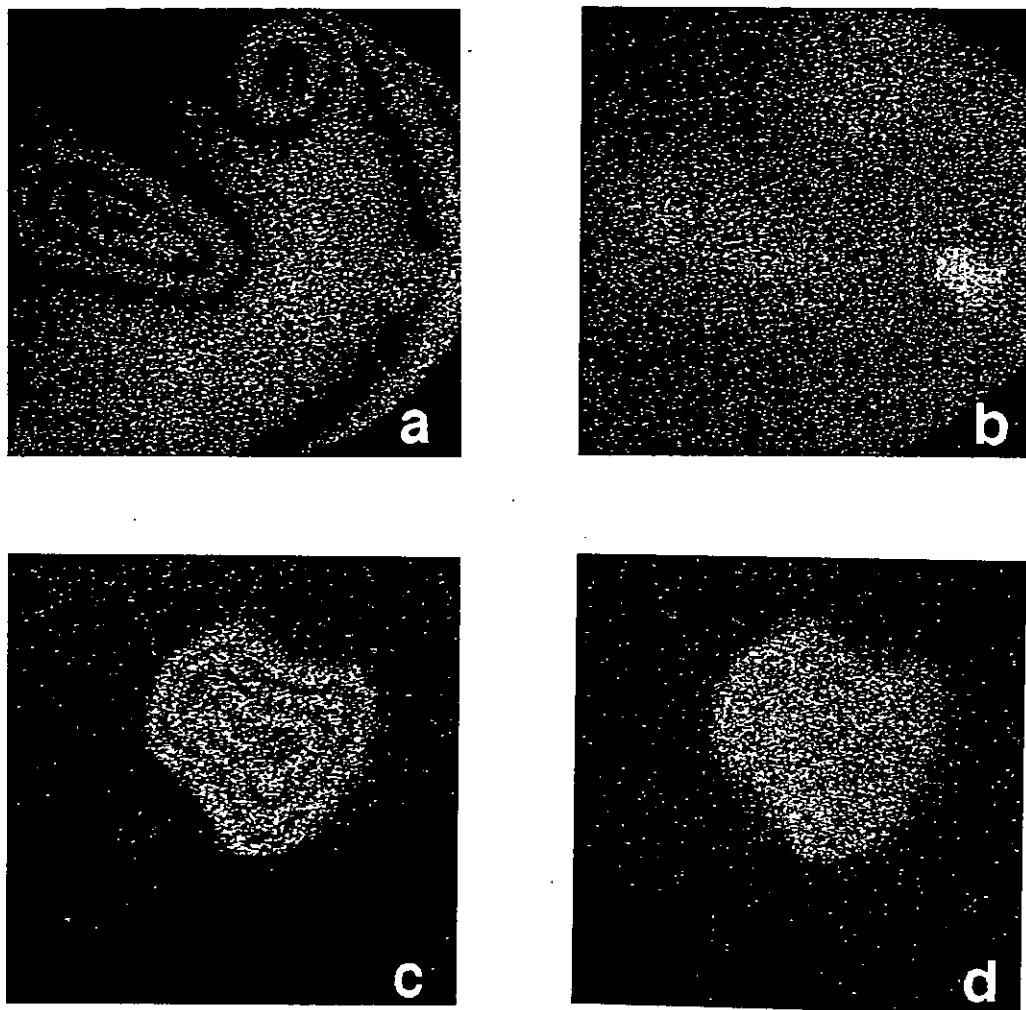
*Figure 6.21. Simulated detachments in a wooden panel: a) ESPI interferogram. b) Correlation image. c) Detail of the small detachment with ESPI. d) Detail of the small detachment with local correlation.*

The experiments described demonstrate that the local correlation method is suited to the detection of subsurface detachments in primed wooden panels. The results presented can be attributed to the pronounced micro displacements of the surface corresponding to the damaged areas and to the accentuated decorrelation effects related to the scattering properties of the objects investigated.

## 6.5. Conclusions

The method of local correlation of laser speckle has been presented both theoretically and experimentally. A correlation coefficient has been introduced and expressed as a function of the absolute difference of speckle intensities. In practice, speckle decorrelation has been detected as bright areas in the subtraction image of two speckle patterns recorded at different times. Since no reference beam was necessary, the experimental setup was very simple and insensitive to external disturbances.

The proposed technique has been applied to the study of stone decay caused by salt crystallisation phenomena. The formation of efflorescence on the surface of porous stone materials has been investigated. The experiments have been performed on stone samples subjected to ageing cycles, which accelerated the deterioration process. The method allowed the early detection of salt efflorescence together with a precise distribution of its intensity. The experiments have highlighted the influence that the geometric shape, and the material defects, such as the "tubuli", have on the water evaporation process.

In principle, the method is only sensitive to surface microstructural changes. However, since stone surfaces are not totally reflecting, local variations inside the volume can also alter the value of the correlation coefficient. A quantification of surface change is therefore not trivial as it would need a detailed knowledge of the surface and volume scattering properties of the stone. Nevertheless, the correlation diagrams, obtained by monitoring the evaporation stage of salt crystallisation cycles, described in detail the temporal dependence of the efflorescence rate.

Other possible applications of the local correlation method have been explored. In the study of stationary vibrations, correlation measurements have proved effective for determining the resonant frequencies, and identifying the modes of a vibrating plate. Digital subtraction has been performed between the speckle patterns recorded with the plate at rest and during vibration. As decorrelation occurred only for the surface elements undergoing tilt or in-plane displacements, the antinode points of the vibration modes were revealed.

Moreover, detachments between the priming layers of wooden samples have successfully been detected. In the experiments, decorrelation was caused by thermal deformation of the primed surfaces. The results of the correlation tests have been confirmed by ESPI inspection.

214

Finally, it is noted that future work could be developed along two main lines. The former consists of continuing the correlation studies on salt efflorescence mechanisms in other stone materials. Important results for the conservation work could also be achieved by performing *in-situ* measurements. The latter concerns the application of local correlation methods to the study of other phenomena involving micro structural changes of rough surfaces, such as crack propagation.

## 6.6. References

[1] Chuang K.C., "Application of the optical correlation measurement to detection of fatigue damage", Materials Evaluation, (1968) 26 116-119

[3] Indebetouw G., Tschudi T., Herziger G., "Quality control of small mechanical pieces using optical correlation techniques", Applied Optics, (1976) 15 516-522

[2] Owen R.B., Liu H.K., "Optical correlation of surface displacement", Optical Engineering (1979) 18 266-272

[4] Hinsch K.D., McLysaght, Wolff K., "Tilt-compensated real-time holographic speckle correlation", Applied Optics, 31 5937-5939

[5] Leger D., Mathieu E., Perrin J.C., "Optical Surface Roughness Determination Using Speckle Correlation Technique", Applied Optics (1975) 14 872-877

[6] Genceli O.F., Schemm J.B., Vest C.M., "Measurement of size and concentration of scattering particles by speckle photography", Journal of the Optical Society of America A, (1980) 70 1212-1218

[7] Chu T.C., Ranson W.F., Sutton M.A., Peters W.H., "Applications of digital-image-correlation techniques to experimental mechanics", Experimental Mechanics, (1985) 25 232-244

[8] Owner-Petersen M., "Decorrelation and fringe visibility: on the limiting behavior of various electronic speckle-pattern correlation interferometers" Journal of the Optical Society of America A, (1991) 8 1082 -1089

[9] Yamaguchi I., "Speckle displacement and decorrelation in the diffraction and image fields for small object deformation", Optica Acta, (1981) 28 1359-1376

[10] Ennos A.E., "Speckle interferometry", in "Laser Speckle and related Phenomena", J.C.Dainty, ed. (Springler-Verlag, Berlin, 1975), pp 203-253

[11] Goodman J.W, "Statistical properties of laser speckle patterns", in "Laser Speckle and related Phenomena", J.C.Dainty, ed. (Springler-Verlag, Berlin, 1975), pp 9-75

[12] Arnold A., Zehnder K., "Stone weathering on monuments", in "The conservation of monuments in the Mediterranean basin. Proceedings of the 1ª International Symposium Bari 7-10 June 1989", F.Zezza, ed. (Grafo, 1990) pp 38-46

[13] Gauri K.L., Holdren G.C., "Pollutant effects on stone monuments", Environmental Science & Technology, (1981) 15 386-390

[14] Alessandrini,G., Bocci, A., Bugini, R., Emmi, D., Peruzzi, R., Realini, M., "Stone materials of Noto (Siracusa) and their decay", Proceeding of the 7th International Congress on Deterioration and Conservation of Stone, Lisbon, Portugal, 15-18 June 1992, 11-20

[15] Alessandrini, G., Toniolo, L., Cariati, F., and Pozzi, A., "The dolomitic stone of the Richini courtyard in Milan: the problem of the colour and of the provence", Science and Technology for Cultural Heritage, in press

[16] Paoletti D., Schirripa Spagnolo G., Facchini M., Zanetta P., "Digital Correlation of Speckle Images for Stone Surface Diagnostics during Cyclic Salt Crystallisation", in FRINGE'93 Proceedings of the 2nd International Workshop on Automatic Processing of Fringe Patterns, Bremen (Germany) 19-21 October 1993, (ed. Jüptner W., Osten W.), Akademie Verlag (1993) 473-475

[17] Oppenheim A.V., Schafer R.W., "Digital signal processing", Prentice Hall (1975)

[18] Timoshenko S.P., "Vibration problems in engineering", (1955), 3rd ed., Van Nostrand

# Conclusions

Detailed summaries and remarks regarding the experimental results are presented in the concluding sections throughout the chapters of the thesis. In these conclusions, the thesis' work will be discussed from a more general point of view, including novel applications and future developments.

The conclusions are divided into three parts: non destructive testing via interferometric techniques, optical contouring, and local correlation of laser speckle. The implications in the field of artwork conservation are presented and some recommendations to be followed during the measurements are included.

## Non destructive testing via interferometric techniques

The development and testing of portable systems for interferometric inspection of artifacts has been one of the major achievements of this work. The measurements performed in-situ (churches and restoration laboratories) demonstrated the use of ESPI as a practical NDT tool for artwork diagnostics. The main characteristics of the ESPI systems developed are high measurement accuracy, full-field inspection, and real-time operation. The original design of the portable systems is based on the use of optical fibres, which allow a considerable reduction of the number of optical elements and alignments. The two instruments developed consist of a compact and lightweight optical head mounted on a tripod, a laser source, which is connected to the optical head with an optical fibre, a PC unit for acquisition and processing of the speckle images, and a monitor for displaying the interferometric fringes.

An important feature of these instruments is real-time fringe formation, which is very useful during the measurements. Frame by frame subtraction allows the operator to be immediately aware of the occurrence of unwanted effects such as rigid body movements, and vibrations. Moreover, real-time measurements are well-suited to the analysis of thermal deformation as the heating parameters (heating time, distance heat source-object) can readily be optimised (see Sec. 4.1.5.).

A variety of defects can be detected by monitoring thermal deformation related to heating (or cooling) of the object surface. The temperature of the surface is usually changed by a few degrees with a flow of moderately warm air or with the radiation from an IR lamp. The use of a lamp is preferred as the heating is more uniform and air turbulence effects are minimised.

It is also noted that the experimental arrangement for holding the object has to be carefully considered. Several tests may be necessary before reaching a satisfactory solution for the best visualisation of defects. Out-of-laboratory measurements should be performed in rooms or areas as far as possible from sources of vibrations. Abrupt changes of ambient light during real-time monitoring may result in a loss of fringe contrast. This can be avoided by protecting the measuring setup with curtains or screens.

Because of the high sensitivity of the technique to micrometric displacements, it is important that the object has a rigid support. Mural frescoes, paintings on wood, and on terracotta can readily be investigated, whilst the inspection of paintings on canvas, not considered in the thesis, seems to be more complicated. Pulsed holography could be applied as an alternative technique, but the interferograms will be strongly affected by the natural motion of the canvas and the detection of defects would be very difficult.

In most cases, it is possible to infer the nature of the defects from the shape of the interferometric fringes. Closed rings are typical of detachments, whilst interrupted fringes indicate the presence of cracks. In the future, by using a software for image composition, a map of the surface defects will be obtained for a whole artifact. This map will provide unique documentation of the conservation state. Automatic recognition of defects is still an open problem among scientists, although some studies are being made in the field of fringe analysis. If a picture of the inspected area is stored, the size and location of defects can precisely be determined (see Sec. 4.3.3.3.).

The results obtained before and after consolidation of detachments confirmed the importance of interferometric techniques for controlling the effectiveness of repair work. An interesting application could also be the evaluation of the conservation conditions in museums. Consider, for example, the deformation effects associated with the thermal gradients produced by the illumination lamps of an exhibition. Moreover, according to the results obtained on violins (Sec.4.2.), studies on the mechanical properties of wooden planks or joints used for restoration could be performed. The areas of stress concentration will readily be identified and useful hints for the design of structural elements will be obtained.

As long as ESPI measurements are concerning the detection of flaws, the use of digital image processing can be limited to enhancing the fringe contrast. The accurate evaluation of the interferometric phase is necessary for deformation studies, such as those performed on violins (see Sec.4.2.). In this case, the optical setup requires the addition of a phase-shifting device or micrometer adjustments, which can readily be arranged and give excellent results in the laboratory. In-situ, however, external disturbances may introduce unwanted phase-shifts, which affect the results. From the studies presented in see Sec.3.3. it can be concluded that digital techniques based on the processing of a single interferogram, such as Fourier analysis with additional carrier fringes, are most suited to in-situ measurements. However, it should be noted that Fourier based techniques fail to solve fringe discontinuities and retrieve a correct phase distribution only if the spatial frequency bandwidth is limited.

Future developments of portable ESPI systems should consider a larger area of inspection, which for paintings and frescoes is now approximately 10 x 10 cm. In order to increase the dimensions of the inspected area, the parameters to be varied are the optical power and the sensitivity of the video camera. Compact frequency-doubled $Nd^{3+}$:YAG lasers are now available with 200 mW continuous wave power at 532 nm, and a coherence length of approximately 150 m. Innovative performances are also expected from the single-mode laser diode. The CCD market is constantly growing offering a variety of sensors with improved characteristics at reasonable prices. For all these reasons, it is likely that surfaces of paintings or frescoes up to 50 x 50 cm will soon be investigated. It should be noted that for a fixed number of CCD pixels, the larger the inspected area, the smaller the lateral resolution of interferograms. It would therefore be desirable to study the possibility of zooming on details during ESPI measurements.

Although in the present work the portable systems have only been tested in relation to artworks, they can directly be applied to other more conventional areas of NDT inspection, such as composite materials. Future research could be devoted to improve the mechanical stability of the optical head by designing a special tripod or a new vibration free system. The use of a train of laser pulses, synchronised with the videocamera acquisition time, could also be investigated in order to enhance the fringe quality.

Finally, a brief comparison is made between ESPI and some of the NDT techniques presented in Chapter 1, in order to highlight the role of interferometric tests in artwork diagnostics. The techniques able to detect faults in the surface region of artifacts are raking light, thermography, X-rays, and ultrasonic testing. Raking light is very simple

and rather inexpensive. However, only detachments accompanied with swellings of the surface can be detected and information about the extension of the damaged area is not very accurate. Thermography can, in principle, detect surface anomalies which are of the same type as those revealed by interferometric techniques. However, the sensitivity of thermography to several factors (temperature, thermal emissivity, conductance, reflectivity) may cause some difficulties for a correct interpretation of the results on artworks. The resolution of thermographic images is lower than that of ESPI interferograms and the equipment is much more expensive. X-ray radiography is substantially used for the analysis of volume properties, although cracks normal to the surface are detected. Ultrasonic testing is not as common in artwork diagnostics as in other fields. In some cases, ultrasound may alter some features of the artifact since a contact is usually necessary with the inspected object and the mechanical waves may cause damage to the artifact materials. In conclusion, given the numerous advantages over other non-destructive testing techniques (non-contacting nature, speed of inspection, relatively low cost), the proposed interferometers appear to have great potential for routine inspection of artworks.

## Optical contouring

An optical contour system is intrinsically non contact and non intrusive. These features make it very attractive for measuring the surface geometry of artworks. The accuracy required is strongly dependent on the dimensions of the area to be inspected and the precise aim of the measurements. For monitoring erosion processes, which are very slow, a sensitivity of some microns is necessary. A depth resolution of a few tenths of a millimetre is desirable to contour macroscopic details or defects in statues. More coarse measurements with an accuracy of the order of a few centimetres can be sufficient for large objects such as church facades, historical buildings, etc.

The contour measurements, presented in this thesis, were based on holography and fringe projection. For these techniques, depth resolution lies in the range from a few microns to some millimetres. The lateral resolution was determined by the demagnification factor of the imaging system and by image digitisation, i.e. number of pixels per image. In-house developed systems have been used to measure the surface profiles of small objects and specimens of weathered stone. As in the previous case of NDT measurements, particular attention has been given to simplify the optical layout in favour of instrument portability. In this respect, the dual-fibre fringe projection system is probably the most interesting result, even for its prototype design.

In order to minimise the number of geometrical parameters necessary for the extraction of contour data, collimated illumination of the object must be chosen. This also has the advantage that the real contour profile is related to the interference phase by a simple mathematical expression, which can readily be calculated with image processing techniques. However, the size of the inspected area is limited by the dimensions of the collimating optical elements.

Among other factors, the scattering properties of the surfaces have considerable effects on the fringe contrast of contour interferograms. Experiments demonstrated that the algorithms used for phase extraction can successfully handle poorly contrasted interferograms. Measurements can therefore be performed on diffusing objects of different materials and colours. However, the presence of geometrical discontinuities may cause shadowing effects, which prevent phase retrieval for the shadowed areas of the surface. It should be noted that FFT based algorithms usually fail in the vicinity of fringe discontinuities. For this reason they are best suited to measure surfaces with smooth profiles.

The systems developed can find immediate application to measure the amount of wear artificially produced on stone specimens with ageing tests. The application in-situ on monuments for monitoring natural erosion phenomena is still a challenge and requires detailed studies and further experimental work. The main difficulties are related to the extremely low speed of the deterioration processes, which implies an accurate repositioning of the instruments in time intervals of days or months between two successive measurements.

Finally, other applications are presented here in order to highlight the great potential of optical contouring in art. The comparison of the actual state of a damaged surface with the 3D data, obtained from the intact original, will greatly enhance the quality of repair work. This is of the utmost importance when the surface has been severely chipped or when some parts are irreparably lost. In the research field, the digital representation of a surface could be used for the analysis of symmetries or chiselling features in statues. These studies could eventually lead to the discovery of the procedures followed during the making of an artwork and to a deeper understanding of the artist's creative process.

Optical techniques for the contouring of large objects can be used for the production of replicas. A copy is often desired to replace the original for display outdoors where the action of atmospheric and pollutant agents jeopardises the surface conditions. From the acquisition of form data, it could be possible to build reliable mathematical models for the analysis of the static and dynamic response of architectural elements and structures.

These results can give important guidance on the protection against ambient and environmental factors (e.g. traffic, visitors, seismic movements, wind action, etc.) which might alter the static *equilibrium* with dangerous effects on monuments stability.

## Local correlation of laser speckle

A novel method has been proposed for the evaluation of local correlation of laser speckle. A correlation coefficient was defined and expressed as a function of the absolute difference between two speckle patterns. In practice, the method has provided an original and unique visualisation of phenomena involving modification of the surface structure in the micrometric range. Measurements can be performed with simple and low cost equipment composed of a laser source and a PC-based acquisition and processing unit.

Of particular interest for the conservation of monuments has been the study of salt efflorescence on the surface of porous stones. The tests, performed on specimens artificially aged, unveiled novel aspects regarding the dynamic properties of salt formation, e.g. spatial distribution of salt activity, influence of material discontinuities and defects. By recording correlation images at fixed time intervals, the whole crystallisation process has been monitored. Diagrams referring to salt formation over many hours have also been obtained and compared for different cycles. As for the case of ESPI measurements, real-time operation is fundamental, especially for determining the time parameters of the tests.

Further studies should investigate surface and volume scattering of the stone microstructure in order to establish their precise role in speckle decorrelation phenomena. This could be very helpful for a better quantitative assessment of the crystallisation phenomena. The method seems to be suited for in-situ inspection since it is not as sensitive as interferometric methods to external vibrations. However, for outdoors operation, it should be noted that surface wetting (rain, dew, moisture, etc.) could make measurements very difficult because of the strong speckle decorrelation associated with water movements on the inspected area.

Local correlation images of stationary vibrations can be used as an alternative to holographic and speckle interferograms for the identification and visualisation of vibration modes. The theoretical analysis regarding the relation between the time-averaged correlation coefficient and surface tilt during vibration can be a starting point for quantitative measurements of the vibration amplitude.

Measurements of surface changes associated with the growth of bio-indicators of pollutants such as certain species of lichens could be an interesting contribution to environmental sciences. On the basis of the results obtained for wooden specimens with primed surface layers, the potential of local correlation of laser speckle as an NDT technique could further be investigated.

# Appendices

## A. Programs for image processing

### A.1. C source code

In this section, the source code of six programs is presented. **PHASE.C, UNWRAP.C, REALTIME.C,** and **LOC_COR.C** have been written for PC operation and have been compiled with Microsoft® C version 6.00. running under MS-DOS® O.S. version 5.00.

**SHIFT_2.C** and **CARRIER.C** are fragments of larger codes written for a workstation Sun Sparc-10 under UNIX O.S. 4.3.1. Routines for performing basic operations in the Fourier plane from the software package KHOROS 1.0 patch 5 have been used. The images have been acquired and stored with a PC-based system. Further conversion into the KHOROS format has been necessary before processing the interferograms.

## A.1.1. Phase.c

/*PHASE.C extracts the phase from 4 interferograms shifted by π/2.
This program operates on images stored in the buffer memory (512 x 512 x 4 pages) of a
IT FG-100 frame grabber hosted in a personal computer. Some functions of the software
library ITEX100 have been used*/

```
/* Constants */
# define PI 3.141592654
```

```
/* External Functions */
BYTE        brpixel(int,int);        /*returns the value of a pixel (from itex100.h)*/
void        bwpixel(int,int,BYTE);   /*writes a value to a pixel (from itex100.h)*/
double      atan(double);            /*evaluates the arctangent (from math.h)*/
```

```
/* Main program*/
main() {
unsigned int   x,y,st_x,st_y,end_x,end_y;   /*pixel co-ordinates*/
double         phased;                       /*phase value in double precision*/
BYTE           phase;                         /*integer phase value in the range 0-255*/
BYTE           im1,im2,im3,im4;               /*im(n) is a pixel value of image (n)*/
int            d1,d2;                         /*difference between two pixel values*/

for (y=st_y; y<=end_y;y++)
        for (x=st_x; x<=end_x;x++)  {
                im1=brpixel(x,y);
                im2=brpixel((512+x),y);
                im3=brpixel(x,(512+y));
                im4=brpixel((512+x),(512+y));
                d1=im4-im2;
                d2=im1-im3;
                phased=ph2pi(d1,d2);
                phase=tobyte(phased);
                bwpixel(x,y,phase);  }
}
```

```
/* Functions */
double
ph2pi(a,b)                                    /*evaluates the arctan modulo 2π*/
int          a,b;  {
double       z,p;

if (b!=0)       z=atan((double)(a)/(double)(b));
else if (a>0)   z=PI/2;
else if (a<0)   z=-PI/2;
if (b>=0)       p=z;
else            p=z+PI;
return(p);      }
```

```
BYTE
tobyte(d)       /*converts the phase from double precision to a value in the range 0-255*/
double       d;  {
BYTE         p;
p=(BYTE)((d+PI/2)*128/PI);
return(p);      }
```

## A.1.2. Unwrap.c

/*UNWRAP.C reconstructs the absolute map of phase from the phase values wrapped in the range 0-2π.
This program operates on one phase image stored in a page of the buffer memory of a IT FG-100 frame grabber. Some functions of the software library ITEX100 have been used*/

```c
/* Constants */
# define THRESHOLD 128              /*threshold value*/


/* Main program */
main() {
unsigned int    x,y,st_x,st_y,end_x,end_y;    /*pixel co-ordinates*/
int             d;                            /*difference between two pixel values*/
BYTE            os=128;                       /*offset or fringe order*/
BYTE            v_os=128;                     /*offset along the vertical direction*/
BYTE            max_os=128, min_os=128        /*maximum and minimum values of os*/
BYTE            n_fringes;                    /*number of fringes in the wrapped map*/
BYTE            old_val, new_val;             /*wrapped and unwrapped pixel values*/
BYTE            os_val;                       /*offset value*/
for (y=st_y; y<=end_y;y++) {                  /*evaluation of the offset map*/
        for (x=st_x; x<=end_x;x++) {
                woffset(x,y,os);
                d=deltah(x,y);
                os+=doffset(d);
                update(); }
        d=deltav(st_x,y)
        v_os+=doffset(d);
        os=v_os;
        update(); }
n_fringes=max_os-min_os;                      /*calculation of the unwrapped values*/
if (n_fringes!=0)for (y=st_y; y<=end_y;y++)
        for (x=st_x; x<=end_x;x++) {
                old_val=brpixel(x,y);
                os_val=brpixel(x,(y+512));
                old_val-=min_os;
                new_val=(old_val+(os_val*256))/(n_fringes+1);
                bwpixel(x,(512+y),new_val); }
else    puts("Unwrapping is not necessary");
}


/* Functions */
int
deltah(x,y)                                  /*returns the difference between two*/
int             x,y; {                       /*adjacent pixels along the horizontal*/
int             p;                           /*direction*/
p=brpixel(x+1,y)-brpixel(x,y);
return(p); }


int
deltav(x,y)                                  /*returns the difference between two*/
int             x,y; {                       /*adjacent pixels along the vertical*/
int             p;                           /*direction*/
p=brpixel(x,y+1)-brpixel(x,y);
return(p); }
```

```
int
doffset(d)                                    /*return the offset increment if any*/
int             d; {
.int            p=0;
if (d<=THRESHOLD)
        ++p;
else if (d>= +THRESHOLD)
        --p;
return(p);  }


void                                          /*writes the offset map*/
woffset(x,y,o)
int             x,y;
BYTE            o;
{ bwpixel(x,(512+y),o);  }


void                          /*updates the offset minimum and maximum values*/
update() {
if (os>max_os) max_os=os;
else if (os<min_os)     min_os=os;  }
```

## A.1.3. Realtime.c

/*REALTIME.C performs real-time subtraction between the current frame and an image stored in page 1 of the frame buffer.
This program operates on a PC equipped with a DATA TRANSLATION DT2862 frame grabber (512 x 512 pixels x 4 pages). Some functions (is_) are from the library DT-IRIS*/

```
/* Main program*/
main() {
int     n,i=1;          /*indexes*/
int     abs_lut[512];   /*resulting lut array for absolute subtraction*/
char    name[20];       /*image name*/
char    fname[20];      /*image file name*/
```

/*Initialisation of the hardware and software routines*/
```
is_initialize(); is_select_input_frame(1); is_select_output_frame(1); is_set_sync_source(1);
is_init_luts(); is_select_ilut(0); is_select_olut(0); is_frame_clear(0);
for (i=0;i<512;i++) {                   /*Definition of the resultant lut*/
        n=256-i;
        abs_lut[i]=abs(n);  }
is_load_rlut(2,abs_lut);
/*acquires the reference image on page 1*/
is_load_olut_sval(0,0,0,255,0);         /*puts 0 to green*/
is_load_olut_sval(0,255,255,0,0);       /*puts 255 to red*/
is_display(1);                          /*displays the image in page 1 on the monitor*/
is_passthru();                          /*grabs images from the video camera*/
saveim(1);                              /*stops acquisition and saves the image on disk if
                                        desired*/
/*acquires images and shows the absolute subtraction on page 0*/
is_init_luts();
is_select_input_frame(0);
is_select_output_frame(0);
is_alu_passthru(38,1,2);                /*subtracts the images */
saveim(0);                              /*stops subtraction and saves the image on disk if
                                        desired*/
```

228

```c
is_end();
}
```

/* *Functions* */
*void*
saveim(frame)                          /*freezes the acquisition in frame and saves the
                                        image on disk if desired*/

```c
int             frame; {
char    y;      /*yes or no answer*/
int     j;      /*index*/
puts("\n\n Press any key + <CR> to stop subtraction"); scanf("%1s",&y);
is_freeze_frame();
puts("\n\n Do you want to save the image? (y/n)");  scanf("%1s",&y);
if (y=='y') {
        for(j=0;j<20;j++)
                name[j]='\0';
        for(j=0;j<20;j++)
                fname[j]='\0';
        puts("Insert the name without the extension:");  scanf("%s",name);
        strcat(fname,name);  strcat(fname,".img");
        is_save(frame,0,1,0,fname);}}
```

## A.1.4. Loc_cor.c

/*LOC_COR.C performs the calculation of the correlation coefficient $\delta=1-\rho$ ($\rho$ is defined
by Eqt.(6.3)) over a specified Area of Interest (AoI) at regular time intervals. The weight
of the specimen is also monitored by reading the weight data from a Sartorius Research
R 200 D balance connected through a RS232 interface.
This program operates on a PC equipped with an Imaging Technology OFG Vision Plus
frame grabber (1024 x 512 pixels). Functions from the ITEX library (ofg_) and from the
ECL v 1.0 library (xc_) have been used for controlling the frame grabber and the
RS-232 interface, respectively.*/

/* *Global variables* */
```c
int     imgs;           /*number of subtraction images to be recorded*/
time_t  dt1;            /*time interval between two subtraction images (min)*/
time_t  dt2;            /*time interval between two speckle images (sec)*/
char    name[20],fname[20];    /*image and file names*/
int     start_x, start_y, width_x, width_y;      /*Parameters of the AoI*/
char    fweights[14],faver[14],favers[14];       /*filenames for the weight, average, and
                                                  squared average values*/
double  we_store[1000],m_store[1000],m2_store[1000];  /*arrays of data;weight,average of
                                                       speckle intensities,squared
                                                       average of speckle intensities*/
int     we_i, m_i, m2_i,imag_n;         /*counters*/
```

/* *Main program* */

```c
main() {
time_t  dt,t,t1;
char    c;

hardw_init();  rs232_init();_    .... /*Initialisation of the hardware and software routines*/
input_data();                   /*reads input data*/
init_filenames();               /*writes the filenames*/
dt1 *= 60L;
time(&t1);                      /*reads the time*/
get_weight();                   /*reads the weight from the balance*/
```

```
acquisition();                    /*acquires and subtract the speckle images*/
media(PAGE2_I);                   /*calculates the average*/
media2(PAGE1_I);                  /*calculates the average of the squared values*/
imag_n+=1;
do {                              /*repeats the operation at time intervals dt*/
  time(&t);
  dt = (long)difftime(t,t1);
  if (dt > dt1) {
    time(&t1);
    get_weight();
    acquisition();
    media(PAGE2_I);
    media2(PAGE1_I);
    imag_n+=1; }}
while (imag_n < imgs);
save_tables();                    /*saves data to files*/
}


/* Functions */
void
init_filenames(void) {
memset(fweights,0,12);                            /*empties the filename*/
strcat(fweights, name);  strcat(fweights, "we.dat");/*writes the new filename*/
memset(faver,0,12);                              /*empties the filename*/
strcat(faver, name);  strcat(faver, "m.dat");    /*writes the new filename*/
memset(favers,0,12);                             /*empties the filename*/
strcat(favers, name);  strcat(favers, "m2.dat"); } /*writes the new filename*/


void
save_tables(void) {
FILE *save;
int n;
save = fopen(fweights,"w");
for( n = 0 ; n < we_i ; n++ )
fprintf(save,"%f\t", we_store[n]);
fclose(save);
save = fopen(faver,"w");
for( n = 0 ; n < m_i ; n++ )
fprintf(save,"%ld\t", (long)m_store[n]);
fclose(save);
save = fopen(favers,"w");
for( n = 0 ; n < m2_i ; n++ )
fprintf(save,"%ld\t", (long)m2_store[n]);
fclose(save); }


void
media2(gaoi)
int gaoi; {
int     xm2,ym2,nm2=0;            /*counters*/
int     m2pval=0;                 /*pixel value*/
long    m2p2val=0;                /*squared pixel value*/
double  mean=0.0;                 /*mean value: sum of all pixels in an image*/
char    media_c[20];              /*string*/

memset(media_c,0,20);             /*empties the filename*/

for( ym2 = start_y; ym2 < (start_y+width_y); ym2++ )
  for( xm2 = start_x; xm2 < (start_x+width_x); xm2++ ) {
    m2pval = ofg_rpixel(gaoi,xm2,ym2);
    m2p2val = ((long)(m2pval)*(long)(m2pval));
```

```c
      mean += (double)(m2p2val); }
    m_store[m_i] = mean;
    m_i++;
    gcvt(mean,15,media_c); }        /*converts to string type*/


void
media(gaoi)
int gaoi; {
int       xm,ym,nm=0;    /*counters*/
int       mpval=0;       /*pixel value*/
double    mean=0.0;      /*mean value: sum of all pixels in an image*/
char      media_c[20];   /*string*/
memset(media_c,0,20); /*empties the filename*/
for( ym = start_y; ym < (start_y+width_y); ym++ )
  for( xm = start_x; xm < (start_x+width_x); xm++ ) {
    mpval = ofg_rpixel(gaoi,xm,ym);
    mean += (double)(mpval); }
  m2_store[m2_i] = mean;
  m2_i++;
  gcvt(mean,15,media_c); }        /*converts to string type*/


void
get_weight(void) {        /*gets the weight from the balance*/
                          /*puts the data in an ASCII file readable from MATLAB */
int       n, count;
char      rx_str[32];
char      rx_ch;
memset(rx_str,0,32);      /*empties the filename*/
xc_flush(COM1);           /*clears the memory buffer*/
count = 10;
while ( (rx_ch = (char)xc_getc(COM1) ) != 0x0a );        /*waits for the first character of
                                                          the weight*/
  if( xc_get(COM1, rx_str, &count))                      /*get string from balance*/
  rx_str[1] = 0;
  strcat(rx_str, &rx_str[2]);
  we_store[we_i] = atof(rx_str);
  we_i++; }


void
acquisition(void) {
time_t    dta,ta,t1a;
char      fnumber[5];     /*image file number*/
char      fname[14];      /*filename for saving images*/
memset(fname,0,12);       /*empties the filename*/
strcat(fname, name);      /*writes the new filename*/
itoa(imag_n,fnumber,10);
strcat(fname, fnumber);
strcat(fname, ".ofg");
puts(fname);
ofg_snap(CAMERA,PAGE1_I);
time(&t1a);
ofg_im_save(PAGE1_I,EIGHT_BIT,fname,"");
do {
time(&ta);
dta = (long)difftime(ta,t1a);
if (dta >= dt1a) {                        /*snaps the second image in page 1*/
  ofg_snap(CAMERA,PAGE1_I);
  ofg_im_restore(PAGE2_I,fname);          /*restore the first image in 512-1024*/
  ofg_oparea(PAGE2_I,PAGE1_I,A_MINUS_B,ABSOLUTE);      /*makes the difference*/
```

```
ofg_im_save(PAGE1_I,EIGHT_BIT,fname,""); }}        /*saves the image in page(0) with a
                                                    progressive number*/
while (dta < dt1a);  }
```

## A.1.5. Shift_2.c

/*SHIFT_2.C extracts the phase using FFT algorithms from two interferograms, shifted
in phase by $\alpha$ ($0<\alpha<\pi$).
This program is <u>part</u> of a code developed for Unix O.S. 4.3.1 running on a Sun Sparc-10
(85 Mips & 10 Mflops; 1152 x 900 & 8 bits / 24 screen display). Some functions of the
software library KHOROS 1.0 have been used*/

*struct* xvimage *s1,*s2;   /*Pointers to the complex images (in Khoros format .xv)
                                representing the Fourier Transform of the shifted
                                interferograms*/
/* *Main program*/
{
[...]
```
#define XC_R(i,j,l)   (i*nc*2 + j*2 + l*k)    /*Macros evaluating the position of the Real and*/
#define XC_I(i,j,l)   (i*nc*2 + j*2+1 + l*k)  /*Imaginary parts in a Khoros image*/


nc=s1->row_size;                      /*Number of image columns*/
nr=s1->col_size;                      /*Number of image rows */
k=nc*nr;                              /*Number of image pixels*/


fft1=createimage(nr,nc,...);          /*creates a complex image fft1*/
fft2=createimage(nr,nc,...);          /*creates a complex image fft2*/
mask=createimage(nr,nc,...);          /*creates a complex image mask*/


init_mask(height,width);              /*creates the filter mask*/
lvmul(mask,s1,...);                   /*KHOROS function which multiplies mask
                                      with s1 and puts the result in mask*/
lvfft(mask,...,fft1,...);             /*KHOROS function which performs the
                                      Inverse FFT of mask and puts the result in fft1*/

init_mask();
lvmul(mask,s2,...);
lvfft(mask,...,fft2,...);


ph2pi(fft1);              /*evaluates the arctan modulo 2π, from the complex image and
                          puts the result in an image fi (see ph2pi() in "phase.c")*/
get_alfa();


eliminate_ambiguity();   /*corrects the phase map obtained*/
}
```

/* *Functions* */
*void*
```
init_mask(h,w)                        /*edits the filter mask*/
```
*int*   h,w; {                                  /*mask height (h) and width (w)*/
[...]
```
c1=(float*)(mask->imagedata);         /*address of the data location of mask*/
```
/*clear image*/
```
for(y=0;y<nr;y++)
  for(x=0;x<nc;x++)
        *(c1+XC_R(y,x,0))=*(c1+XC_I(y,x,0))=(float)0.0;
```
/*evaluates the corners of the mask*/
```
st_x = 256-w/2; end_x = 256+w/2+1;
st_y = 256; end_y = 256+h;
```

```c
/*puts to 1 the values of the pixels inside the mask*/
for(y=st_y;y<end_y;y++ )
  for(x=st_x;x<end_x;x++ )
        *(c1+XC_R(y,x,0))=*(c1+XC_I(y,x,0))=(float)1.0;
/*puts to 0 the values of the pixels of a small area about the origin*/
for(y=256;y<260;y++)
for(x=256;x<260;x++)
        *(c1+XC_R(y,x,0))=*(c1+XC_I(y,x,0))=(float)0.0; }


void
get_alfa() {                    /*estimates the phase shift between s1 and s2*/
[...]
alfa=createimage(nr,nc,...);            /*creates a complex image alfa*/
cs1=(float*)(fft1->imagedata);          /*address of the data location of fft1*/
cs2=(float*)(fft2->imagedata);          /*address of the data location of fft2*/
cd=(float*)(alfa->imagedata);           /*address of the data location of alfa*/
for(y=0;y<nr;y++)
  for(x=0;x<nc;x++) {
        r1=*(cs1+XC_R(y,x,0));
        i1=*(cs1+XC_I(y,x,0));
        r2=*(cs2+XC_R(y,x,0));
        i2=*(cs2+XC_I(y,x,0));
        a=r1*i2-i1*r2;
        b=r1*r2 +i1*i2;
        ph2pi(a,b) }}
for(y=0;y<nr;y++)
  for(x=0;x<nc;x++) {
        int nx,dx,ny,dy;
        nx=dx=x+tx;
        ny=dy=y+ty;
        if(dx<0) nx=nc+dx;
        if(dx>=nc) nx=dx-nc;
        if(dy<0) ny=nr+dy;
        if(dy>=nr) ny=dy-nr;
        *(XC_R(ny,nx,0))=*(XC_R(y,x,0));
        *(XC_I(ny,nx,0))=*(XC_I(y,x,0)); }}


void
eliminate_ambiguity(); {                /*corrects the phase map obtained*/
[...]
cs=(float*)(alfa->imagedata);   /*address of the data location of alfa*/
cd=(float*)(fi->imagedata);     /*address of the data location of fi*/

for(y=0;y<nr;y++ )
  for(x= 0;x<nc;x++) {
        float    a,s;
        a=*(cs+X(y,x,0));
        s=*(cd+X(y,x,0));
        *(cd+X(y,x,0))=(a<0.0)?s*(-1.0):s; }}
```

## A.1.6. Carrier.c

/*CARRIER.C extracts the phase from a single interferogram, to which a linear phase
term has been added during the optical recording.
This program is part of a code developed for Unix O.S. 4.3.1 running on a Sun Sparc-10
(85 Mips & 10 Mflops; 1152 x 900 & 8 bits / 24 screen display). Some functions of the
software library KHOROS 1.0 have been used*/

```
struct xvimage *img;        /*Pointer to the complex image (in Khoros format .xv)
                              representing the Fourier Transform of the interferogram*/
/* Main program*/
{
[...]
#define XC_R(i,j,l)   (i*nc*2 + j*2 + l*k)   /*Macros evaluating the position of the Real and*/
#define XC_I(i,j,l)   (i*nc*2 + j*2+1 + l*k) /*Imaginary parts in a Khoros image*/

nc=img->row_size;                   /*Number of image columns*/
nr=img->col_size;                   /*Number of image rows */
k=nc*nr;                            /*Number of image pixels*/

r_image=createimage(nr,nc,...);     /*creates a complex image r_image*/
translate_fft(img,carrier->x_int,carrier->y_int);
lvlpf(img, carrier->o,carrier->t,carrier->c);   /*KHOROS function which performs a low
                                                  pass filter: o, t, c, are the filter order, type
                                                  and cutoff respectively*/
lvfft(img,...,r_image,...);                      /*KHOROS function which performs the
                                                  Inverse FFT of img and puts the result in
                                                  r_image */
ph2pi(r_image);          /*evaluates the arctan modulo 2π, from the complex image
                          (see ph2pi() in "phase.c")*/
}


/* Functions */
void
translate_fft(im,tx,ty)    /*translates the Fourier image in the Fourier plane by the
                            quantities tx,ty*/
struct   xvimage *im;
int      tx,ty; {
copyimagedata(im, &r_image,...);     /*copies img to r_image*/
cs= (float *)(r_image->imagedata);   /*address of the data location of r_image*/
cd= (float *)(im->imagedata);        /*address of the data location of im*/

for( y = 0 ; y < nr ; y++ )
        for( x = 0 ; x < nc ; x++ )  {
        int nx, dx, ny, dy;
        nx = dx = x+tx;
        ny = dy = y+ty;
        if(dx<0) nx = nc+dx;
        if(dx>=nc) nx = dx-nc;
        if(dy<0) ny = nr+dy;
        if(dy>=nr) ny = dy-nr;
        *(cd+XC_R(ny,nx,0)) = *(cs+XC_R(y,x,0));
        *(cd+XC_I(ny,nx,0)) = *(cs+XC_I(y,x,0)); }}
```

## A.2. Holophase II

The software HOLOPHASE II by ROTTENKOLBER HOLO-SYSTEM has been used for the evaluation and processing of holographic interferograms with the four images algorithm (see Sec. 3.3.1.1.). HOLOPHASE II was installed on a Compaq Deskpro 33/e personal computer equipped with a frame grabber, a Digital to Analogue Converter (DAC) card, and a T800 transputer card.

The optical phase is shifted by controlling the position of a piezo-driven mirror with the output voltage of the DAC card. Four images, shifted in phase by $\pi/2$, are acquired by the video camera and stored in the memory buffers of the frame grabber. Once an area of interest has been defined in the form of polygons, automatic processing (phase-shifting and unwrapping) is performed yielding a gray-level image of the absolute phase. Surface displacement can be quantified by supplying the experimental parameters of the measurements. 3D mesh plots and pseudo-colour facilities are included for display purposes.